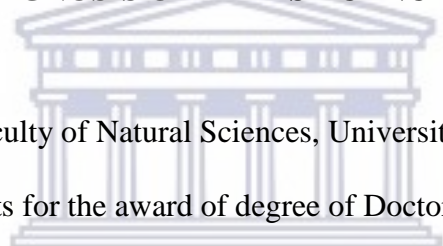




**UNIVERSITY** *of the*  
**WESTERN CAPE**

**FABRICATION OF LUMINESCENT MAGNETIC NANOCOMPOSITES FOR  
DIAGNOSIS OF BREAST CANCER**

A Thesis submitted to the Faculty of Natural Sciences, University of the Western Cape in the fulfillment of the requirements for the award of degree of Doctor of Philosophy in Chemistry



UNIVERSITY *of the*  
WESTERN CAPE  
By

Kiplagat Ayabei

Bsc Chemistry (Jomo Kenyatta University of Agriculture and Technology (JKUAT), Kenya),

MSc Analytical Chemistry (University of Eldoret (UoE), Kenya)

August 2016

## KEYWORDS

---

Magnetic

Nanoparticles

Nanocomposite

Nanocrystals

Breast cancer

Quantum dots

Semiconductor nanocrystals

Inorganic nanocrystals

Luminescence

Cytotoxicity

Molecular beacons

Biomarkers



## DECLARATION

---

I declare that this thesis titled “*Fabrication of luminescent magnetic nanocomposites for diagnosis of breast cancer*” is my original piece of work and has not been presented to any other institution for examination. All the information sourced from literature has been indicated and acknowledged in the form of referencing.

KIPLAGAT AYABEI

Signature..... Date .....



UNIVERSITY of the  
WESTERN CAPE

## ABSTRACT

---

### **Fabrication of luminescent magnetic nanocomposites for diagnosis of breast cancer**

K. Ayabei

PhD. Thesis, Department of Chemistry, University of the Western Cape

In this study we were able to synthesize separately iron oxide magnetic nanoparticles, InP/ZnSe and CdTe/ZnS quantum dots. The iron oxide nanoparticles were coupled with InP/ZnSe QDs to form the luminescent magnetic nanocomposite. The magnetic nanoparticles of the type iron oxide ( $\alpha\text{-Fe}_2\text{O}_3$ ) were synthesized using co-precipitation method owing to its advantages. The fluorescing material InP/ZnSe quantum dots were synthesized using hot injection technique. Meso-2,3-dimercaptosuccinic acid, 3-mercaptopropionic acid, and L-cysteine were used to functionalize the iron oxide nanoparticles. The synthesized InP/ZnSe quantum dots were made water soluble by carrying out ligand exchange processes. The synthesized magnetic nanoparticles were characterized using high-resolution transmission electron microscopy (HRTEM), X-ray diffractometer (XRD), Fourier transform infra-red spectroscopy (FTIR) and superconducting quantum interference device (SQUID). The quantum dots were characterized using photoluminescence Nanolog (PL), HRTEM, XRD, and FTIR. The fluorescent nanocomposite ( $\alpha\text{-Fe}_2\text{O}_3\text{-InP/ZnSe}$ ) was characterized using PL, SQUID, and HRTEM.

The synthesized iron oxide nanoparticles had an average size ranging from 6-13 nm. Functionalization of the particles did not change their sizes significantly. The InP/ZnSe quantum dots had a size range between 4-5 nm. The XRD analysis revealed that the iron oxide nanoparticles had a cubic lattice structure and not face-centered cubic suggesting that the

material was maghemite and not magnetite. On the other hand, the XRD analysis of InP/ZnSe QDs revealed that its structure matched Zinc-blende structure. The FTIR results revealed that the desired functional groups present in the ligands were successfully conjugated to the nanoparticles. For instance, Fe-O bond was observed at around  $580\text{ cm}^{-1}$ , O-H at  $3432\text{ cm}^{-1}$  and thiol group at  $2929\text{ cm}^{-1}$  for meso-2,3-dimercaptosuccinic acid capped  $\alpha\text{-Fe}_2\text{O}_3$  magnetic nanoparticles. The magnetic saturation of the bare magnetic nanoparticles was  $65.67\text{ emu/g}$  whereas the fluorescent magnetic nanocomposite had a much less magnetic saturation of  $6.03\text{ emu/g}$ . The energy dispersive spectroscopy (EDS) also confirmed that all the elements of the nanocomposite were actually present in the designed material.

We carried out cytotoxicity studies for the iron oxide nanoparticles, functionalized iron oxide nanoparticles, InP/ZnSe quantum dots and  $\alpha\text{-Fe}_2\text{O}_3$ -InP/ZnSe nanocomposite. The cytotoxicity studies revealed that all the synthesized materials were less toxic with cell viability greater than 90 % for all. The prepared iron oxide particles were bioconjugated to MUC 1 binding aptamers via streptavidin conjugation. The magnetic nanoparticles were utilized to isolate MUC 1 proteins from lysates prepared from MCF-7 breast cancer cells. Lysates extracted from MCF 12A were used as a control. The suitability of an aptamer conjugated to iron oxide for biomarker enrichment for the first time was demonstrated. The CdTe/ZnS QDs synthesized were used to substitute the traditionally organic fluorophores in the design of molecular beacons. The use of this material resulted in the design of sensitive and stable molecular beacon. The designed MB was able to detect as low as 200 picomolar (pm) of the complementary target and up to  $2\text{ ng}/\mu\text{L}$  of the cDNA extracted from MCF 7 cultured cells.

## DEDICATION

---

This work is dedicated to my family



UNIVERSITY *of the*  
WESTERN CAPE

## ACKNOWLEDGEMENTS

---

To this far, I wish to thank the Almighty God for His good guidance and tender care. He has granted me good health, strength and provided directions at all times of need. My sincere appreciation goes to my supervisors Prof. Martin Onani, Prof. Mervin Meyer and Prof. Teresa Akenga for providing technical support and being available at all times to be consulted for scientific guidance. My gratitude also goes to Prof. Paul Tarus for his valuable connections that enabled me to attend my doctorate studies in South Africa.

I wish to thank all members of Organometallic and Nanomaterials research group namely Mduduzi, Shane, Asanda, Leoni, Thandikhaya, Leandre, Garvin, Shonii, Diyoka, Vuyokazi, Sihle, Hillary and Roz for their support and creating conducive work space in the laboratory. Sincere thanks to Dr. Paul Mushonga and Linda Ouma for their orientation to the glove box, Schlenk line techniques, and PL nanolog machine. I am also very grateful to members of NIC Biolabels unit Nicole, Habeeb, Marius, Namhla, Chipampe, Riziki, Atherton, Phatu, Nandi, Aaron, Mustafah, Lauren and all other members. Wish also to appreciate research group members from Prof. Dejene's group in the University of the free state (QwaQwa campus).

I extend also my gratitude to anyone who in one way or the other contributed to the analysis of my samples. In regard to the analysis I wish to sincerely appreciate Dr. Maskini (PL), Dr. Remy (XRD), Mr. Josephs (HRSEM), Mr. Lesch and all Technicians.

I would wish to thank National Research Foundation and DST/MINTEK Nanotechnology Innovation Centre for financial support. Many thanks go to my family, friends and people of my society who facilitated my coming to South Africa.

May the Lord Almighty bless you more and more in all your endeavors.



UNIVERSITY *of the*  
WESTERN CAPE



## PUBLICATIONS AND CONFERENCES ATTENDANCE

---

### Publications

1. **Kiplagat, A.**, Onani, M. O., Meyer, M., Akenga, T. A., & Dejene, F. B. (2015). Synthesis and characterization of luminescence magnetic nanocomposite. *Physica B: Condensed Matter*, 1–9. <http://doi.org/10.1016/j.physb.2015.08.037>
2. **Kiplagat, A.**, Sibuyi, N. R. S., Onani, M. O., Meyer, M., & Madiehe, A. M. (2016). The cytotoxicity studies of water-soluble InP/ZnSe quantum dots. *Journal of Nanoparticle Research*, 18(6), 147. <http://doi.org/10.1007/s11051-016-3455-5>
3. Paulsen, Z., Onani, M. O., Allard, G. R. J., **Kiplagat, A.**, Okil, J. O., Dejene, F. B., & Mahanga, G. M. (2015). The effect of varying the capping agent of magnetic / luminescent Fe<sub>3</sub>O<sub>4</sub> – InP / ZnSe core – shell nanocomposite. *Physica B: Physics of Condensed Matter*, 1–7. <http://doi.org/10.1016/j.physb.2015.09.005>
4. The development of nanotechnology-based detection system for the diagnosis of breast cancer biomarkers- **In progress**
5. Magnetic nanoparticle conjugates for more efficient capturing of cancer biomarkers- **In progress**
6. The shell optimization of gold-coated iron oxide nanoparticles and demonstration of ease in surface modification- **In progress**

## Conferences attendance

1. **Kiplagat Ayabei**, Martin O. Onani, Teresia A. Akeng'a, and Mervin Meyer "*Adaptation of inorganic nanocrystals for more stable and sensitive molecular beacons for biomarker detection*" **PACN Congress 2015 - Healthcare: From discovery to delivery**, 17<sup>th</sup>-19<sup>th</sup> November 2015 at the University of Nairobi in Kenya- **Oral presentation**
2. **Kiplagat Ayabei**, Martin O. Onani, Teresa A. Akeng'a, Paul Mushonga and Mervin Meyer, "*Luminescent magnetic nanoparticles for biomedical applications*" Advanced materials world congress (AMWC, 2015), Sweden- **Poster presentation**
3. **Kiplagat Ayabei**, Martin O. Onani, Mervin Meyer, Teresa A. Akenga, Francis B. Dejene, 2015. "*Syntheses and characterization of luminescent magnetic nanocomposite for biomedical applications*" The 6<sup>th</sup> South African conference on photonic materials-2015, Mabula lodge, South Africa - **Oral presentation**
4. **Kiplagat Ayabei**, Martin O. Onani, Mervin Meyer, Teresa Akenga. "*Magnetic nanoparticle conjugates for more efficient capturing of cancer biomarkers*" PACN congress 2014, Biodiversity and global challenges: A chemical science approach, UN conference center, Addis Ababa, Ethiopia-**Poster presentation**
5. **Kiplagat Ayabei**, Martin O. Onani, Teresia A. Akeng'a, and Mervin Meyer "*Adaptation of inorganic nanocrystals for more stable and sensitive molecular beacons for biomarker detection*" DST/MINTEK annual NIC workshop Grahams Town, South Africa. **Oral presentation**

## TABLE OF CONTENTS

---

KEYWORDS .....	ii
DECLARATION.....	iii
ABSTRACT .....	iv
DEDICATION .....	vi
ACKNOWLEDGEMENTS.....	vii
PUBLICATIONS AND CONFERENCES ATTENDANCE.....	ix
TABLE OF CONTENTS .....	xi
LIST OF FIGURES .....	xv
LIST OF TABLES.....	xviii
TABLE OF ABBREVIATIONS .....	xix
1 CHAPTER ONE .....	1
1.1 Introduction.....	1
1.2 Cancer .....	1
1.3 Breast Cancer .....	2
1.4 Screening techniques of Breast Cancer .....	2
1.5 Mammography .....	3
1.6 Serum Biomarkers.....	4
1.7 Breast cancer studies .....	5
1.8 Aptamers .....	8
1.8.1 Aptamer applications .....	9
1.9 Molecular Beacons.....	9
1.10 Nanotechnology and nanomaterials .....	14
1.10.1 Magnetic nanoparticles (MNPs).....	14
1.10.2 Synthesis of magnetic nanoparticles.....	14
1.10.3 Co-precipitation method.....	15
1.10.4 Magnetic Properties of magnetic nanoparticles.....	20
1.10.5 Applications of magnetic nanoparticles .....	21
1.11 Quantum dots (QD).....	22
1.11.1 Photoluminescence process of quantum dots .....	23

1.11.2	Ligand exchange strategies.....	29
1.11.3	Cytotoxicity of indium based QDs .....	30
1.12	Fluorescent magnetic nanocomposites .....	32
1.12.1	Synthetic approaches of fluorescence magnetic nanocomposites .....	33
1.12.2	Properties fluorescent magnetic nanocomposites .....	43
1.12.3	Biomedical applications of fluorescence magnetic nanocomposite .....	54
1.13	Purpose of the study/aim of the study .....	63
1.14	Problem statement.....	63
1.15	Significance of the study.....	65
1.16	Objectives.....	66
2	CHAPTER TWO: EXPERIMENTAL.....	67
2.1	Introduction.....	67
2.2	Experimental reagents .....	67
2.3	Characterization and apparatus .....	68
2.4	Experimental procedures.....	69
2.4.1	Synthesis of iron oxide ( $\alpha$ -Fe <sub>2</sub> O <sub>3</sub> ) nanoparticles.....	69
2.4.2	Functionalization of iron oxide ( $\alpha$ -Fe <sub>2</sub> O <sub>3</sub> ) nanoparticles with 3-mercaptopropionic acid.....	69
2.4.3	Functionalization of $\alpha$ -Fe <sub>2</sub> O <sub>3</sub> nanoparticles with L-cysteine.....	70
2.4.4	Functionalization of $\alpha$ -Fe <sub>2</sub> O <sub>3</sub> with dopamine hydrochloride.....	70
2.4.5	Functionalization of iron oxide ( $\alpha$ -Fe <sub>2</sub> O <sub>3</sub> ) nanoparticles with meso-2, 3-dimercaptosuccinic acid .....	71
2.5	Application experiments of the synthesized iron oxide nanoparticles .....	71
2.5.1	Immobilization of streptavidin to iron oxide nanoparticles .....	71
2.5.2	Electrophoretic mobility shift assay (EMSA).....	72
2.5.3	MUC 1 protein capturing .....	74
2.5.4	Quantification of captured proteins using Qubit.....	75
2.5.5	Detection of captured proteins using MALDI-TOF-MS.....	76
2.6	Synthesis of InP/ZnSe quantum dots .....	76
2.6.1	Preparation of Zinc precursor .....	76
2.6.2	Preparation of selenium precursor .....	76
2.6.3	Synthesis of InP/ZnSe nanocrystals.....	77

2.6.4	Size sorting procedure .....	77
2.6.5	Ligand exchange process .....	78
2.6.6	Immobilization of streptavidin to InP/ZnSe nanocrystals.....	79
2.7	Synthesis of CdTe/ZnS quantum dots .....	80
2.8	Streptavidin attachment to 3-MPA capped CdTe/ZnS .....	81
2.9	Synthesis of the Molecular beacon.....	81
2.10	Cell culture and cDNA synthesis .....	81
2.11	Synthesis of the Molecular beacon.....	82
2.12	Detection of the target complementary target and cDNA .....	83
2.13	Synthesis of the $\alpha$ -Fe <sub>2</sub> O <sub>3</sub> -InP/ZnSe nanocomposite .....	83
2.14	Cytotoxicity studies.....	84
2.14.1	Cell culture .....	84
2.14.2	Cytotoxicity studies of iron oxide ( $\alpha$ -Fe <sub>2</sub> O <sub>3</sub> ) nanoparticles.....	85
2.14.3	Cytotoxicity of the InP/ZnSe quantum dots .....	85
2.14.4	Cytotoxicity of the $\alpha$ -Fe <sub>2</sub> O <sub>3</sub> -InP/ZnSe quantum dots .....	85
2.14.5	MTT assay.....	86
2.15	Conclusion .....	86
3	CHAPTER THREE: SYNTHESIS AND CHARACTERIZATION OF IRON OXIDE NANOPARTICLES ..	88
3.1	Introduction.....	88
3.2	Synthesis and characterization of iron oxide nanoparticles.....	88
3.2.1	FTIR analysis of magnetic iron oxide nanoparticles.....	92
3.2.2	XRD data analysis for bare iron oxide nanoparticles.....	94
3.2.3	Magnetic properties of the iron oxide nanoparticles .....	97
3.3	Functionalization of iron oxide magnetic nanoparticles.....	98
3.3.1	Functionalization of $\alpha$ -Fe <sub>2</sub> O <sub>3</sub> with meso-2, 3-dimercaptosuccinic acid (DMSA).....	100
3.3.2	Functionalization of $\alpha$ -Fe <sub>2</sub> O <sub>3</sub> nanoparticles with 3-mercaptopropionic acid.....	108
3.3.3	Functionalization of iron oxide with L-Cysteine .....	109
3.3.4	Magnetic properties of L-cysteine capped Iron oxide.....	112
3.4	Electrophoretic mobility shift assay (EMSA) studies .....	113
3.5	Biomarker enrichment using MNP-MUC 1 binding aptamer .....	116
3.6	Cytotoxicity studies of bare iron oxide and functionalized iron oxide nanoparticles.....	120

3.7	Conclusion .....	122
4	CHAPTER FOUR: SYNTHESIS AND CHARACTERIZATION OF InP/ZnSe QUANTUM DOTS .....	123
4.1	Introduction.....	123
4.2	Synthesis and characterization of InP/ZnSe quantum dots .....	123
4.3	Optical properties of InP/ZnSe nanocrystals.....	129
4.3.1	Monitoring core and shell development of InP/ZnSe nanocrystals using UV-Vis .....	129
4.4	PL characteristics of the aliquots obtained during synthesis of InP/ZnSe characteristics .....	132
4.5	Quantum yield calculations .....	134
4.6	Scale-up synthesis of InP/ZnSe nanocrystals.....	136
4.7	Fluorescing intensities of InP/ZnSe nanocrystals.....	143
4.8	Band gap calculations .....	144
4.9	Size sorting.....	147
4.10	Ligand exchange process .....	149
4.11	Streptavidin Conjugation .....	153
4.12	Cytotoxicity of InP/ZnSe nanocrystals.....	155
4.13	Application of quantum dots in Molecular beacons design .....	157
4.13.1	Surface modification of the quantum dots and design of the MB .....	164
4.14	Application of the QD based molecular beacon for biomarker detection .....	168
4.15	Conclusion .....	171
5	CHAPTER FIVE: SYNTHESIS AND CHARACTERIZATION OF THE LUMINESCENCE NANOCOMPOSITE.....	172
5.1	Introduction.....	172
5.2	Synthesis of Fe <sub>2</sub> O <sub>3</sub> -InP/ZnSe nanocomposite .....	172
5.3	Magnetic properties of the nanocomposite .....	177
5.4	Band gap of the nanocomposite .....	179
5.5	Cytotoxicity of the Fe <sub>2</sub> O <sub>3</sub> -InP/ZnSe nanocomposite.....	181
5.6	Conclusion .....	182
6	CHAPTER SIX: SUMMARY OF RESULTS, CONCLUSION AND RECOMMENDATION FOR FURTHER STUDY.....	183
6.1	Introduction.....	183
6.2	Conclusion .....	183
6.3	Recommendations and Future work.....	185
7	Reference .....	187

## LIST OF FIGURES

---

Figure 1.1: Schematic diagram showing behaviour of molecular beacons in presence of the target <sup>33</sup> .....	10
Figure 1.2: Vibrating sample magnetometer diagram for three samples of Fe <sub>3</sub> O <sub>4</sub> synthesized at pH of 12, 11.5 and 11. Reprinted with permission from Ahmadi <i>et. al.</i> <sup>63</sup> Copyright (2012) Springer .....	20
Figure 1.3: Schematic diagram of typical photoluminescence process .....	23
Figure 1.4: Influence of UV irradiation on the quantum yield. Reprinted with permission from Li and Reiss <sup>84</sup> .....	27
Figure 1.5: Synthesis of InP nanocrystals using an alternative source of phosphorous. Reprinted with permission from Li <i>et. al.</i> <sup>83</sup> .....	28
Figure 1.6: Schematic diagram of a ligand exchange process .....	29
Figure 1.7: (A and B) WST-8 Proliferation of assay on A549 and SH SY5Y cells with increasing concentration of InP/ZnS and CdSe/ZnS. Reprinted with permission from Brunetti <i>et. al.</i> <sup>95</sup> .....	31
Figure 1.8: Magnetization curves of Fe <sub>3</sub> O <sub>4</sub> (dashed line) and Fe <sub>3</sub> O <sub>4</sub> -CdSe/ZnS nanoclusters: “Reprinted with permission from Jeong <i>et. al.</i> <sup>121</sup> . Copyright©2014 American Chemical society .....	44
Figure 1.9: The varying PL intensity (a) 100µL hydrophobic QDs in cyclohexane (b) silica coated 100µL of QDs (c) fluorescing magnetic nanoparticles with 100 of QDs and 100µL MNPs (d) fluorescing magnetic nanoparticles with 100 µL of QDs and 100µL MNPs. Reprinted with permission from Zhang <i>et. al.</i> <sup>128</sup> .....	51
Figure 3.1: High resolution transmission electron microscopy micrograph images for bare Iron oxide nanoparticles .....	89
Figure 3.2: Histogram showing size distribution of bare iron oxide nanoparticles .....	90
Figure 3.3: FTIR spectra of bare iron oxide nanoparticles .....	93
Figure 3.4: XRD pattern for bare iron oxide nanoparticles .....	94
Figure 3.5: Magnetic properties of the as-prepared iron oxide nanoparticles .....	97
Figure 3.6: HRTEM micrographs of DMSA capped iron oxide nanoparticles .....	101
Figure 3.7: Histogram showing size distribution of DMSA capped iron oxide nanoparticles .....	102
Figure 3.8: Energy dispersive spectroscopy images for DMSA capped iron oxide nanoparticles .....	103
Figure 3.9: FTIR Spectrum of bare iron oxide nanoparticles (a) and DMSA functionalized iron oxide nanoparticles (b) .....	104
Figure 3.10: XRD pattern for DMSA capped iron oxide nanoparticles .....	106
Figure 3.11: 3-mercaptopropionic acid capped iron oxide nanoparticles .....	108
Figure 3.12: FTIR spectrum of L-Cysteine capped Iron oxide nanoparticles .....	110
Figure 3.13: Magnetic properties of L-cysteine functionalized iron oxide nanoparticles .....	112
Figure 3.14: EMSA micrograph showing mobility of MUC1 aptamer incubated with increasing amounts of the lysates .....	114
Figure 3.15: Evaluation of specificity of MUC 1 binding aptamers on MUC 1 proteins expressed on MCF 7, MCF-12A and free aptamer was used as a control .....	115
Figure 3.16: MALDI-TOF-MS spectrum of trypsinized human mucin 1 .....	118
Figure 3.17: The MALDI-TOF-MS spectra corresponding to the isolated proteins (A2) and the spectrum for the control (C1) experiment .....	119
Figure 3.18: Cytotoxicity studies of bare and functionalized iron oxide nanoparticles using MCF-12A and KMST 6 cell lines .....	121
Figure 4.1: HRTEM micrographs showing distribution of InP/ZnSe nanocrystals .....	125
Figure 4.2: Histogram showing size distribution of the synthesized InP/ZnSe nanocrystals .....	126

Figure 4.3: XRD patterns of the prepared InP/ZnSe nanocrystals.....	127
Figure 4.4: Uv-vis for aliquots collected during growth of the core InP nanocrystals .....	130
Figure 4.5: Uv-vis spectra of the InP/ZnSe aliquots taken after 1 hour and 2 hours during development of the ZnSe Shell .....	131
Figure 4.6: The normalized photoluminescence spectra of the four aliquots taken during synthesis of InP/ZnSe nanocrystals .....	133
Figure 4.7: (A) PL spectra's for InP/ZnSe sample dissolved in hexane and (B) rhodamine 6G standard dissolved in ethanol both spectra's were used for quantum yield calculations .....	135
Figure 4.8: The normalized photoluminescence properties of InP/ZnSe nanocrystals for small scale (A), scaled up by factor of two (B), scaled up by factor of four (C) and scaled up by factor of six (D). .....	138
Figure 4.9: HRTEM micrograph for InP/ZnSe nanocrystals synthesized in small scale(A) the HRTEM micrograph images for InP/ZnSe nanocrystals obtained in up scaling by a factor of two(B) .....	140
Figure 4.10: Histogram showing size distribution of InP/ZnSe nanocrystals obtained in small scale synthesis (A) and scaled up synthesis (B).....	141
Figure 4.11: The UV/Vis spectra of the aliquots taken during synthesis of InP/ZnSe nanocrystals in small scale (A) UV/Vis spectra for the aliquots of InP/ZnSe nanocrystals in scaled up by a factor of two (B) .....	142
Figure 4.12: The fluorescence intensities for aliquots of InP/ZnSe nanocrystals synthesized in small (A) and scaled up by a factor of 2 (B).....	143
Figure 4.13: The band gaps of the aliquots obtained during growth of core/shell of the InP/ZnSe nanocrystals .....	146
Figure 4.14: The band gap of the purified InP/ZnSe nanocrystals .....	147
Figure 4.15: The normalized photoluminescence spectra for different fractions of nanocrystals obtained during size sorting process .....	148
Figure 4.16: Diagram showing effective transfer of quantum dots from the organic layer to aqueous layer .....	150
Figure 4.17: PL spectra of the InP/ZnSe nanocrystals after the ligand exchange process .....	152
Figure 4.18: The FTIR spectra of 3-Mercaptopropionic capped InP/ZnSe nanocrystals.....	153
Figure 4.19: UV-VIS spectra confirming success in introduction of streptavidin .....	154
Figure 4.20: Cytotoxicity studies of InP/ZnSe nanocrystals using MCF-12A and KMST 6 cell lines.....	156
Figure 4.21: HRTEM micrographs of CdTe/ZnS quantum dots (A) Streptavidin modified CdTe/ZnS quantum dots .....	158
Figure 4.22: The determined hydrodynamic sizes of the 3-MPA capped CdTe/ZnS (A) and streptavidin modified CdTe/ZnS (B) .....	159
Figure 4.23: Absorption (A) and FTIR (B) spectra for CdTe/ZnS quantum dots.....	161
Figure 4.24: The photoluminescence characteristics of CdTe/ZnS quantum dots (A) Tauc's plot for band gap determination of CdTe/ZnS nanocrystals.....	163
Figure 4.25: PL spectra for equal amounts of QD with and without the streptavidin (A) comparison of fluorescence intensity of bare quantum dot and the formed molecular beacon (B) .....	164
Figure 4.26: Fluorence spectra comparing emission spectrum of free QDs (A) and the constituted molecular beacon (B).....	166
Figure 4.27: Comparison of discrete fluorescence intensities obtained from same sample of QD and MB at different excitation and emission wavelengths using BioTek Synergy H1 Hybrid Multi-Mode Microplate Reader (A) Fluorescence of the free QD and MB ready for target introduction measured by using POLARstar Omega microplate reader (B) .....	167
Figure 4.28: Detection of varied concentrations of complementary target using QD-based molecular beacon .....	169
Figure 4.29: Detection of target present in lower concentration of cDNA using QD-based molecular beacon .....	170
Figure 5.1: The HRTEM micrograph of Fe <sub>2</sub> O <sub>3</sub> - InP/ZnSe nanocomposite.....	173
Figure 5.2: Energy dispersive spectroscopy spectrum for $\alpha$ -Fe <sub>2</sub> O <sub>3</sub> -InP/ZnSe nanocomposite .....	174
Figure 5.3: PL spectra of InP/ZnSe nanocrystals dispersed in hexane (A) PL spectra of $\alpha$ -Fe <sub>2</sub> O <sub>3</sub> -InP/ZnSe nanocomposite dispersed in PBS (B).....	175



Figure 5.4: Photoluminescence spectra of InP/ZnSe (green line) and InP/ZnSe-Fe<sub>2</sub>O<sub>3</sub> nanocomposite ....176  
Figure 5.5: Magnetic nanomaterial of bare iron oxide and luminescence magnetic nanocomposite .....178  
Figure 5.6: The band gap of the synthesized  $\alpha$ -Fe<sub>2</sub>O<sub>3</sub>-InP/ZnSe nanocomposite.....180  
Figure 5.7: Cytotoxicity of the  $\alpha$ -Fe<sub>2</sub>O<sub>3</sub>-InP/ZnSe nanocomposite carried out using MCF 12A and KMST 6 cell lines  
.....181

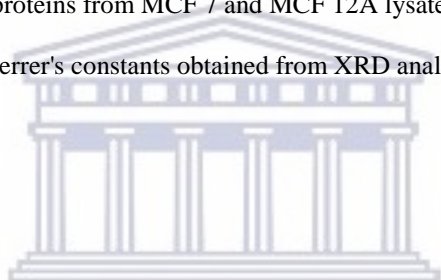


UNIVERSITY *of the*  
WESTERN CAPE

## LIST OF TABLES

---

Table 2.1: Experimental details for incubation of aptamer and the Lysates extracted from MCF-7 cells.....	95
Table 2.2: Experimental details of MUC1 capturing process using MNP-Aptamer complex.....	95
Table 2.3: Experimental details of MUC1 capturing process using MNP-Aptamer complex.....	97
Table 3.1: Estimation of iron oxide particle size from XRD data .....	117
Table 3.2: Summary of ligands, their structures and functional groups of interest .....	121
Table 3.3: Estimation of DMSA capped iron oxide particles size using XRD data .....	129
Table 3.4: Concentration of captured proteins from MCF 7 and MCF 12A lysates .....	139
Table 4.1: Summary of calculated Scherrer's constants obtained from XRD analysis .....	151



UNIVERSITY *of the*  
WESTERN CAPE

## TABLE OF ABBREVIATIONS

---

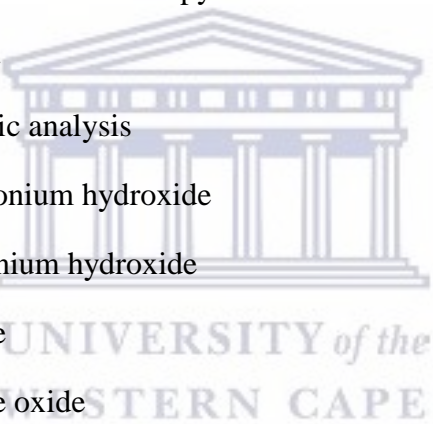
ADM	Adriamycin
AEAPS	N-(2-aminoethyl)-3-aminopropyltrimethoxysilane
AuNP	Gold nanoparticles
BNC	Bifunctional nanocomposite
BNP	Bifunctional nanoparticles
BSA	Bovine serum albumin
CdS	Cadmium sulphide
CFLMNPs	Chitosan-ferroferic oxide doped cadmium telluride quantum dot nanoparticles
CHCA	Cyano-4-hydroxycinnamic acid
CLMNP	Chitosan luminescence magnetic nanocomposites
CMCH	Carboxymethylation
CT	Computerized tomography
CTAB	Cetyltrimethylammonium bromide
DABCYL	4-(4'-dimethylaminophenylazo) benzoic
DCD	Dermcidin
DIPA	Diisopropanolamine
DLS	Dynamic light scattering
DMEM	Dulbecco's modified Eagle's medium
DMSA	Dimercaptosuccinic acid
DMSO	Dimethoxysulfoxide
DSC	Differential scanning calorimetry
DVB	Divinylbenzene

EDAC	1-ethyl-3-(3-dimethylaminopropyl) carbodiimide hydrochloride
EDS	Energy dispersive X-ray spectroscopy
EDTA	Ethylenediaminetetraacetic acid
EGF	Epidermal growth factor
ELISA	Enzyme linked immunosorbent assay
EMSA	Electrophoretic mobility shift assay
FBS	Fetal bovine serum
FITC	Fluorescein isothiocyanate
FMNPS	Fluorescent magnetic nanocomposites
FRET	Fluorescence resonance energy transfer
FTIR	Fourier transform infra-red spectroscopy
FWHM	Full width at half maximum
GMA	Glycidylmethacrylate
GPC	Glycerophosphocholine
GPE	Glycerophosphoethanolamine
HPLC	High performance liquid chromatography
HRSEM	High resolution scanning electron microscopy
HRTEM	High resolution transmission electron microscopy
HSA	Human Serum Albumin
IDT	Integrated DNA technologies
IgG	Immunoglobulin G
IO	Iron oxide
JCPDS	Joint committee on powder diffraction standards
LDH	Lactate dehydrogenase
LFD	Lateral flow device

LSCM	Laser scanning confocal microscopy
MALDI-TOF	Matrix assisted laser desorption/ionization- time of flight
MB	Molecular beacons
MIPA	Alkanoaminesisopropanolamine
MNC	Magnetic nanocomposite
MNP	Magnetic nanoparticles
3-MPA	3-Mercaptopropionic acid
MSA	Mercaptosuccinic acid
MTT	3-(4, 5-dimethylthiazol)-2, 5-diphenyltetrazolium bromide
NC	Nanocomposite
NCBI	National centre of biotechnology information
NIC	Nanotechnology innovation centre
NP	Nanoparticle
ODA	Octadecylamine
ODE	1-octadecene
PACN	Pan African chemistry network
PE	Phosphoethanolamine
PC	Phosphocholine
PCR	Polymerase chain reaction
PDDA	Poly (diallyldimethylammonium chloride)
PEG	Polyethylene glycol
PL	Photoluminescence
PLGA	Poly(lactic-co-glycolic acid)
PXRD	Powdered X-Ray diffraction
QD	Quantum dots



QY	Quantum yield
RNA	Ribonucleic acid
SA	Stearic acid
SELEX	Systematic evolution of ligands by exponential enrichment
SEM	Scanning electron microscopy
SPIONS	Superparamagnetic iron oxide nanoparticles
SQUID	Semiconducting quantum interference device
TBE	Tris borate EDTA
TE	Tris EDTA
TEM	Transmission electron microscopy
TEOS	Tetraethoxysilane
TGA	Thermogravimetric analysis
TMA	Tetramethylammonium hydroxide
TMAOH	Etramethylammonium hydroxide
TOP	Trioctylphosphine
TOPO	Trioctylphosphine oxide
UV	Ultra violet
UVP	Ultra violet products limited
VEGF	Vascular endothelial growth factor
VSM	Vibrating sample magnetometer
XRD	X-ray diffractometer



# 1 CHAPTER ONE

## 1.1 Introduction

This chapter describes the key aspects of the study. These include definition, origin, and brief causes of cancer. The current molecular methods of breast cancer diagnosis have been thoroughly reviewed. Three classes of nanomaterials have also been described namely magnetic nanomaterials, quantum dots and fluorescing magnetic nanocomposites (fluorescing materials coupled with magnetic nanomaterials). In regard to these materials, we reviewed synthetic strategies, properties, and biological applications. The chapter ends with identifying the problem statement, the significance, and the objectives of the study.

## 1.2 Cancer

Cancer is a broad group of diseases involving uncontrolled cell growth. It involves an uncontrollably division of cells forming a malignant tumor, which eventually invade the neighboring cells. Cancer may also spread to more distant parts of the body through the lymphatic system or blood stream. The net result is the cell death and therefore the body. There are over 200 different types of cancer that are known to affect human beings<sup>1</sup>. The biggest problem which faces man is that the immune system cannot differentiate cancerous cells from normal cells and this makes the treatment of cancer a conundrum<sup>2</sup>.

The causes of cancer are diverse, complex and partially understood. The most commonly suspected causes of cancer include the use of tobacco, dietary factors, exposure to some radiations, lack of physical activity and environmental pollutants<sup>3</sup>. Many cancers can be prevented by avoiding smoking, eating less meat and carbohydrates and more vegetables, maintaining healthy weight (doing regular exercises), minimizing sunlight exposure and

being vaccinated against infectious diseases<sup>4</sup>. Despite numerous researches carried out in cancer biology including the development of drugs, and therapies for their treatment for many years, the survival rates have not significantly increased till today. This is probably due to the scarcity of tools for timely diagnosis and targeted drug delivery<sup>5,6</sup>. The following section discusses one example of cancer, the breast cancer which is of late becoming prevalent, and therefore a major concern.

### **1.3 Breast Cancer**

The breast cancer originates most commonly from the inner lining of milk ducts or the lobules that supply ducts with milk<sup>7</sup>. The ductal carcinoma in turn originates from the milk ducts while the lobular carcinomas originate from the lobules. The breast cancer is common amongst women but it can also occur in men<sup>7</sup>. Globally, breast cancer accounts for 22.9 % of all cancers (excluding non-melanoma) in women<sup>8</sup>. In 2012, breast cancer caused 522,000 deaths worldwide which accounts for 13.7% of cancer deaths in women. According to a current report dated on 8<sup>th</sup> April 2014 by South African medical research council breast cancer is ranked top five in South Africa. Lung cancer is the leading cause of cancer in South Africa accounting for 17% of all the cancer deaths. This is followed by oesophagus cancer which accounts for 13%, cervix cancer accounting for 8%, breast cancer accounting for 8% and liver cancer which accounts for 6% of all cancers<sup>9</sup>.

### **1.4 Screening techniques of Breast Cancer**

The mammographic imaging is the most effective approach for diagnosing breast cancer in women older than 50 years of age. Although new improvements are being made in the resolution of these imaging techniques, tumors smaller than 5 mm usually pass



undiagnosed. The breast tissues for young women are dense making the technique less sensitive. Moreover, the effectiveness of mammography has not been established<sup>10</sup>. Finally, high-grade tumor cells cannot be diagnosed with 1 to 2 years of regular mammography imaging. For these reasons, new approaches should be developed in order to improve diagnosis of breast cancer and to increase the overall and disease-free survival rates of patients who are diagnosed with this disease<sup>11,12</sup>. However, the signs and symptoms of a tumor often present themselves when it is already too late for medication. Microscopic examination of sample tissues is more invasive and involves extraction of tissues for imaging which is also painful.

Current methods of breast cancer screening like self-breast examination and the mammography have several drawbacks. For instance, not everybody can carry out self-breast examination and mammography which is rare and very expensive. Other investigation diagnostic tools include medical tests such as CT scans, X-rays, and endoscopy.

### **1.5 Mammography**

This is a process of using low- energy X-rays around 30 kV to examine human breast. The goal of mammography is the early detection, typically through detection of characteristic masses and/or micro-calcifications. Like all X-rays, mammograms use doses of radiation to create images. The images are analyzed by radiologists for any abnormal findings. Ultrasound, ductography, positron emission mammography and magnetic resonance imaging (MRI) are adjuncts to mammography. Ultrasound technique is typically used for further evaluation of masses not seen on mammograms. Ductograms are still used in some institutions for evaluation of bloody nipple discharge when the mammogram is non-

diagnostic. MRI can be useful for further evaluation of questionable findings as well as for screening pre-surgical evaluation in patients with known breast cancer to detect any additional lesions that might change the surgical approach, for instance from breast conserving lumpectomy to mastectomy<sup>13</sup>.

The US preventive services task force recommended in 2009 that mammography is done every two years in women between ages of 50-74<sup>14</sup>. The Canadian task force on preventive health care (2012) and the European cancer observatory (2011) recommended mammography every 2-3 years between the ages 50-69<sup>14</sup>. These task force reports point out that in addition to unnecessary surgery and anxiety, the risks of more frequent mammograms include a small but significant increase in breast cancer induced by radiation<sup>15</sup>.

## **1.6 Serum Biomarkers**

The serum tumor biomarkers are soluble molecules released into the bloodstream by cancer cells or other cell types belonging to tumor microenvironment<sup>16</sup>. The measurement of these molecules is considered an economic and non-invasive diagnostic assay which is able to give information about the presence or absence of the disease as well as its evolution.

In particular, the ideal serum tumor biomarker should be able to assist in (i) early detection of a disease (ii) prediction of the response or resistance to specific therapies, and (iii) monitoring the patient after primary therapy<sup>17</sup>. Advances in breast cancer control can be greatly aided by early detection, thereby facilitating diagnosis and treatment of breast cancer in its pre-invasive state prior to metastasis. The most efficacious screening

modality utilized in the clinic is mammography, though lesions less than 0.5 cm in size remain undetectable by present technology. Importantly, however, even though a breast lesion may be detected, given the low sensitivity/specificity of mammography, approximately 4-fold more women (than those with breast malignancies) have resultant biopsies<sup>18</sup>.

Early detection of breast cancer does allow for increased treatment options. Unfortunately, however, in the absence of good serum/plasma biomarkers many breast cancer patients are diagnosed too late in the disease process (i.e. after the tumors metastasize) for surgical resection to be an effective option. Several approaches are currently available for the identification of tumor antigens. Many studies have shown that several proteins change in cancer. These changes may cause measurable alterations and secretion of biomarker proteins to body fluids. These biomarkers may be promising in diagnosing the development or the progress of the disease and the treatment monitoring<sup>19</sup>.

### **1.7 Breast cancer studies**

Breast cancer diagnosis has assumed many different strategies over the years. Most strategies compare expressions obtained in the normal and cancerous cell as well as the serum. In a study by Lin *et. al.*<sup>20</sup>, high-throughput sequencing was used to detect Mitochondrial DNA mutations in the blood of breast cancer patients. Mitochondrial DNA mutations have been identified in several types of cancer cells suggesting their possible use as potential markers for breast cancer diagnosis. Equally, phosphorus metabolite ratios have been reported as potential biomarkers in the breast cancer diagnosis and treatment monitoring.

Stehouwer *et. al.*<sup>21</sup> investigated metabolite ratios of phosphomonoester to phosphodiester; phosphoethanolamine (PE) to glycerophosphoethanolamine (GPE), and phosphocholine (PC) to glycerophosphocholine (GPC) in glandular tissue, and their potential effect on the menstrual cycle. They reported that metabolite ratios analyzed on group level gave negligible variation throughout the menstrual cycle. Hence variation of phosphorus metabolite ratios cannot be used as indicators for the presence or absence of breast cancer.

In an alternative strategy, the use of blood-based biomarkers for the early detection of breast cancer was reported by Brauer *et. al.*<sup>22</sup>. An assay of serum samples via matrix-assisted laser desorption ionization-time of flight mass spectrometry from a rat model of mammary carcinogenesis was used. They found elevated levels of a fragment of the protein dermcidin (DCD) associated with early progression of N-methyl nitrosourea-induced breast cancer, demonstrating significance at weeks 4 ( $p = 0.045$ ) and 5 ( $p = 0.004$ ), a time period during which mammary pathologies rapidly progress from ductal hyperplasia to adenocarcinoma. The highest serum concentrations were observed in rats bearing palpable mammary carcinomas. Increased DCD was also detected with immunoblotting methods in 102 serum samples taken from women just prior to breast cancer diagnosis. To validate these findings in a larger population, they applied a 32-gene *in vitro* DCD response signature to a data set of 295 breast tumors and assessed correlation with intrinsic breast cancer subtypes and overall survival. In conclusion, they presented novel evidence that DCD levels may increase in early carcinogenesis, particularly among more aggressive forms of breast cancer.

Chen *et. al.*<sup>23</sup> developed a sensor which was the first attempt to apply Thioflavin T that possesses outstanding structural selectivity for G-quadruplex in DNA amplification

techniques; they proposed that this may represent a promising path towards direct breast cancer detection in saliva at the point of care.

Heer *et. al.*<sup>24</sup> studied the relationship between the expression level of VEGF and CA15.3 and the progression of breast cancer diagnosis. The expression level of VEG-kncF and CA15.3 in 30 cases of patients with breast cancer, 30 cases of patients with benign breast cancer diseases and 60 healthy women were detected. In their remarks, they concluded that detection of VEGF and CA15.3 could be used as an important reference index for the diagnosis, evaluation and prognosis of breast cancer.

Bamford *et. al.*<sup>25</sup> provides a method and computerized system for detecting gene expression in tissue samples and diagnostic applications for breast cancer. The computer-based specimen analyzer is configured to detect a level of expression of genes in a cell sample by detecting dots that represent differently stained genes and chromosomes in a cell. The metrics are fed to a classifier that separates genes from chromosomes. The results of the classifier are counted to estimate the expression level of genes in the tissue samples. Critical evaluation of the suggested biomarkers such as mitochondrial DNA mutations, phosphorus metabolite ratios, dermcidin, and fibronectin among others are grouped as potential biomarkers. The other designed methods suffer from low sensitivity. For instance, mammography has a false-negative (missed cancer) rate of at least 10 percent. This is partly due to dense tissues obscuring cancer and the fact that the appearance of cancer on mammograms has a large overlap with the appearance of normal tissues. A meta-analysis review of programs in countries with organized screening found 52% over-diagnosis. Research shows<sup>26</sup> that false-positive mammograms may affect women's well-being and behavior.

## 1.8 Aptamers

The term aptamer is derived from Latin word 'aptus' meaning 'to fit'. They were discovered in the 1990s based on the development of *in vitro* selection and amplification technique coined as systematic evolution of ligands by exponential enrichment (SELEX). They are synthetic short oligonucleotides that are designed to selectively and specifically bind specific targets<sup>27</sup>. They are comprised of DNA, RNA and peptide which can bind to molecules such as DNA, RNA, ions, glucosides, proteins, whole bacteria and cells<sup>28</sup>. In addition, aptamers are considered to be equal or even surpass antibodies in regard to selectivity, specificity and affinity<sup>27</sup>.

Aptamer like antibodies can bind, track and inhibit target molecules<sup>28</sup>. Unlike antibodies, aptamers require formation of a 3-D structure for the target binding giving them a high binding affinity<sup>27</sup>. They also have long shelf life, non-toxic and can be synthesized with a target which does not have immunogenicity<sup>28</sup>. Their selection through *in vitro* state gives them the advantage of synthesizing the aptamers for any given target without requiring cell lines or animals hence aptamers can be selected against toxic or non-immunogenic targets. The other advantage of aptamers is that once selected they can be synthesized with high reproducibility, purity and in large quantities. Provided that the critical sequence responsible for target binding is not interfered aptamers allow the introduction of functional groups while retaining its affinity. In addition, aptamers are very stable and can attain their active conformation after thermal denaturation which is not the case with antibodies<sup>29</sup>.

### **1.8.1 Aptamer applications**

Aptamers have attracted great attention in various fields and they have been used for biosensing, disease diagnosis, drug delivery, and therapy. The common pre-requisite for this application is the desire to have an element with recognition unit. Aptamers are suitable for these applications due to their excellent specificity and high affinity for their targets. In addition, the development of nanotechnology has allowed conjugation of aptamers to functionalized nanomaterials paving the way to a design of theranostic components for various diseases<sup>30</sup>. Aptamers have also found applications in the design of biosensors better known as APTA sensors. A number of recognition molecules are usually employed for clinical diagnosis. Antibodies are more often used in biosensor detection methods, however, the detection of analytes in complex samples might be hampered by the nature and synthesis of these protein receptors. The drawbacks of using antibodies as recognition molecules in the design of biosensors can be circumvented by using aptamers. Recently, APTA sensors have been used for the detection of biomarkers in blood, urine, and other body fluids. Aptasensors have also found application in detection of microorganisms and viral proteins. These are useful for detection, identification, and quantification of microbial pathogens for public health protection<sup>31</sup>.

### **1.9 Molecular Beacons**

Molecular beacons (MBs) are single-stranded oligonucleotides that are able to detect specific complementary targets commonly nucleic acid. It constitutes the loop, a stem at both ends and a fluorophore at one end and a quencher at the other end of the strands. In the absence of the target, the stem keeps the fluorophore and the quencher in close proximity hence no fluorescence is observed. The loop portion is usually between 15-35

nucleotides that hybridize to the target sequence of specific complementary nucleic acid<sup>32</sup>. In the presence of the complementary target/ or the cDNA is expected to be bound to the loop hence increase in fluorescence due to increase in the distance between the quencher and the fluorophore<sup>33</sup> as demonstrated in Figure 1.1 below. .

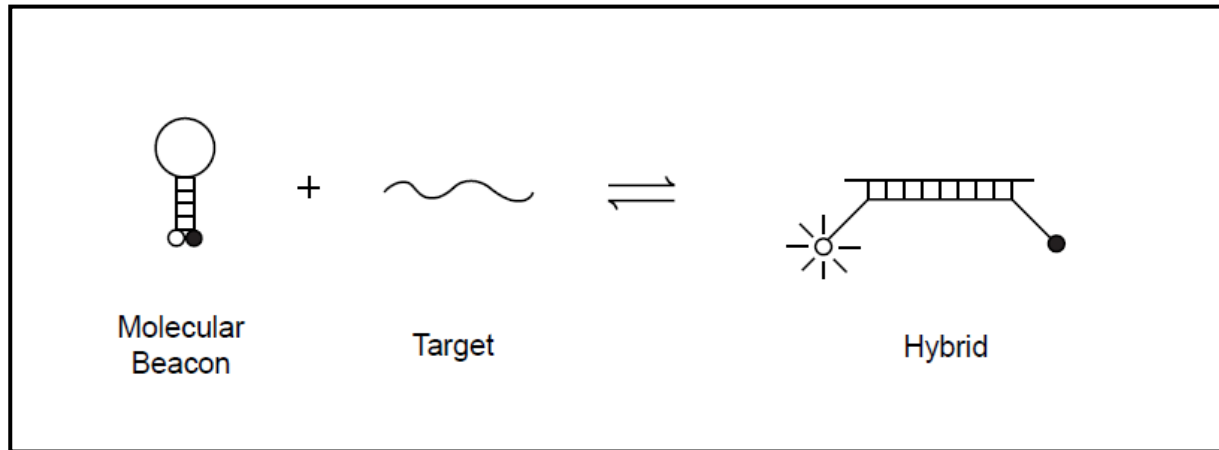


**Figure 1.1: Schematic diagram showing behaviour of molecular beacons in presence of the target<sup>33</sup>**

The stem must be unrelated to the target sequence and is formed by annealing two complementary arms (to ensure that MB remains closed) found on either side of the probe and usually five to seven nucleotide long<sup>34,33</sup>. Molecular beacons have also been designed to bind and recognize specific nucleotide sequence such as DNA and mRNA allowing for the detection of intracellular mRNA molecules<sup>35</sup>. Stem and the probe length have been reported to influence significantly both binding specificity and hybridization rates of molecular beacons<sup>36</sup>. In their review, they also pointed out that higher background fluorescence is observed when short-stemmed MBs are used unlike the long-stemmed at



37 °C. This phenomenon could be attributed to a larger fraction of the short stemmed type existing in the open random conformation at this temperature.

The quenching effect is as a result of fluorescence resonance energy transfer (FRET) efficiency 'E' is defined by Förster theory<sup>37</sup> given by the following equation 1.1.

$$E = \frac{R_0^6}{R^6 - R_0^6} \dots\dots\dots\text{equation 1.1}$$

Where  $R_0$  is Förster radius (the distance at which transfer efficiency is 50 %)  $R$  is the distance between the centers of the fluorophore and acceptor.

Molecular beacons are synthesized automatically whereby the quencher is introduced during DNA synthesis. The fluorophore is manually linked to one end through amino or sulfhydryl group<sup>33</sup>. The commonly used fluorophores include 6-carboxyfluorescein (6-FAM), TET (emit in green range), tetramethylrhodamine, Alexa 546, Cyanine 3 (Cy 3), Texas Red, Cyanine (Cy5) (emit at the red range). On the other hand, the commonly used quenchers include Iowa black, Dabcyl, 1.4 nm nanogold among others. Conventionally, organic dyes and fluorescent proteins are used as the fluorophore for the molecular beacon design; however, they can easily be photodegraded.

Quantum dots (semiconductor nanocrystals) are promising new class of fluorescent labels due to their brightness, resistance to photobleaching and multicolor fluorescence emission properties<sup>38</sup>. Some studies have been conducted by incorporating QDs in the design of molecular beacon. Kim *et. al.*<sup>37</sup> purchased CdSe/ZnS from Evident Technologies and used them to design of molecular beacon. They confirmed an overlap between the emission spectrum of the inorganic QDs and the absorption spectrum of the 4-(4'-dimethylamino phenyl azo) benzoic acid (DABCYL) just like organic fluorophores. The overlap which is about 90 % is known to promote FRET efficiency. In their work, they were able to test the

MBs with their complementary target and for non-specific complementary sequences. They reported improved lifetime as compared to the organic MBs. Lastly, they reported the need for improvements in respect to relatively low signal to background ratio as compared to organic MBs.

In another study Cady *et. al.*<sup>39</sup> compared performance of MBs prepared through covalent amide linkage and streptavidin-biotin interactions. They purchased carboxyl-modified and streptavidin-modified 525 nm QDs from Quantum Dot Corporation (Hayward, CA). When they hybridized the two sets of MBs with 200 pmol of the target they observed 57 % increase in fluorescence from amide linked MBs compared to streptavidin linked MBs. They noted however that in both cases the difference in fluorescence between the MB hybridized with the complementary target and non-specific target was approximately 50%. They also conjugated the QDs to Iowa black, 1.4 nm Nanogold and Dabcyl quenching moieties to form different types of MBs. However, it is worth noting that the QDs used here have been classified as non-environmental friendly.

In general, semiconductor nanocrystals have numerous advantages over organic dyes which include tunable colors by changing the particle size, a single wavelength for simultaneous excitation of different-sized QDs, high stability against photobleaching, narrow and symmetrical emission peaks<sup>37</sup>. Guo *et. al.*<sup>40</sup> developed a molecular beacon microarray based on quantum dots. Their microarray was able to detect label-free DNA targets with high specificity and sensitivity. They highlighted the advantage of re-usability of the MB microarray and the ability to apply the technique to be used in determining a large number of genetic variations simultaneously. They concluded that the MB microarray can be useful in for DNA mutation studies and disease diagnosis.

Molecular beacons have found various applications which include monitoring minor changes at a signal cell level by detecting and quantifying any changes in gene expression in a living cell using real-time PCR, and also for multiplex detection<sup>41</sup>. Owing to their sensitivities they can be used to monitor the cleavage of double-strand DNA by restriction endonuclease-based on nucleic acid ligation by using real-time PCR<sup>42</sup>.

Orrus *et. al.*<sup>43</sup> reported that MBs were designed to detect specific gene mutations in patient thyroid carcinoma tissues by measuring fluorescence intensity using real-time PCR. Culha *et. al.*<sup>44</sup> coupled MB to a biochip which was applied for the detection of breast cancer gene BRCA1 in solution. They determined the limit of detection to be 70 nM. The first application of MBs in bladder cancer detection was reported by Zhao *et. al.*<sup>45</sup> using survivin modified MBs. They were able to detect the expression levels of survivin in human bladder cancer. Xue *et. al.*<sup>46</sup> have also demonstrated the sensitivity and specificity of survivin MBs towards survivin mRNA in cervical cancer compared to western blot and immunohistochemistry.

In another study, Deng *et. al.*<sup>47</sup> designed a molecular beacon and used to detect maripitase; a type II transmembrane serine protease both *in vitro* and *in vivo*. In their design, they used FITC dye as the fluorophore and Au nanoparticle as the quencher. They used peptide substrate (GRQSRAGC) to link the fluorophore and the quencher. The design showed sensitivity and specificity in both *in-vitro* and *in vivo* suggesting its suitability in imaging protease in the living organism. Recently, Adegoke *et. al.*<sup>48</sup> synthesized quaternary QDs of the type CdZnSeTeS and conjugated them to a probe in order to design MB. Through enhanced signal transduction, they were able to detect two strains of influenza virus H1N1

RNA. Their designed molecular beacon depicted increase in fluorescence when the 0-14 copies/mL of H1N1 RNA was added.

## **1.10 Nanotechnology and nanomaterials**

### **1.10.1 Magnetic nanoparticles (MNPs)**

Recently, magnetic nanoparticles have attracted enormous interest in various fields due to their unique and tunable properties. They have controllable sizes that range from few nanometers to tens of nanometers. Their sizes are smaller or comparable to those of a cell (10-100  $\mu\text{m}$ ), a virus (20-450 nm), a protein (5-50 nm) or a gene (2 nm wide and 10-100 nm long). In the biomedical field, magnetic nanoparticles are of great interest because they can function in cellular and molecular level hence allowing biological interactions. The promising applications of magnetic nanoparticles range from storage media<sup>49</sup>, magnetic memory devices<sup>50</sup>, bioseparation<sup>51</sup>, magnetic targeting<sup>52,53</sup>, drug delivery<sup>53,54</sup>, cancer therapy using magnetic hyperthermia<sup>54,55</sup>, biosensing and contrasting agent for magnetic resonance imaging<sup>55, 56</sup>. Strategies are being put in place to modify their surfaces to avoid aggregation of the bare magnetic nanoparticles which restricts their applications<sup>57</sup>.

### **1.10.2 Synthesis of magnetic nanoparticles**

The ability to synthesize magnetic nanoparticles of desired properties has become a core research for many researchers<sup>58,59</sup>. The choice of synthetic method is crucial since it dictates ultimate properties of the MNPs. There exists various approaches in the synthesis of magnetic nanoparticles which include but not limited to high temperature solventless thermal decomposition, co-precipitation, microemulsion, polyol-mediated sol-gel,

hydrothermal synthesis, and polymer template method<sup>60</sup>. Of these methods, co-precipitation is the most popularly used because it tends to be green, simple and large amount of the product is yielded within a single synthesis.

### 1.10.3 Co-precipitation method

The co-precipitation emerges to be the most preferred choice among available synthetic routes. This method produces water dispersible magnetic nanoparticles, high yields, cost effective, less time – consuming and easily scalable for large production. Furthermore, it provides an eco-friendly route that avoids the use of hazardous solvents and the reaction is carried out at low temperatures and pressures. However, the control of particle size, crystallinity, and magnetic properties via this route remains a challenge<sup>51,61</sup>.

Highly superparamagnetic ferrites nanoparticles have been synthesized by one– step aqueous co-precipitation route by Klaber *et. al.*. In a modified synthetic route Alkane amines isopropanolamine (MIPA) and di-isopropanolamine (DIPA) were used in place of commonly used sodium hydroxide, ammonium hydroxide, and tetraalkylammonium hydroxide. They successfully obtained Fe<sub>3</sub>O<sub>4</sub>, CoFe<sub>2</sub>O<sub>4</sub>, and MnFe<sub>2</sub>O<sub>4</sub> nanoparticles with sizes of 4.9-6.3, 4.2-4.8, and 9.3-11.7 nm, respectively. The method in this instant provided high yield production of MNPs featuring improved magnetic properties<sup>62</sup>.

In another reported synthesis of magnetic nanoparticles carried out by co-precipitation, the effect of varying pH was investigated<sup>63</sup>. The synthesis was carried out at the pH of 12, 11.5 and 11 and they obtained average diameters of Fe<sub>3</sub>O<sub>4</sub> were 9.66, 13.22, and 20.62, respectively. The reaction was carried out under argon atmosphere with ultra-sonication at 25 °C using potassium hydroxide as the alkaline precipitant. They investigated crystal structure of Fe<sub>3</sub>O<sub>4</sub> using Siemens D5000 X- ray diffractometer. Graphite-

monochromatized high-intensity Cu- K $\alpha$  radiation ( $I = 1.5406\text{\AA}^0$ ) was used. The results showed six characteristic peaks for Fe<sub>3</sub>O<sub>4</sub> nanoparticles ( $2\theta = 30.16, 35.48, 43.13, 53.49, 56.91$  and  $62.71$ ), their marked indices were (220), (311), (400), (422), (511), and (440). These peaks matched very well with the magnetite characteristic peaks (JCPDS card no. 19-0629) which confirmed the inverse spinel structure of the particles<sup>63</sup>.

Zinc-doped iron oxide has been synthesized successfully in the past by Marand *et. al.*. Doping was done by varying amounts of zinc according to the following stoichiometric ratio Zn<sub>x</sub>Fe<sub>3-x</sub>O<sub>4</sub> ( $x=0, 0.025, 0.05, 0.075, 0.1$  and  $0.125$ ). Chlorides of Fe<sup>3+</sup>, Fe<sup>2+</sup>, and Zn<sup>2+</sup> were mixed in hydrochloric acid according to the above stoichiometric ratio. The precipitant 2 M NH<sub>4</sub>OH was added dropwise to the initial concentration with vigorous stirring at 70 °C. The black precipitate was separated by applying external magnetic field. Unlike the above, the inert gas used here was atmospheric N<sub>2</sub>. X-ray diffraction studies revealed that the single phase nanoparticles were formed with cubic spinel structures with diameters varying from 11.13 to 12.81 nm. The particles relayed high superparamagnetic properties at room temperature with a high level of a maximum saturation magnetization of 74.60 emu/g. The band gaps in all the Zn- doped NPs were higher than the pure Fe<sub>3</sub>O<sub>4</sub>. However, it was observed that as percent doping increased the band gap value decreased from 1.26 eV to 0.43 eV<sup>64</sup>. High purity iron ore tailing has been recently utilized through acid leaching method to synthesize nanoscale magnetic Fe<sub>3</sub>O<sub>4</sub> via ultrasonic- assisted chemical precipitation. Briefly, Fe(OH)<sub>3</sub> precipitate was washed several times with distilled water and hydrochloric acid added to obtain FeCl<sub>3</sub> solution. FeCl<sub>3</sub> solution was mixed with FeSO<sub>4</sub>.7H<sub>2</sub>O in a way to obtain a ratio of Fe<sup>3+</sup>: Fe<sup>2+</sup> of 1.5:1. The mixture was put under ultrasonic agitation with the addition of sodium hydroxide dropwise until a

black precipitate was formed. The process was carried out at 65 °C for 30 minutes in ultrasonic water bath. The prepared Fe<sub>3</sub>O<sub>4</sub> particles were washed several times with repeated cycles of de-ionized water and ethanol. The magnetic nanoparticles were dried in a vacuum at 74 °C. The magnetite particles obtained had an average diameter of 15 nm and exhibited high superparamagnetic properties<sup>65</sup>.

Magnetite NPs were recently synthesized by facile co-precipitation method in rotating packed bed. The variables of rotating speed, flow rates of reactants and precipitant and concentration of reactants were investigated by Lin and Jui-Min. The experimental results revealed that high rotating speed, larger flow rate of reactants, and precipitants were associated with the smaller size of the nanoparticles. Fourier transform infra-red analysis (FTIR) confirmed the successful synthesis of Fe<sub>3</sub>O<sub>4</sub> NPs depicted by a strong peak at 580 cm<sup>-1</sup> and a weak one at 436 cm<sup>-1</sup> which are related to Fe-O functional group. The wet particles were dried in a vacuum oven at 60 °C for 12 hours. The average diameter of the nanoparticles prepared was approximately 6.4 nm as revealed by HRTEM analysis and further calculation using the software (NIH, ImageJ)<sup>66</sup>. Nearly well dispersed Fe<sub>3</sub>O<sub>4</sub> NPs were synthesized by a novel route using ionic liquid assisted co-precipitation. The ionic liquid of 1- methylimidazoliumtetrafluoroborate ([BMIN] BF<sub>4</sub>) was used as templates at 70 °C. It was realized that the sizes of the particles and magnetic properties strongly depended on the amount of ionic liquid used. The average diameters of the NPs were 8-17 nm. The particles exhibited high superparamagnetism with magnetic saturation for various samples ranging from 46.2 – 69.4 emu/g as measured by SQUID<sup>67</sup>. Magnetic Fe<sub>3</sub>O<sub>4</sub>-Chitosan was prepared by a new co-precipitation method under 0.45 T static magnetic fields. The iron (II) chloride and iron (III) chloride at the molar ratio 1:2 were dissolved in

2 % acetic acid solution of chitosan. The resulting solution was precipitated at room temperature by adding 30 % sodium hydroxide under magnetic field at the controlled pH (10-10.4). The resulting mixture was washed several times using phosphate buffer and dried in an oven at 60 °C for later use. Application of external magnetic field during synthesis showed a considerable influence. The magnetic saturation obtained was 29.72 emu/g and 13.37 emu/g with and without an external magnetic field, respectively<sup>68</sup>.

Magnetic nanoparticles of type  $\text{Co}_{0.5-x}\text{Mn}_x\text{Zn}_{0.5}\text{Fe}_2\text{O}_4$  were synthesized recently by coprecipitation, where x varied from 0 to 0.5 at intervals of 0.1. The crystalline nature of the NPs was confirmed to be broad single cubic phase using XRD with crystal size ranging from 5-8 nm. The group noted also that the saturation magnetization decreased linearly by an increase in the amount of Mn, however, they noted also that the Curie temperature increased first with few substitutions of manganese ions, then decreased up to 441K and finally increased above the initial  $M_s$ <sup>69</sup>.

Mamani *et. al.*<sup>70</sup> synthesized magnetic nanoparticles from ferrous oxide through coprecipitation. They coated the synthesized material with a lauric acid and dispersed them in an aqueous medium containing Renex -100® as a surfactant. The experiment was done in nitrogen atmosphere. Solutions of 0.1M  $\text{Fe}^{3+}$  and 0.2M  $\text{Fe}^{2+}$  were mixed in 1.5M HCl and the precipitant ammonium hydroxide added until pH of 12 was reached. The synthesized nanomaterials yielded stable colloidal suspension with distinct physicochemical properties. Further analysis with TEM and dynamic light scattering (DLS), showed polydispersed nanoparticles with average diameter of 9 nm. Sodium citrate and oleic acid have been successfully grafted onto the surface of  $\text{Fe}_3\text{O}_4$  that was



synthesized by co-precipitation. The synthesized MNPs displayed excellent dispersion capability demonstrated by a reduction in surface energy and dipolar attraction of the NPs. Wei *et. al.*<sup>71</sup> synthesized four samples of iron oxide nanoparticles under different experimental conditions. The synthetic process involved dissolving of Fe<sup>3+</sup> and Fe<sup>2+</sup> at the molar proportion of 1:2 in ethanol/or deionized water. The precipitant used was 3 M sodium hydroxide which was added using peristaltic pump under constant stirring for 30 minutes until a pH of 10 was attained. Afterward, the sodium citrate and oleic acid were added in that order and left standing for 12 h. The synthesized material was aged and digested at the temperature maintained for 30 minutes and cooled to room temperature. The resulted particles were washed with repeated cycles of water and ethanol until the pH was 7, finally, the product was dried at 60 °C for 6 hours under vacuum<sup>71</sup>. The crystalline structure was investigated using XRD measurements. The XRD peaks matched well with characteristic peaks of inverse cubic spinel structure (JCPDS 19-0629), the XRD analysis further revealed that the crystalline structure of Fe<sub>3</sub>O<sub>4</sub> MNPs remained unchanged after surface modification with both sodium citrate and oleic acid. Distribution and morphology were investigated using TEM which revealed spherical homogeneous particles with a diameter of about 12-15nm which was in agreement with XRD analysis. The prepared Fe<sub>3</sub>O<sub>4</sub> showed ferromagnetic behaviors, for instance, four samples prepared in this study at different experimental conditions had magnetic saturation values of 50.61, 61.56, 56.05 and 55.43 emu/g. The smallest particles were of size 12.6 nm with magnetic saturation of 50.61 emu/g when the size increased to 13.4 nm under the same conditions the saturation magnetization increased to 61.56 emu/g. They attributed such ferrimagnetic to smaller diameters than that of a critical threshold of Fe<sub>3</sub>O<sub>4</sub> (25 nm)<sup>71</sup>.

#### 1.10.4 Magnetic Properties of magnetic nanoparticles

Magnetic properties of nanoparticles depend on chemical composition, particle size, and morphology<sup>72</sup>. Surfactants or coatings that are used either to minimize aggregation/or functionalize magnetic nanoparticles influence their magnetic properties<sup>73</sup>. In a typical study by Ahmadi *et. al.*<sup>63</sup> magnetic properties of Fe<sub>3</sub>O<sub>4</sub> were investigated using vibrating sample magnetometer and the results are displayed in Figure 1.2 below. Three samples were prepared at the pH of 12, 11.5 and 11. The saturation magnetization of the samples was equal to 64.15, 70.75 and 72.70 emu/g respectively. These values were significantly larger than the reported data where longer molecules and also compared to L-cysteine used in this study.

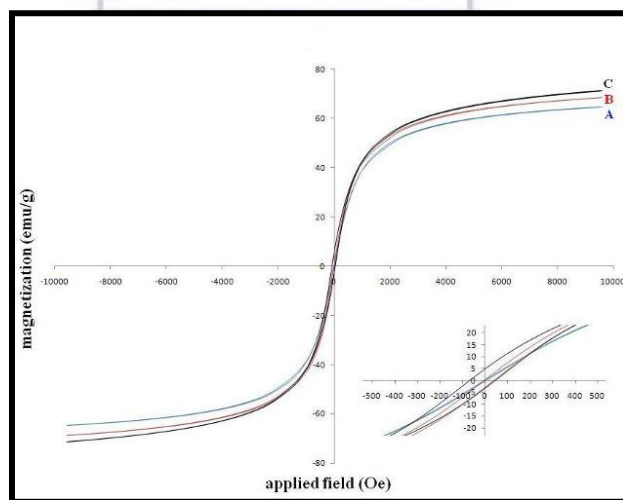


**Figure 1.2: Vibrating sample magnetometer diagram for three samples of Fe<sub>3</sub>O<sub>4</sub> synthesized at pH of 12, 11.5 and 11. Reprinted with permission from Ahmadi *et. al.*<sup>63</sup> Copyright (2012) Springer**

Superparamagnetic effect of iron oxide nanoparticles loaded with anticancer gemcitabine and fluorescein isothiocyanate antibody was confirmed using vibrating sample magnetometer (VSM 7300 magnetometer). The hysteresis loop was obtained by applying

a maximum magnetic field of 7500 Oe. The study revealed that the magnetization saturation of the multifunctional nano-biocomposite to be 54.97 emu/g. The magnetic retentivity and coercivity were found to 2.25 emu/g and 57.75 Oe, respectively. The measurement was done at 20 °C and a plot of magnetic saturation (Ms in emu/g) versus applied a magnetic field (H in Oe) given<sup>74</sup>.

Kiplagat *et. al.*<sup>75</sup> reported magnetic properties of iron oxide nanoparticles, functionalized iron oxide nanoparticles and iron oxide coupled with InP/ZnSe quantum dots. In their study, they established that use of short ligands such as dopamine and L-cysteine does not reduce significantly the magnetic saturation of the iron oxide nanoparticles. Paulsen *et. al.*<sup>76</sup> reported significant reduce in magnetic saturation when they coupled iron oxide to InP/ZnSe QDs from around 65 emu/g to 5.7 emu/g.

#### **1.10.5 Applications of magnetic nanoparticles**

Iron oxide nanoparticles of the type Fe<sub>3</sub>O<sub>4</sub> has a great potential to be used as a contrast agent for magnetic resonance imaging. Superparamagnetic or paramagnetism can create a magnetic field around themselves when exposed to an external magnetic field; hence, the image intensity decreases at particles accumulation regions as a result of rapid dephasing of the spins through a so-called susceptibility effect. This makes image contrast to improve due to the enhancement of signal intensity difference between target tissues and the other untargeted tissues<sup>77,78</sup>. The MNPs have been used as MRI contrast agents where rats were used for *in vivo* studies. The rats were anesthetized and MRI scans was done six hours after administration of samples of Fe<sub>3</sub>O<sub>4</sub>. The dose given were 2.5 mg (Fe<sub>3</sub>O<sub>4</sub>)/kg body weight and MRI studies were performed at 1.5 T using knee coil for transmission and reception of the signal. A subcutaneous injection was done on the right hand, after six

hours it was noted that accumulation occurred on the lymph nodes and none was noticed on the left-hand side of the animal. The study proved successful due to imaging of lymphatic system using iron oxide as a contrast agent<sup>79</sup>.

Mandal *et. al.* carried out a study by preparing multifunctional nanobiocomposite for targeted drug delivery in cancer therapy. Iron oxide nanoparticle of 15 nm in diameter was used as a contrast agent to enhance MRI and the anticancer drug gemcitabine. *In vitro* studies were done to compare cancer cell lines that were treated with the nanobiocomposite and untreated cell lines. The study revealed black spots on the gastric cancer cell lines that were treated with the nanobiocomposites whereas no reduction in the signal of the untreated cells. The group concluded that the iron oxide nanobiocomposite can act as an MRI contrast agent and as a targeted drug delivery system *in vivo* experiments using rats as an animal model<sup>74</sup>.

### **1.11 Quantum dots (QD)**

Quantum dots are inorganic semiconductor nanocrystals. They are well-known candidates for use as fluorescent materials because of their high photostability, high emission quantum yield, narrow emission peak and size dependent wavelength tunability in comparison to organic dyes and fluorescent proteins as mentioned earlier. These attractive features make inorganic quantum dots best suitable for biomedical applications in areas such as DNA detection, cellular imaging, protein trafficking, and dynamic studies of cell motility. Furthermore, the inorganic quantum dots are more robust than their organic counterparts, property which leads to reduced photobleaching under light thus allowing real-time monitoring of biological events over extended periods of time<sup>80</sup>.

In spite of numerous attractive optical features, the quantum dots suffer some drawbacks when applied for the *in vivo* imaging. These include; 1) the emitting light in the visible region cannot penetrate through the skin of the animal subjects and thus the need for development of quantum dots of near infrared region (NIR)<sup>78</sup>; 2) Quantum dots are reported to flicker when they are within the cellular specimen<sup>81,82</sup> hence need for multifunctional nanomaterial for imaging.

### 1.11.1 Photoluminescence process of quantum dots

Inorganic semiconductors exhibit good optical and optoelectronic properties. This is due to confinement of carrier motion and discreteness of electronic states. This kind of confinement is also known as quantum size effect. The impact of quantum size effect makes InP nanoparticles to have large exciton Bohr radius (11.3 nm) and relatively narrow band gap (1.35 eV). This situation results to larger exciton Bohr radius compared to nanoparticle diameter leading to quantization effect. Figure 1.3 shows the photoluminescence mechanism.

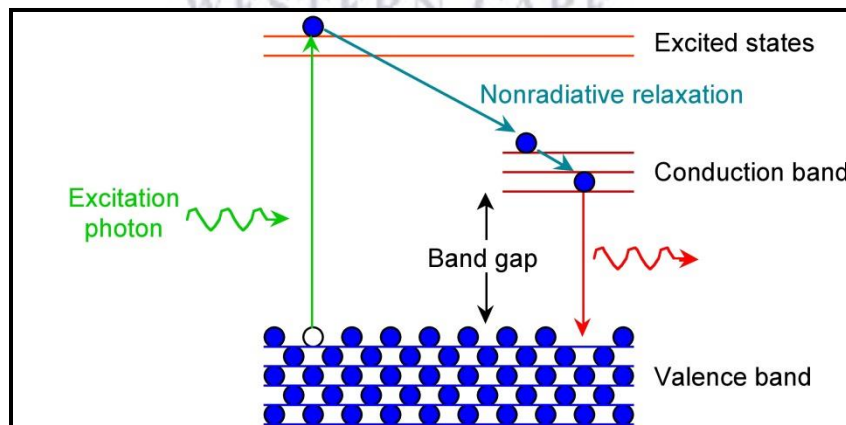


**Figure 1.3: Schematic diagram of typical photoluminescence process**

Semiconductors derived from group III-V compounds especially the nitrides and phosphides are referred to as “greener” since the constituent elements are more environmentally friendly compared to Cd, Pb, Hg or Te. Despite admirable characteristics of group III-V semiconductors, their applications are sparse due to significant difficulty on their synthesis, unlike group II-VI analogues<sup>83</sup>. The InP is one of the most promising semiconductors due to its size-tunability emission in the visible and near-infrared spectral range with a bulk band gap of 1.35 eV and low intrinsic toxicity<sup>84</sup>. In addition, InP exhibits a larger dielectric constant, lower effective  $e^-$  and  $h^+$  masses, and weaker phonon coupling leads to pronounced quantization effects and greater photostability<sup>85</sup>. However, Indium phosphide nanocrystals synthesized and dispersed in organic solvents demonstrates very low band edge photoluminescence due to surface traps, dangling bonds, stacking faults, and high activation barrier for carrier de-trapping.

Again, due to large surface to volume ratio, the photo-excited electrons in the conduction bands are extensively trapped into the surface states. The trap sites and surface states defects are among the contributing factors for photo-degradation and quenching sites. The trap of the electrons or holes induces non-radiative recombination hence reduced luminescence. The photoluminescence efficiencies of quantum dots can be enhanced by eliminating both the anionic and cationic dangling bonds at their surfaces. The surface defects can be eliminated physically by thermal treatment or chemically via the introduction of organic capping or inorganic shell at the surface leading to enhanced photoluminescence<sup>86</sup>. Overcoating the core of semiconductors, especially with wider band gap shell, improves challenges of quantum inefficiency, instability, and color saturation<sup>87</sup>. The concept of the core-shell structure was developed around 1990, where CdSe quantum

dots were coated with ZnS shell. Development of the core-shell structure resulted in improved quantum yield, clear band-edge emission, and suppression of broad red-shifted trap emission. Hine and GuyotSionnest in 1996 synthesized CdSe capped with ZnS, the prepared CdSe/ZnS were stable at room temperature and showed enhanced band-edge luminescence by 50 % quantum yield<sup>88</sup>.

In regard to the applications, the inorganic semiconductors have been used as fluorescing labelling for both *in vivo* cellular visualization and *in vitro* assay<sup>89</sup>. In the past organic and genetically encoded fluorophores were widely applied for bio-imaging. However, they are known to suffer from various drawbacks including photophysical properties such as broad absorption/emission profiles as well as low photo-bleaching thresholds<sup>90</sup>. Strategies have been put forward in the last one decade to overcome synthetic difficulties. The improvement in this area has been on the fluorescent properties of InP quantum dots approach, especially for groups II-VI QDs. Other strategies seek an alternative source of phosphorous to improve synthetic approaches. The main reason being that the most relied on P(TMS)<sub>3</sub> is highly unstable, expensive, highly flammable and relatively toxic<sup>91</sup>.

In 2011 Byun *et. al.*<sup>91</sup> synthesized InP/ZnS via a solvothermal process for 24 hours at 180 °C using P(N(CH<sub>3</sub>)<sub>2</sub>)<sub>3</sub> as a source of phosphorous. When the core and the shell growth were complete, they subjected the synthesized QDs to size-sorting processing, by which red to green-emitting QDs with quantum yield (QY) of 24-60% were produced. The TEM images indicated that the prepared quantum dots had average sizes of 2.3 -3.3 nm which were small compared to their Bohr excitonic radius of 15 nm hence they belonged to quantum confinement regime. In another strategy, to increase photoluminescence of In-

based quantum dots, Kim *et. al.*<sup>92</sup> passivated InP core with ZnSe. The group was able to fabricate InP/ZnSe with an average diameter of 3 nm by using hot injection method and with P(TMS)<sub>3</sub> as the source of phosphorous. The passivation of InP core with ZnSe led to an increase in photoluminescence by a factor of 6.8 compared to that of InP. They were able to investigate the structure and morphology of the nanocrystals using HRTEM and XRD. The HRTEM images revealed lattice fringes with a spacing of 0.34 nm which was in agreement with 0.3388 nm between the (111) planes of Zinc-blende of InP structure. This observation suggested that the ZnSe shell was very thin and also that it was a monolayer hence they were able to observe the lattice structure of the core. The main shortcoming with their synthetic procedure was that after injection of P(TMS)<sub>3</sub> at 200 °C they had to allow growth of InP core for several days at 280 °C making the process time-consuming.

In another report Mushonga *et. al.*<sup>93</sup> improved photoluminescence of InP/ZnSe and obtained the same quality of QDs within a short reaction duration. The group synthesized InP/ZnSe via hot injection technique and further doped InP/ZnSe with silver (Ag), iron (Fe) and cobalt (Co). In their research, they used non-coordinating solvent 1-octadecene. Their method yielded InP/ZnSe nanocrystals with an average diameter of 1.95 nm with a lattice-fringe distance of 0.29 nm. They were able to demonstrate that ZnSe shell was able to passivate the InP core. The passivation resulted in a blue-shift and reduction of about 1.4 times in the ratio of trapped related emission to band edge emission. Li and Reiss<sup>84</sup> synthesized InP/ZnS using single step method without precursor injection. In their strategy, the quantum efficiency reached 70% which was attributed to the method of synthesis. In their study, they chose a ratio of In:P to be between 1.5-1.9:1 while the ratio



of In:Zn:S was 1:1:1. The ratio of 1:1:1 yielded highly photostable nanocrystals even after irradiation under UV light for more than 45 hours in the presence of oxygen. When the ratio of In:Zn:S was lowered to 1:0.3:0.3, the quantum dots formed was quite unstable, they noted that the quantum yield decreased drastically from 68% to 50 % within 15 hours of UV radiation. Figure 1.4 shows the effect of the ratio of the components on the photostability of the prepared quantum dots. The photostability test was done by exposing the quantum dots to UV light in the presence of oxygen.

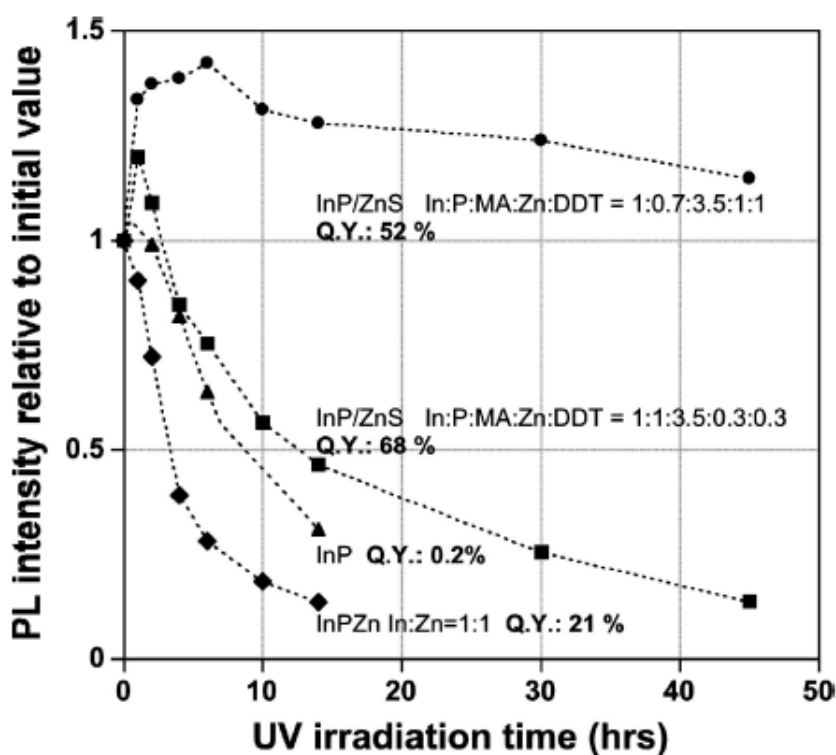


**Figure 1.4: Influence of UV irradiation on the quantum yield. Reprinted with permission from Li and Reiss<sup>84</sup>**

In another strategy to obtain an alternative source of phosphorous for the synthesis of Indium based quantum dots, Li *et. al.*<sup>83</sup> synthesized InP/ZnS quantum dots using PH<sub>3</sub> gas

generated in situ from calcium phosphide ( $\text{Ca}_3\text{P}_2$ ). The  $\text{PH}_3$  gas was generated as shown in the following Figure 1.5.

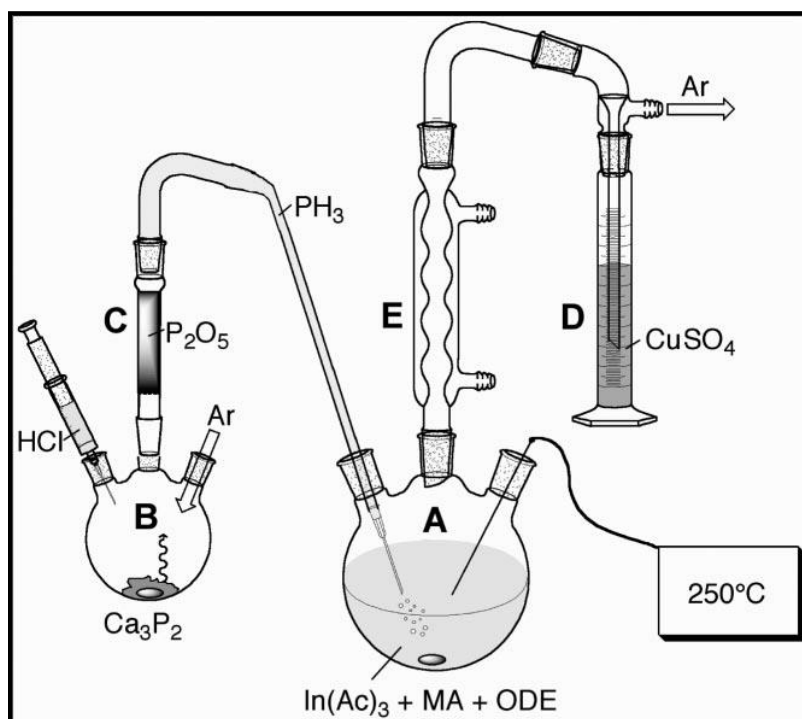


**Figure 1.5: Synthesis of InP nanocrystals using an alternative source of phosphorous. Reprinted with permission from Li *et. al.*<sup>83</sup>**

According to the group the use of an air-stable source of phosphorous drastically reduced the cost of synthesis of indium-based quantum dots. The XRD analysis showed that the lattice structure of the prepared InP core nanocrystals had a cubic zinc blende structure and no signs of formation of Indium oxide ( $\text{In}_2\text{O}_3$ ). They estimated the size of the nanocrystals to be 2.63 nm using Scherrer's formula. The researcher's noted that upon addition of Zinc stearate to the prepared core the photoluminescence increased significantly prior to addition of sulphur source. The quantum yield of the final product InP/ZnS was calculated to be 22 %<sup>83</sup>.

Kim *et. al.*<sup>94</sup> with the aim of increasing quantum efficiency developed a multishell InP quantum dots. They were able to fabricate InP/ZnSe/ZnS colloidal nanocrystal solutions with a quantum yield of 40%<sup>94</sup>.

### 1.11.2 Ligand exchange strategies

Ligand exchange involves phase transfer of the native hydrophobic surfactant on the nanocrystals surfaces and replacing it with the hydrophilic one. Figure 1.6 shows a schematic representation of a typical ligand exchange process.

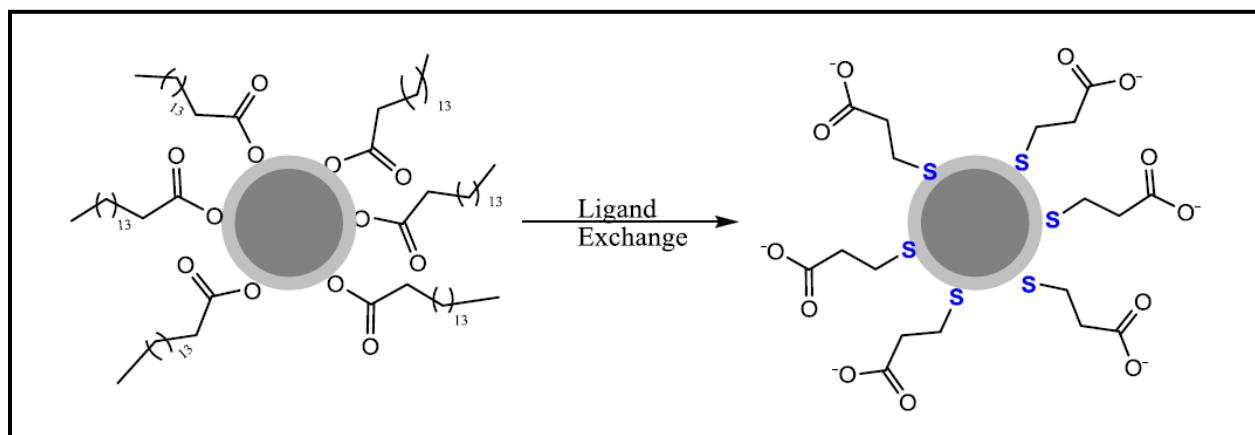


**Figure 1.6: Schematic diagram of a ligand exchange process**

Li *et. al.*<sup>84</sup> prepared water soluble InP/ZnS through reactive phase transfer and photochemical processing. In another strategy to prepare water soluble InP/ZnS, Brunetti *et. al.*<sup>95</sup> transferred QD solution (5 mM, 200  $\mu$ L) to 800  $\mu$ L butanol, 1000  $\mu$ L borate buffer (pH 9, 200 mM) and (8  $\mu$ L, 10  $\mu$ M) 3-mercaptopropionic acid. They heated the mixture to 50  $^{\circ}$ C for 15 minutes and washed/filtered (10 kDa molecular weight cut-off filter-Vivaspin 500) in four cycles using of 50 mM borate buffer pH 9. The QDs were dispersed in the desired buffer and stored at 4  $^{\circ}$ C for future use.

### 1.11.3 Cytotoxicity of indium based QDs

Quantum dots (QDs) are an interesting class of nanomaterials, and have found applications in imaging in biology and medicine. The applications of these semiconductor nanocrystals come alongside with serious concerns about toxicity and safety. In this section of the thesis, various cytotoxic studies of indium based quantum dots are presented. Quantum dots containing CdSe, CdTe, and CdS have been known to be highly toxic and carcinogenic for living systems<sup>95</sup>. Recently, Brunetti *et. al.*<sup>95</sup> assessed the toxicity of InP/ZnS by conducting both *in vivo* and *in-vitro* studies. In their experiment, they compared the toxicity of InP/ZnS and CdSe/ZnS. Epithelial cell line A549 (human lung carcinoma) and the neuronal cell line SHSY5Y (human neuroblastoma) were cultivated in the presence of increasing concentrations of either CdSe/ZnS or InP/ZnS from 1pM -5 nM. Cell viability was measured after 24 hours and 48 hours of incubation using water-soluble tetrazolium salt (WST-8 Test). Figure 1.7 A and B compares cell viability of CdSe/ZnS and InP/ZnS using A549 and SH SY5Y cell lines.

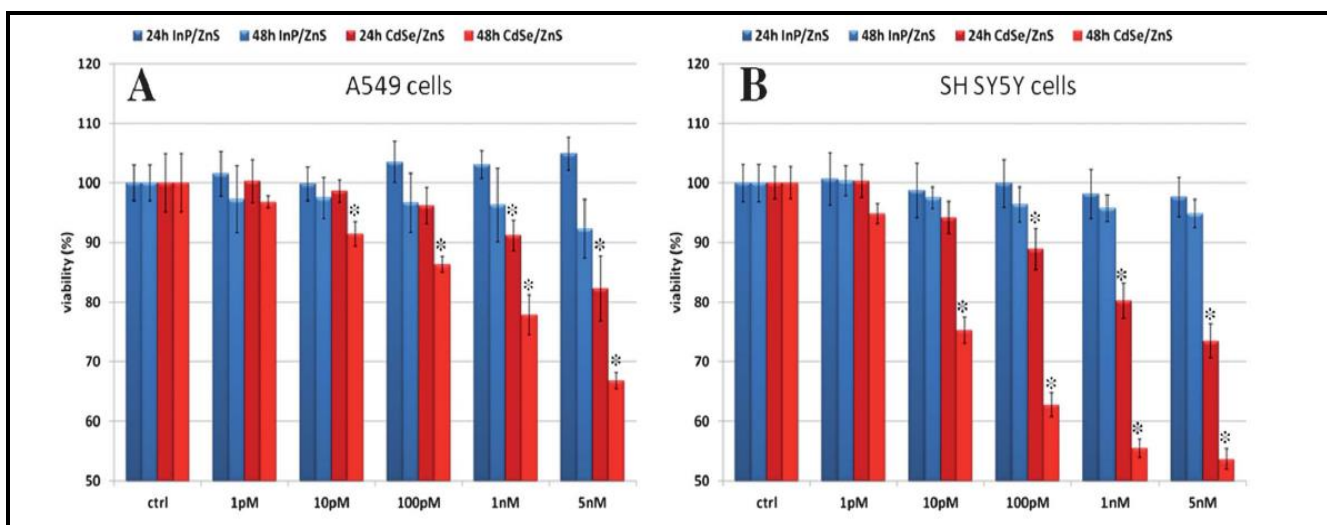


**Figure 1.7: (A and B) WST-8 Proliferation of assay on A549 and SH SY5Y cells with increasing concentration of InP/ZnS and CdSe/ZnS. Reprinted with permission from Brunetti *et. al.*<sup>95</sup>**

The toxicity effect of CdSe/ZnS was observed 24 hours after incubation at 1nM concentration. Detectable reduction in cell viability was observed for CdSe/ZnS QD concentration as low as 10 pM. The highest toxicity was found to be neuronal cell line with a 27 % viability loss after 24 hours and increased to 46 % after 48 hours with 5 nM concentrations of CdSe/ZnS. On the other hand, InP/ZnS showed an insignificant reduction in cell viability of less than 10 % in both cell lines. *In vivo* investigations were carried out using *drosophila* fruit flies. The choice of *drosophila* was because of the short life time, high genetic homology with the human genome and limited ethical issues. The fruit flies were fed with food containing 100 pM and 500 pM concentrations of InP/ZnS or CdSe/ZnS. Real-time qPCR was used to clarify mechanism underlying QD toxicity by investigating variations in expression levels of genes involved in stress response and DNA damage such as *hsp70*, *hsp83*, *p53* and *dress* genes. The proteins Hsp70 and hsp83 are

proteins expressed in the stress response and are part of the heat shock family. Upon feeding the *drosophila* with 100 mM CdSe/ZnS hsp70 and hsp83 were overexpressed by 3-5 times. The same proteins were over-expressed up to 10 times when the flies were fed with 500 nM of CdSe/ZnS. In contrast, the *drosophila* fed with InP/ZnSe did not present any significant increase in gene concentration. There was sufficient evidence for systematic toxicity of CdSe/ZnS<sup>95</sup>.

### **1.12 Fluorescent magnetic nanocomposites**

In the recent past, magnetic materials and semiconductor inorganic materials have been developed and applied as independent subjects. Numerous research on their properties have been conducted and many theories about them put forward not only in the chemistry but also in the field of physics<sup>96</sup>. Related to this but on the biomedicine, the biotechnological processes such as imaging, tracking, and separating biological molecules or cells desire submicrometer particles featuring characteristics such as magnetization and fluorescence<sup>97</sup>. Therefore, the development of multifunctional nanomaterial can make such processes more efficient and simpler for diverse therapies including cancer diagnosis and treatment<sup>98,99</sup>. The nanocomposite in this sense, would constitute nanoparticles with both magnetic and optical properties. The magnetic-fluorescing nanoparticles can be used as an all-in-one diagnostic tool based on magnetic resonance imaging<sup>96</sup>. The fluorescing part emitting at appropriate wavelength can be utilized in visual imaging by fluorescence imaging microscope. The nanocomposite would therefore, allow optical tracking of biological processes as well as magnetic manipulations<sup>100</sup>.

In addition, in this part of the literature review, we will discuss various approaches developed in the fabrication of nanocomposite materials, their properties, and applications. The properties discussed hereinafter will confine itself to sizes of the constituted nanocomposite based on HRTEM, XRD, and HRSEM. The quenching effects on the magnetic properties and the fluorescing capabilities will also be investigated. Applications will confine itself to cell imaging, drug delivery, MRI imaging and any other medical related application in the biomedical field.

### **1.12.1 Synthetic approaches of fluorescence magnetic nanocomposites**

Since 2004 several strategies have been laid out to synthesize various types of nanocomposites that suit medical application. Properties of the as-prepared nanocomposites have been investigated and also their applications evaluated. In 2004 Wang *et. al.*<sup>97</sup> described for the first time the formation of the luminescent magnetic nanocomposite. Their nanocomposite material consisted of a core  $\gamma$ -Fe<sub>2</sub>O<sub>3</sub> and a shell of CdSe/ZnS quantum dots at their surface. The nanometric ferrofluid was stabilized and functionalized further with meso-2,3-dimercaptosuccinic acid (DMSA). Eventually, the surface was covered with free thiol (-SH) and carboxyl (-COOH) residues which could enable them to form a covalent bond with various ligands. On the other hand, luminescent CdSe/ZnS quantum dots were separately prepared following the procedure developed by Peng *et. al.*<sup>101</sup>. Thiol functional group that was introduced initially to the surface of the ferrofluid was utilized to couple the magnetic beads and the luminescent quantum dots. The group was faced with miscibility challenge since they had dispersed the magnetic bead in water and the quantum dots in chloroform. The challenge was overcome by having a mixture of chloroform, water, and methanol in the ratio of 10:5:1. In this mixture, the

quantum dots and the ferrofluid were introduced in a ratio of 100:1. The QDs were introduced in large excess to minimize the problematic aggregation of the magnetic beads. The nanocomposite was finally achieved under vigorous stirring of aqueous and organic mixture for 1 hour.

Amala *et. al.*<sup>98</sup> developed Au/Fe<sub>3</sub>O<sub>4</sub> nanocomposite by a convenient two-step bottom-up approach with useful optical and magnetic properties. They separately prepared Fe<sub>3</sub>O<sub>4</sub> by commonly preferred method of co-precipitation and the Au nanoparticles by rapid synthesis technique. In brief, the Au nanoparticles were prepared by mixing the HAuCl<sub>4</sub> with the appropriate amount of cetyltrimethylammonium bromide (surfactant) followed by slow addition of 0.5 M NaBH<sub>4</sub> (reducing agent). The Fe<sub>3</sub>O<sub>4</sub> were prepared by utilizing Fe<sup>2+</sup>, Fe<sup>3+</sup> and NaOH as the base (precipitant). The two aqueous nanometric solutions were mixed at the ratio of 1:1 of Fe<sub>3</sub>O<sub>4</sub> to Au and subjected to solvothermal process and stirred for 15 minutes and later transferred to a Teflon-lined autoclave and then kept in the furnace at 300 °C for 4 hours. The same was repeated but at a ratio of Au: Fe<sub>3</sub>O<sub>4</sub> altered to 2:1.

By using aptamers conjugated to magnetic graphene/gold nanocomposite, Xiong *et. al.*<sup>99</sup> developed a novel method for specific enrichment and rapid analysis of thrombin in biological samples using matrix-assisted laser desorption/ionization-time of flight-mass spectroscopy (MALDI-TOF-MS). Separately, magnetic graphene was prepared by the solvothermal method reported in the past works<sup>102</sup>. Gold colloids were also prepared following procedure reported in earlier works [81]. The prepared magnetic graphene was dispersed in aqueous solution of 0.2% polyelectrolyte poly (diallyl dimethyl ammonium



chloride) containing 20 mM tris-base and 20 mM NaCl and stirred for 20 minutes. They added three portions of 100 mL of prepared colloid gold nanoparticles to the mixture under vigorous stirring. Finally, the obtained nanocomposite was washed with three cycles of deionized water and later dried under vacuum at 60 °C for 6 hours. The resulting magnetic graphene/Au hybrid nanocomposite had an ultra-high surface area for aptamer immobilization<sup>99</sup>.

A nanocomposite material that constituted carboxymethyl chitosan-based folate/Fe<sub>3</sub>O<sub>4</sub>/CdTe for targeted drug delivery and cell imaging was recently prepared by shen *et. al.*<sup>103</sup>. They synthesized the magnetic core of chitosan-fluorescence magnetic nanoparticles (CFMNPS) following the procedure described in earlier work<sup>104</sup>. A carboxymethylation (CMCH) process was used to modify the chitosan. The CMCH was dissolved in a buffer and activated the carboxylate groups by an addition of 1-ethyl-3-(3-dimethylaminopropyl) carbodiimide hydrochloride solution (EDAC). A suspension of Fe<sub>3</sub>O<sub>4</sub> was added to the active solution of CMCH and sonicated for 5 minutes then vibrated for 2 hours at room temperature to facilitate binding. The complex was separated, rinsed and dried overnight under vacuum at 60 °C. The complex Fe<sub>3</sub>O<sub>4</sub>/CMCH was suspended at a concentration of 50 mg/mL buffer for further use. Separately, thioglycolic acid (TGA) capped CdTe was prepared by hydrothermal and precipitated in excess anhydrous ethanol and dissolved in deionized water. The TGA functionalized CdTe allowed successful binding between CdTe and Fe<sub>3</sub>O<sub>4</sub>/CMCH. The coupling process was achieved by first activating TGA-CdTe using 1-ethyl-3-(3-dimethylaminopropyl) carbodiimide hydrochloride and irradiated with natural light for 24 hours and finally sonicated for 10 min to obtain active QDs. Optimization process on the ratio of

$\text{Fe}_3\text{O}_4:\text{CdTe}$  was carried out to obtain considerable PL intensity. To stabilize CdTe in aqueous solution, the complex  $\text{Fe}_3\text{O}_4/\text{CMCH}/\text{CdTe}$  was soaked in 2.5 mL of 1-ethyl-3-(3-dimethylaminopropyl) carbodiimide hydrochloride activated CMCH. The mixture was vibrated for 1 hour to enhance CMCH shell formation on the nanocomposite. Lastly, the nanocomposite was washed thoroughly with buffer solution and freeze-dried to obtain dry chitosan luminescence magnetic nanoparticles. The chitosan luminescence magnetic nanoparticles were further conjugated to the folate. Folate was activated first using 1-ethyl-3-(3-dimethylaminopropyl) carbodiimide hydrochloride then chitosan luminescence magnetic nanoparticles added dropwise while stirring. The product folate-conjugated chitosan luminescence magnetic nanoparticles were rinsed and freeze dried<sup>103</sup>.

Xu *et. al.*<sup>105</sup> synthesized luminescent superparamagnetic nanocomposites of the type  $\text{Fe}_3\text{O}_4/\text{SiO}_2\text{-CdSe-ZnS}$ . They synthesized  $\text{Fe}_3\text{O}_4$  nanoparticles by co-precipitation and modified its surface by a silica shell. The coated magnetic fluid was soaked in citric acid to introduce  $-\text{SH}$  functional group. On the other hand, water-soluble QDs were synthesized following a procedure reported in earlier works<sup>106</sup>. The QDs were dissolved in chloroform and their surface modified using mercaptopropionic acid to make them water soluble. Finally, their nanocomposite was formed by quickly adding QD solution to the  $\text{Fe}_3\text{O}_4/\text{SiO}_2\text{-SH}$  solution and the product was left to stir at 35 °C for 12 hours. The orange product was separated with a magnet from the solution<sup>105</sup>.

In another strategy to synthesize a nanocomposite, Roychowdhury *et. al.*<sup>107</sup> synthesized fluorescent-magnetic  $\text{Fe}_3\text{O}_4/\text{ZnS}$  nanocomposites. They first synthesized magnetic nanoparticles by chemical precipitation following a reported procedure<sup>108</sup>. The  $\text{Fe}_3\text{O}_4/\text{ZnS}$

was prepared by dispersing required amount of  $\text{Fe}_3\text{O}_4$  powders in  $\text{Zn}(\text{NO}_3)_2$  salt solution. The disodium sulphite salt solution was added dropwise with immense sonication. The precipitate was separated by centrifuge, washed with deionized water and dried under vacuum for one week. The dried precipitate was heat-treated at  $200\text{ }^\circ\text{C}$ .

Recently, Zhang *et. al.* prepared highly fluorescent magnetic nanoparticles of the type  $\text{Fe}_3\text{O}_4$ -CdSe. First, Topo-capped bare/core CdSe and Shell/core QDs were synthesized by hot injection following the procedure reported in earlier works by Li *et. al.*<sup>109</sup>. During the synthetic process, the color of the solution changed from colorless, to green and finally to red which was an indication of QDs formation. The TOPO-capped QDs were precipitated by adding dry ethanol, centrifuged, washed with methanol and dried in a vacuum for further surface modification prior to coupling with the magnetic nanoparticles. The shell/core of the QDs was formed by dissolving CdSe in hexane mixed with octadecyl amine (ODA) and 1-octadecene (ODE). The mixture was heated to  $100\text{ }^\circ\text{C}$  to remove hexane from the system. The temperature was raised to  $240\text{ }^\circ\text{C}$  to allow injection of Cd, Zn, and S precursors which were prepared following procedure by Li *et. al.*<sup>109</sup>. The product was diluted with hexane followed by methanol to precipitate the nanocrystals. The shell creation resulted in the formation of seven layers CdSe/CdS/CdS/ $\text{Cd}_{0.75}\text{Zn}_{0.25}\text{S}$ / $\text{Cd}_{0.5}\text{Zn}_{0.5}\text{S}$ / $\text{Cd}_{0.25}\text{Zn}_{0.75}\text{S}$ /ZnS. The formation of the seven layers was confirmed by electron dispersive spectroscopy (EDS) and XRD. On the other hand,  $\text{Fe}_3\text{O}_4$  were prepared by hydrothermal method. Fluorescent magnetic nanoparticles were prepared by mixing the prepared quantum dots and the magnetic nanoparticles in chloroform and tetraethoxysilane (TEOS) were added to a flask with continuous stirring.

The microemulsion was formed within thirty minutes. The product was separated from the microemulsion and washed several times<sup>105</sup>.

Ma *et. al.*<sup>110</sup> prepared bifunctional nanocomposite of the type CdTe-SiO<sub>2</sub>- $\gamma$ -Fe<sub>2</sub>O<sub>3</sub>. The silica-coated superparamagnetic nanoparticles (SiO<sub>2</sub>- $\gamma$ -Fe<sub>2</sub>O<sub>3</sub>) were prepared using coprecipitation method. The silica coat was incorporated by ultrasonication  $\gamma$ -Fe<sub>2</sub>O<sub>3</sub> in the water-in-oil reverse microemulsion of water/TritonX-100/n hexylalcohol/cyclohexane followed by an addition of concentrated ammonia and TEOS. To obtain NH<sub>2</sub>-SiO<sub>2</sub>- $\gamma$ -Fe<sub>2</sub>O<sub>3</sub> nanoparticles, an appropriate amount of SiO<sub>2</sub>- $\gamma$ -Fe<sub>2</sub>O<sub>3</sub> was dispersed in a mixture of methanol and glycerol followed by an addition of N-(2-aminoethyl)-3-aminopropyltrimethoxysilane (AEAPS). The amino-functionalized silica coated magnetic nanoparticles was washed with ethanol and dispersed in PBS at pH 7.4. The MPA capped-CdTe was attached to NH<sub>2</sub>-SiO<sub>2</sub>- $\gamma$ -Fe<sub>2</sub>O<sub>3</sub> through 1-ethyl-3-(3-dimethylaminopropyl) carbodiimide hydrochloride coupling and the nanocomposite was obtained<sup>111</sup>. They dispersed the QDs in PBS containing 5 mg 1-ethyl-3-(3-dimethylaminopropyl) carbodiimide hydrochloride added and after 15 minutes of incubation, the NH<sub>2</sub>-SiO<sub>2</sub>- $\gamma$ -Fe<sub>2</sub>O<sub>3</sub> was added. The coupling reaction was allowed to occur for two hours under gentle shaking at room temperature. Eventually the bifunctional nanoparticles were then collected by magnetic separation and dispersed in PBS awaiting further use<sup>110</sup>.

In another work by Li *et. al.*<sup>112</sup> reported a successful synthesis of Fe/C/YBO<sub>3</sub>:Eu<sup>3+</sup> with both magnetic and photoluminescence properties. They started by synthesizing Fe<sub>3</sub>O<sub>4</sub> through coprecipitation and coated it with a carbon surface. The amorphous carbon acted as a couplant and a conductor of the excited electrons between the magnetic part and the

luminescent part. The carbon layer was achieved by adding glucose into turbid liquid, ultrasonicated for half an hour and autoclaved at 200 °C for 4 hours. The resulting Fe<sub>3</sub>O<sub>4</sub>/C nanoparticles was separated using a magnet, washed with distilled water and ethanol, then dried under vacuum at 50 °C for 12 hours. The next step was to synthesize Fe<sub>3</sub>O<sub>4</sub>/C/YBO<sub>3</sub>:Eu<sup>3+</sup> nanocomposite. Firstly, Yttrium oxide, Europium oxide and boric acid were dissolved in nitric acid. The pH was adjusted to 9 using concentrated ammonia and at once Fe<sub>3</sub>O<sub>4</sub>/C was added. The solution was stirred for 30 min and later autoclaved at 180 °C for 8 h. The NPs were separated, washed and dried in the vacuum for 12 hours. Finally, the Fe/C/YBO<sub>3</sub>:Eu<sup>3+</sup> was synthesized by placing Fe<sub>3</sub>O<sub>4</sub>/C/YBO<sub>3</sub>:Eu<sup>3+</sup> inside a muffle furnace at 800 °C for 3 hours under protection of N<sub>2</sub>. The reduction occurred between the mid carbon layer and the Fe<sub>3</sub>O<sub>4</sub> core. During the process, the Fe<sub>3</sub>O<sub>4</sub> was reduced completely to Fe and the product Fe/C/YBO<sub>3</sub>:Eu<sup>3+</sup> was achieved<sup>112</sup>.

Tong *et. al.*<sup>113</sup> synthesized double shell structured nanocomposite of the type Fe<sub>3</sub>O<sub>4</sub>/Y<sub>2</sub>O<sub>3</sub>:Eu<sup>3+</sup>/Y<sub>2</sub>O<sub>3</sub>:Eu<sup>3+</sup> with both magnetic and fluorescent properties. They started by synthesizing PEG-coated Fe<sub>3</sub>O<sub>4</sub> NPs through co-precipitation method. The PEG was used here to stabilize the NPs, make them water soluble due to its hydrophilicity and to render them biocompatible. Secondly, Fe<sub>3</sub>O<sub>4</sub>/C composite were synthesized in situ through carbonization. Typically, Fe<sub>3</sub>O<sub>4</sub> were dispersed in glucose solution and the mixture autoclaved at 200 °C for 4 h. The product Fe<sub>3</sub>O<sub>4</sub>/C was separated with an aid of external magnet washed and dried under vacuum for 24 h at 60 °C. The product Fe<sub>3</sub>O<sub>4</sub>/C/Y<sub>2</sub>O<sub>3</sub>:Eu<sup>3+</sup> was obtained by dispersing Fe<sub>3</sub>O<sub>4</sub>/C in a solution of urea and Ln (NO<sub>3</sub>)<sub>3</sub> (Ln= Y, Eu:Eu<sup>3+</sup>, doping concentration was at 5 %). The mixture was sonicated for 20 minutes and heated to 90 °C under vigorous stirring. The product was separated and

further dried at 100 °C overnight. The final product was obtained by calcining the previous product at 500 °C to remove carbon sphere and subjecting it to further calcination at 700 °C for 2 h to complete the conversion to oxide<sup>113</sup>.

Wang *et. al.*<sup>114</sup> in another study synthesized magnetic and fluorescent bi-functional silica composite nanoparticles via reverse micro-emulsion method. They first prepared monodispersed iron oxide MNPs through co-precipitation method and added tetramethylammonium hydroxide (TMA) to peptize the MNPs. Separately, the group prepared a mercaptosuccinic acid (MSA) capped CdTe prepared using hydrothermal route. A freshly prepared NaHTe solution was added to CdCl<sub>2</sub> in the presence of MSA at pH of 11.2 in an ice-water bath. The mixture was autoclaved and maintained at 160 °C for 50 minutes. The CdTe obtained were water compatible with high quantum yield of 75.3%. The nanocomposite MNPs-QDs/SiO<sub>2</sub> was prepared by reverse microemulsion method at room temperature. The cyclohexane was used as a continuous phase, triton-100 used as a surfactant and n-hexanol as a co-surfactant, respectively. The MNPs and QDs were added to the solution of cyclohexane and the surfactants with continuous stirring. After 30 minutes of stirring, NH<sub>4</sub>OH and PDDA solutions were added. Hydrolysis was initiated by adding TEOS to the micro-emulsion system and the reaction progressed in the dark for 24 hours. The micro-emulsion was broken by adding acetone. The resultant MNPs-QDs/SiO<sub>2</sub> was washed with a sequence of isopropyl alcohol, ethanol and water. The bifunctional nanocomposite was ready for further use.

Ahmed *et. al.* successfully incorporated CdTe QDs into Fe<sub>3</sub>O<sub>4</sub> MNPs for imaging the colon carcinoma cells. The CdTe QDs were synthesized following procedure reported in

an earlier work reported by Gaponik *et. al.*<sup>115</sup>. The Fe<sub>3</sub>O<sub>4</sub> NPs used here were synthesized by co-precipitation method. The MNPs were capped with citrate through an addition of sodium citrate during synthesis. The fluorescent-magnetic nanocomposite (FMNPs) was assembled based on procedure reported by Ahmed *et. al.*<sup>116</sup>. Descriptively, the citrate-capped Fe<sub>3</sub>O<sub>4</sub> were dispersed in CTAB solution under vigorous stirring. The CdTe-QDs were added and the mixture stirred at room temperature. The FMNPs were collected by external magnet and washed with repeated cycles of milliQ water and redispersed in milliQ water to await further use<sup>117</sup>.

Ye *et. al.*<sup>118</sup>. developed nanocarrier system for multimodal imaging and drug cancer delivery. The nanocarrier constituted superparamagnetic iron oxide nanoparticles (SPION) and manganese-doped Zinc sulfide (Mn:ZnS) quantum dots loaded with anticancer drug busulfan. The SPIONS were synthesized via thermal decomposition route. In brief, the Fe-oleate complex in octyl ether was decomposed at 297 °C in the presence of an oleic acid. The Fe<sub>3</sub>O<sub>4</sub> obtained was stabilized in oleic acid and dispersed in dichloromethane containing 9.1 mg/mL of iron. The Mn:ZnS QDs were synthesized following a nucleation-doping strategy reported earlier by Zhang *et. al.*<sup>119</sup>. In the initial stage, the manganese stearate (MnSt<sub>2</sub>) was prepared by an addition of a methanolic MnCl<sub>2</sub> solution into a mixture of stearic acid (SA) and tetramethylammonium hydroxide (TMAOH). The resulting MnSt<sub>2</sub> was mixed with 1-dodecanethiol in 1-ODE and the mixture degassed at 100 °C. It was followed by addition of sulphur and ZnAc<sub>2</sub> in that order at a temperature of 250 °C. The obtained Mn:ZnS NPs was washed with acetone and finally re-dispersed in dichloromethane. In the end, the nanocomposite was constituted by mixing poly(lactic-co-glycolic acid) (PLGA), SPIONs and Mn:ZnS PVA solution (1:20 oil to water ratio) using

probe-type sonicator to form an emulsion. This mixture was left to agitate the whole night to evaporate the organic solvent<sup>118</sup>.

In a recently published article by Murugan and Jebaranjitham<sup>120</sup>, a typical synthesis of a dendrimer grafted on core-shell of Fe<sub>3</sub>O<sub>4</sub> stabilized with AuNPs for enhanced catalytic degradation of Rhodamine B in a kinetic study was presented. They synthesized Fe<sub>3</sub>O<sub>4</sub> NPs using a co-precipitation technique and coated them with oleic acid to minimize agglomeration. They then prepared a polymer coated shell, Fe<sub>3</sub>O<sub>4</sub>-poly (4-MS-DVB-GMA). Separately, the 4-methylstyrene (4-MS), divinylbenzene (DVB) and glycidyl methacrylate (GMA) was added to polyethylene glycol dissolved in hot water and stirred. The mixture of the monomers was added to the ferrofluid dispersed in ethanol and left to react for 4 hours at 80 °C. The product Fe<sub>3</sub>O<sub>4</sub>-poly (4-MS-DVB-GMA) was dried and amino functionalized by the addition of 1, 6- diamino hexane. The dendrimers PAMAM-G (1) and PAMAM-G (2) were individually grafted to the surface of the amino-functionalized nanocomposite. The different types of magnetic-dendrimer nanocomposite were individually complexed with AuNPs using HAuCl<sub>4</sub> as the metal precursor. Each magnetic-dendrimer nanocomposite was separately dispersed in ethanol and aqueous solution of HAuCl<sub>4</sub> added to each matrix solution and then stirred at room temperature for 2 hours. The ionic state of Au<sup>3+</sup> attached to the magnetic-dendrimer nanocomposite in the form of the Fe<sub>3</sub>O<sub>4</sub>-poly-(4-MS-DVB-GMA) Au<sup>3+</sup> was reduced to Au<sup>0</sup> using NaBH<sub>4</sub>. The final product was in form of Fe<sub>3</sub>O<sub>4</sub>-poly (4-MS-DVB-GMA)-PAMAM-AuNPs which was ready now for a catalytic activity. In a related study, Jeong *et. al.*<sup>121</sup> developed interesting multifunctional Fe<sub>3</sub>O<sub>4</sub>-CdSe/ZnS nanoclusters coated with lipid A aimed at dendritic cell-based immunotherapy.



In a typical synthetic procedure the magnetic nanoclusters were prepared by a hydrothermal method and CdSe/ZnS nanocrystals were prepared by a reported method by Bae *et. al.*<sup>122</sup>. The conjugation of Fe<sub>3</sub>O<sub>4</sub> to CdSe/ZnS was successfully achieved by introducing a thiol group to the surface of the Fe<sub>3</sub>O<sub>4</sub>. The precipitate of thiol modified nanocluster were washed three times with PBS and dispersed in PBS. Aqueous CdSe/ZnS was added to PBS/toluene (aqueous/organic phase) containing a thiol-modified Fe<sub>3</sub>O<sub>4</sub>. To facilitate coupling, the solution were magnetically stirred for 24 hours at 80 °C<sup>121</sup>.

### **1.12.2 Properties fluorescent magnetic nanocomposites**

When separate, the magnetic nanoparticles (MNPs) exhibit superior magnetic properties. These properties might or might not be retained when these MNPs are conjugated to other components. Equally, the inorganic nanocrystals (QDs) exhibit excellent photoluminescence characteristics which might be quenched when conjugated to MNPs or other substances. Incorporation of a fluorescent material within an inorganic nanocrystal may modify its band gap energy as well as the luminescence properties<sup>123</sup>. The material Fe<sub>3</sub>O<sub>4</sub>-CdSe/ZnS synthesized by Jeong *et. al.*<sup>121</sup> demonstrated excellent optical and magnetic properties. The high superparamagnetic nature of Fe<sub>3</sub>O<sub>4</sub> core was always attributed to the large sizes of the nanoparticles which exhibit higher magnetization<sup>118</sup>. Their TEM and XRD analyses confirmed the core as highly crystalline with approximate diameter of 6-10 nm. The quantum dots synthesized were highly fluorescent with QY > 80 % and an approximate diameter of 6 nm. The QDs showed tint of green fluorescence at room temperature and strong green fluorescence under UV light in the dark ( $\lambda=365$ ). It was observed that these quantum dots prepared, retained their fluorescence abilities even after coupling with MNPs and undergoing subsequent chemical and biological processes.

The stability of these MNCs was established over a period of 6 months while stored under DI water. The scanning electron microscopy (SEM) confirmed that CdSe/ZnS NPs uniformly coated the Fe<sub>3</sub>O<sub>4</sub> clusters. The saturation magnetization reduced from 55.5 emu/g to 31.9 emu/g for the Fe<sub>3</sub>O<sub>4</sub> and the Fe<sub>3</sub>O<sub>4</sub>-CdSe/ZnS, respectively. Figure 1.8 below illustrates the decrease in saturation magnetization of the Fe<sub>3</sub>O<sub>4</sub> before and after coupling it with the CdSe/ZnS.

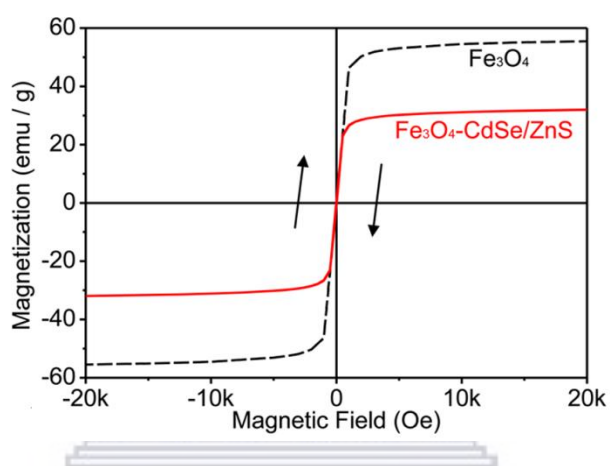


**Figure 1.8: Magnetization curves of Fe<sub>3</sub>O<sub>4</sub> (dashed line) and Fe<sub>3</sub>O<sub>4</sub>-CdSe/ZnS nanoclusters: “Reprinted with permission from Jeong *et. al.*<sup>121</sup>. Copyright©2014 American Chemical society**

A quick response to a permanent magnet and the disappearance of fluorescence upon accumulation of MNCs in solution confirmed that the MNCs formed in this study had both superparamagnetic and fluorescent properties at the same time<sup>121</sup>.

A dendrimer grafted shell of Fe<sub>3</sub>O<sub>4</sub> stabilized with gold nanoparticles synthesized by Murugan *et. al.*<sup>120</sup> exhibited excellent magnetic properties. The magnetic properties of the Fe<sub>3</sub>O<sub>4</sub> core, OA-Fe<sub>3</sub>O<sub>4</sub> and core shelled magnetic composites namely Fe<sub>3</sub>O<sub>4</sub>-Poly(4-MS-DVB-GMA)-PAMAM-G(0)-AuNPs, -PAMAM-G(1)-AuNPs and -PAMAM-(2)-AuNPs

were investigated using vibrating sample magnetometer (VSM) at room temperature with applied magnetic field sweeping from -2 to 2 KOe. It was noticed that the saturation magnetization reduced with increase in the amount of the applied field as follows 70.3, 67.2, 57.8, 35.3 and 10.6 emu/g, respectively. The decreased  $M_s$  value was attributed to the higher generation dendrimer and the formation of a dense shell and which showed higher non-magnetic behavior. The decreasing  $M_s$  value could also be as a result of the surface order interactions of the magnetic spin moment and the disturbance in  $Fe_3O_4$  spinel structure by the dendrimers<sup>120</sup>.

Shen *et. al.* developed novel composite that constituted folate conjugated to carboxymethylchitosan-ferroferric oxide doped CdTe (CFLMNPs), the composite retained their magnetic and fluorescence properties prior and after the composite was constituted. The magnetic properties that emanated from the  $Fe_3O_4$  reduced upon the step by step fabrication towards the achievement of the CFLMNPs. The saturation of magnetization decreased to 45.6 emu/g from 83.2 emu/g. On the other hand, the fluorescence properties of the nanocomposite was shown to be affected by the pH, temperature, irradiation of natural light and the concentration of the precursors at the course of the syntheses. The PL intensity decreased with pH. For example, it was observed that below the pH of 4 the PL intensity was almost completely quenched. The decline in PL intensity with pH could be attributed possibly to the destruction of stability of CdTe and also the difficulty in their loading to the  $Fe_3O_4$  core<sup>103</sup>. Equally, at the pH > 9, the PL intensity reduced due to the formation of cadmium hydroxide as reported in earlier work<sup>124</sup>. The PL intensity proved to be dependent on the reaction temperature in which the nanocomposite was formed or the loading temperature of the QDs by the core. In particular, as the reaction temperature goes

from 278K to 328K, the PL intensity of the product decreased. A possible reason for this observation is that the trap energy level malfunctions due to the change of the trap sites of the CdTe QDs at high temperature<sup>125</sup>. The observed red shift in the fluorescence emission peak may be attributed to the dipolar-dipolar interaction of the interior nanocrystals<sup>126</sup>. This observation therefore suggests that upload of QDs to the magnetic core could be done at lower temperatures to minimize loss of the PL intensity. The influence of the irradiations of the natural light on the QDs on the PL intensity was investigated and reported. It was observed that the irradiation of QDs prior to coupling process increased the fluorescent intensity of the resulting product<sup>103</sup>. The researchers indicated that this fact was due to the light activation which led to the removal of the flaws at the surface of the QDs. The optical irradiation facilitates the decomposition of TGA into S<sup>2-</sup> and then forms CdS shell on CdTe surface. Hence, the growing of CdS shell greatly improves the surface trap structure of a CdTe QDs leading to an enhanced PL intensity<sup>97</sup>. Also, the PL intensity was shown to be dependent on the ratio of QD:MNPs. Increased ratio of QD:MNP resulted in an increase in the PL intensity implying that at higher ratios more QDs are adsorbed by the MNPs. When the ratio of QD:MNP was equal, say 1:1, it was observed that the PL intensity was very weak<sup>103</sup>.

Wang *et. al.* synthesized and characterized the nanocomposite of the type  $\gamma$ -Fe<sub>2</sub>O<sub>3</sub>-CdSe/ZnS. The properties of the as-prepared nanocomposite were investigated using various techniques. The TEM analysis revealed that the particles had average diameter of 12 nm with minimal aggregation and evidence of successful formation of the nanocomposite material. The energy dispersive spectrum (EDS) of the nanocomposite showed the presence of the Cd, Se, Zn and S on the surface of the iron oxide particles. A

slight blue shift was observed with a decrease in the quantum yield of the nanocomposite material which was attributed to changes in the electronic density on the surface of the QDs resulting from the immobilization of the magnetic nanoparticles. The luminescence lifetime of the nanocomposite increased from  $27\pm 3$  ns to  $65\pm 5$  ns. This increment in the excited state lifetime was due to the quenching interactions between the magnetic nanoparticles and the fluorescing quantum dots as well as the close parking<sup>97</sup>.

Xu *et. al.* synthesized nanocomposite that constituted the core  $\text{Fe}_3\text{O}_4$  coated with the  $\text{SiO}_2$  coupled to the CdSe/ZnS. The magnetic and fluorescent properties were investigated from the core through the shell and up to coupling with the QDs. The results showed that the  $\text{Fe}_3\text{O}_4$  core had high magnetic saturation value of 73.7 emu/g, however, the  $M_s$  value reduced to 46.5 emu/g upon introduction of the shell  $\text{SiO}_2$  to the core, and further reduced to 15.4 emu/g on the coupling of the silica coated core to the QDs. Prior to the coupling processes, the CdSe/ZnS gave excellent fluorescence properties with a quantum yield of 30 %. However, coupling of iron oxide (IO) NPs to QDs resulted in quenching of these excellent properties of the QDs. To investigate these quenching effects, the percentage of IO in the nanocomposite material was varied between 0-51 %. It was noticed that the fluorescence intensity reduced with the increasing percentage of the IO in the nanocomposite material<sup>105</sup>.

Amala *et. al.*<sup>98</sup> combined Au NPs and  $\text{Fe}_3\text{O}_4$  magnetic core to form a novel nanocomposite material. The XRD analysis of these samples confirmed that Au/ $\text{Fe}_3\text{O}_4$  nanocomposite was an inverse spinel structure and its spectral data matched the reference (JCPDS No. 01-1174). Also, the XRD further confirmed the influence of the ratio between the Au and the  $\text{Fe}_3\text{O}_4$  as shown by the two independent samples prepared in their study. Further analysis

of the two samples by TEM revealed that the Au and the Fe<sub>3</sub>O<sub>4</sub> NPs were successfully welded. The TEM analysis further showed that with the increasing concentration of Au nanoparticles in the mixture yields highly monodisperse NPs despite the fact that no capping agent was used. The magnetic properties of the nanocomposite material were also investigated at different temperatures and variable external field. At room temperature the two samples gave the Ms values of 12.776 emu/g and 14.3673 emu/g. These values are approximately 3 times lower than the Ms value of the Fe<sub>3</sub>O<sub>4</sub> which was indication of successful coupling to Au nanoparticles. It was observed that the saturation magnetization for both samples decreased as the temperature approached room temperature. Furthermore, it was observed that as the temperature increased the values of both the coercivity and the retentivity decreased though not to zero at the room temperature.

Roychowdhury *et. al.* synthesized nanocomposite material of the type Fe<sub>3</sub>O<sub>4</sub>/ZnS by a simple chemical dispersion. The main goal was to investigate the effects of the MNPs on the optical properties of the ZnS. The 20%, 30% and 50 % amounts of Fe<sub>3</sub>O<sub>4</sub> were used in various investigations of the nanocomposite. The morphology, optical and magnetic properties of the three sets of the nanocomposites material was investigated. The estimated sizes of the bare Fe<sub>3</sub>O<sub>4</sub> and ZnS were 15 nm and 4 nm, respectively whereas the resulting nanocomposite materials from the investigations had sizes ranging from 15-25 nm. The PL spectrum of the pure ZnS sample exhibited a strong peak centered at a wavelength of 341 nm along with asymmetric curve in the region 400 to 450 nm. The peak position did not change with the increase in magnetite concentration which illustrates that the different defect related to energy levels relative to the valence band remained nearly constant.

However, the magnetic properties of the  $\text{Fe}_3\text{O}_4/\text{ZnS}$  were lowered with the increase in the concentration of the ZnS. This observation was expected because the ZnS is diamagnetic thus reduces the strength of the dipolar interaction among the present magnetic nanoparticles<sup>108</sup>.

Tong *et. al.* synthesized and investigated properties of the  $\text{Fe}_3\text{O}_4/\text{Y}_2\text{O}_3:\text{Eu}^{3+}/\text{Y}_2\text{O}_3:\text{Eu}^{3+}$ . The composite exhibited both luminescent and magnetic properties. The group used vibrating sample magnetometer and photoluminescence spectroscopy to investigate the optic and magnetic properties. The resulting nanocomposite material was spherical in shape with minimal aggregation and an approximate diameter of 200 nm. It was noticed that the fluorescence of the nanocomposite increased with increasing amount of the fluorescing layer. The obtained nanocomposite material managed to fluoresce in spite the quenching emanating from the black magnetite core. The magnetization saturation decreased significantly from 55.85 emu/g for  $\text{Fe}_3\text{O}_4/\text{C}$  which was the starting material to 1.99 emu/g for the product  $\text{Fe}_3\text{O}_4/\text{Y}_2\text{O}_3:\text{Eu}^{3+}/\text{Y}_2\text{O}_3:\text{Eu}^{3+}$ . It is worth noting that despite the drop in the  $M_s$  strength of the product, it was still suitable for magnetic separation and targeting applications<sup>113</sup>. Wang *et. al.*<sup>114</sup> in 2009 synthesized another set of bifunctional composite that constituted the CdTe and the  $\text{Fe}_3\text{O}_4$ . The PL analysis gave a blue shift with a broad spectrum when the QDs were attached to the silica surface. The possible reason for this observation was attributed to corrosion of QDs during silica deposition. The quenching effect of MNPs on the PL intensity was further investigated. The results showed that the PL intensity gradually decreased with increasing amount of the MNPs. The increase of the magnetic nanoparticles in the nanocomposite was observed to cause blue shift in the emission spectra. This observation could be due to the charge-transfer

transitions in the mixed valence compound. It could have been also caused by a rearrangement of the structure of magnetic nanoparticles and QDs when they are more compact giving rise to the energy transfer between the two components<sup>127</sup>. The magnetic properties of the bare and the bi-functional nanoparticles were investigated using the vibrating sample magnetometer up to the fields of 10 T. The magnetic saturation reduced from 55 emu/g for the uncoated magnetic nanoparticles to 13.1 emu/g for the bi-functional nanocomposite material. The possible reason for this observation could be that there is the diamagnetic contribution of silica shell surrounding the magnetic core. The SEM and TEM images confirmed that the MNs-QDs/SiO<sub>2</sub> nanoparticles were well dispersed at an average diameter of 50 nm<sup>114</sup>.

Zhang *et. al.* successfully synthesized seven layered nanocrystal of the type CdSe/CdS/CdS/Cd<sub>0.75</sub>Zn<sub>0.25</sub>S/Cd<sub>0.5</sub>Zn<sub>0.5</sub>S/Cd<sub>0.25</sub>Zn<sub>0.75</sub>S/ZnS/ZnS quantum dots and coupled it with Fe<sub>3</sub>O<sub>4</sub> nanoparticles. This unique multilayered QDs were synthesized following a reported procedure and the formation of the layers was confirmed by the elemental analysis (EDS) and the XRD<sup>128</sup>. This study showed that the mole ratio of the QDs to the MNPs affected the PL intensity of the nanocomposites. According to the group, the MNPs acted as a photon absorber from the adjacent QDs giving a decrease in the quantum yield (QY) of the fluorescent magnetic nanocomposite (FMNPs). It was observed that the seven layered QDs retained the original QY upon encapsulation, however, upon the introduction of the MNPs, the QY decreased significantly. In the figure 1.9 below, there is a clear illustration of the effects of the subsequent surface modifiers on the PL intensity of the QDs towards the formation of the fluorescence magnetic nanoparticles.



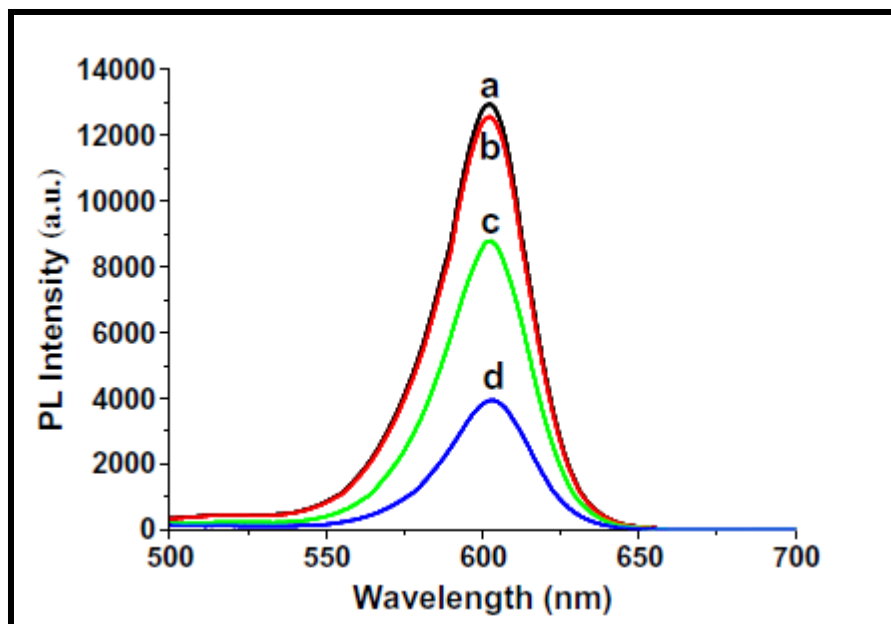


**Figure 1.9:** The varying PL intensity (a) 100 $\mu$ L hydrophobic QDs in cyclohexane (b) silica coated 100 $\mu$ L of QDs (c) fluorescing magnetic nanoparticles with 100 of QDs and 100 $\mu$ L MNPs (d) fluorescing magnetic nanoparticles with 100  $\mu$ L of QDs and 100 $\mu$ L MNPs. Reprinted with permission from Zhang *et. al.*<sup>128</sup>

A general conclusion from the graph was that the resistance to the change of the QY was because of the lattice mismatch between the CdSe and the CdS unlike in the CdSe and ZnS. Analysis of the magnetic properties of FMNPs using the VSM was found to be 2.6 emu/g at 300K. The magnetic remanence of the sample was almost zero suggesting that the synthesized FMNPs exhibited superparamagnetism<sup>78</sup>. Also, Ahmed *et. al.* prepared the QDs with the MNPs which possessed distinct magnetic and fluorescent properties which they used in the imaging of the colon carcinoma cells. The quantum dots used in this particular case were CdTe capped with thiol functional group whereas the MNPs were coated with positively charged CTAB. The prepared nanocomposite was highly fluorescing such that after isolation with a permanent magnet, the supernatant liquid

showed an ignorable PL intensity. This observation was a clear indication that the QDs were successfully incorporated to the surface of MNPs. In contrast to the other nanocomposite, there was a red shift to 540 nm for fluorescent magnetic nanoparticles (FMNPs) compared to 522 nm of the uncoupled QDs. However, the shapes of the PL spectra for the FMNPs were broader when compared to PL spectra of the bare QDs. The FMNPs prepared showed remanence and coercivity of zero implying that the FMNPs would respond to the external magnetic field and redisperse when the external magnetic field is removed. The  $M_s$  of as-prepared FMNPs as expected dropped from 71 to 65 emu/g. The decrease in the saturation magnetization was attributed to the fact that the  $Fe_3O_4$  surface was covered by a non-magnetic material. The FMNPs were stable in aqueous solution at room temperature which was because of the cationic surfactant layer between the QDs and the MNPs<sup>117</sup>.

A nanocomposite material of the type  $Fe/C/YBO_3:Eu^{3+}$  was prepared by Li *et. al.*<sup>112</sup> and investigated their luminescent and magnetic properties. The middle carbon layer between the magnetic particles and luminescent particles were aimed at reducing the quenching property which could occur via direct contact between the magnetic and luminescent material and thus conduct electrons. The excitation spectra of  $Fe/C/YBO_3:Eu^{3+}$  occurred at 592 nm with a broadband maxima at 292 nm which was attributed to a charge-transfer band between the  $O^{2-}$  and the  $Eu^{3+}$  because the  $Eu^{3+}$  f-f transfer is difficult to be seen. The vibrating specimen magnetometer VSM was used to investigate the trend in magnetic properties for the core  $Fe_3O_4$  and the subsequent products  $Fe_3O_4/C$  and  $Fe/C/YBO_3:Eu^{3+}$ . It was noted that the value of the saturation which was 2.17 emu/g was lower than the  $M_s$  value of the  $Fe_3O_4$  and the decrease attributed to the shell of phosphor powder.

In another strategy for synthesizing the bifunctional composites, Ma *et. al.*<sup>110</sup> coupled the  $\text{NH}_2\text{-SiO}_2/\gamma\text{-Fe}_2\text{O}_3$  with the MPA-capped CdTe QDs. The prepared composite exhibited both superparamagnetic characteristics and excellent luminescence properties. The recorded saturation magnetization of the bifunctional nanoparticles was 10.8 emu/g. This  $M_s$  value incidentally was much lower compared to 83.2 emu/g of the  $\gamma\text{-Fe}_2\text{O}_3$ . The decreased magnetism property was possibly due to the thick silica coat which was applied on the MNPs. Nonetheless, the magnetic property of the Bifunctional nanoparticles (BNPs) was still sufficient for the bioseparation process. The photoluminescence spectra for these BNPs showed a slight blue shift compared to non-coated QDs. This was an indication of the successful coupling between the MNPs and the QDs. In spite of the blue shift observed, the BNPs demonstrated intense red fluorescence under the UV light. When the external magnetic field is placed outside the vial containing the BNPs, the color of the solution changed to transparent when observed under UV light and could disperse when the external magnetic field is removed. This was a clear demonstration that the as-prepared BNPs had good magnetic properties as well as excellent fluorescence properties.

Xiong *et. al.*<sup>99</sup> utilized the excellent known properties of gold nanoparticles to prepare magnetic graphene/gold nanocomposite MagG/Au for the specific enrichment and rapid analysis of thrombin. The SEM and TEM images showed that the spherical magnetite beads were highly monodispersed in graphene nanosheets. The as-prepared MagG/Au had large surface area and high-density hydrophilic group. The combined properties of the nanocomposite provided easy separation as well as pre-concentration of the analyte and also amplified the loading amount of aptamer for signal amplification.

### 1.12.3 Biomedical applications of fluorescence magnetic nanocomposite

In the last decade, biomedical strategies have been focused towards the development of submicrometer particles with multiple features such as magnetization, fluorescence, and biological activities. The components with such multimodal properties are highly desirable specifically for the biomedical diagnosis and therapy<sup>129,130</sup>. In this part of the thesis, we focus on the application of the nanocomposite materials derived from the magnetic nanoparticles (particles with magnetic properties) and semiconductor inorganic nanocrystals QDs (nanoparticles with fluorescing functionalities). The emphasis will be on the application of the recently developed nanocomposites materials for cell separation, drug delivery, cellular imaging and utility of their magnetic property as MRI contrasting agents. Recently, Jeong *et. al.*<sup>121</sup> illustrated intracellular uptake of multifunctional nanoclusters (MNCs) of the type  $\text{Fe}_3\text{O}_4\text{-CdSe/ZnS}$  by dendrimeric cells (DCs). They demonstrated use of multifunctional nanoclusters loaded to dendritic cells for imaging, tracking, and isolating the targeted cells. Specifically, *ex vivo* labelling of the DCs with MNCs-lipid A complex enhances their migration to the draining lymph nodes and to the tumor antigen-specific T cells responses for the *in vivo* applications. The DCs were prepared from the mice following a reported procedure<sup>131</sup>. They observed that the multifunctional nanoclusters were engulfed by the dendrimers. The intracellular uptake of the MNCs by the DCs gradually increased in a concentration-dependent manner. The MNCs were distributed throughout the cytoplasm and an uptake mechanism was believed to occur via a phagocytosis<sup>121</sup>. The MNCs-loaded DCs were efficiently separated and enriched with the aid of a permanent magnet. The separation and enrichment of the

labelled cells could be useful to enhance the fluorescence and superparamagnetic signals when tracing the cells *in vivo*. An evaluation was carried out to ascertain the viability of the MNC-loaded DCs and their suitability for the MRI applications. A few deductions were made. Firstly, there was no observed significant change on the stability of the DCs containing varying amounts of the MNCs incubated over a period of 7 days. Secondly, maturation markers of the DCs were examined after loading the MNCs and which did not affect the surface expression of the maturation markers. Also, the DCs loaded with the different concentrations of MNCs were applied *in vitro*. This study revealed that the T<sub>2</sub> relaxation time for the MRI gradually reduced and the image darkened. The group further activated the MNCs loaded DCs with lipid A. It is known that the MNCs-lipid A complexes can boost DC-mediated immune responses<sup>132</sup>. Lipophilic monophosphoryl lipid A is a potent stimulator for DC activation and widely used to manufacture pathogenetic nanostructures<sup>133</sup>. It was illustrated that there was the surface expression of the activation markers when MNCs-lipid A complex was incubated with DCs for 18 h. Migration of fluorescent labelled DCs enhanced their monitoring from the footpads of the mice to the draining lymph nodes after 2 days of injection<sup>121</sup>.

The magnetic and the fluorescence bifunctional nanocomposites materials were recently applied by Ma *et. al.*<sup>110</sup> for the detection of the lung cancer cells in human. In order to capture the cancer cells, the bifunctional nanocomposite materials (BNCs) (QDs-SiO<sub>2</sub>/γ-Fe<sub>2</sub>O<sub>3</sub>) were conjugated to the anti-CEA antibodies. Human lung adenocarcinoma SPCA-1 cells, human leukemic K562 cells and human embryonic lung fibroblasts MRC-5 cells were cultured at 37 °C using RPM1-1640 medium supplemented with 10 % fetal bovine serum in a humidified atmosphere containing 5 % CO<sub>2</sub>. To perform the target capturing by

immuno- nanoparticles, the SPCA-1 cells were detached using a 0.25 % trypsin-EDTA solution and collected by the centrifugation techniques. The SPCA-1 was collected and its concentration determined using the hemocytometry. These immuno-nanoparticles were added and incubated for 45 minutes followed by a magnetic separation. The control experiments consisted of bare BNPs which were incubated with SPCA-1 cells. The immuno-nanoparticles were incubated with CEA-negative and MRC-5 cells under the same conditions. The confocal fluorescence microscopy was used to observe the cells. It was observed that a red fluorescence was emitted from the cell surface which showed that the antigens were recognized by the antibodies on the immuno-nanoparticles. It was further observed that one-to-one correspondence between the cells shown in the bright and the dark fields not only exhibited that the immuno-nanoparticles were optically and biologically active but also illustrated an availability of the strategy for lung cancer detection. A negligible signal was observed on the cells with SPCA-1 and bare BNCs. The immuno-particles incubated with CEA-negative showed no signal whereas the cells containing MRC-5 had few signals due to non-specific binding. A feasibility study involving the incubation immuno-nanoparticles with pleural effusions showed the fluorescence at the surface of the cells. The group indicated that the technique is less labor intensive, less time consuming and provides rapid analyses of the clinical samples.

In another strategy to image the colon carcinoma cells, Ahmed *et. al.*<sup>117</sup> engineered a multifunctional nanoparticles. They incorporated quantum dot into magnetic nanoparticles and formed a fluorescence magnetic nanoparticles (FMNPs). They further conjugated these FMNPs to hCC49 antibodies having the affinity to sialylated sugar chain of the TAG-72 region of LS174T cancer cells. The successful conjugation with hCC49

antibodies to FMNPs was confirmed using enzyme-linked immunosorbent assay (ELISA) where the high signal was observed compared to the bare FMNPs. The specific binding between the FMNPs and the cancer cells were evaluated by the incubation of the hCC49-FMNPs complex with the LS174T cancer cells. A green fluorescence around the nucleus was observed using confocal laser scanning microscopy for *in vitro* studies. The negative control was carried out by incubating LS174T cancer cells with FMNPs without the hCC49 antibodies conjugated to them and as expected showed no green fluorescence around the nucleus. To evaluate the specificity of hCC49-FMNP complex, the complex was incubated with the HEK293 cells. It was observed that there was no green fluorescence on the surface of the cells. *In vitro* studies showed less toxicity of the FMNPs at 64 fold dilutions. The end result was that an antibody conjugated to FMNPs demonstrated their potential as probes for imaging and ultimately provide a new class of multimodal diagnostics NPs for the complex biological systems<sup>117</sup>.

In a typical application of multimodal nanocomposite, Ye *et. al.*<sup>118</sup> developed both cellular imaging and drug delivery system. They fabricated the multimodal nanocomposite by encapsulating inorganic imaging agents (superparamagnetic iron oxide nanoparticles and manganese-doped zinc sulfide quantum dots) by poly (lactic-co-glycolic acid) (PLGA) and loaded it with anticancer drug busulfan. *In vitro* studies were done for the imaging and the efficacy of PLGA in the drug delivery. The fluorescing imaging of the murine macrophage cell line containing PLGA-SPION-Mn: ZnS exhibited strong fluorescence intensity in the cell plasma area compared to the untreated cells over the same period of incubation. The corresponding high fluorescence imaging compared to the low fluorescence of untreated cells demonstrated their efficacy in the cellular uptake of

PLGA-SPION-Mn:ZnS. The *In vivo* studies were done to ascertain the suitability of the PLGA-SPION-Mn:ZnS as the MRI contrast agents. Rat models were injected with PLGA-SPION-Mn:ZnS. There was an observed rapid decrease in the signal in the liver and the spleen after the injection. Specifically seven minutes after injection the liver imaging became darker indicating accumulation of PLGA-SPION-Mn:ZnS. The minimal signal intensity appeared after 4 h of the post-injection and remained low for the rest of the experimental time. The efficiency of PLGA-SPION-Mn:ZnS in drug delivery was demonstrated using the dialysis method at the pH of 7.4. The initial concentration of busulfan in a mixture of dichloromethane and PBS was 5 mg/mL and the loading efficiency of the busulfan in the PLGA vesicles was calculated to be  $89\pm 2\%$ . The percentage release of busulfan out of the dialysis bag reached 80% after 5 h. The degradation of the drug carrier was also tested and found that 12 % of lactic acid was degraded and released at the pH 7.4 and 37 °C after a period of 5 weeks. These results clearly demonstrated that the PLGA can function as a multifunctional diagnostic and therapeutic tool for the cancer treatment<sup>118</sup>.

The ability of the fluorescent magnetic nanoparticles to be utilized for analyte enrichment was currently demonstrated by Zhang *et. al.*<sup>78</sup>. In their study the amino-FMNPs were labelled with goat anti-human IgG as the specific probes. The immunofluorescence assay for the positive and the negative control were carried out in the standard reported format. The positive control constituted a highly carboxylated microspheres coated with human IgG molecules while the negative control constituted BSA bonded to human IgG molecules and microspheres. The carboxylated microspheres were used to anchor the antigen. The antibody-FMNPs were able to capture the target and separated using a



magnet giving rise to the enriched microspheres. The immunofluorescence on the positive control microspheres was brighter while nothing was observed for the negative control. The positive and negative controls were characterized under a flow cytometry. The data indicated that more than 98% human IgG sensitized PS microspheres were captured by the anti-human IgG labelled FMNPs<sup>78</sup>. It has been reported that the magnetic nanoparticles with superparamagnetic or ferromagnetic properties have attracted attention for the *in vivo* medical treatments because they can interact with the induced electromagnetic fields of the various frequencies so that they can penetrate through the wide range of the materials including body tissues. This property allows the particles to be manipulated, tracked, imaged and remotely heated<sup>134,135</sup>. Such properties open up the possibilities for an application in the hyperthermia cancer treatments<sup>136</sup>.

Recently, Xu *et. al.*<sup>105</sup> developed multifunctional nanocomposite material constituting Fe<sub>3</sub>O<sub>4</sub>/SiO<sub>2</sub>-CdSe/ZnS for radio frequency nano hyperthermia. In this study, it was demonstrated that the nanocomposite materials can be successfully uptaken by the pancreatic human cancer cells (Panc-1) upon 24 h incubation. Below the 50 µg/mL concentrations of the fluorescence magnetic nanocomposite materials showed virtually no cytotoxicity towards the Panc-1 cell. The same observation was observed when less than 200 µg/mL of the nanocomposite materials was exposed to 3-(4, 5-dimethylthiazol)-2, 5-diphenyltetrazolium bromide (MTT) or lactate dehydrogenase (LDH) release measurement. Nano hyperthermia process was demonstrated by incubating 0.5, 0.83, 1.66 and 5 µg/ mL of fluorescent-magnetic nanocomposites with human pancreatic cells in 35 mm culture dishes containing 0.5x10<sup>6</sup> cells/dish. The cells were then subjected to 350 kHz, 5 kW, of radio frequency induction for 2 to 10 minutes. Within 2 minutes of radio

frequency exposure treatment, most of the Panc-1 cells (99.2%) were observed to die. The apoptosis process, in this case, proved to be traceable because of the unique optical properties of the QDs. It was also confirmed that the structure –controlled IQ had reasonable magnetic properties, self-heating temperature rising characteristics and high biocompatibility. The outcome of this study proved that this type of fluorescence magnetic nanocomposites possessed a bio-potential material for an application in the *in vivo* nanohyperthermia and cancer treatment<sup>105</sup>.

Wang *et. al.*<sup>97</sup> were among the pioneers to engineer bionanocomposite materials and test their applications. The group immobilized anticycline E antibodies on the surface of the  $\alpha$ -Fe<sub>2</sub>O<sub>3</sub>-CdSe/ZnS of the as-prepared nanocomposite. The anticyclone antibody used in this case binds specifically to cycline, this kind of protein is specifically expressed on the surface of breast cancer cells. The details of the study involved the suspension of the nanocomposite material in the phosphate buffer solution at pH of 7.4, the mouse anticycline E antibody is added followed by 1-ethyl-3-(3-dimethylaminopropyl) carbodiimide hydrochloride coupling reagent. The mixture was gently shaken for 1 hour, separated using a magnet and washed. The coated antibody was re-suspended in the PBS and incubated for 15 minutes with MCF-7 breast cancer cells in a serum solution. The captured cells were separated together with the fluorescing magnetic nanoparticles using permanent magnet. The control experiments were carried out by using particles not labelled with the antibodies. The control luminescent particles which did not capture the antigen were easily distinguished from the captured cells because of the 3-4 orders of the magnitude size difference. The separated breast cancer cells were easily observed with the help of the fluorescence imaging microscopy<sup>137</sup>.

In advancement to utilize the nanocomposite material for drug delivery, Shen *et. al.*<sup>103</sup> loaded adriamycin (ADM) anticancer drug to folate-conjugated nanocomposite. Briefly, 25 mg of CFLMPs was added to 30 mL of ADM and shaken for 24 hours at room temperature. The nanocomposite was rinsed to remove unbound ADM and the suspension centrifuged at 6000 rpm for 10 min. The supernatant fluid was collected and the concentration of unbound ADM determined using Uv-vis spectrophotometer. The loading efficacy of the drug was determined. Releasing ability was evaluated by sinking ADM loaded CFLMNPs in different buffers at a pH of 7.4 and 5.3 at  $37 \pm 1$  °C in a bath with gentle shaking. The suspension of magnetic nanocomposite was separated using a magnet and concentration of ADM determined. The *in vitro* cytotoxicity of the blank and ADM-loaded CFLMNPs was evaluated using the MTT assay with L02 and HepG2 cell lines. The same cells were used for cellular imaging by using the laser scanning confocal microscopy (LSCM). Phenolic hydroxyl groups and alkaline amino groups in ADM were utilized to bind an amino group and the hydroxyl group in the chitosan forming intermolecular hydrogen bonded complexes. The loading amount of the ADM reached a maximum of 439.2 mg/g. The releasing capability were estimated using simulated normal body fluid (PBS, pH 7.4) and acidic environment pH 5.3 at 37 °C. Over the period of 24 hours, the cumulative release observation was 36% and 15 % at the pH of 5.3 and 7.4. The cumulative release increased with the increase in the reaction time, for instance after 72 hours it was 47 % and 19% at pH 5.3 and 7.4, respectively. The cytotoxicity studies for the blank and ADM loaded CFLMNPs were carried out. The result revealed low toxicity for both. The cell viability was 85 % and 70 % when tested for L02 and HepG2 cells respectively. For imaging purposes, blank and ADM loaded CFLMNPs were loaded onto

the L02 and HepG2 cells and the binding and morphological changes of the cells observed. The amount of nanocarriers was higher in the HepG2 cells than in L02 cells under the same conditions. They established a binding mechanism by using another control experiment of folate conjugated and non-conjugated CLMNPs. They found out that the non-folate CLMNPs were able to enter the cells by non-specific endocytosis process. The uptake of folate conjugated particles into HepG2 was more significant to the L02 cells. The transport mechanism of the folate-conjugated particles was by the folate receptor-mediated endocytosis mechanism due to the high expression of folate receptor at the surface of the tumor. Also, it was noticed that the small size of CFLMNPs had easier access to cancer cells<sup>103</sup>.

Owing to rising advances into the use of aptamers in place of antibodies, Xiong *et. al.*<sup>99</sup>. prepared a nanocomposite bioconjugated to a thiolated binding aptamer (TBA). They used 6.75 nmol TBA pretreated with 2.5 nM TCEP and 500 nM acetate buffer (pH 5.2) for 1 hour. The TCEP-activated TBA was then incubated for 16 hours with MagG/Au. The aptamer conjugated nanocomposite was washed with a binding buffer and stored in a tris-HCl buffer at 4 °C. The functionalized nanocomposites was tested for thrombin enrichment using various concentration of thrombin (0.1 -250 ng $\mu$ L<sup>-1</sup>) and also tested with real sample. Appropriate amount of MagG/Au/TBA in binding buffer solution was equilibrated with various concentrations of thrombin and each set incubated for one hour at room temperature under vigorous shaking. The specificity of TBA-conjugated MagG/Au nanocomposites on thrombin was demonstrated. This was done by replacing thrombin (target) with four unmatched proteins namely human bovine serum (HAS), myoglobin, ribonuclease b, transferrin and biological sample fetal calf serum, at

concentration of  $100 \text{ ng}\mu\text{L}^{-1}$  which was 20 fold of thrombin ( $5 \text{ ng}/\mu\text{l}$ ). No target signal was observed on the mass spectrum which was a sufficient evidence for specificity. The MagG/Au/TBA was separated and washed with the PBS and  $\text{NH}_4\text{HCO}_3$  to remove unbound species. The mixture was resuspended in  $\text{NH}_4\text{HCO}_3$  buffer, heated to  $100 \text{ }^\circ\text{C}$  for 30s and treated with trypsin for digestion overnight at  $37 \text{ }^\circ\text{C}$ . A  $1 \mu\text{L}$  supernatant of analyte was pipetted onto a MALDI target plate, followed by  $20 \text{ pg}$  of peptide DF-8 or  $200 \text{ pg}$  of peptide ER-10 as the internal standard and  $0.5 \mu\text{L}$  of Cynano-4-hydroxycinnamic acid (CHCA) as the matrix for mass spectrometry analysis. For the application of the TBA- conjugated MagG/Au, various concentrations of thrombin was added to the 10-fold diluted human serum and incubated for one hour. Their MALDI-TOF-MS results showed a peak at  $m/z$  1194.6 and by comparing it with b and y ions with that in thrombin standard; it confirmed that the peak belonged to the thrombin. In this study it was clearly demonstrated that the technique used herein with aptamer modified nano-platform has the powerful ability for rapid analysis for protein biomarkers in biofluids and is worth pursuing for promising results in the future<sup>99</sup>.

### **1.13 Purpose of the study/aim of the study**

To develop a nanomaterial (s) with fluorescence and magnetic properties that can be utilized for breast cancer diagnostic studies

### **1.14 Problem statement**

To try and contain cancer, several types of research involving the development of drugs and therapies for cancer treatment are documented but there is not yet any significant increment in the survival rates <sup>5,138</sup>. Diagnosis of any disease followed by targeted treatment strategies is the only viable solution to contain it. Cancer can be detected in a

number of ways including the presence of signs and symptoms, screening tests or medical imaging. Once a possible cancer is detected, a microscopic examination of the sample is carried out. The examination of the sample tissue must involve pathologists. Other investigation diagnostic tools include medical tests such as CT scans, X-rays, and endoscopy. However, the signs and symptoms of a tumor often present themselves when it is already too late for medication.

Microscopic examination of sample tissues is more invasive and involves extraction of tissues for imaging which is also painful. There is, therefore, the need for a method which is non-invasive and that is rapid in terms of process and results output. The recent advancements in the discovery of biomarkers have opened avenues that for exploring targeting diagnostic approaches. Once identified, the biomarkers can be conjugated to artificial detection agents which may be either magnetic or luminescent or both. Current methods of breast cancer screening like self-breast examination and the mammography have several drawbacks. For instance, not everybody can carry out self-breast examination and mammography. Mammography is rare and very expensive. Although new improvements are being made in the resolution of these imaging techniques, tumors smaller than 5 mm usually go undiagnosed. Moreover, as dense breast tissue decreases the mammographic sensitivity in young women, the effectiveness of mammography has not been established<sup>10</sup>. The use of biomarkers for cancer diagnosis has several advantages. These advantages include the measure of biomarkers in biological fluids such as blood and urine which can be obtained with minimal inconvenience to subjects undergoing diagnosis. This, in turn, should lead to high compliance rates. For many biomarkers, automated assays are available, thus allowing the processing of large numbers of samples

in a relatively short period of time. Also, the tests for biomarkers provide quantitative results with objective endpoints. Eventually, the assays for biomarkers are relatively cheap.

### **1.15 Significance of the study**

By integrating knowledge and techniques of nanochemistry and biotechnology better diagnostic methods can be obtained. Highly superparamagnetic nanoparticles and fluorescing nanoparticles of quantum dots show outstanding characteristic that could be suitable for disease diagnosis. The magnetic-fluorescing nanoparticles can be used as an all-in-one diagnostic tool, which can be used in imaging based on magnetic resonance imaging<sup>96</sup>. The fluorescing part emitting at appropriate wavelength can be utilized in visual imaging by fluorescence imaging microscope. Nanocomposite would therefore, allow optical tracking of biological processes as well as magnetic manipulations<sup>100</sup>.

InP based quantum dots (QDs) have recently been viewed as a potential alternative to cadmium (Cd) based QDs<sup>139</sup>. Therefore, designing a multifunctional nanocomposite based indium QDs could be advantageous. The nanotechnology innovation centre (University of the Western Cape, bio label unit) has identified certain proteins that over express themselves at the surface of the cancerous cell (biomarkers). These genes are capable of being used for potential development of serum markers in the diagnosis of breast cancer or early detection of poor-outcome breast cancer. However, it has been found that these proteins are present in a very low concentration which makes the diagnosis process challenging but not impossible.

The immune receptor of the identified biomarkers may be conjugated to the multifunctional nanocomposite and used for diagnostic studies. Synthesizing functionalized nanocomposite and bio-conjugating them to the recognition molecules can capture and isolate the cleaved proteins present in the blood. The captured and isolated biomarkers from the blood serum may be utilized for diagnosis. On the other hand, the photostable quantum dots may be used to substitute the organic dyes and fluorescent proteins that are often used in the design of molecular beacons (MBs). Incorporation of QDs in the design of MBs may enhance the sensitive detection of biomarkers hence reducing cost biomarker discovery.

#### 1.16 Objectives

- To synthesize and characterize  $\alpha$ -Fe<sub>2</sub>O<sub>3</sub> superparamagnetic nanoparticles (SPION)
- To synthesize and characterize indium based quantum dots
- To synthesize and characterize cadmium based quantum dots
- To couple the iron oxide nanoparticles with InP/ZnSe quantum dots to form luminescent magnetic nanocomposite
- To characterize the luminescent magnetic nanocomposite
- To determine the cytotoxicity of the synthesized  $\alpha$ -Fe<sub>2</sub>O<sub>3</sub> , InP/ZnSe and the constituted nanocomposites
- To determine the ability of the aptamer- attached to iron oxide nanomaterials in capturing and isolating the target proteins
- To synthesize quantum dot based molecular beacon for biomarker detection



## 2 CHAPTER TWO: EXPERIMENTAL

### 2.1 Introduction

In this chapter we described experimental procedures and the reagents used for the synthesis of the materials. The synthetic procedures for magnetic iron oxide nanoparticles, functionalization strategies, InP/ZnSe quantum dots and the fabrication of the nanocomposite have been described. Further we described bioconjugation steps necessary for introduction of aptamers to the surface of the iron oxide nanoparticles. On the cytotoxicity, we described reagents used for cell culture and how the cells we cultured. We described step by step the MTT assay that was used to evaluate toxicity of iron oxide nanomaterials, the InP/ZnSe and the fabricated luminescent magnetic nanocomposite. Finally, we described synthesis of molecular beacons starting from synthesis of the QDs all the way to the evaluation of the MBs for gene detection.

### 2.2 Experimental reagents

All the reagents used were of analar grade and were used as purchased without further purification. The following is the list of reagents used. iron (III) chloride, hydrated iron (II) sulphate, 25 % aqueous ammonium hydroxide, ultra-pure water, distilled water, deionized water, polyethylene glycol (PEG), l-cysteine, 3-mercaptopropionic acid, 2,3-meso-dimercaptosuccinic acid, indium acetate, tris(trimethylsilyl)phosphine (P(TMS)<sub>3</sub>), palmitic acid, zinc undecylenate, selenium powder, 1-octadecene (ODE), tri-octylphosphine(TOP), hexane, acetone, 2-propanol, chloroform, phosphate buffer solution (PBS, pH 11 and pH 7.4), boric acid, butanol, 50 % glutaraldehyde, tween-20, ethanolamine, streptavidin, ammonium hydrogen carbonate, trypsin, MUCIN 1 binding

aptamer (Integrated DNA technologies (IDT)), TE buffer( Tris-HCl and EDTA), MCF-12A breast cells (American Type Culture Collection), KMST-6 skin fibroblast cells, Dulbecco's modified Eagle's medium (DMEM), DMEM-F12, 3-(4,5- dimethylthiazol-2-yl)-2,5-diphenyltetrazolium bromide (MTT), hydrocortisone, epidermal growth factor (EGF), were purchased from Sigma-Aldrich. dulbecco phosphate buffered saline, penicillin-streptomycin, were obtained from Lonza. Fetal bovine serum (FBS) was purchased from BioChrom, insulin from Roche and dimethylsulfoxide (DMSO)(Merck).

### **2.3 Characterization and apparatus**

A number of the following equipment was used during synthesis and characterization of the nanomaterials. ultrasonicator (NIC), thermoshaker, vortex, heating block, autoclave, photoluminescence (PL) spectroscopy nanolog model HORIBA FL3-22-TRIAX, high resolution transmission electron microscopy (HRTEM TECNAI F30ST-TEM and high resolution scanning electron microscopy (HRSEM), semiconducting quantum interference device (SQUID) sourced from University of Johannesburg, powdered X-ray diffractometer (Ithemba labs), native PAGE, SDS-PAGE, electrophoresis tank, ultraviolet spectrophotometer, matrix-assisted laser desorption/ionization-time of flight mass spectrophotometer (MALDI-TOF-MS), fourier transform infra-red spectrophotometer (FTIR), fluorescence microplate reader, Qubit<sup>®</sup> 2.0 fluorimeter Invitrogen, BioTek synergy H1 hybrid multi-mode microplate reader Gen5 software.

## 2.4 Experimental procedures

### 2.4.1 Synthesis of iron oxide ( $\alpha$ -Fe<sub>2</sub>O<sub>3</sub>) nanoparticles

Iron oxide nanoparticles were prepared by co-precipitation method. Salts of Fe<sup>3+</sup> and Fe<sup>2+</sup> were dissolved in ultra-pure water at the molar ratio of 1:2. The mixture was transferred to three 3 necked flask and purged with inert gas. The mixture was continuously stirred and 6 mL of 25 % ammonium hydroxide was injected rapidly and the temperature set at 50 °C for 2 hours. The product was isolated using magnetic decantation and washed with several cycles of distilled water. The product was dried in an oven for 24 hours at temperatures of 60 °C.

### 2.4.2 Functionalization of iron oxide ( $\alpha$ -Fe<sub>2</sub>O<sub>3</sub>) nanoparticles with 3-mercaptopropionic acid

The thiol group present in 3-mercaptopropionic acid which is known to have a high affinity for nanomaterial surface was utilized to functionalize the  $\alpha$ -Fe<sub>2</sub>O<sub>3</sub> nanoparticles. To determine appropriate concentration (without destroying the nanoparticles) of 3-mercaptopropionic acid various ranges of concentrations were prepared and dried  $\alpha$ -Fe<sub>2</sub>O<sub>3</sub> powder was introduced. 0.01 M, 0.1M, 0.5 M and 1 M were prepared in a volume of 10 mL distilled water and 50 mg of  $\alpha$ -Fe<sub>2</sub>O<sub>3</sub> powder introduced to each. The mixtures in the vials were ultra-sonicated for 2 hours and later left standing for 12 hours. Finally, the particles were isolated using a magnet and dried, ready for FTIR analysis and further applications.

### 2.4.3 Functionalization of $\alpha$ -Fe<sub>2</sub>O<sub>3</sub> nanoparticles with L-cysteine

L-cysteine is known to have three different functional groups namely thiol (-SH), amino (NH<sub>2</sub>) and the carboxyl (-COOH). The presence of these functional groups makes L-cysteine suitable capping agent for nanomaterials designed for biological applications since it allows subsequent bioconjugation of other molecules. The functionalization process of  $\alpha$ -Fe<sub>2</sub>O<sub>3</sub> was achieved by immersing known amount of the  $\alpha$ -Fe<sub>2</sub>O<sub>3</sub> powder in a known concentration of L-cysteine. Since optimization on the amount of  $\alpha$ -Fe<sub>2</sub>O<sub>3</sub> versus the concentration had not been reported, a quick optimization procedure was adopted in this study by choosing three ranges of concentrations. The three ranges of concentrations prepared in 10 mL distilled water were 0.01 M, 0.05 M and 0.1 M and to each 50 mg of the  $\alpha$ -Fe<sub>2</sub>O<sub>3</sub> was introduced to attain particle concentration of 5 mg/mL. All the mixtures were ultra-sonicated for 2 hours while changing ultrasonicator water after every 30 minutes. The mixture was then left standing overnight.

### 2.4.4 Functionalization of $\alpha$ -Fe<sub>2</sub>O<sub>3</sub> with dopamine hydrochloride

Dopamine has been known to enable bio-conjugation of antibodies to nanomaterials without the need for linkage chemistry as reported by Tunturk *et. al.*<sup>140</sup>. In a typical process to functionalize the Fe<sub>2</sub>O<sub>3</sub> nanoparticles with dopamine, two ranges of concentrations of dopamine were chosen. 0.001 M and 0.005 M dopamine concentration were prepared in 15 mL vials and to each dry  $\alpha$ -Fe<sub>2</sub>O<sub>3</sub> powder was added to achieve a concentration of 5 mg/mL. The mixture was ultrasonicated for two hours while changing the water in the ultrasonicator after every 30 minutes. The ultrasonication was stopped and they were left standing for 24 hours. The particles were then isolated, washed and dried at 60 °C in an oven overnight.

#### **2.4.5 Functionalization of iron oxide ( $\alpha$ -Fe<sub>2</sub>O<sub>3</sub>) nanoparticles with meso-2, 3-dimercaptosuccinic acid**

Fabrication of the nanocomposite was the core of this study and hence a molecule that could couple the two different types of nanomaterials was a pre-requisite. Meso-2,3-dimercaptosuccinic acid (DMSA) was found appropriate due to the presence of two thiol and two carboxyl functional groups. The high affinity of thiol group towards attachment to the surface of the Fe<sub>2</sub>O<sub>3</sub> was considered. We relied on steric hindrance chemistry to allow one thiol group to be used and leaving the other for the conjugation to the surface of InP/ZnSe QDs. A solution containing DMSA was prepared by dissolving 5 mg of DMSA in 1 mL dimethylsulfoxide and added to 10 mg/mL of  $\alpha$ -Fe<sub>2</sub>O<sub>3</sub> in toluene. The mixture was mechanically stirred for 24 hours. They were separated and washed with several cycles of normal PBS and later dispersed in 1 mL PBS (pH 7.4) awaiting further application and analysis.

### **2.5 Application experiments of the synthesized iron oxide nanoparticles**

#### **2.5.1 Immobilization of streptavidin to iron oxide nanoparticles**

Glutaraldehyde chemistry was used to attach the streptavidin to the surface of the functionalized magnetic nanoparticles as reported in earlier works<sup>141</sup>. The L-cysteine functionalized iron oxide nanoparticles were conjugated to streptavidin (SA). In short, the functionalized 10 mg iron oxide nanoparticles were dispersed in 2 mL phosphate buffer solution and ultra-sonicated for 15 minutes. The mixture was divided into two (1 mL each), one set was used and the other stored. Eventually, the desired amount of glutaraldehyde 50 % (w/w) was introduced to make 10% (v/v) glutaraldehyde solution and

the solution stirred for 3 hours at room temperature. The particles were isolated from the solution and washed with several cycles using 1 % PBS and re-suspended in PBS containing 0.05 % tween-20. Finally, 50  $\mu$ L of 1 mg/mL streptavidin was introduced and the mixture incubated for 10 hours at 4 °C with vigorous stirring. Active aldehyde residual groups were terminated by adding excess ethanolamine and stirred for 2 hours at room temperature. The product was washed with PBS to remove unreacted SA and other impurities and separated using a magnet. The clean product was re-suspended in 5 mL PBS awaiting further analysis and application.

### **2.5.2 Electrophoretic mobility shift assay (EMSA)**

Our first task was to evaluate the binding capability of MUC-1 binding aptamers that we purchased from integrated DNA technologies (IDT) solutions. The aptamers had the sequence 5'-GCA GTT GAT CCT TTG GAT ACC CTG G-3' and modification was done in the 5' end with biotin. The aptamers were dissolved in TE buffer (Tris-HCl, pH 8 and EDTA) as per the manufacturer's instructions and stored at -20 °C awaiting further use. Electrophoretic mobility shift assay was performed to evaluate the binding affinity of the MUC 1 binding aptamers on proteins expressed on MCF-7 cells. The electrophoretic gel was prepared by mixing de-ionised water (7.38 mL), 1 X TBE (1.23 mL), Bisacrylamide (12 %, 3.69 mL), ammonium persulfate (APS) (10 %, 200  $\mu$ L) and TEMED (10  $\mu$ L). 1  $\mu$ L of the MUC1 binding aptamers was separately incubated with different volumes of MCF-7 lysates. The lysate and MUC 1 binding aptamer were mixed in phosphate buffered saline solution (1 x PBS). The detailed experimental setup is presented in Table 2.1.

**Table 2.1: Experimental details for incubation of aptamer and the Lysates extracted from MCF-7 cells**

	1 <sup>st</sup> well ( $\mu\text{L}$ )	2 <sup>nd</sup> well ( $\mu\text{L}$ )	3 <sup>rd</sup> well ( $\mu\text{L}$ )	4 <sup>th</sup> well ( $\mu\text{L}$ )	5 <sup>th</sup> well ( $\mu\text{L}$ )	6 <sup>th</sup> Well ( $\mu\text{L}$ )
PBS	19	18	14	9	4	1
MCF 7 lysate	0	1	5	10	15	18
Aptamer	1	1 $\mu$	1	1	1	1
Total	20	20	20	20	20	20

The EMSA set up was pre-run for one hour using 1X TBE buffer and the samples were loaded into various wells and loading dye was loaded into a different well to enable monitor the movement of the samples. To each well 10  $\mu\text{L}$  of the sample was loaded. The control consisted of DNA MUC1 binding aptamer alone. Again, we repeated with lysates extracted from MCF 7 and MCF 12 A to establish the specificity of the MUC 1 binding aptamer. The experimental details are shown in Table 2.2.

**Table 2.2: Evaluation of specificity of MUC 1 binding aptamer using MCF 7 and MCF 12A cultured cells**

	1 <sup>st</sup> well ( $\mu\text{L}$ )	2 <sup>nd</sup> well ( $\mu\text{L}$ )	3 <sup>rd</sup> well ( $\mu\text{L}$ )	4 <sup>th</sup> well ( $\mu\text{L}$ )	5 <sup>th</sup> well ( $\mu\text{L}$ )
PBS	9	9	9	9	19
MCF 7 lysates	10	10	0	0	0
MCF 12 A lysates	0	0	10	10	0
Aptamer	1	1	1	1	1
Total	20	20	20	20	20

The electrophoretic gel was prepared and pre-run as described earlier. To each well 10  $\mu$ L of the sample was loaded. The control consisted of 1 $\mu$ L DNA MUC1 binding aptamer diluted to 20  $\mu$ L using PBS and loaded in the last well.

### **2.5.3 MUC 1 protein capturing**

The streptavidin conjugated to the iron oxide conjugates (MNP-SA) was incubated for one hour with MUC 1 binding aptamers. Briefly, 15  $\mu$ L of the MNP-SA conjugates was incubated with 1  $\mu$ L of MUC 1 binding aptamer for one hour. It was then washed with repeated cycles of PBS to remove excess aptamer that was not bound to MNP-SA conjugates. The optimized amount of lysate was then added to the MNP-Aptamer conjugates and incubated for 1 hour. It was then isolated using a magnet and washed with three cycles of 100  $\mu$ L PBS to remove uncaptured proteins. The control experiment consisted of incubation of MNP-Aptamer complex without the lysates. The conjugate was separated using a magnet and re-suspended in 30  $\mu$ L of PBS. The experimental details are presented in Table 2.3.



**Table 2.3: Experimental details of MUC1 capturing process using MNP-Aptamer complex**

Experiment		MNPs(beads)-Streptavidin complex( $\mu\text{L}$ )	Biotin-Aptamer ( $\mu\text{L}$ )	Lysate ( $\mu\text{L}$ )	PBS ( $\mu\text{L}$ )	Total volume ( $\mu\text{L}$ )
MCF 7	1	15	1	6	4	30
	2	15	1	6	4	30
	3	15	1	6	4	30
MCF 12A	1	15	1	6	8	30
	2	15	1	6	8	30
	3	15	1	6	8	30
3 (Control)	1	15	1	0	14	30
	2	15	1	0	14	30

#### 2.5.4 Quantification of captured proteins using Qubit

The Qubit samples were prepared in 0.5 mL thin-walled PCR tubes. The working solutions was prepared as follows;  $(1 \times n) \mu\text{L}$  of Quanti-iT Reagent was combined with  $(199 \times n) \mu\text{L}$  Quant-It buffer, where n is equal to the number of samples plus 3 for the standards. The three standards were prepared by mixing 190  $\mu\text{L}$  of the working solution with 10  $\mu\text{L}$  of standard 1, standard 2 and standard 3. Typically, 20  $\mu\text{L}$  of the sample of interest was mixed with 180  $\mu\text{L}$  of the working solution. The mixture was then vortexed carefully to avoid the formation of bubbles for 2-3 seconds and incubated for 15 minutes. All the PCR-tubes were covered with aluminum foil to avoid degradation of the fluorescing Quanti-iT reagent. The samples were then read using Qubit<sup>®</sup>2.0 fluorimeter Invitrogen supplied by life Technologies.

### **2.5.5 Detection of captured proteins using MALDI-TOF-MS**

The MNP-Aptamer and MUC 1 complex which had been re-suspended in 30  $\mu\text{L}$  of PBS was separated from the PBS. The isolated sample was re-suspended in 10  $\mu\text{L}$  of 50 mM TCEP in parafilm tubes and incubated at 60  $^{\circ}\text{C}$  for one hour. The sample was allowed to cool at room temperature for 30 minutes. 1  $\mu\text{L}$  of ammonium acetate was added and incubated in the dark for 1 hour. 33  $\mu\text{L}$  of 50 mM TEAB was added to adjust the volume to 45  $\mu\text{L}$ . Again, 5  $\mu\text{L}$  trypsin to the sample, parafilm and incubated at 37  $^{\circ}\text{C}$  for 18 hours. The particles were isolated and the sample speed vac to dryness. Lastly, 10  $\mu\text{L}$  of 0.1 % TFA was added and one drop of the sample was loaded to the MALDI-TOF-MS plate.

## **2.6 Synthesis of InP/ZnSe quantum dots**

### **2.6.1 Preparation of Zinc precursor**

Zinc precursor was synthesized using a procedure developed by Mushonga *et. al.*<sup>93</sup> with minor modifications. Briefly, 0.4319 g of zinc undecylenate was accurately weighed into a clean three-necked flask and 9.5 mL ODE was added. It was then transferred into Schlenk line where it was degassed for few seconds and turned to nitrogen. Meanwhile, 0.5 mL of trioctylphosphine was measured and sealed within a glove box and all of it transferred to the contents of the three-necked flask. The contents of the flask were refluxed for 1 hour with stirring at 140  $^{\circ}\text{C}$  under inert atmosphere until the solution became clear.

### **2.6.2 Preparation of selenium precursor**

A similar procedure for the synthesis of Zinc precursor was adopted from<sup>93</sup>. In a typical process, 78.96 mg of selenium powder was accurately weighed and transferred into a three-necked flask, dissolved in 9.5 mL 1-octadecene and quickly degassed in a Schlenk

line. 0.5 mL TOP was added to the flask contents and refluxed for 1 hour with vigorous stirring.

### **2.6.3 Synthesis of InP/ZnSe nanocrystals**

The procedure developed by Mushonga<sup>93</sup> was adopted for the synthesis of the InP/ZnSe with some modifications. Briefly, Indium acetate was mixed with palmitic acid at the molar ratio of 1:3 using non-coordinating solvent 1-octadecene. The components were mixed in a three-necked flask, transferred into Schlenk line and heated to 120 °C under vacuum and maintained for 1.5 hours. Prior to injection of P (TMS)<sub>3</sub> the flask was switched to nitrogen gas and the temperature raised to 300 °C. The temperature was retained at 300 °C for 2 hours. Meanwhile, Zinc and Selenium precursors had already been prepared see the preceding sections 2.5.1 and 2.5.2. The temperature of the main reaction was lowered to 180 °C from 300 °C. The precursors were injected at an exact temperature of 180 °C. 3.75 mL of zinc precursor was injected first followed by 1.5 mL selenium precursor after 10 minutes. The temperature was raised to 230 °C and retained at that temperature for 2 hours. A total of four samples were collected during the synthetic process. The final product was dispersed in hexane and precipitated using acetone and re-suspended in acetone. We were eager also to investigate the effect of scaling up the synthesis to see the difference. Basically, to scale up we doubled and tripled up all the volumes that were used during synthesis of InP/ZnSe and its precursors.

### **2.6.4 Size sorting procedure**

Size sorting was done by following a procedure by designed by Byun *et. al.*<sup>91</sup> with lots of modifications. The crude product of synthesized InP/ZnSe was dispersed in approximately

5 mL hexane. The product was centrifuged for 10 minutes to remove unreacted material and other unwanted material. The supernatant was collected and known volumes of acetone added using a syringe until a precipitate just appeared. The precipitate and the supernatant were separated by centrifugation. The second set of the sample was recovered by addition of 20 mL acetone. The same process was repeated by adding known volume of acetone to the supernatant and recovering the precipitate until a clear solution was obtained. PL analysis was done to obtain the emission wavelength and FWHM (Full width at half maximum) of each sample precipitated at the subsequent steps. HRTEM images were also obtained to actually compare the sizes of the precipitates collected at subsequent steps.

#### **2.6.5 Ligand exchange process**

Several strategies were adopted from literature to make the prepared quantum dots water-soluble. The InP/ZnSe nanocrystals were originally dispersed in hexane since they had been prepared using non-coordinating organic solvents. Ligand exchange process was essential not only to make quantum dots water dispersible but also to suit its desired possible applications. Palmatic acid which was used to grow and stabilize the core that contributed to the hydrophobicity of the prepared quantum dots. Two approaches were adopted from literature employing 3-mercaptopropionic acid to substitute and displace the palmatic acid from the surface of the InP/ZnSe nanocrystals. In the first approach, the quantum dots that were dispersed in hexane were centrifuged to remove unreacted materials and immediately precipitated using excess acetone. The pellet was collected via centrifugation and dispersed in chloroform. Meanwhile, 0.88 mL of MPA was dissolved in 1 mL PBS of pH 11. 1 mL of chloroform containing the quantum dots was mixed with the

prepared MPA in PBS and them were stirred for more than 4 hours with the aim of seeing the coloured material (QDs) crossing from the organic layer to the aqueous layer of the mixture.

An alternative approach was adopted from Brunetti *et. al.*<sup>95</sup> to carry out ligand exchange. In this approach, the quantum dots were transferred into the aqueous environment by addition of 1 mL borate buffer (pH 9, 200mM), 0.8 mL butanol, 3-mercaptopropanoic acid (8  $\mu$ L, 10  $\mu$ M) to InP/ZnSe (200  $\mu$ L, 5  $\mu$ M). The mixture was heated at 50 °C and vigorously stirred for 15 minutes. The aqueous layer containing the quantum dots was separated and 1000  $\mu$ L of borate buffer and 800 $\mu$ L butanol added. The mixture was stirred vigorously for another 15 minutes. The quantum dots were recovered by precipitation using ethanol and dispersing them in 50 mM borate buffer. The process of precipitation using ethanol and dispersion in 50 mM borate buffer was repeated four times to clean the quantum dots. Finally, the product was dispersed in PBS (pH 7.4) and stored at 4 °C awaiting further application. PL, UV and FTIR analysis was done to evaluate which of the two methods was successful in terms of introducing carboxyl group (-COOH) to the quantum dots.

#### **2.6.6 Immobilization of streptavidin to InP/ZnSe nanocrystals**

Streptavidin was conjugated to the surface of quantum dots following a procedure reported by Stanisavljevic *et. al.*<sup>142</sup> with some modifications. (200  $\mu$ L, 150 mg/mL) InP/ZnSe mercaptopropionic acid capped quantum dots were diluted to 1000  $\mu$ L and the pH adjusted to 7 using MPA solution (20  $\mu$ L of pure MPA diluted to 1000  $\mu$ L using distilled water). The mixture was stirred for 1 hour at room temperature. The control

experiment was set by diluting (200  $\mu\text{L}$ , 150 mg/mL) of the carboxylated QDs to 1000  $\mu\text{L}$  using the same MPA solution. The streptavidin–InP/ZnSe NCs conjugates were separated by centrifuging for 80 minutes (10,000 rpm). The supernatant was disposed and the precipitate was dissolved in PBS pH 7.4. The conjugates were then washed with two cycles of PBS (pH 7.4) and the QDs were finally resuspended in 100  $\mu\text{L}$  of PBS. UV-vis spectrophotometer was used to confirm success in the conjugation of the streptavidin to the surface of the QDs. The UV-Vis spectra were obtained for the two samples prepared in the same way but with and without streptavidin.

## 2.7 Synthesis of CdTe/ZnS quantum dots

CdTe/ZnSe was prepared by adopting method from literature<sup>143</sup> with modifications. Briefly, NaHTe was prepared by dissolving appropriate amounts of  $\text{NaBH}_4$  (1 mmol) and Te (0.04 mmol) in 10 mL of deionized water. The solution was heated at 80  $^\circ\text{C}$  for 30 minutes to form NaHTe. Separately, 0.4 mmol  $\text{CdCl}_2$  and 0.6 mmol of MPA were dissolved in 15 mL of deionized water at pH 11.7, forming the Cd/MPA precursor. The mixture was heated to 80  $^\circ\text{C}$  and 5 mL NaHTe solution was injected. The temperature was raised and maintained at 100  $^\circ\text{C}$  for 2 hours allowing the growth of CdTe nanocrystals. The reaction was carried out under an inert atmosphere. Thereafter, the solution was rapidly cooled down on the ice and added to a mixed zinc and sulphur precursor solution which was prepared by adding 1 mL solution containing zinc acetate (0.1 M) and thiourea (0.1 M) to a final volume of 15 mL of deionized water (pH 11.5). The solution was transferred to three neck flask (100 mL), attached to a Schlenk line. The solutions were degassed and subsequently heated to 90  $^\circ\text{C}$  for 1 hour which allowed the growth of MPA-capped CdTe/ZnS QDs. The solution was cooled down to room temperature, centrifuged

to get rid of unwanted products and precipitated to obtain a pellet of the QD. The pellet was finally dried at room temperature.

## **2.8 Streptavidin attachment to 3-MPA capped CdTe/ZnS**

The mass of the dry pellet was determined using analytical balance and dispersed in a known amount of PBS to obtain known QD concentration. 1 mL of the QD was mixed with 40  $\mu$ L of the streptavidin and incubated for 3 hours at room temperature. The reaction occurred in the presence of EDC (10  $\mu$ L, 0.38 mg/mL) and NHS (10  $\mu$ L, 0.5 mg/mL). The product was centrifuged for 20 minutes at 10,000 rpm and the pellet re-dispersed in PBS so as to retain the initial QD concentration.

## **2.9 Synthesis of the Molecular beacon**

The bioconjugation process was adopted from<sup>39</sup> with modification. 100  $\mu$ M of streptavidin modified quantum dots were added to 2  $\mu$ M of biotinylated oligo having Iowa Black at the 3'end. The mixture was incubated at room temperature for at least 2 hours with vigorous shaking (850 rpm, thermomixer comfort). The control consisted streptavidin modified quantum dots diluted with PBS to equal volume as the experiment containing the probe.

## **2.10 Cell culture and cDNA synthesis**

Both cell lines MCF7 and MCF12A were obtained from American Type Culture Collection (ATCC) USA. Both cell lines were cultured in a 1:1 mixture of Ham's F12 medium and Dulbecco's modified Eagle's medium according to ATCC protocol. Total RNA was isolated from both cell lines using Total RNA and protein Isolation kit NucleoSpin<sup>®</sup> Macherey-Nagel. The RNA for these cell lines was electrophoresed on 1% agarose gels, which contained 7  $\mu$ L of Gel Red Nucleic acid stain (BIOTIUM). To

confirm the integrity of the RNA, the gel was run with Pac Basic system (BIO-RAD) at 90 V constant voltages for 60 minutes. cDNA was synthesized for MCF7 and MCF12A using Transcriptor First Strand cDNA synthesis Kit (Roche). The RT-PCR conditions were as follows: 95 °C for 5 min (Initial denaturation), 94 °C for 30 sec (Denaturation) 59 °C for 30 sec (Annealing), 72 °C for 45 sec (Extension), 72 °C for 10 min (Final extension) and 4 °C (∞). The cDNA was quantified using NanoDrop ND-100 spectrophotometer.

All the sequences of the biomarker were chosen by NCBI after which they were sent to IDT (Integrated DNA technology) for synthesizing of the probe. The primers were designed by using the primer3 plus and later synthesized by Inqaba Biotechnical Industries (Pty) Ltd. The sequence was designed to hybridize specific nucleic acid sequence for the target. A stem of 5 nucleotides (short) was conjugated to both ends of the probe sequence that could allow the formation of the molecular beacon. The 3' end of the oligos was modified with biotin-tetramethylene glycol (Biotin-TEG). The probe was re-suspended using 10 mM of DTT (Dithiothreitol) in 1X Tris HCl-EDTA buffer (pH 7.5) with the final concentration kept at 100 µM of the Oligos and stored at -20 °C until used.

### **2.11 Synthesis of the Molecular beacon**

The bioconjugation process was adopted from<sup>39</sup> with modification. 100 µM of streptavidin modified quantum dots were added to (2 µL, 100 µM) of biotinylated oligo having Iowa Black at the 3'end. The mixture was incubated at room temperature for at least 2 hours with vigorous shaking (850 rpm, thermomixer comfort). The control consisted of streptavidin quantum dots diluted with PBS to equal volume as the experiment containing the probe.



## 2.12 Detection of the target complementary target and cDNA

Different concentrations of the complementary sequences (50 nm, 100 nm, 500 nm, 1500 nm and 2000 nm) were used. The chosen concentrations were spaced enough to take care of machine fluctuations which are often attributed to non-uniform spectral of light sources. Again, we repeated with lower concentrations of the target (200 ppm, 600 ppm, and 1000 ppm). Finally, to confirm the sensitivity of our designed molecular beacon we tested with cDNA extracted from MCF 7 and MCF 12 cells. The initial concentration of the cDNA synthesized from both cells was 200 ng/ $\mu$ L. We evaluated the performance of the MB using 2 ng/ $\mu$ L, 10 ng/ $\mu$ L, 20 ng/ $\mu$ L and 30 ng/ $\mu$ L of cDNA synthesized from MCF 7. Again, we repeated with lower concentrations of 2 ng/ $\mu$ L, 4 ng/ $\mu$ L, 6 ng/ $\mu$ L, 8 ng/ $\mu$ L and 10 ng/ $\mu$ L. To test specificity we used cDNA synthesized from non-cancerous cells MCF-12A at concentrations of 2 ng/ $\mu$ L, 4 ng/ $\mu$ L, 6 ng/ $\mu$ L, 8 ng/ $\mu$ L and 10 ng/ $\mu$ L.

## 2.13 Synthesis of the $\alpha$ -Fe<sub>2</sub>O<sub>3</sub>-InP/ZnSe nanocomposite

The nanocomposite was constituted following a procedure developed by Wang *et. al.*<sup>97</sup> with lots of modifications. Bare iron oxide nanoparticles was functionalized with meso-2,3- dimercaptosuccinic acid (DMSA). The overall aim was to utilize the two thiol groups present in DMSA in the coupling of the InP/ZnSe and  $\alpha$ -Fe<sub>2</sub>O<sub>3</sub>, where the thiol groups are anchored to the surface of nanoparticles. Briefly, 5 mg of DMSA was dissolved in 1 mL DMSO and added to 10 mg of Fe<sub>2</sub>O<sub>3</sub>dispersed in 1 mL toluene. The mixture was stirred for 24 hours and washed with several cycles of PBS and resuspended in 1 mL of phosphate buffer solution. 200  $\mu$ L of meso-2, 3-dimercaptosuccinic acid capped iron oxide nanoparticles were added to 300  $\mu$ L of water soluble InP/ZnSe quantum dots. The mixture was shaken using a thermal shaker for 10 hours at room temperature. The nanocomposite

was refined by removing large and uncoupled magnetic nanoparticles. The refining process was achieved by vortexing the nanocomposite and placed close to a magnet, the material that responded slowly to the magnet were quickly pipetted to another clean tube. The process was repeated until the overall brown color of the quantum dots was achieved with minimal traces of black Iron oxide nanoparticles. Several analytical techniques used to analyze the nanocomposite namely UV-Vis spectrophotometer to determine absorbance and diffuse reflectance, XRD to determine the morphology, HRTEM to determine dispersibility, HRSEM to examine surface morphology, energy dispersive spectroscopy (EDS) and TGA to determine elemental composition of the nanocomposite, SQUID to determine the magnetic susceptibility, Photoluminescence spectroscopy to determine the optical properties of the material including the quantum yield. All the properties were compared to those of individual magnetic nanoparticles and InP/ZnSe.

## **2.14 Cytotoxicity studies**

### **2.14.1 Cell culture**

The *in vitro* study was carried out using non-cancerous cell lines, KMST-6 skin fibroblast cells and MCF-12A breast cells (American Type Culture Collection). The cells were sub-cultured and maintained at 37 °C under a humidified atmosphere (5 % CO<sub>2</sub>). KMST-6 was grown in Dulbecco's modified Eagle's medium (DMEM) and MCF-12A in DMEM-F12 (Lonza). All media were supplemented with 10 % fetal bovine serum (Gibco), and 1 % antibiotic cocktail containing 50 U/mL of penicillin and 50 mg/mL of streptomycin. 20 ng/mL human epidermal growth factor (Sigma), 500 ng/mL hydrocortisone (Sigma) and 0.01 mg/mL bovine insulin (Roche).

#### **2.14.2 Cytotoxicity studies of iron oxide ( $\alpha$ -Fe<sub>2</sub>O<sub>3</sub>) nanoparticles**

Cytotoxicity studies of the Iron oxide nanoparticles were done to ascertain their safety in regard to handling and future applications. Higher concentration than earlier reported studies was done and two different types of non-cancerous cells were used for this purpose. KMST6 and MCF-12A. 0.1 g/mL, 0.2 g/mL, 0.3 g/mL, 0.4 g/mL and 0.5 g/mL concentration of iron oxide nanoparticles were prepared.

#### **2.14.3 Cytotoxicity of the InP/ZnSe quantum dots**

Indium based quantum dots has to be perceived to be less toxic compared to the dominant cadmium-based quantum dots. Many studies have been focused on the toxicity of InP/ZnS, in this study, we present for the first time the comprehensive study on the cytotoxicity of InP/ZnSe through an *In vitro* test. The cytotoxicity was studied using non-cancerous KMST 6 and MCF12A cell lines. The cell lines were exposed to 0.1 mM, 0.2 mM, 0.3 mM, 0.4 mM and 0.5 mM of InP/ZnSe quantum dots.

#### **2.14.4 Cytotoxicity of the $\alpha$ -Fe<sub>2</sub>O<sub>3</sub>-InP/ZnSe quantum dots**

The toxicity of the nanocomposite was determined using both KMST-6 and MCF-12A cell lines. The only challenge we had was to determine the initial concentration. We took 200, 400, 600, 800 and 1000  $\mu$ L of the crude product and diluted each to 2000  $\mu$ L and denoted them C1, C2, C3, C4, and C5, respectively. C5 represents the highest concentration and decreasing through to C1. These various concentrations were incubated with the KMST 6 and MCF-12A cell and incubated for 24 hours. Similar procedure was adopted as for the other nanoparticles.

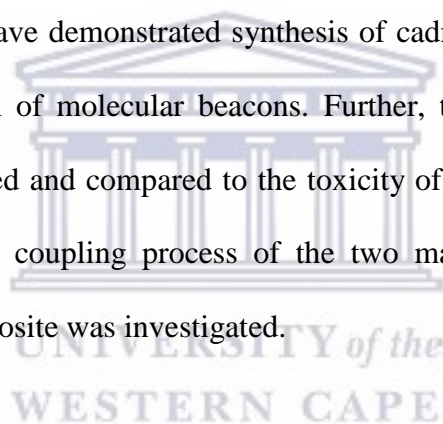
#### 2.14.5 MTT assay

The *in vitro* cytotoxicity of the synthesized nanoparticles was tested using a modified MTT cell viability assay adapted from<sup>144,145</sup>. The cells were grown in 96-well plates at  $1 \times 10^4$  cells/mL density, 100  $\mu$ L per well and incubated for 24 h. The nanoparticles were added to the cells at defined concentrations of and incubated for 24 hours. Post treatment, the media was discarded and the wells were washed twice with 150  $\mu$ L of sterile phosphate buffered saline (PBS) to remove excess nanoparticles. Fresh medium containing 10  $\mu$ L of MTT reagent (5 mg/mL stock) was then added per well and the plate was incubated for four hours at 37 °C. The media was replaced with 100  $\mu$ L of DMSO to solubilize the formazan crystals and further incubated for 10 mins. The color intensity was quantified by measuring the absorbance at 570 nm using a PolarSTAR Omega microplate reader (BMG Labtech), 650 nm was used as a reference wavelength. To avoid interference of the nanoparticles on spectrophotometry readings, the absorbance readings were corrected by treating the cells with the same concentration of the nanoparticles in triplicate and undergo the same steps but no MTT solution was added to the wells. These readings were then subtracted from the cells treated with the same concentration that had MTT. The cell viability was expressed as the percentage ratio of mean absorbance of treated cells against mean absorbance of untreated cells multiplied by 100. The same was done for all nanoparticles, that is, bare and functionalized iron oxide nanoparticles, InP/ZnSe nanocrystals, and  $\alpha$ -Fe<sub>2</sub>O<sub>3</sub>-InP/ZnSe nanocomposite.

#### 2.15 Conclusion

This chapter provides a summary of a synthetic steps of iron oxide nanoparticles, InP/ZnSe nanocrystals, CdTe/ZnS QDs and  $\alpha$ -Fe<sub>2</sub>O<sub>3</sub>-InP/ZnSe nanocomposite. We have

gone ahead and described the procedure that we adopted to determine the toxicity of the nanoparticles. Synthetic procedure of bare iron oxide nanoparticles and functionalization procedures were explicitly described. In regard to iron oxide nanoparticles, their application for enrichment for biomarkers was described in details. The cytotoxicity of bare and capped iron oxide nanoparticles was investigated. The cytotoxicity studies lay better foundation for further future applications including *in vivo* studies of the synthesized materials. The second part describes the synthesis of water soluble InP/ZnSe quantum dots achieved via ligand exchange process. Conjugation of streptavidin to the quantum dots was detailed described. Due to compromised fluorescing properties of indium-based QDs we have demonstrated synthesis of cadmium based quantum dots and used them in the design of molecular beacons. Further, the cytotoxicity studies of the material were investigated and compared to the toxicity of cadmium-based quantum dots in literature. Lastly, the coupling process of the two materials is described and only toxicity of the nanocomposite was investigated.



### 3 CHAPTER THREE: SYNTHESIS AND CHARACTERIZATION OF IRON OXIDE NANOPARTICLES

#### 3.1 Introduction

This chapter presents the results and discussion on synthesis, characterization, functionalization and application of iron oxide nanoparticles. Co-precipitation method of synthesis, which was adopted to synthesize the material, has been discussed and related studies cited. Functionalization of the iron oxide using L-cysteine, meso-2,3-dimercaptosuccinic acid, 3-mercaptopropionic acid, and related characterization has been discussed. Finally, cytotoxicity and the application of the material have been presented. Related researches have been included to support our findings.

#### 3.2 Synthesis and characterization of iron oxide nanoparticles

Several strategies have been adopted to synthesize iron oxide nanoparticles which include hydrothermal synthesis, micro-emulsion, chemical precipitation, oxidation of the  $\text{Fe}(\text{OH})_2$  using hydrogen peroxide ( $\text{H}_2\text{O}_2$ ), X-ray irradiation and microwave irradiation among others. Chemical co-precipitation is considered to be simple and cheaper. Despite this, it has however been criticized for yielding non-uniform particles<sup>65</sup>. In this study, co-precipitation method was chosen to synthesize the iron oxide magnetic nanoparticles owing to its advantages of the small size, ability to synthesize large quantity at once, requires minimal maturation temperature, and it does not use any organic solvents hence the method appears “greener”. The co-precipitation procedure was adopted from Zhao *et al.*<sup>146</sup> with some modifications. The ratio of  $\text{Fe}^{3+}$  to  $\text{Fe}^{2+}$  was maintained at 2:1, aqueous ammonia solution was used as a precipitant, the maturation temperature of 50 °C was chosen, the pH of  $\approx$  9-10 was maintained and the reaction was allowed to go on for two

hours. A large amount of the nanoparticles were obtained, separated with an aid of a permanent magnet and washed with several cycles of water. The particles were dried in an oven at low temperatures overnight. The particles were grounded and stored at room temperature awaiting further applications. High-resolution transmission electron microscopy (HRTEM) was used to determine the sizes of the synthesized nanoparticles and also monitor the changes in sizes before and after surface modification. Figure 3.1 below shows HRTEM micrograph of bare iron oxide nanoparticles

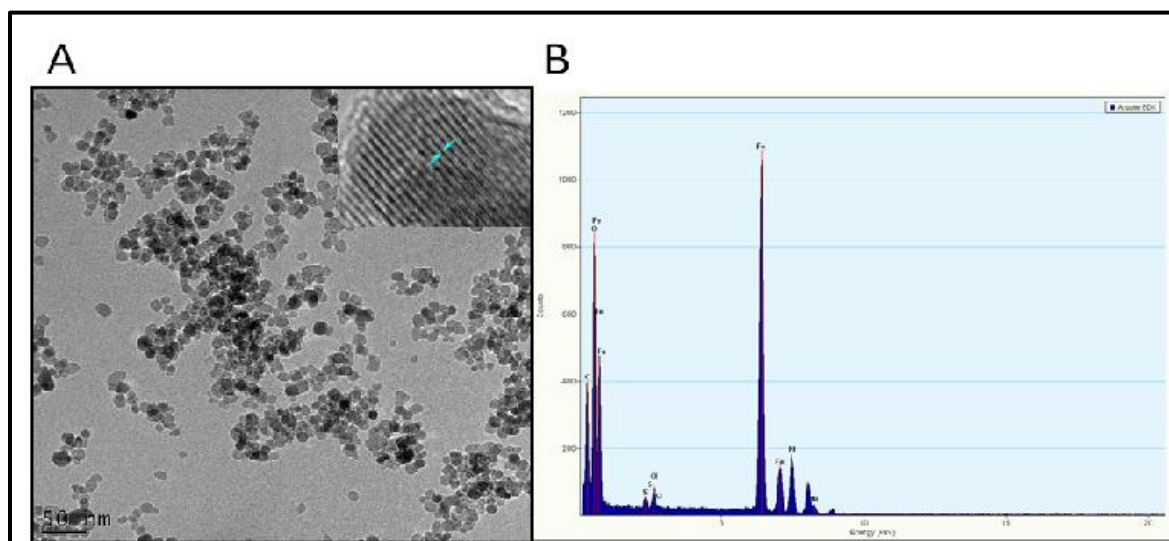


**Figure 3.1: High resolution transmission electron microscopy micrograph images for bare Iron oxide nanoparticles**

Figure 3.1(A) shows that the synthesized iron oxide nanoparticles were fairly dispersed which is a pre-requisite property for biomaterials. The witnessed partial agglomeration could be due to small sizes of the particles and also presence of  $-OH$  functional groups at the surfaces of the particles making them highly hydrophilic. The darker particle images could be as a result of the overlap of the particles due to the high concentration of the

nanoparticles applied to the HRTEM sample holder (copper grid). The inset in Figure 3.1(A) is an HRTEM image of single isolated nanoparticle. The lattice fringes had a distant spacing of 0.204 nm which indicates that the particles are highly crystalline. Figure 3.1(B) shows the energy dispersive spectroscopy image. Sun *et. al.*<sup>147</sup> synthesized iron oxide nanoparticles through seed-mediated method. Their TEM images showed that the  $\alpha$ -Fe<sub>2</sub>O<sub>3</sub> nanoparticles are monodisperse and that self-ordered nanoparticle is achieved if the solvent is allowed to evaporate slowly. They also observed lattice fringes from 6 nm isolated nanoparticle which was very similar to the fringes for the particles observed in our study. The distance between the fringes has been estimated to be 2.98 Å, which corresponds to (220) planes in the spinel structure of Fe<sub>3</sub>O<sub>4</sub>. We selected randomly more than 50 particles from the HRTEM micrograph and used them to estimate the sizes of the bare iron oxide nanoparticles. The imageJ software was used to estimate the particle sizes and hence the histogram constructed (Figure 3.2).

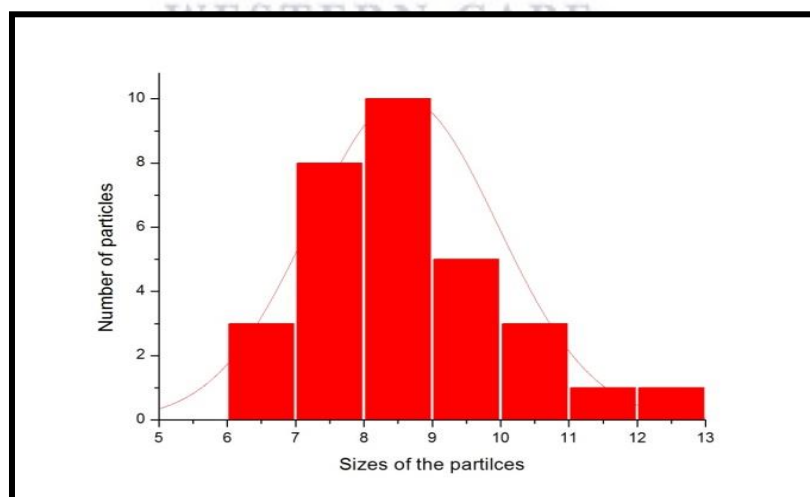


**Figure 3.2: Histogram showing size distribution of bare iron oxide nanoparticles**

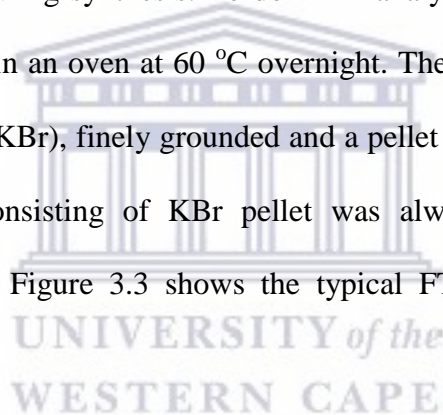


The obtained micrographs together with imageJ software were used to estimate the average size of the synthesized nanoparticles. The diameter of the particles was determined using imageJ software and the size distribution was found to range from 6-13 nm and the average size of 8.5 nm. Zhao *et. al.*<sup>146</sup> synthesized iron oxide ( $\text{Fe}_3\text{O}_4$ ) through chemical precipitation at the pH of 12 where they obtained nanoparticles with an average size of 12 nm. However, when they coated the nanoparticles with a polymer the average size increased to 10.67  $\mu\text{m}$  with the size distribution of 6.6-17.4  $\mu\text{m}$ . Recently, Marand *et. al.*<sup>64</sup> adopted co-precipitation to synthesize Zn-doped  $\text{Fe}_3\text{O}_4$  nanoparticles for biomedical applications. They varied the percentage of Zinc in the magnetic material ( $\text{Zn}_x\text{Fe}_{3-x}\text{O}_4$ ) between 0-14 %. In their work, the XRD pattern revealed the structure of the material to be a single phase with inverse cubic spinel structure with sizes ranging from 11.13-12.82 nm. The highest saturation magnetization was recorded at room temperature to be 74.60 emu/g when x was equal to 0.075. They discovered that as the percentage of zinc increases in the doped iron oxide nanoparticles the band gap of the resulting material decreases from 1.26 eV to 0.43 eV. In another interesting work, Houshiar *et. al.*<sup>148</sup> synthesized cobalt ferrite nanoparticles ( $\text{CoFe}_2\text{O}_4$ ) by three methods namely combustion, co-precipitation and precipitation. The nanoparticles resulting from the three methods of synthesis were compared with respect to size, structural and magnetic properties. The XRD data analysis revealed that the nanoparticles prepared by combustion were the largest and the least sizes achieved through precipitation. The average sizes were 69.5 nm, 49.5nm, and 34.7nm for particles prepared by combustion, co-precipitation and precipitation, respectively. They measured the magnetic saturation (Ms) and found to be 56.7 emu/g, 55 emu/g and 47.2

emu/g for particles synthesized by combustion, co-precipitation, and precipitation, respectively.

### 3.2.1 FTIR analysis of magnetic iron oxide nanoparticles

Fourier transformed infrared (FTIR) analysis was performed to gain the insight on the nature of the bond interactions involved in the formation of the iron oxide nanoparticles. We considered essential to establish the type of bonds present in the nanoparticles before any form of surface modification. The major peaks expected from FTIR spectra for iron oxide ( $\alpha$ -Fe<sub>2</sub>O<sub>3</sub>) nanoparticles are basically peaks associated with Fe-O or O-H bonds if the water was trapped during synthesis. To do FTIR analysis, the synthesized iron oxide nanoparticles was dried in an oven at 60 °C overnight. The dried sample was mixed with dry potassium bromide (KBr), finely grounded and a pellet was prepared. Prior to running the sample, a blank consisting of KBr pellet was always run for the purposes of background corrections. Figure 3.3 shows the typical FTIR spectra of bare magnetic nanoparticles.



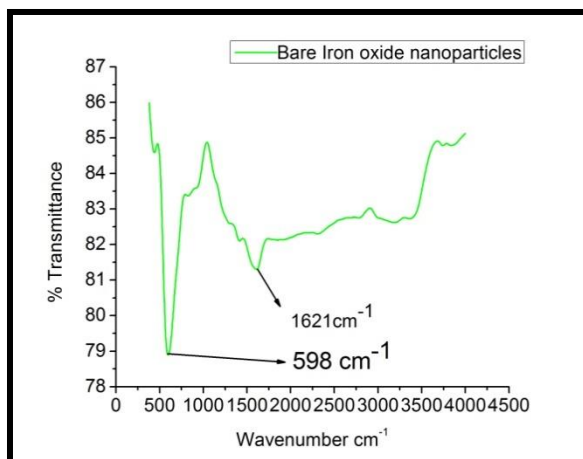


**Figure 3.3: FTIR spectra of bare iron oxide nanoparticles**

From the FTIR spectra (Figure 3.3) the narrow strong peak at  $598\text{ cm}^{-1}$  was ascribed to Fe-O bond whereas the weak peak at  $1621\text{ cm}^{-1}$  was assigned to bending vibration of O-H bond. The presence of -OH functional group on the dried iron oxide nanoparticles could be possibly be due to co-precipitation method where basic solution is used. Possibly, the -OH functional groups originating from the basic media are chemically entrapped during synthesis. Similar FTIR analysis was done for iron oxide nanoparticles ( $\text{Fe}_3\text{O}_4$ ) given by Lin *et. al.*<sup>149</sup>. They observed four peaks, a strong one at  $580\text{ cm}^{-1}$  and a weak one at  $436\text{ cm}^{-1}$  they ascribed the two peaks to the vibration of Fe-O bond. They observed the third peak at  $1578\text{ cm}^{-1}$  which they assigned it to bending vibration of O-H bond. Finally, the fourth peak was a broad one observed at  $3421\text{ cm}^{-1}$  and attributed to the stretching vibration of O-H bond. In another study Wei *et. al.*<sup>71</sup> synthesized iron oxide material ( $\text{Fe}_3\text{O}_4$ ) and carried out the FTIR analysis. In their study, they observed two peaks at  $580\text{ cm}^{-1}$  and  $634\text{ cm}^{-1}$  which they assigned both to Fe-O bonds. They observed another peak

at  $3398\text{ cm}^{-1}$  and ascribed it to O-H bonds. The spectroscopic technique, therefore, confirmed that the material constituted to types of bonds Fe-O and some O-H.

### 3.2.2 XRD data analysis for bare iron oxide nanoparticles

The sizes and structural patterns of bare iron oxide nanoparticles were investigated by carrying out powder X-ray diffraction (PXRD) analysis to supplement the HRTEM estimations. The PXRD analysis was performed using X-ray diffractometer (Bruker AXS D8) fitted with  $\text{CuK}\alpha = 1.54\text{ \AA}$  as an X-ray source. The powder X-ray patterns were collected by varying  $2\theta$  ( $2\theta$ ) from  $8\text{-}95^\circ$  at room temperature and is shown in Figure 3.4 below.

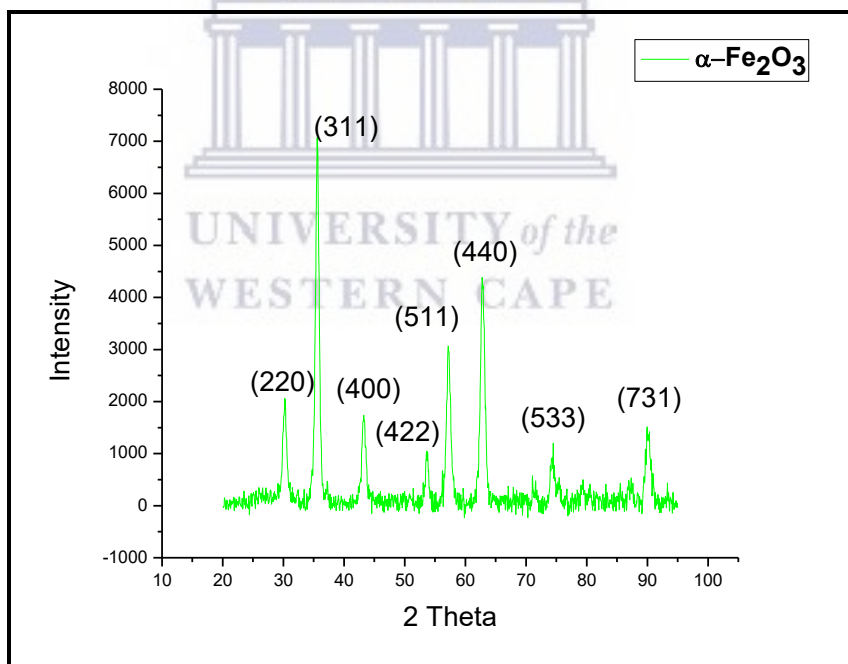


**Figure 3.4: XRD pattern for bare iron oxide nanoparticles**

The XRD pattern was used to deduce the size and the crystalline structure of the synthesised iron oxide nanoparticles. The sizes of the particles corresponding to five major peaks were determined and the average value obtained. The nanocrystals size was estimated using Debye Scherrer's formula as shown below:-

$$L = \frac{K*\lambda}{\beta*\cos \theta_{\beta}} \dots\dots\dots\text{Equation 3.1}$$

Where L - is the thickness of the crystalline (particle size), K - is a constant dependent on the crystallite shape,  $\lambda$  - X-ray wavelength,  $\beta$  - is full width at half maximum or integral breadth and  $\theta_{\beta}$  - is the Bragg's angle.

The calculated values for the sizes and other parameters of Scherrer's equation for iron oxide nanoparticles are presented in Table 3.1

**Table 3.1: Estimation of iron oxide particle size from XRD data**

Peak	2 Theta (Degrees)	Theta (Degrees)	Theta (Radians)	Lambda	FWM (Degrees)	FWHM (Degrees)	FWHM (Radians)	Size (nm)
Peak 1	30.26	15.13	0.26	0.15	1.41	0.70	0.01	10.90
Peak 2	35.59	17.79	0.31	0.15	1.54	0.77	0.01	9.79
Peak 3	57.18	28.59	0.50	0.15	1.41	0.70	0.01	9.91
Peak 4	53.61	26.80	0.47	0.15	1.43	0.71	0.01	9.92
Peak 5	89.96	44.98	0.78	0.15	1.65	0.82	0.01	6.82
<b>Average</b>								<b>9.47</b>

The particle sizes estimated from Scherrer's formula was found to be 9.74 nm for the bare iron oxide nanoparticles. The values were quite comparable to the sizes estimated from HRTEM micrographs where the diameter of the bare iron oxide was estimated to be 8.5 nm. The XRD pattern was matched with JCPDS no. 00-039-1346 and 00-019-0629 for maghemite ( $\alpha$ -Fe<sub>2</sub>O<sub>3</sub>) and magnetite (Fe<sub>3</sub>O<sub>4</sub>), respectively. The best match for the iron

oxide nanoparticles was found to be for maghemite and not magnetite. This match obtained for our samples was contrary to the authors expectation and was possibly due to oxidation. It is possible that the thermal oxidation could occur during the drying of the samples in an oven or during ultrasonication process. The XRD findings are also supported by changes in the color of the particles from black to dark brown after the drying and subsequent ultrasonication. Mamani *et. al.*<sup>150</sup> synthesized iron oxide nanoparticles and investigated their crystalline phase using X-ray diffractometer (Rigaku D/max- $\gamma$ , Japan). Their X-ray diffraction pattern corresponded to an inverted spinel structure for the magnetite. The conversion of magnetite to maghemite was explained by Mamani *et. al.*<sup>150</sup> which was attributed to the conversion of the magnetite to maghemite due to the exothermic oxidation during thermal characterization processes<sup>150</sup>. The oxidation took place during the analysis using the differential scanning calorimetry (DSC) at around 756K. The oxygen diffused to the core of the particles leading to conversion to maghemite phase as shown in the following equation:-



In another study, Zhao *et. al.*<sup>146</sup> observed six XRD peaks for their synthesized iron oxide nanoparticles. Their XRD pattern matched JCPDS file (PDF no. 65-3107) suggesting that the magnetite  $\text{Fe}_3\text{O}_4$  had spinel structure. Meng *et. al.*<sup>151</sup> also synthesized magnetic nanocrystals by chemical co-precipitation. Their XRD data revealed that the synthesized material had face-centered cubic structure, the diffraction pattern matched JCPDS file (no 3-863). They further utilized the XRD data to estimate the grain size of the magnetic nanoparticles to be 8.9 nm using Scherrer's equation.

### 3.2.3 Magnetic properties of the iron oxide nanoparticles

Recently, great interest has been geared towards the use of magnetic nanoparticles in areas such as bio-nanotechnology and biomedicine due to its attractive diverse properties presented by this material compared to the bulk material<sup>150</sup>. The magnetic properties of the synthesized nanomaterial were investigated using superconducting quantum interference device (SQUID). The hysteresis curves were obtained by placing 10.06 mg of the bare iron oxide sample on the SQUID holder. The measurement was carried out by varying the applied external field between -30 KOe to +30 KOe while holding the temperature at 300K. The hysteresis curve is presented in Figure 3.5 below.

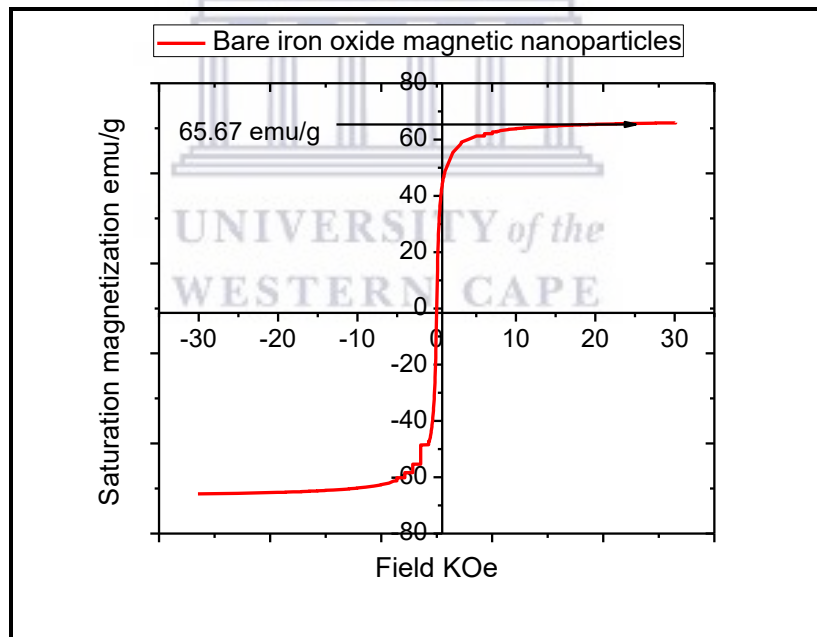


**Figure 3.5: Magnetic properties of the as-prepared iron oxide nanoparticles**

The magnetic saturation for the synthesized magnetic material was determined to be 65.67 emu/g. This observation shows that the synthesized material was actually superparamagnetic. Similar observation was made by Zhao *et. al.*<sup>146</sup> when they synthesized iron oxide nanoparticles with an average size of 12 nm, their particles had a saturation magnetization of 68.58 emu/g. The difference in our reported results and those of Zhao *et. al.*<sup>150</sup> is attributed to the difference in particles size. The sizes of our particles were smaller compared to their particles hence the difference in magnetic saturation. The effect of size on magnetic saturation was observed by Meng *et. al.*<sup>151</sup> where the magnetic saturation increased from 61.51 emu/g to 70.53 emu/g when the size increased from 8.9 nm to 12.2 nm. In another study, Mamani *et. al.*<sup>150</sup> synthesized ferrous oxide nanoparticles using co-precipitation method, they measured magnetization as a function of temperature to obtain zero fields cooled and field cooled curve. They varied the temperature from 10K to 250K while the external field was held at 100 KOe.

### **3.3 Functionalization of iron oxide magnetic nanoparticles**

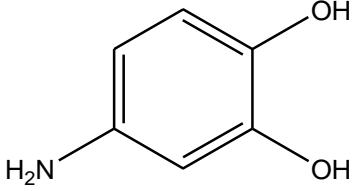
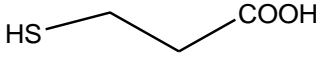
Functionalized iron oxide magnetic nanoparticles have demonstrated significant contribution in the field of clinical diagnostics and therapeutics. Their contribution includes magnetic separation of labelled cells, therapeutic drug, gene and radionuclide delivery, radio frequency methods for the catabolism of tumors via hyperthermia and contrast agents for magnetic resonance imaging applications<sup>152</sup>. Pre-requisite for every biological application is a proper surface modification dictates its interaction with the environment and ultimately affect the colloidal activity of the particles<sup>153</sup>. The ligand molecules bound to the particle surface not only controls the growth but also prevents



aggregation of the particles. Minimal aggregation is achieved due to repulsion between the particles. The repulsive forces between particles could possibly originate from electrostatic repulsion, steric exclusion or hydration layer on the surface of the nanoparticles. Usually, the ligand molecules are bound to the surface of the particles by attractive interaction such as chemisorption, electrostatic or hydrophobic interactions mostly provided by functional groups within the molecule. Various chemical functional groups such as carboxyl, amino, and thiol among others possess high affinity for inorganic surfaces<sup>153</sup>. In this study, we chose some ligand molecules to functionalize the magnetic nanoparticles. The choices of the ligand were basically guided by the chemical functional groups present in them and also a ligand that could easily allow for further bioconjugation. In short we chose meso- 2, 3-dimercaptosuccinic acid, L-cysteine, dopamine and lastly 3-mercaptopropionic acid. The table below is the summary of the ligands, their structures and the functional groups of interest.

**Table 3.2: Summary of ligands, their structures and functional groups of interest**

Ligand	Structure	Functional groups
Meso-2,3-dimercaptosuccinic acid		-SH, -COOH
L-cysteine		SH, NH <sub>2</sub> , -COOH

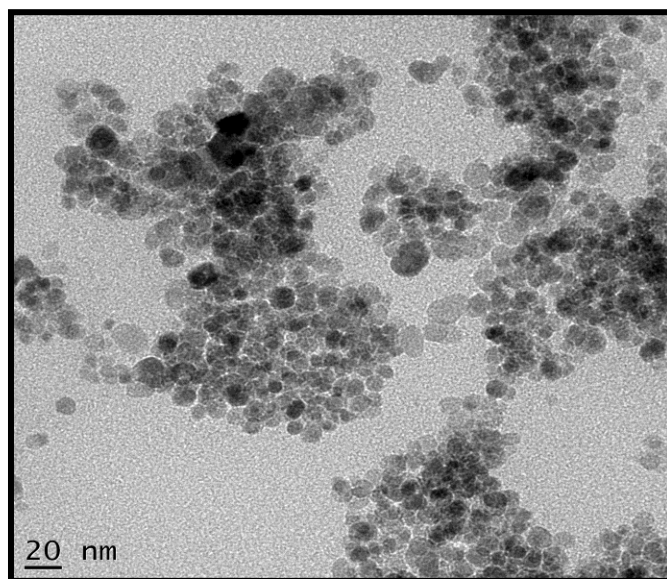
Dopamine		-NH <sub>2</sub> , -OH
3-Mercaptopropionic acid		SH, -COOH

Despite the hydroxyl functional groups having higher affinity for iron oxide surface, consideration was put on ligands with plenty of functional groups that could allow further conjugation. Their success and challenges in introduction to the surface of iron oxide are discussed herein

### 3.3.1 Functionalization of $\alpha$ -Fe<sub>2</sub>O<sub>3</sub> with meso-2, 3-dimercaptosuccinic acid (DMSA)

Iron oxide nanoparticles were functionalized with DMSA following a procedure reported by Singh *et. al.*<sup>154</sup> with some modifications. The iron oxide nanoparticles were dispersed in toluene and the DMSA dissolved in dimethylsulfoxide. DMSA is an organosulphur compound with two different functional groups. Two carboxyl(-COOH) and two thiol(-SH) groups. The particular ligand was chosen to allow coupling of iron oxide nanoparticles and InP/ZnSe quantum dots discussed in chapter four of this thesis. DMSA is an active chelating agent and is frequently used in water treatment of lead (Pb) and other metal poisoning. For instance, Singh *et. al.*<sup>154</sup> coated Iron oxide magnetic nanoparticles with DMSA and used it for removal of toxic metals namely Cr<sup>3+</sup>, Co<sup>2+</sup>, Ni<sup>2+</sup>, Cu<sup>2+</sup>, Cd<sup>2+</sup>, Pb<sup>2+</sup> and As<sup>3+</sup> and bacterial pathogens (*Escherichia Coli*). They were able to demonstrate that surface engineered magnetic nanoparticles were able to adsorb the metal ions from wastewater reaching almost 100 % efficiency at higher pH. The dried iron

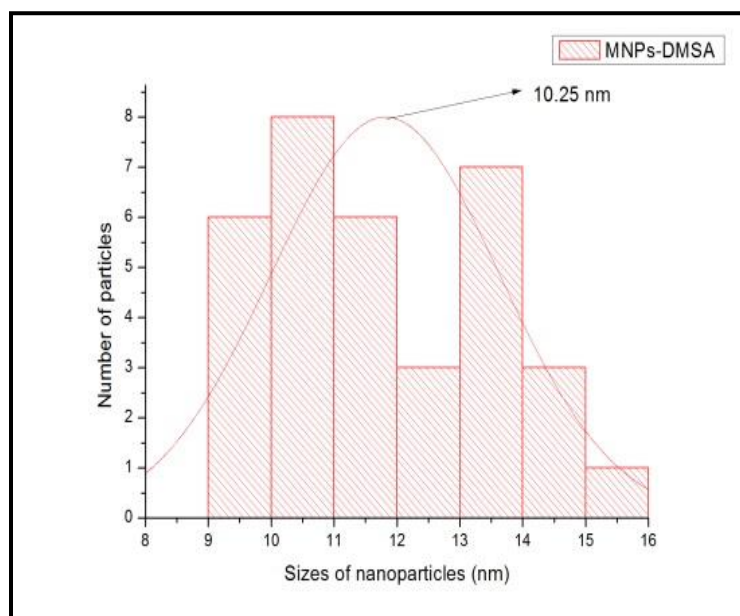
oxide sample was dried and grounded to attain dry powder. The dry powder of the nanoparticles was dispersed in water and HRTEM image obtained (Figure 3.6)



**Figure 3.6: HRTEM micrographs of DMSA capped iron oxide nanoparticles**

The capping of the iron oxide nanoparticles with the DMSA resulted to partial agglomeration. From our own understanding, the presence of two thiol functional groups in DMSA can actually lead to coupling the nanoparticles hence the witnessed agglomeration. Similar, observation was made by Haddad *et. al.*<sup>155</sup> where they noted that after functionalization with DMSA led to partial aggregation of the particles, however, there was no substantial change in the size of the particles. The same phenomenon was observed by Singh *et. al.*<sup>154</sup>, they carried out measurement of polydispersity index using DLS after functionalizing the Fe<sub>3</sub>O<sub>4</sub> nanoparticles with different ligands containing carboxyl, amine and thiol groups. They noted that there was an invariable change in polydispersity index ( $\sigma < 5\%$ ) for carboxyl, thiol, and amine-capped MNPs. The

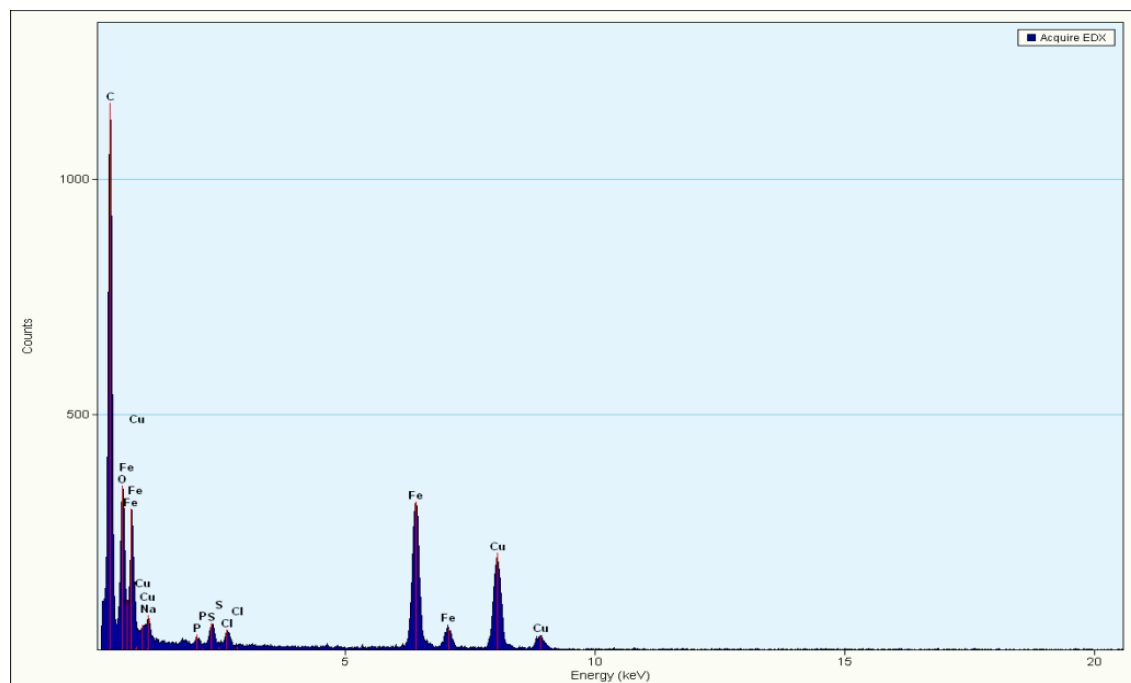
dispersion is attributed to the presence of organic layers. Precisely the carboxylate groups of the conjugating molecules are strongly coordinated to the iron cations on the surface of  $\alpha\text{-Fe}_2\text{O}_3$  leaving the thiol and amine groups extended into water medium conferring high aqueous stability of the  $\text{Fe}_3\text{O}_4$  nanoparticles. In addition, the repulsive forces which may originate from the nanoparticles contribute to their stabilization. Figure 3.7 is a histogram showing the size distribution of DMSA capped iron oxides is given.



**Figure 3.7: Histogram showing size distribution of DMSA capped iron oxide nanoparticles**

The size distribution were found to range from 9-16 nm with an average diameter of 10.25 nm. The average size of DMSA capped iron oxide nanoparticles increased slightly compared to the bare iron oxide nanoparticles. Similar observation was noted by Haddad *et. al.*<sup>155</sup> discussed earlier. Energy dispersive spectroscopy (EDS) was carried out also on

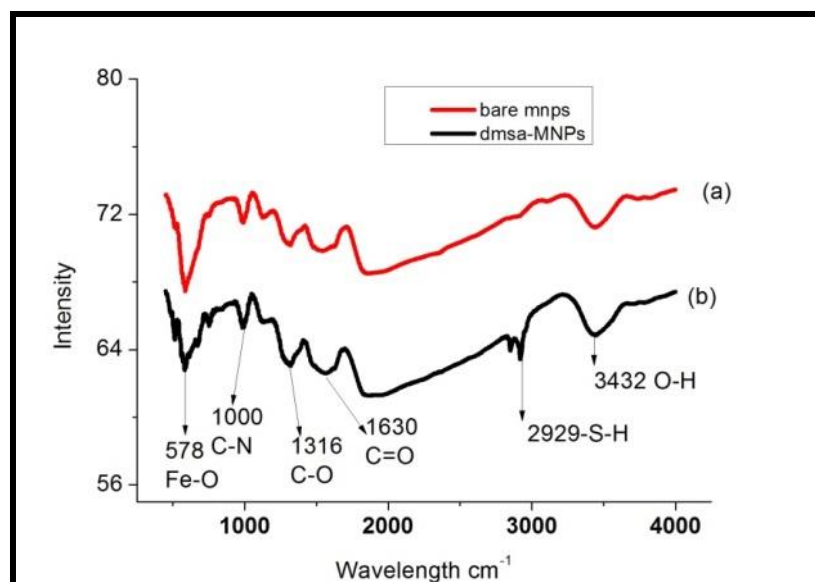
the functionalized iron oxide nanomaterials. Figure 3.8 below shows the EDS spectra that was obtained after functionalization of the oxide with the DMSA.



**Figure 3.8: Energy dispersive spectroscopy images for DMSA capped iron oxide nanoparticles**

The spectra show that new elements of DMSA were successfully incorporated into the final product. The EDS results are supported by FTIR results which confirm that the iron oxide particles were successfully functionalized.

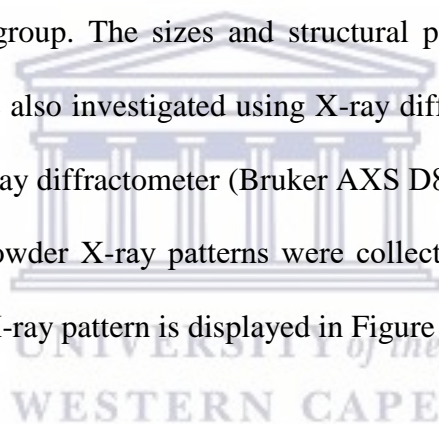
The FTIR spectra for bare magnetic nanoparticles is shown in Figure 3.9 (a) and DMSA functionalized iron oxide nanoparticles shown on Figure 3.9 (b).



**Figure 3.9: FTIR Spectrum of bare iron oxide nanoparticles (a) and DMSA functionalized iron oxide nanoparticles (b)**

The FTIR spectra in figure 3.9 (a) and 3.9 (b) demonstrated the contrast between bare and capped iron oxide nanoparticles. The bands observed at  $1611\text{cm}^{-1}$  and  $600\text{cm}^{-1}$  were attributed to C=O and Fe-O peaks respectively. Similar results were observed by Singh *et al.*<sup>154</sup> for their DMSA capped iron oxide nanoparticles. They ascribed strong peak at  $588\text{cm}^{-1}$  to Fe-O stretching vibrational mode of the  $\text{Fe}_3\text{O}_4$ . Likewise, a medium peak observed at  $1700\text{cm}^{-1}$  was attributed to C=O. They could not account for thiol group (-SH) but associated its disappearance to the formation of disulfide linkage (S-S) which overlapped with Fe-O of  $\text{Fe}_3\text{O}_4$  vibrational mode. In this study, however, we differ with their observation on the disappearance of the peak for -SH. We propose that the carboxylate functional group was utilized to anchor the ligand onto the surface of the  $\alpha\text{-Fe}_2\text{O}_3$  nanoparticles and the thiol group was suspended on the surface of the particle which enhanced 1) its hydrophilicity and 2) which enabled us to constitute  $\alpha\text{-Fe}_2\text{O}_3\text{-InP/ZnSe}$

nanocomposite discussed in chapter five of this thesis. The two weak peak appearing at around  $2900\text{ cm}^{-1}$  are attributed to the availability of the thiol group. A study carried out by Haddad *et. al.*<sup>155</sup> also supports our argument, in their study, they functionalized iron oxide nanoparticles with DMSA with the aim of making their particles to be water soluble and also to allow conjugation to a moiety for targeting ligand. According to the group, the DMSA could form stable coating through carboxylated bonding and free thiol was strategical to attach targeting ligands. To justify this observation we functionalized our nanoparticles also with 3-mercaptopropanionic acid discussed in the subsequent section of this thesis. This experiment was further used to confirm the succesful functionalization strategy of the DMSA group. The sizes and structural patterns of DMSA capped iron oxide nanoparticles were also investigated using X-ray diffractometer. The XRD analysis was performed using X-ray diffractometer (Bruker AXS D8) fitted with  $\text{CuK}\alpha = 1.54\text{ \AA}$  as an X-ray source. The powder X-ray patterns were collected with  $2(\theta)$  theta =  $8-95^\circ$  at room temperature. The X-ray pattern is displayed in Figure 3.10.



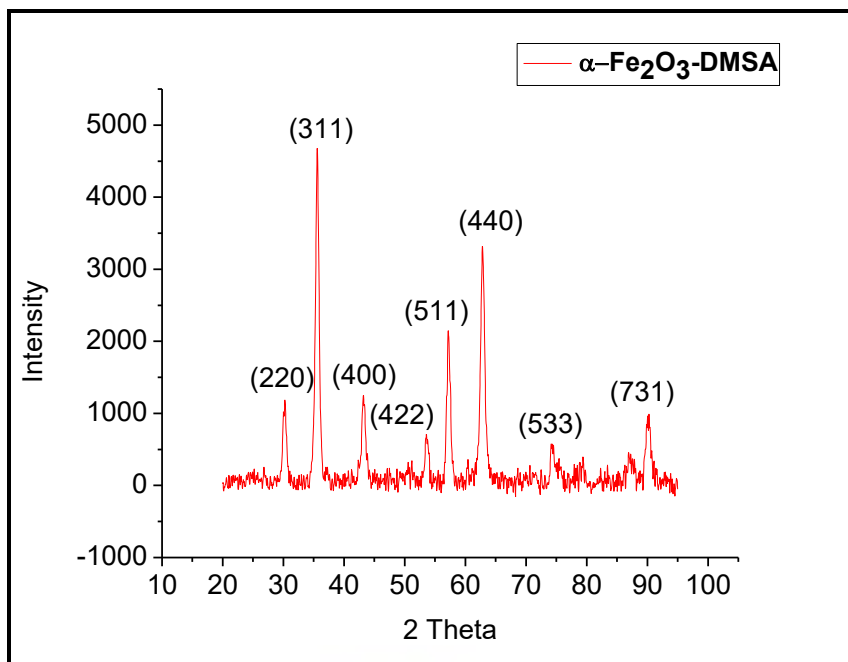


**Figure 3.10: XRD pattern for DMSA capped iron oxide nanoparticles**

The X-ray pattern was used to deduce the structure and the sizes of the synthesized iron oxide nanoparticles. Smooth peaks were chosen from the pattern and Scherrer's formula was used to estimate the sizes of the DMSA capped iron oxide nanoparticles.

The nanocrystals sizes were estimated using Debye Scherrer's formula presented earlier (equation 3.1). The calculated sizes and other parameters of Scherrer's equation for iron oxide nanoparticles are presented in Table 3.2



**Table 3.3: Estimation of DMSA capped iron oxide particles size using XRD data**

Peak	2 Theta (Degrees)	Theta (Degrees)	Theta (Radians )	Lambda	FWM (Degrees)	FWHM (Degrees)	FWHM (Radians)	Size (nm)
Peak 1	30.23	15.12	0.26	0.15	1.20	0.60	0.01	12.77
Peak 2	35.59	17.79	0.31	0.15	1.06	0.53	0.01	14.22
Peak 3	43.27	21.63	0.38	0.15	1.41	0.70	0.01	10.49
Peak 4	53.61	26.80	0.47	0.15	1.20	0.60	0.01	11.81
Peak 5	57.18	28.59	0.50	0.15	1.20	0.60	0.01	11.61
Peak 6	62.84	31.42	0.55	0.15	1.26	0.63	0.01	10.77
Average								11.94

The particle sizes estimated from Scherrer's formula were found to be 11.94 nm for DMSA capped iron oxide nanoparticles. The values were quite comparable to the sizes estimated from HRTEM micrographs where the diameter of capped iron oxide was estimated to be 10.25 nm. Similar studies were carried out by Singh *et. al.*<sup>154</sup> who reported a relatively smaller size for DMSA capped iron oxide nanoparticles. Their XRD, HRTEM and DLS estimations gave the sizes of the nanoparticles to be 6 nm. Their findings is supported by low saturation magnetization of 43.2 emu/g at 20 KOe measured at room temperature. The sizes of their magnetic nanoparticles were lower compared to the sizes synthesized of the particles in this study, however, the thiol-capped magnetic nanoparticles had a higher magnetic saturation of 68.33 emu/g. The XRD pattern was matched with JCPDS no. 00-039-1346 and 00-019-0629 for maghemite ( $\alpha$ -Fe<sub>2</sub>O<sub>3</sub>) and magnetite (Fe<sub>3</sub>O<sub>4</sub>), respectively. The best match for iron oxide nanoparticles was found to be for maghemite. The perfect match of our samples to maghemite which was against the authors expectation was possibly due to oxidation as explained earlier and support by a study conducted by Mamani *et. al.*<sup>150</sup>.

### 3.3.2 Functionalization of $\alpha$ -Fe<sub>2</sub>O<sub>3</sub> nanoparticles with 3-mercaptopropionic acid

The 3-mercaptopropionic acid is a molecule with two functional groups namely carboxyl and thiol groups. This molecule was used to confirm which of the two functional groups (carboxyl and thiol) had a higher affinity for the iron oxide nanoparticle surface. The functionalization process was achieved by ultra-sonication of 3-MPA solution with the iron oxide nanoparticles and the mixture left standing for 24 hours at room temperature. The functionalized particles were separated with an aid of a permanent magnet and cleaned with repeated cycles of distilled water. The particles were gently dried at room temperature and FTIR analysis carried out (Figure 3.11).

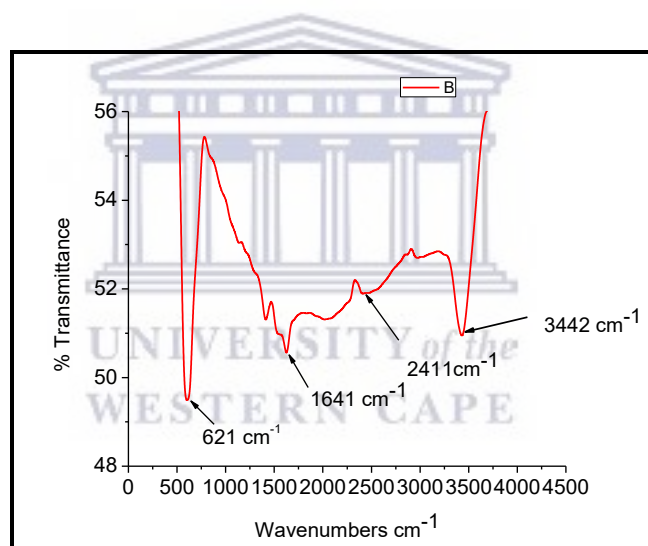


**Figure 3.11: 3-mercaptopropionic acid capped iron oxide nanoparticles**

From the spectroscopic technique, we assigned the peak at 1641 cm<sup>-1</sup> to COO-Fe bond. The strong sharp peak observed at 621 cm<sup>-1</sup> belongs to Fe-O. Lastly, the peaks observed at 2411cm<sup>-1</sup> and 3442 cm<sup>-1</sup> belongs to thiol, and hydroxyl groups, respectively. Similar functionalization strategy was reported by Burks *et. al.*<sup>156</sup>. They synthesized 3-mercaptopropionic acid capped iron oxide nanoparticles. Their success in

functionalization of the iron oxide nanoparticles with 3-mercaptopropionic acid was monitored with FTIR and they assigned observed peaks as follows; a broad band observed at  $3027\text{ cm}^{-1}$  to O-H bond, the band at  $2949\text{ cm}^{-1}$  was assigned to C-H bond for  $\text{CH}_3$ , two peaks at  $2668\text{ cm}^{-1}$  and  $2570\text{ cm}^{-1}$  were assigned to S-H bond, the  $1705\text{ cm}^{-1}$  peak was assigned to C=O and lastly they assigned the band at  $582\text{ cm}^{-1}$  to Fe-O bond. According to the group, the 3-MPA was bound to the iron oxide nanoparticles surface by the COOH group rather than through the SH group. Upon capping of the iron oxide nanoparticles, they observed new bands at  $1516\text{ cm}^{-1}$  and  $1414\text{ cm}^{-1}$  which they assigned to asymmetric and symmetric stretching vibrations of the carboxylate group<sup>156</sup>. Na *et. al.*<sup>157</sup> attributed peaks they observed at  $1393\text{ cm}^{-1}$  and  $1587\text{ cm}^{-1}$  to COO-Fe bond, which may be due to the reaction of hydroxide radical groups on the surface of  $\text{Fe}_3\text{O}_4$  with carboxylate anion of sodium citrate<sup>157</sup>. The unavailability of -COOH group for formation of amide bond with amino group of streptavidin made us to drop this choice for bioconjugation.

### 3.3.3 Functionalization of iron oxide with L-Cysteine

L-cysteine is an attractive molecule which is suitable for surface modification due to the functional groups that it contains. L-cysteine is an amino acid with three functional groups namely thiol (-SH), carboxyl (-COOH) and amino (-NH<sub>2</sub>). It is expected that either thiol group or the carboxyl groups are attached to the surface of the nanoparticle and the amine group and the unutilized functional group will be available for conjugation. Ahmadi and co-workers<sup>63</sup> used co-precipitation method to synthesize L-cysteine capped magnetite nanoparticles of sizes ranging between 10-20 nm. During their synthesis, the co-precipitation method was assisted with ultrasonic radiation technique. The ultrasonication method and use of biological capping agent (L-cysteine) resulted in particles with a

regular distribution of the nanoparticles. The group was able to point out the advantage of L-cysteine capped iron oxide nanoparticles where the particles were less aggregated compared to those synthesized without L-cysteine<sup>63</sup>. The FTIR spectroscopy was used to validate success in the attachment of the L-Cysteine to the iron oxide nanoparticles is shown in Figure 3.12.

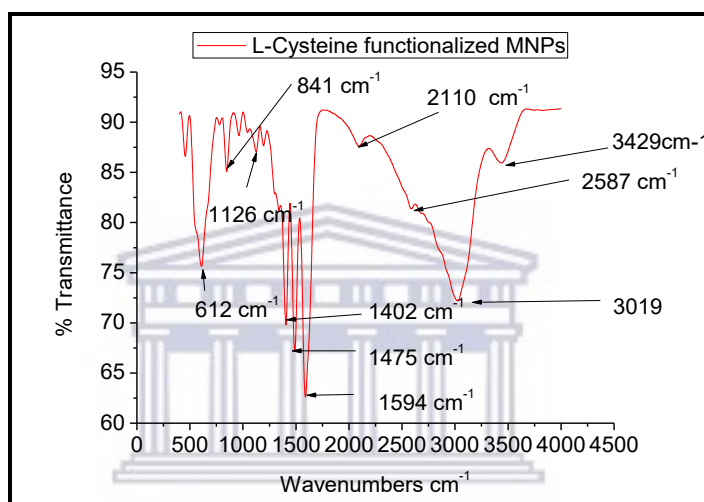


**Figure 3.12: FTIR spectrum of L-Cysteine capped Iron oxide nanoparticles**

From the FTIR spectrum the strong narrow peak at  $612\text{ cm}^{-1}$  belongs to stretching vibrational mode of Fe-O bond. The peaks at  $1475\text{ cm}^{-1}$  and  $1594\text{ cm}^{-1}$  are characteristic peaks of COO-Fe bond. The weak peak appearing at  $841\text{ cm}^{-1}$  could be associated with bending vibration of  $\text{-NH}$ . The weak peak appearing at  $2587\text{ cm}^{-1}$  could possibly be attributed to  $\text{-SH}$  bond. The peak at  $3019\text{ cm}^{-1}$  could possibly be due to the stretch of C-H bond. Lastly, we assign the peak at  $1126\text{ cm}^{-1}$  to the stretch of C-N. In a similar study, White *et. al.*<sup>158</sup> coated magnetic nanoparticles ( $\alpha\text{-Fe}_2\text{O}_3$ ) with poly-L-cysteine they

ascribed a weak peak that appeared on  $799.3\text{ cm}^{-1}$  to bending vibration of  $-\text{NH}_2$ . The blue shift compared to findings of this study could be attributed to the nature of interaction at the surface of the nanoparticles with the molecule. A similar shift in absorption peak was observed when Zhao *et. al.*<sup>146</sup> synthesized polymer (chitosan) coated iron oxide nanoparticles. They observed a strong peak at  $610\text{ cm}^{-1}$  which they associated with the vibration of Fe-O bond. They assigned a peak at  $1520\text{ cm}^{-1}$  to bending of N-H bond due to chitosan bonded to the polymer (poly (HEMA-co-GMA)).



### 3.3.4 Magnetic properties of L-cysteine capped Iron oxide

The magnetic properties of L-cysteine capped iron oxide nanoparticles were investigated using SQUID. The measurements were done at room temperature by varying the magnetic field between -30 to +30 KOe. Whenever non-magnetic molecules are used to coat magnetic nanoparticles it is expected that the magnetic saturation reduces, however, the magnitude of decline is dependent on the size of the capping material. The magnetic saturation curve is shown in Figure 3.13 below.

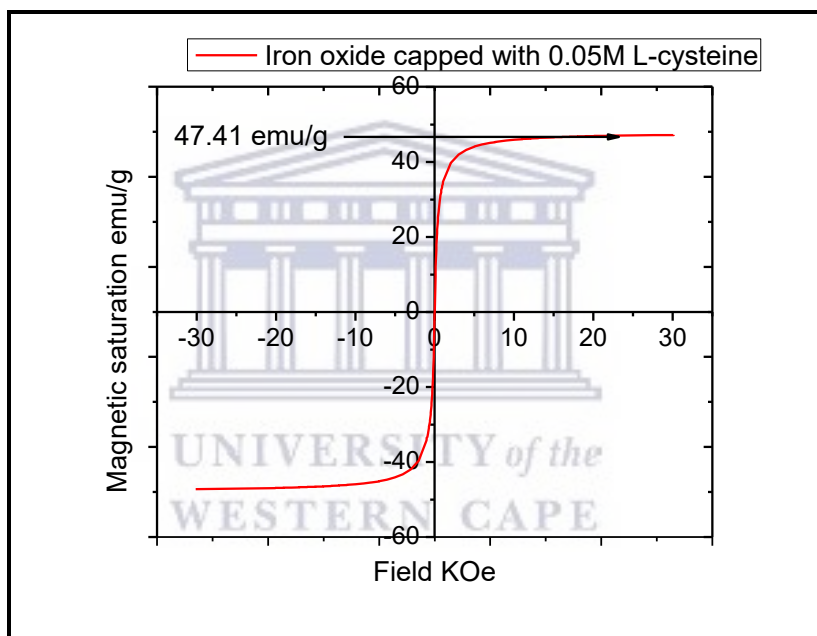


**Figure 3.13: Magnetic properties of L-cysteine functionalized iron oxide nanoparticles**

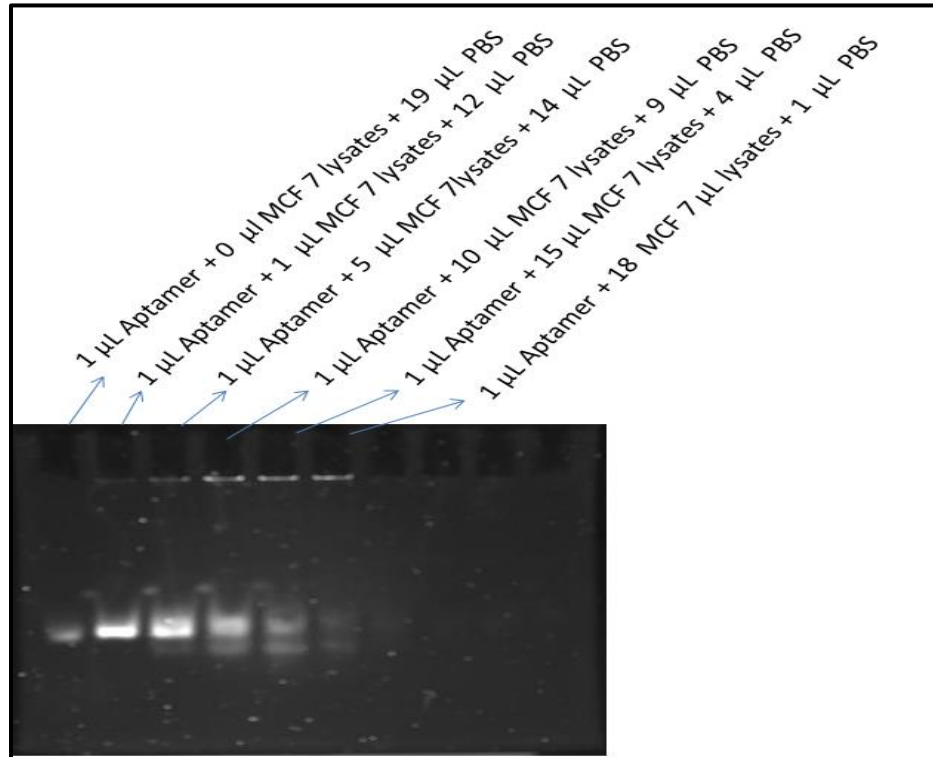
The magnetic saturation of the particles was determined to be 47.41 emu/g. This was a decrease compared to bare magnetic nanoparticles which was 65.67 emu/g. Our findings are in agreement with literature, for instance, Ahmadi *et. al.*<sup>63</sup> capped iron oxide with L-cysteine and investigated its magnetic properties by using vibrating sample magnetometer.

They discovered that the saturation magnetization increases with the size of the nanoparticles. For instance, their particles with sizes of 9.66 nm, 12.22 nm, and 20.62 nm had a magnetic saturation of 64.15, 70.75 and 72.30 emu/g, respectively. They further noted that these values were higher compared to conventional long chain ones such as dextran and polyethylene glycol (PEG) coated iron oxide nanoparticles. However, short-chain capping agents do not enhance stabilization of the ferrofluid. In another study, Zhao *et. al.*<sup>146</sup> witnessed a tremendous decrease in magnetic saturation from 68.08 emu/g to 7.03 emu/g when they coated their Fe<sub>3</sub>O<sub>4</sub> nanoparticles with the polymer (Poly(hydroxyethyl methacrylate-co-glycidyl methacrylate)).

### **3.4 Electrophoretic mobility shift assay (EMSA) studies**

The binding ability of the MUC 1 binding aptamers was evaluated using electrophoretic mobility shift assay technique (EMSA). The technique is classically used to detect protein bound to DNA. The principle behind the technique is that when DNA aptamer is bound to the protein it migrates through polyacrylamide gel slowly compared to free DNA aptamer. The aptamer-protein complex is usually loaded and run on non-denaturing polyacrylamide gel causing separation of DNA-protein complex from free DNA probes<sup>159</sup>. Biotinylated MUC 1 binding aptamer (HPLC purified) with the sequence 5'-GCA GTT GAT CCT TTG GAT ACC CTG G-3' was purchased from Integrated DNA technologies. The recombinant human MUC1 consisted of 142 amino with predicted molecular mass of 15.4 kDa. The binding ability of the purchased aptamer was investigated by setting up six experiments. The lysates used were extracted from cultured MCF 7 cells (cancerous). The constant amount of aptamer was used for each set up while the amount of lysate was varied in an increasing manner and the total volume was made up to 20 µL using PBS

(See Table 2.1). The samples were loaded into the wells of 12 % native polyacrylamide gel. The gel was stained using ethidium bromide and visualized using UVP BioSpectrum® Imaging System. The uninverted image is shown in Figure 3.14 below



WESTERN CAPE

**Figure 3.14: EMSA micrograph showing mobility of MUC1 aptamer incubated with increasing amounts of the lysates**

The binding experiment clearly demonstrated that the amount of the lysate used influenced the success in binding. For instance, when less than 10 microliters were used very little aptamer was bound to the DNA unlike when the volume was greater than 10. This is due to the presence of MUC 1 protein in low amounts compared to total proteins in the MCF-7 lysates. Secondly, an experiment was set up to determine the specificity of the MUC 1 binding aptamers (See Table 2.2). The objective was attained by employing



lysates extracted from MCF-7 and MCF-12 cells. A set up consisting of duplicates of each lysate (MCF7 and MCF 12 )and free DNA aptamer were set up and the results presented in Figure 3.15.

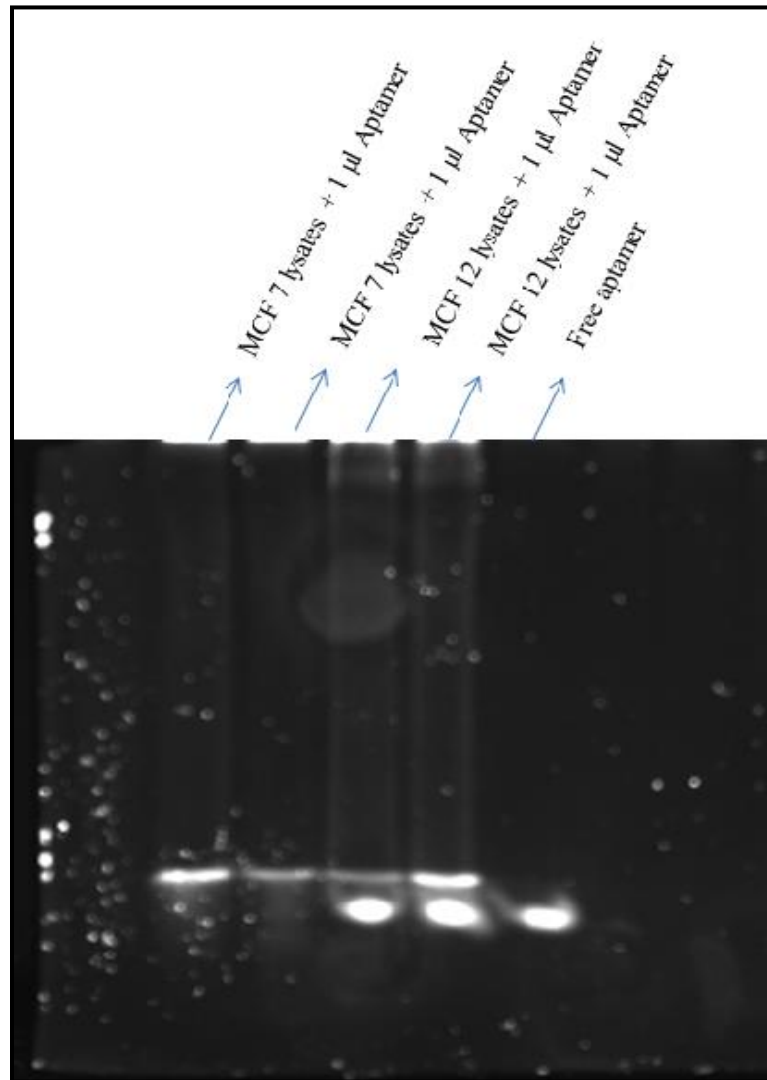


**Figure 3.15: Evaluation of specificity of MUC 1 binding aptamers on MUC 1 proteins expressed on MCF 7, MCF-12A and free aptamer was used as a control**

It was observed that all of 1  $\mu$ L MUC 1 binding aptamer was bound to MUC 1 protein present in MCF-7 cells as seen in the first two wells in Figure 3.15. The interaction of MUC 1 binding aptamer with the lysates extracted from MCF 12 cells showed some partial binding to the aptamer but the majority of the unbound aptamer proceeded further down (3<sup>rd</sup> and 4<sup>th</sup> well). In the last well where free aptamer had been loaded shifted to similar distance with the aptamer that had interacted with the MCF12 lysates. In conclusion, the experiment established that the MUC 1 binding aptamers are specific to MUC 1 proteins and also the binding conditions were established. We went ahead and conjugated MUC 1 binding aptamers to magnetic nanoparticles. The conjugate was used to isolate MUC 1 proteins from lysates extracted from cancerous MCF 7 cells.

### **3.5 Biomarker enrichment using MNP-MUC 1 binding aptamer**

We conjugated biotinylated MUC 1 binding aptamers to magnetic nanoparticles via streptavidin. The aim was to take the advantage of known strong binding affinity of biotin to streptavidin. The interaction between the two is known to be very strong with a dissociation constant of the order of  $10^{-14}$  mol/L. The aptamer conjugated to MNPs was incubated with both MCF 7 and MCF 12A lysates. The incubation process was followed by isolation and thorough washing to remove the temporarily bound proteins. The MNP-aptamer conjugate was re-suspended in PBS and the concentration of the proteins determined using Qubit. The Qubit results are presented in Table 3.3 below.

**Table 3.4: Concentration of captured proteins from MCF 7 and MCF 12A lysates**

Experiment		MNPs(beads)- Streptavidin complex( $\mu\text{L}$ )	Biotin- Aptamer ( $\mu\text{L}$ )	Lysate ( $\mu\text{L}$ )	PBS ( $\mu\text{L}$ )	Total volume ( $\mu\text{L}$ )	Q conc. Actual ( $\mu\text{g}/\text{mL}$ )
MCF 7	7-1	15	1	6	8	30	15.1
	7-2	15	1	6	8	30	15.6
	7-3	15	1	6	8	30	16.2
MCF 12A	12-1	15	1	6	8	30	13.8
	12-2	15	1	6	8	30	10
	12-3	15	1	6	8	30	13.5
3 (Control)	1	15	1	0	14	30	<1
	2	15	1	0	14	30	<1

As seen in Table 3.3 the concentrations of the proteins captured when MNPs are incubated with MCF 7 were higher compared to those incubated with MCF 12A. The controls (MNP-streptavidin without the MUC 1 aptamers) had concentrations below detection limit of the instrument. Since in both cases a protein was captured, a more elaborate technique was required to tell if MUC 1 protein was actually captured hence MALDI-TOF-MS was employed. To identify the proteins captured we used MALDI-TOF-MS to establish the proteins that were captured. First, we trypsinized the purchased MUC 1 protein and performed MALDI-TOF- MS to establish the position of the peaks that corresponds to

masses of the peptides originating from the protein. The MALDI-TOF-MS spectra of the trypsinized MUC1 protein is shown in Figure 3.16

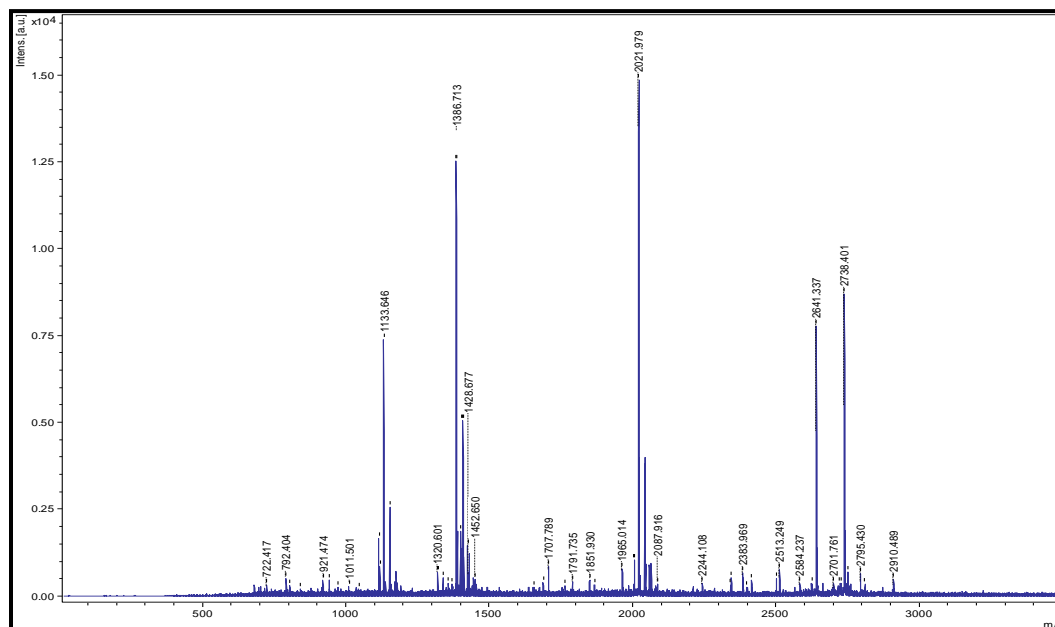


**Figure 3.16: MALDI-TOF-MS spectrum of trypsinized human mucin 1**

To establish the ability of the aptamer functionalized iron oxide nanoparticles to specifically isolate MUC 1 proteins, we prepared two samples and performed MALDI-TOF-MS. The first sample was a labelled A2. It consisted iron oxide nanoparticles bioconjugated to MUC 1 binding aptamer through streptavidin and was incubated with the lysates extracted from MCF 7 cells then washed several times using PBS. The second sample was a control C1 which consisted of the iron oxide bioconjugated to MUC 1 aptamer using the streptavidin but was not incubated with the lysates. The samples were prepared as described in the experimental section and MALDI-TOF-MS analysis

performed. Figure 3.17 is a MALDI-TOF-MS spectrum for the sample A2 and the control C1.

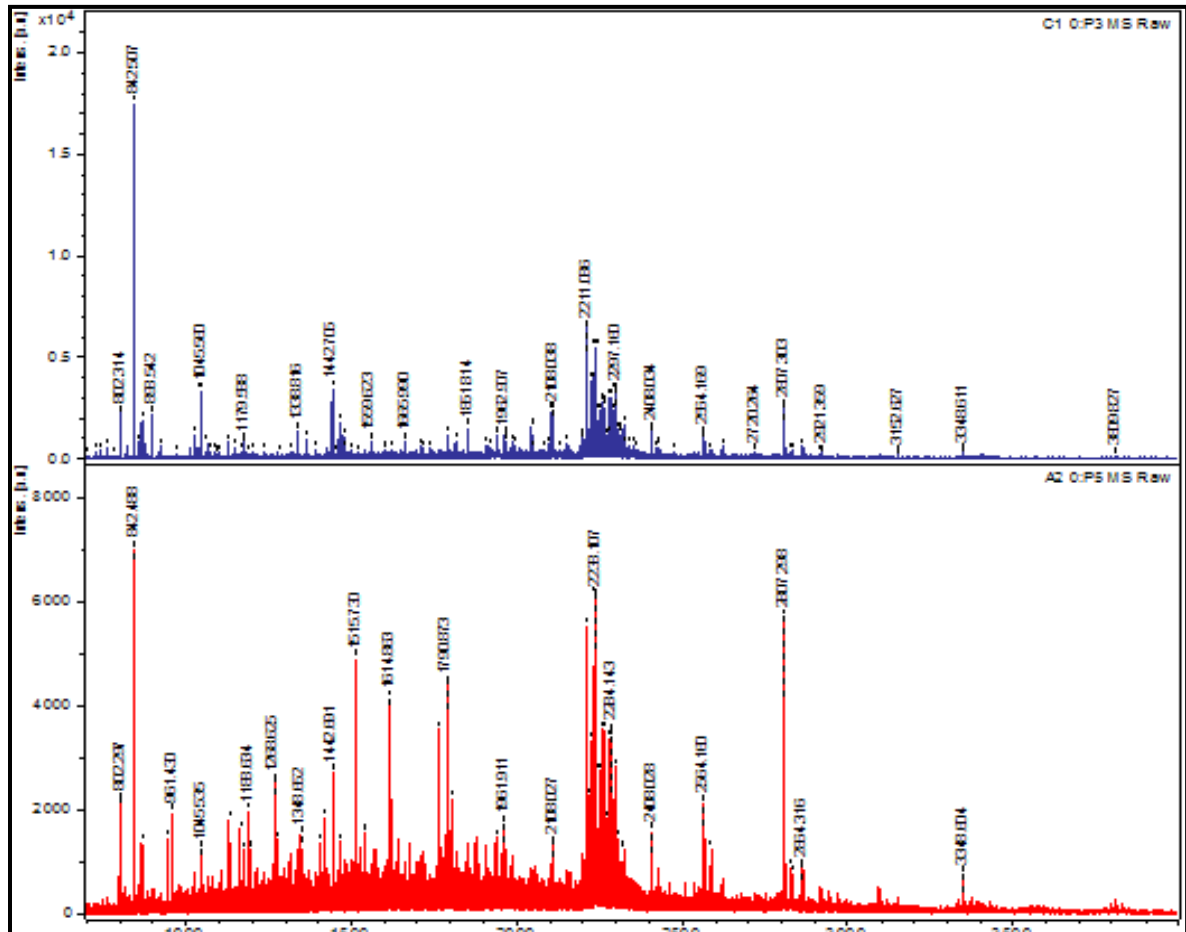


**Figure 3.17: The MALDI-TOF-MS spectra corresponding to the isolated proteins (A2) and the spectrum for the control (C1) experiment**

By comparing the two spectrums it should be noticed that the intensity of the peaks originating from the sample are higher than those of the control. This suggests that indeed there were some proteins that were captured in addition to the streptavidin and biotin that were already conjugated to the surface of the iron oxide nanoparticles. The other peaks observed in the spectrum originated from trypsin which was used for sample digestion to identify whether MUC 1 protein was actually captured, the entry number ([P15941](#)) of

Mucin 1-human was obtained from unitProtKB and taken to ExPASy in order to identify the corresponding peptide masses. Furthermore, by assessing the MALDI-TOF-MS spectrum in Figure 3.16 and the spectrum for the samples where the MUC 1 was isolated from the lysates using aptamer functionalized MNPs we established some similarities. Xiong *et. al.*<sup>99</sup> developed a method based on aptamer-conjugated magnetic graphene/gold nanocomposite for specific enrichment and analysis of thrombin in biological samples. They used MALDI-TOF-MS to identify the success in enrichment of the thrombin. It was very easy for them to identify the peptide mass originating from thrombin since they had used a pure protein. When they applied the technique to analyse presence of thrombin in real samples, multiple peaks were observed but narrowed to the peak which had been seen in the standard to actually belong to thrombin.

### **3.6 Cytotoxicity studies of bare iron oxide and functionalized iron oxide nanoparticles**

In order to determine the toxicity of the bare and functionalized iron oxide nanoparticles, we carried out an extensive *in vitro* (cell culture) cytotoxicity study. The KMST6 and MCF-12A which were both non-cancerous cell lines were used for this study. Various concentrations of MNPs were prepared ranging from 0.1 mg/mL to 0.5 mg/mL. The cell line of MCF-12A and KMST6 cell lines were each placed in eight wells and exposed to a similar concentration of the nanoparticles. The same was repeated for bare MNPs, DMSA capped MNPs, dopamine capped MNPs and L-cysteine capped MNPs all concentrations for the two cell lines. The untreated cells were used as a negative control and ceramide used as a positive control. The cell viability was measured 24 hours using the MTT assay<sup>144</sup> after incubation of the cells with the nanoparticles.

The cell viability was expressed as the percentage ratio of mean absorbance of treated cells against mean absorbance of untreated cells according to the formula;

$$\% \text{ Cell viability} = \frac{\text{Sample}}{\text{control}} \times 100$$

Based on this formula, the cell viability for all the wells and all the cell lines were calculated and the average value was obtained. The summarized cytotoxicity results are presented in Figures 3.18

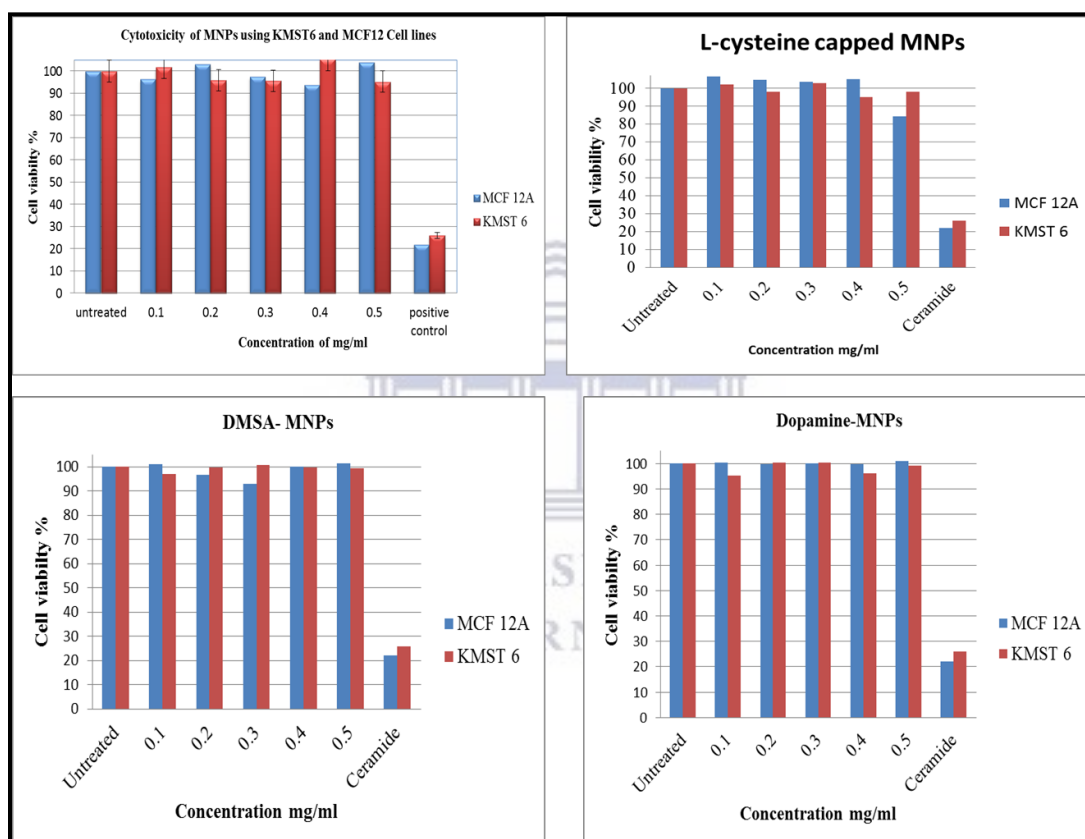


**Figure 3.18: Cytotoxicity studies of bare and functionalized iron oxide nanoparticles using MCF-12A and KMST 6 cell lines**

When the concentrations of the magnetic nanoparticles were varied from 0.1 to 0.5 mg/mL the least cell viability increased from 90 % in all cases. This suggested that the synthesized bare and functionalized MNPs are less toxic. When different molecules are

used in surface modification they affect the toxicity of the nanoparticles, for example, Liu *et. al.*<sup>160</sup> carried out cytotoxicity study of iron oxide coated with acridine orange using 293T cells. They varied the concentration of the iron oxide from 0 to 80 µg/mL and observed cell viability greater than 78%. The lower cell viability observed here could be attributed to acridine orange used and not the iron oxide. The ligands chosen in our study appeared not to affect the toxicity of the iron oxide nanoparticles despite using higher concentration compared to the concentration reported by Liu *et. al.*<sup>160</sup>.

### 3.7 Conclusion

Iron oxide nanoparticles were successfully synthesized by co-precipitation method. Large amounts of the particles were synthesized within 2 hours using water as the solvent at room temperature. Particles of less than 12 nm were synthesized with the good magnetic saturation of 68 emu/g. The iron oxide particles were successfully functionalized using L-cysteine, 3-MPA, dopamine and meso-2,3-dimercaptosuccinic acid. The choice of these surfactants appeared not to affect the magnetic saturation of the iron oxide nanoparticles. Success in functionalization allowed bioconjugation of streptavidin through glutaraldehyde chemistry and hence conjugation of MUC 1 binding aptamer. During the enrichment process, the aptamer conjugated to the nanoparticles were able to efficiently and specifically isolate MUC1 proteins from MCF 7 lysates. This was confirmed by quantification of the proteins using the Qubit followed by MALDI-TOF-MS analysis. The *in vitro* investigation on cytotoxicity of magnetic nanoparticles against MCF-12A and KMST 6 cell lines revealed that the particles are less to with less than 10 % reduction in cell viability.



## 4 CHAPTER FOUR: SYNTHESIS AND CHARACTERIZATION OF InP/ZnSe QUANTUM DOTS

### 4.1 Introduction

This chapter presents the results for the synthesis and characterization of InP/ZnSe QDs. In regard to InP/ZnSe QDs we have discussed photoluminescence characteristics of the crude product and the aliquots. We have demonstrated the size sorting process of the prepared QDs, ligand exchange and streptavidin conjugation. Again, we have shown the possibility of scaling up the synthesis of InP/ZnSe QDs. We have calculated the band gap and quantum yield of InP/ZnSe QDs. Furthermore, we have compared the photoluminescence and fluorescence properties of the products obtained by up scaling the synthesis. Pertaining InP/ZnSe QDs we have shown how streptavidin can be attached to InP/ZnSe QDs and also we carried out cytotoxicity studies. The chapter ends with demonstration of application of CdTe/ZnS QDs for the design of molecular beacons. We have presented the synthesis, characterization and application of the designed molecular beacons in gene detection.

### 4.2 Synthesis and characterization of InP/ZnSe quantum dots

The techniques that are usually adopted for the synthesis of nanocrystals are generally of two types namely organometallic synthesis route based on high temperature thermolysis of the precursors/dehalosilylation<sup>161</sup> and the other method is synthesis through the aqueous medium using polyphosphates<sup>162</sup> or thiols<sup>163</sup> as stabilizing agents. The hot injection technique is known to be a successful method for synthesis of InP, where  $\text{P}(\text{SiMe}_3)_3$  is introduced to indium carboxylate salt at high temperatures close to  $300\text{ }^\circ\text{C}$ <sup>164</sup>. At such high temperatures the  $\text{P}(\text{SiMe}_3)_3$  releases the  $\text{P}^{3-}$  to the  $\text{In}^{3+}$  without going through redox

processes. The known sources of  $P^{3-}$  are phosphine gas ( $PH_3$ ), white phosphorous ( $P_4$ ), tris(trimethylsilyl)phosphine and tris(trimethyl germyl)phosphine  $P(GeMe_3)_3$ <sup>165</sup>. In a typical process, the reactive  $P(SiMe_3)$  is consumed immediately hence the need for the presence of monomers to extend the growth period of the nanocrystals<sup>165</sup>. Few studies have been focused on the synthesis of InP/ZnSe nanocrystals. In our literature search, we established that only two researchers have attempted to synthesize this type of material and much have focused on the synthesis of InP/ZnS nanocrystals. In the current study, much effort was concentrated on the synthesis process in order to gain insight in regard to the challenge it poses. Furthermore, we attempted to answer the question pertaining to the unpopularity of InP/ZnSe among the QDs tested for potential biological application. Kim *et. al.*<sup>92</sup> synthesized InP/ZnSe nanocrystals for the first time in 2010. They synthesized InP first and later passivated its surface with ZnSe. The InP quantum dots were synthesized using trioctylphosphine oxide, chloroindium oxalate and Tris(trimethylsilyl)phosphine dissolved in trioctylphosphine. The synthesis was carried out under nitrogen for several days. The product was dispersed in butanol and precipitated in methanol. They passivated the core with ZnSe shell, Zn, and Se precursors were saturated in the glove box using TOP and injected into a hot solution of TOPO containing InP quantum dots. The reaction occurred over a 24 hour period and the final product was obtained by centrifugation and dispersed in n-hexane. The group pointed out that with ZnSe passivation increased the photoluminescence by six fold, however, they never reported on the quantum yield of the material. The second group to report the synthesis of InP/ZnSe nanocrystals was Mushonga *et. al.*<sup>93</sup>. They reported on a new shorter route for the synthesis of InP/ZnSe quantum dots whereby all necessary processes lasted less than 12 hours. They used

palmitic acid, non-coordinating solvent and different sources of Indium, Zinc and Selenide in comparison to the first group. They maintained the In:P ratio at 1:3 but used high temperatures similar to Kim *et. al.*<sup>92</sup>. They successfully fabricated highly fluorescent InP/ZnSe quantum dots with a quantum yield of 6 %. In this study we adopted the approach employed by Mushonga *et. al.*<sup>93</sup> with few modifications. The reaction temperatures and the molar ratios were equally held constant. The trend of the fluorescing properties of the synthesized InP/ZnSe was monitored during the nucleation of the core and the development of the shell. The quantum dots nanocrystals were characterized by HRTEM (model-TECNAI F30ST). The quantum dots obtained in this study were polydisperse, the HRTEM micrograph is shown in Figure 4.1.

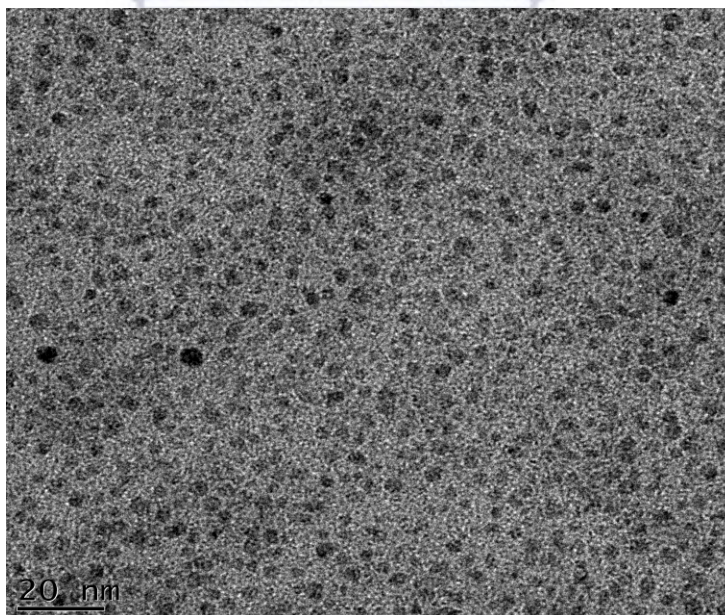


**Figure 4.1: HRTEM micrographs showing distribution of InP/ZnSe nanocrystals**

The HRTEM micrograph together with ImageJ software was used to estimate the average size of the synthesized quantum dots. Below is a histogram showing the size distribution of the prepared InP/ZnSe nanocrystals (Figure 4.2).

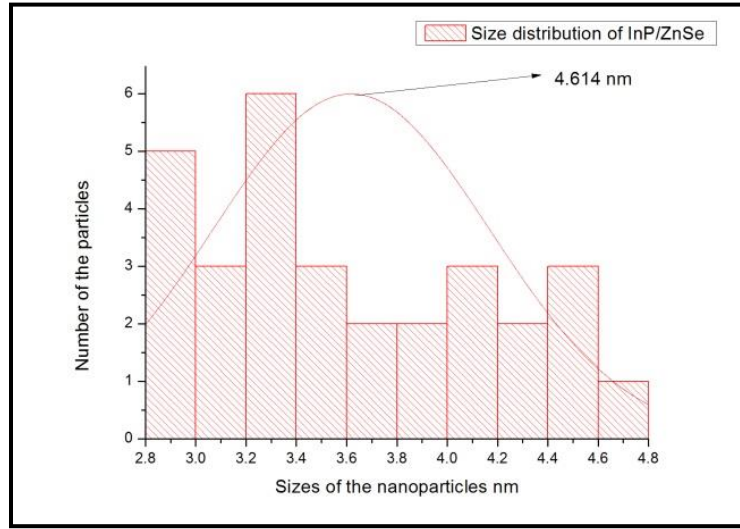


**Figure 4.2: Histogram showing size distribution of the synthesized InP/ZnSe nanocrystals**

More than 50 particles were randomly selected from the HRTEM micrograph and used to determine their sizes. The particles had a size distribution ranging from 2.8-4.8 nm with an average size of 4.61 nm. Kim *et. al.*<sup>92</sup> obtained relatively smaller particles of 3 nm, though it was an estimation of only three nanoparticles obtained from HRTEM. They estimated the lattice fringe spacing to be 0.34 nm which was in agreement with the spacing of 0.3388 nm between (111) planes of zinc-blende InP structure. To establish structural properties of the synthesized InP/ZnSe nanocrystals and also to confirm their sizes, a powdered X-Ray diffraction (PXRD) analysis was performed. The PXRD analysis was performed using X-ray diffractometer (Bruker AXS D8) fitted with  $\text{CuK}\alpha = 1.5418 \text{ \AA}$  as an X-ray source. The powdered X-ray patterns were collected by varying the angle theta ( $2\theta$ ) from 8 to 95 degrees at 25 °C. Figure 4.3 below shows the XRD pattern of the as-prepared InP/ZnSe nanocrystals.

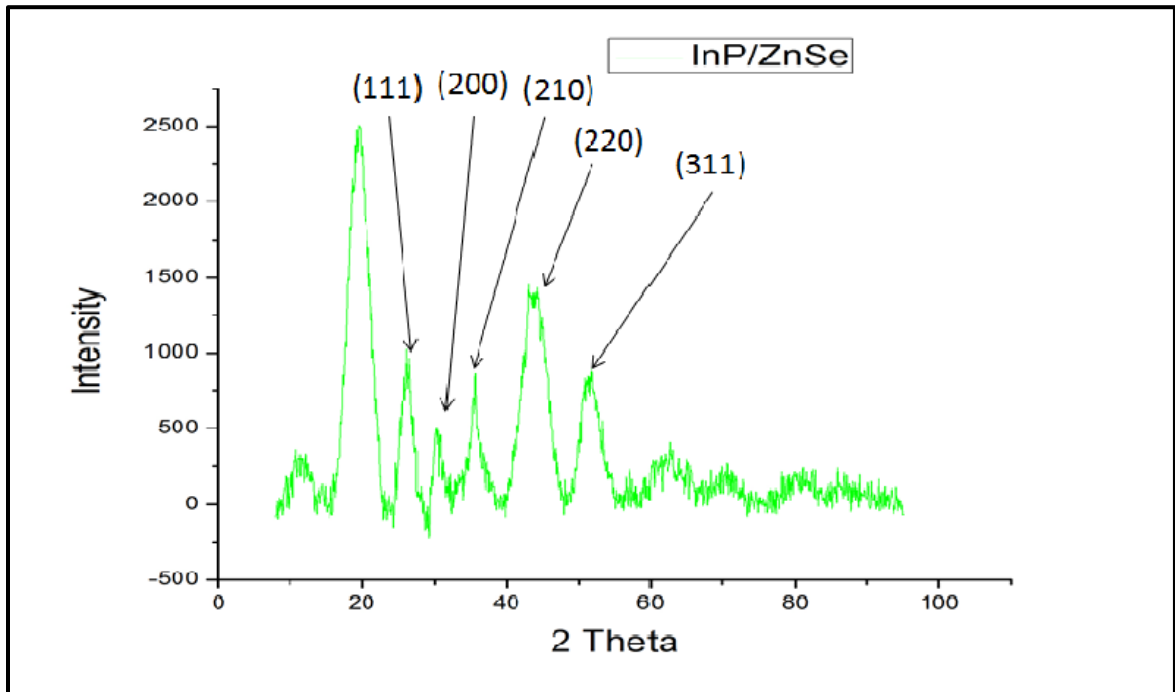


**Figure 4.3: XRD patterns of the prepared InP/ZnSe nanocrystals**

To establish the structural pattern of the InP/ZnSe nanocrystals the data was matched with JCPDS file for InP JCPDS no. 00-032-0452 and ZnSe (stilleite) JCPDS no's. 00-037-1463. According to this database, theoretically both InP and ZnSe have face-centered cubic structures with major characteristics peaks at  $2\theta \approx 26, 43$  and  $51^\circ$  for InP and at  $27, 45$  and  $53$  degrees for ZnSe with hkl values of (111), (220) and (311), respectively. There was a perfect match between the X-ray pattern and JCPDS file for InP. There was an approximate match between the obtained ZnSe XRD diffraction patterns with that of the JCPDS file. The close proximity of the position where the peaks for InP and ZnSe contributed to the matching of the peaks originating for the separate materials. This could also be attributed to the manner of interaction between the core and the shell. Similar observation was observed by Kim *et. al.*<sup>92</sup> when they separately investigated the X-ray

diffraction patterns of both InP and InP/ZnSe nanocrystals. They found a perfect match between bulk Zinc-blende and InP, where peaks observed at (111), (210) and (311) showed a perfect match. The X-Ray pattern of InP/ZnSe nanoparticles had peaks that were close to (111), (210) and (311) which they attributed to the development of the shell ZnSe. They believe also that the passivation of the core could have occurred with minor atomic reconstruction due to lattice mismatch between zinc-blende InP and Zinc-blende ZnSe. In the current study, we were able to determine the lattice fringe distance to be 0.164 nm. The value is quite comparable to that one observed by Kim *et. al.*<sup>92</sup> for the same material. The nanocrystal size was estimated using Debye Scherrer's formula shown in equation 4.1 below

$$L = \frac{K*\lambda}{\beta*\cos \theta_{\beta}} \dots\dots\dots\text{equation 4.1}$$

Where L - is the thickness of the crystalline (particle size), K - is a constant dependent of the crystallite shape,  $\lambda$  - x-ray wavelength,  $\beta$  - is full width at half maximum or integral breadth and  $\theta_{\beta}$  - is the Bragg's angle.

Three peaks were chosen from the X-ray pattern as shown in Figure 4.3. Only peaks with smooth and normal distribution were chosen for size calculation. The determined variables and the constants for Scherrer's formula are summarized in Table 4.1 below.

**Table 4.1: Summary of calculated Scherrer's constants obtained from XRD analysis**

Peak	2 Theta (Degrees)	Theta (Degrees)	Theta (Radians)	Lambda	FWM (Degrees)	FWHM (Degrees)	FWHM (Radians)	Size (nm)
Peak 1	19.60	9.80	0.17	0.154	3.50	1.75	0.0305	4.36
Peak 2	26.33	13.17	0.23	0.15	2.88	1.44	0.03	5.66
Peak 3	35.53	17.77	0.31	0.15	3.29	1.64	0.03	5.08
Average								5.03

The particle size was determined from each peak and the average value was calculated to obtain a fair approximation of the particles size. The calculated average size of the InP/ZnSe nanocrystals was determined to be 5.03 nm. The small particle size is evidenced by relatively broad peaks as seen in the X-ray pattern. The estimated particle size from XRD data is quite comparable to the estimated HRTEM images which were found to be 4.61 nm.

### 4.3 Optical properties of InP/ZnSe nanocrystals

#### 4.3.1 Monitoring core and shell development of InP/ZnSe nanocrystals using UV-Vis

The nucleation and growth of InP/ZnSe nanocrystals were monitored using UV-Vis during synthesis using aliquots. During development of the core (InP), two aliquots were taken 1 hour and 2 hours after injecting the precursor. In particular, it was of interest to monitor the formation of InP nanocrystals prior to injection of the shell precursors. Figure 4.4 shows UV-VIS spectra of two aliquots taken during the core development

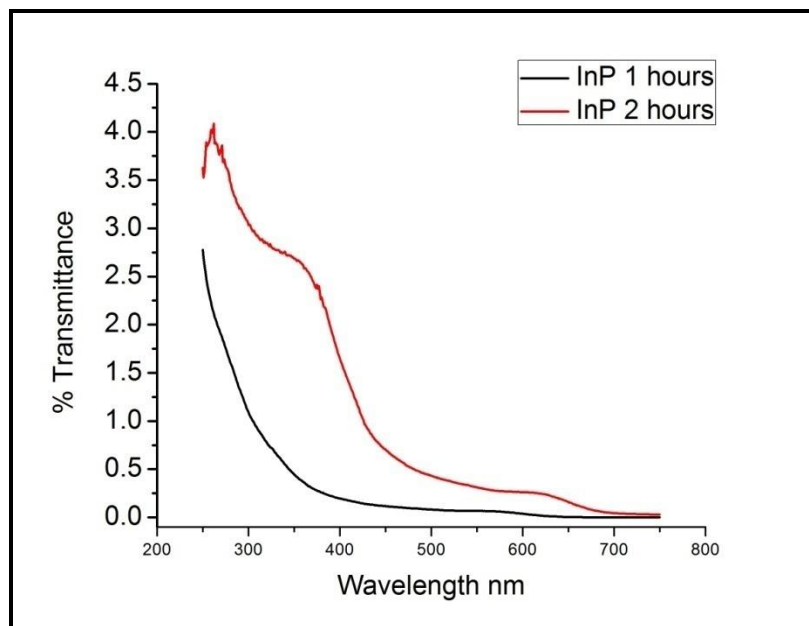


**Figure 4.4: Uv-vis for aliquots collected during growth of the core InP nanocrystals**

The Figure 4.4 clearly demonstrates that after one-hour injection of  $P(TMS)_3$ , no intermediate or few nanocrystals had been formed. However, it could be seen that during the first one hour of the synthesis, there were signs of nanocrystals development as witnessed by small and broad spectra observed at around 595 nm. At the end of the second hour, two peaks are observed in the spectra, the first at around 365 nm and the second at 617 nm. This observation is similar to the observation made by Gary *et. al.*<sup>166</sup> when they investigated the steps involved in the nucleation and growth of the InP nanocrystals. In their study, they established that there are no intermediates formed during the synthesis but instead the magic-sized clusters are formed followed by heterogeneous growth to the formation of InP quantum dots. During their synthesis, the InP at 160 °C using 1-octadecene as the solvent, they observed two absorption peaks at 386 nm and 520 nm.



They attributed the former peak to magic-sized clusters and latter peak at 520 nm to the development of InP nanocrystals.

Success in the formation of the core was followed by the development or deposition of the shell. The ZnSe shell was injected into a hot solution containing the core InP. A zinc precursor prepared from zinc undecylenate was injected into the solution at temperatures of 180 °C followed by a selenium precursor at the same temperatures. Two aliquots were taken during the development of the shell (ZnSe) and the UV spectra are shown in Figure 4.5.

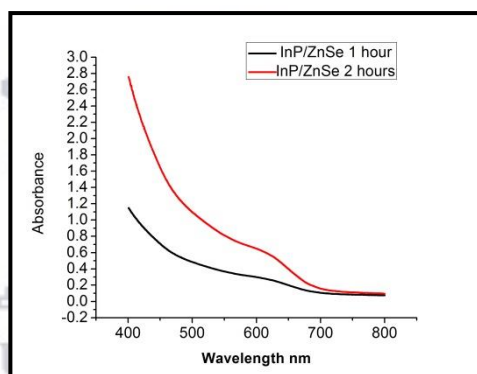


**Figure 4.5: UV-vis spectra of the InP/ZnSe aliquots taken after 1 hour and 2 hours during development of the ZnSe Shell**

Figure 4.5 shows the UV-Vis absorption spectra for the aliquots of InP/ZnSe taken after first and second hour during the development of the ZnSe shell. It can be seen that the shoulder for the product collected after 1 hour was quite small compared to the shoulder observed after two hours. The InP/ZnSe shoulder observed after 1 and 2 hours was only one which appeared at 620 nm and 627 nm, respectively. This was in contrast to the UV-Vis spectra observed 2 hours during the development of the core (InP). There was also

significant red shift after the injection development of the core from 617 nm for InP (formed after 2 hours) to 620 nm for InP/ZnSe (formed after 1 hour) and finally to 627 nm after two hours of shell development. Generally, during shell development there was a red shift, however, in all cases, the peak appeared broad. We discovered also that with an increase in a number of moles of the phosphorous most probably the UV-vis spectra could be slightly narrow, however, the resultant solution were intense dark brown. The resulting QDs could not be suitable for our studies hence, we maintained the In:P at 1:3 and below. Li *et. al.*<sup>84</sup> synthesized InP/ZnS via heating up technique in one pot synthesis and monitored the growth using UV-vis technique. They mixed all the precursors for In, P, Zn and S and quickly raised the temperatures to 300 °C. The Uv-vis of the aliquot taken 30 minutes after the start of the synthesis was weak and broad at around 430 nm, however, there was a huge red shift after 2 hours at the temperature of 300 °C. Park *et. al.*<sup>167</sup> used UV-vis to observe spectral changes when they coated InP core with Cd. They noted that the absorption peak red shifted from 540 nm to 580 nm, however, they could not explain the reason behind the red shift.

#### **4.4 PL characteristics of the aliquots obtained during synthesis of InP/ZnSe characteristics**

The growth of the quantum dots was also monitored by investigating the photoluminescence characteristics of the aliquots taken during the core and shell development. Mushonga *et. al.*<sup>93</sup> took two aliquots after 30 and 120 minutes during the growth of the InP core, they observed that there was no significant change in the emission wavelength. However, they noted that there was slight blue shift from 579 nm for InP (core) to 574 nm for the InP/ZnSe. The blue shift is to the contrary and is attributed to

photoluminescence of ZnSe shelled InP nanocrystals is contributed by defect emission in comparison to bare InP<sup>92</sup>. The normalized photoluminescence spectra for the four aliquots taken during synthesis is shown in figure 4.6 below

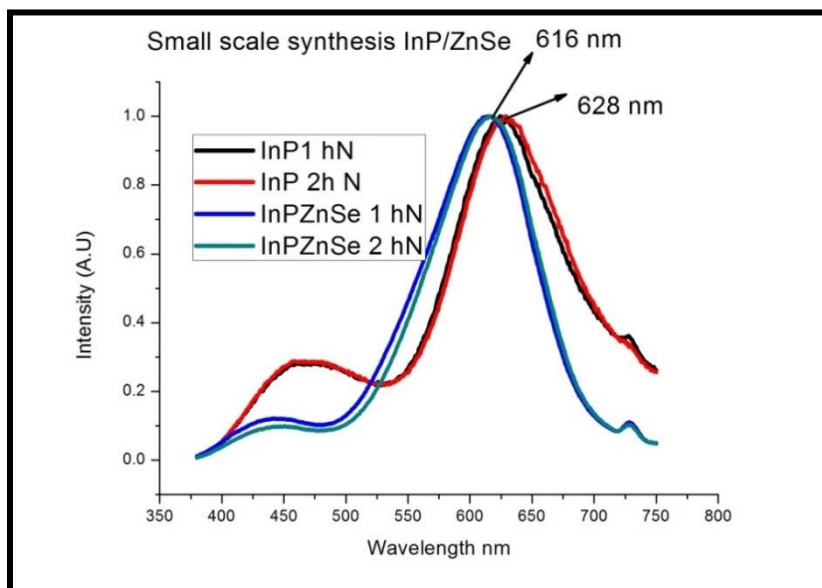


**Figure 4.6: The normalized photoluminescence spectra of the four aliquots taken during synthesis of InP/ZnSe nanocrystals**

Similar observation was made to that observed by Mushonga *et. al.*<sup>93</sup> though at a different emission wavelengths. The aliquots taken during development of the core had emission wavelength of 628 nm for both aliquots collected at the difference of one hour. The aliquots taken after 1 and 2 hours during core development had similar emission wavelength of 616 nm. The slight blue shift could be because of the defects explained above. The contrary was observed by Park *et. al.*<sup>167</sup> during the synthesis of InP coated separately with Cd and CdS. The emission peak of the InP core was 580 nm which increased to 627 nm for InPCd. It was not clear as to the cause of the red shift though speculated to be due to the passivation of the surface defect and doping into InP which

occurred upon addition of cadmium ions. They further noted that the quantum yield of InP increased from 1 % to 36 % for InPCd nanocrystals when 0.05 mmol was added. When 0.1 mmol of cadmium was added, the InP emission peak increased to 651 nm and gave a low quantum yield of 23 %. Further increase of amount of cadmium to 0.2 mmol caused a decrease of the quantum yield to 21%.

#### 4.5 Quantum yield calculations

When a fluorescing material absorbs a photon of light, an excited energetically state is formed. The fate of the excited species is varied depending on the nature or type of the material but the end result is deactivation from the excited state which is usually accompanied by loss of energy and hence the species falls back to the ground state. The deactivation process may occur through fluorescence (loss of energy by emission of a photon), internal conversion and vibrational relaxation and intersystem crossing and subsequent non-radiative deactivation. Fluorescence quantum yield can be defined therefore as the ratio between the photons absorbed to the number of the photon emitted through fluorescence. Quantum yield gives the chances at which excited species could be deactivated through fluorescence and not any other non-radiative mechanisms. To calculate the quantum yield of our sample, we adopted comparative method developed by William *et. al.*<sup>168</sup> which involves the use of well-characterized standards. The logic behind this technique is that standard and test samples with similar absorbance values excited at same wavelength is believed to be absorbing the same number of photons hence the simple ratio of their integrated fluorescence intensities could give the ratio of the quantum yield of the standard and the test sample. Since the quantum yield of the standard is known then the quantum yield of the sample can be calculated.

The quantum yield of the prepared InP/ZnSe was calculated using equation 4.2 below. The data was obtained from both UV-Vis measurements and the PL measurements. Rhodamine 6 G dissolved in absolute ethanol was used as the standard while the sample was dispersed in hexane. The parameters of the following equation were obtained from UV/Vis and PL measurements and used in the calculation of the quantum yield.

$$QY = QY_{std} \times \frac{I}{I_{std}} \times \frac{A_{std}}{A} \times \frac{n^2}{n_{std}^2} \dots\dots\dots\text{equation 4.2}$$

Where:- QY- Quantum yield,  $QY_{std}$ - Quantum yield of the standard, I- the Integral result of the area recorded, A- Absorbance, n- refractive index of the solvent

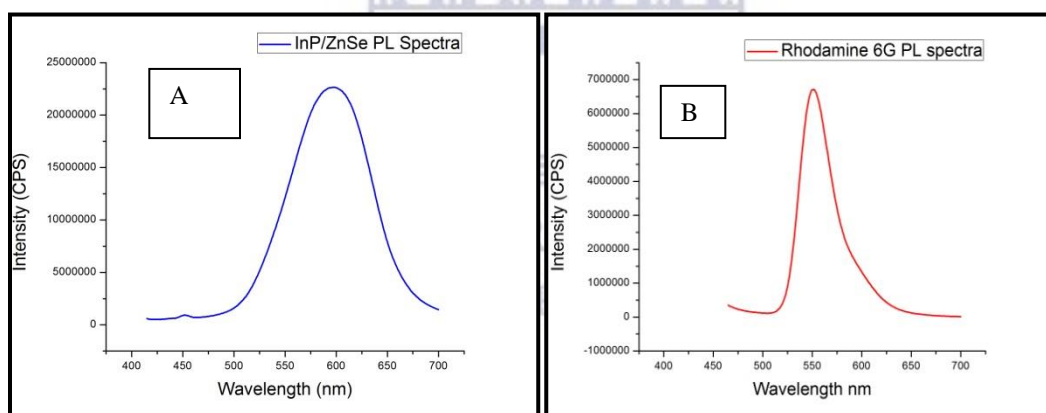


**Figure 4.7: (A) PL spectra's for InP/ZnSe sample dissolved in hexane and (B) rhodamine 6G standard dissolved in ethanol both spectra's were used for quantum yield calculations**

Equation 4.2 was used to calculate the quantum yield as follows:-

$$QY = 0.95 \times \left( \frac{36550}{3.11957} \right) \times \left( \frac{0.0478}{0.0391} \right) \times \left( \frac{1.3727}{1.36} \right)^2 = 13.68 \%$$

The quantum yield for InP/ZnSe was determined to be 13.68 %. The value was high compared to the value of the same product reported earlier<sup>93</sup>. The difference in the value of quantum yield was attributed to slight modification of synthetic procedure. It should be noted also that the quantum yield of the prepared material is higher compared to the quantum yield of InP/ZnS QDs reported by Xi *et. al.*<sup>169</sup> where quantum efficiency of 3-5% was reported. The low quantum yield of quantum dot material in III-V cannot afford to compete with quantum dots of groups II-VI due to broad emission profiles emanating from poor particle dispersibility which could be due to current synthetic methods<sup>165</sup>. In our own view, there is a need in future to optimize the synthetic procedures or come up with a totally new synthetic method for the group III-V quantum dots and a new source of phosphorous.

#### **4.6 Scale-up synthesis of InP/ZnSe nanocrystals**

The greatest challenge of quantum dots during synthesis is the ability to synthesize them in large quantities and at the same time retaining the same properties. Li and Reiss<sup>84</sup> view hot injection technique as a limitation to scaling up the synthesis of quantum dots. In their opinion scale up is only possible when heating up technique is employed. By relying also on tris(trimethylsilyl)phosphine as a source of phosphorous precursor for InP type of nanocrystals is also viewed as a limitation for up scale process<sup>83</sup>. As part of this study, we chose to scale up the synthesis of InP/ZnSe and compare the optical and electronic properties of the resulting quantum dots. In particular, the comparison was made with regard to emission wavelength, changes in band gap and fluorescence intensities to validate the investigation. All the properties of the scaled up product were compared to the properties synthesized InP/ZnSe nanocrystals using small volumes and masses of the

precursor reagents. In this study, we scaled up the synthesis with a factor of 2, 4 and 6. The sizes of the particles, the emission profiles, the fluorescence characteristics and absorption spectra of the resulting scaled up properties were compared. Similar to the previous literature reports, the core aliquots were taken in the first and second hour after the injection of  $P(TMS)_3$ . The third and fourth samples were taken after one and two hours after the injection of the shell comprising of zinc and selenium precursors. The PL characteristics of the aliquots were measured during the core and shell development. The normalized PL spectra for the four aliquots taken during synthesis and subsequent scale up are shown in Figure 4.8 below.



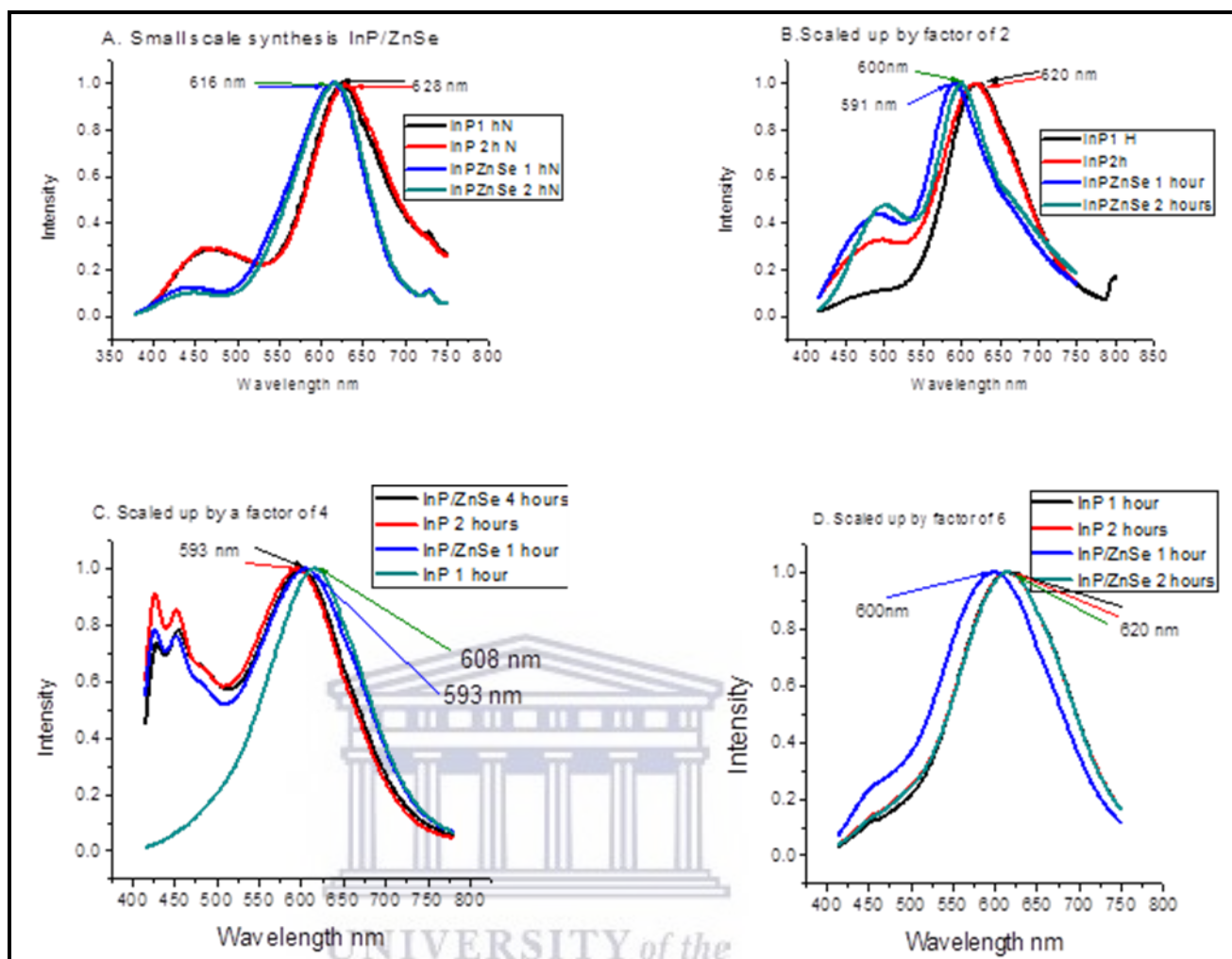


**Figure 4.8:** The normalized photoluminescence properties of InP/ZnSe nanocrystals for small scale (A), scaled up by factor of two (B), scaled up by factor of four (C) and scaled up by factor of six (D).

The maximum emission wavelength of the InP in the small scale synthesis of the QDs was observed at 628 nm for both aliquots collected at 1 and 2 hours during the synthesis procedure. A similar observation was made for the scaled up synthesis where the first two samples of InP gave emission wavelength of 620 nm. Upon deposition of ZnSe shell in both small and scaled up synthesis a slight blue shift was observed. The residual emission



peaks seen around 400 nm-450 nm could possibly be assigned to unreacted ZnSe nanocrystals<sup>170</sup>. Generally, there was no significant photo-spectral difference between the spectra of the synthesized particles using small scale of the InP/ZnSe nanocrystals and the scaled up synthesis. Mushonga *et. al.*<sup>93</sup> reported synthesis of InP/ZnSe where two aliquots were measured after 30 and 120 minutes during the growth of the InP core and observed no significant change in the emission wavelength. However, they noted that there was slight blue shift from 579 nm for InP (core) to 574 nm for the InP/ZnSe. They attributed the blue shift to the surface defects upon passivation of InP by the ZnSe. Contrary observation was made by Park *et. al.*<sup>167</sup> during the synthesis of InP coated separately with Cd and CdS to form InP/Cd and InP/CdS, respectively. However, the difference could have been brought about by the incorporation of Cd in the shell rather than the Zn. The emission peak of the InP core was 580 nm, which increased to 627 nm for the InP/Cd. The quantum yield of the InP increased from 1% to 36% for InP/Cd nanocrystals when 0.05mmol of Cd was added. When the amount of the reactant was increased to 0.1mmol the emission peak increased to 651 nm with a quantum yield of 23 %. Further increase of Cd to 0.2 mmol shifted the emission peak to 751 nm but the quantum yield decreased to 21 %. The increase in quantum yield was attributed to the surface passivation of Cd ions. However, the authors could not explain the cause of the observed red shift but postulated that it could have been due to the surface defect and doping into InP which occurred during the addition of the Cd precursor. In another study, Li *et. al.*<sup>83</sup> scaled up synthesis of InP/ZnS using the PH<sub>3</sub> as a source of phosphorous which was generated *in situ* through the reaction of Ca<sub>3</sub>P<sub>2</sub> and hydrochloric acid. They reported a highly crystalline InP/ZnS nanocrystal with cubic zinc blende structure with an average size ranging from 3-6.4 nm.

They also demonstrated that by varying the molar ratios of the reactants and their reacting flow rates, higher emission wavelength between 650-720 nm is achieved. They attributed the observed small emission peaks beyond 730 to 820 nm to partial slight oxidation of the samples, which occurred before complete growth. They also reported that the quantum yield of the InP varied from 8-22% while the quantum yield of InP/ZnS was 20 %, which is sufficient for opto-electronic and biological labelling.

To compare the physical properties, we carried out HRTEM analysis for the QDs synthesized by small scale and scaled up technique. Representative HRTEM images for small scale and scaled up (by a factor of 2) are presented in figure 4.9 below.

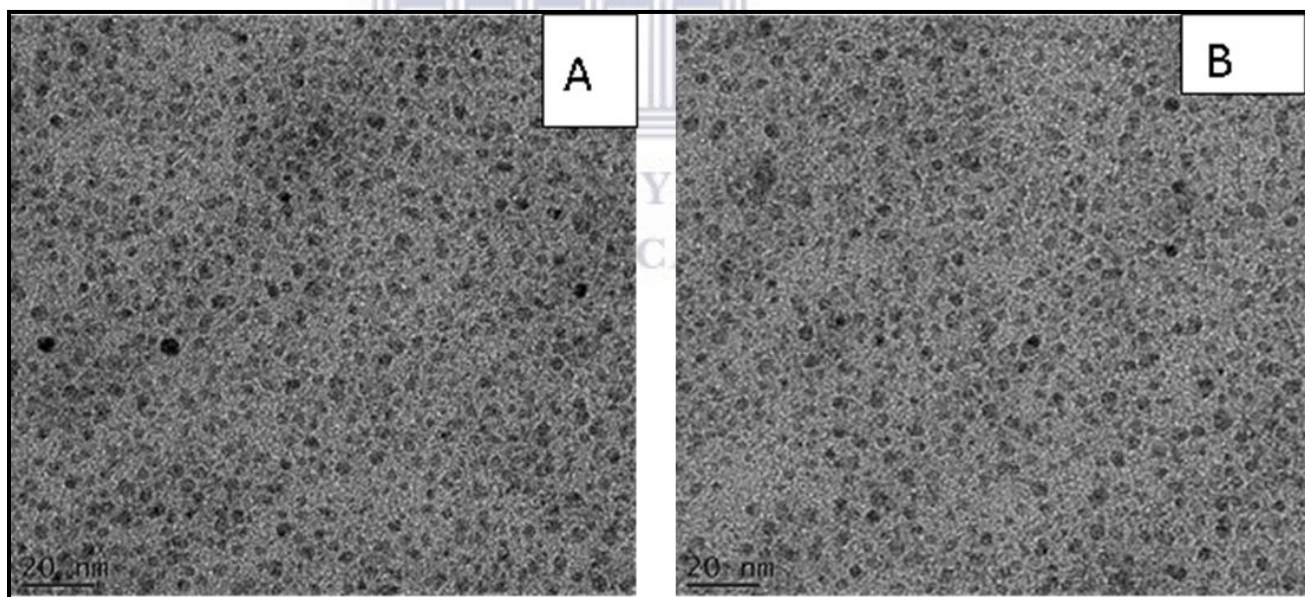


**Figure 4.9: HRTEM micrograph for InP/ZnSe nanocrystals synthesized in small scale(A) the HRTEM micrograph images for InP/ZnSe nanocrystals obtained in up scaling by a factor of two(B)**

The HRTEM micrographs figure 4.9 demonstrate that the synthesized InP/ZnSe nanocrystals both in small and scaled up are monodisperse and spherical. The HRTEM images, together with the ImageJ software<sup>171</sup> were used to estimate the sizes of the synthesized nanocrystals. The sizes of the particles were comparable as shown in the representative histograms shown for small scale synthesis figure 4.10 A and the scaled up synthesis by a factor of 2 figure 4.10 B, producing particles with an average size of 4.18 nm and 4.31 nm, respectively. The scaled up by a factor of 4 and 6 yielded nanocrystals with sizes of 4.13 nm and 4.37 nm, respectively

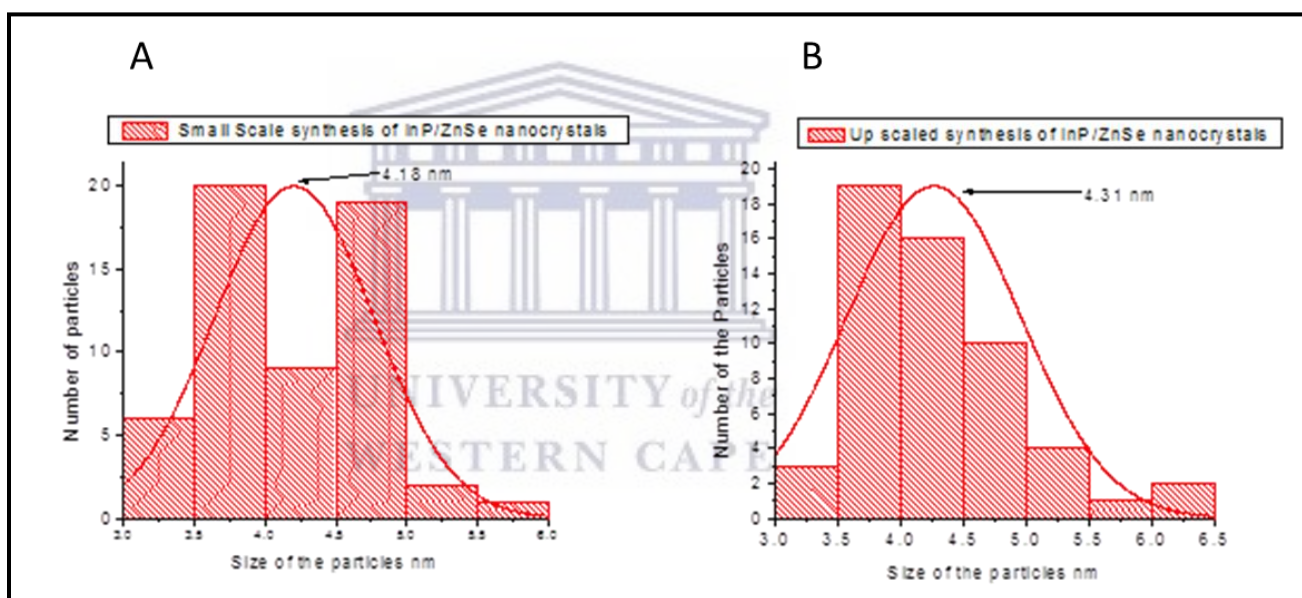


**Figure 4.10: Histogram showing size distribution of InP/ZnSe nanocrystals obtained in small scale synthesis (A) and scaled up synthesis (B).**

The absorption spectra of the resulting products of the scaled up experiments were obtained using UV/Vis spectrophotometer. The aliquots were taken during the

development of the InP core and the ZnSe shell. The representative UV/Vis spectra for the small and scaled up synthesis are presented in Figure 4.11.

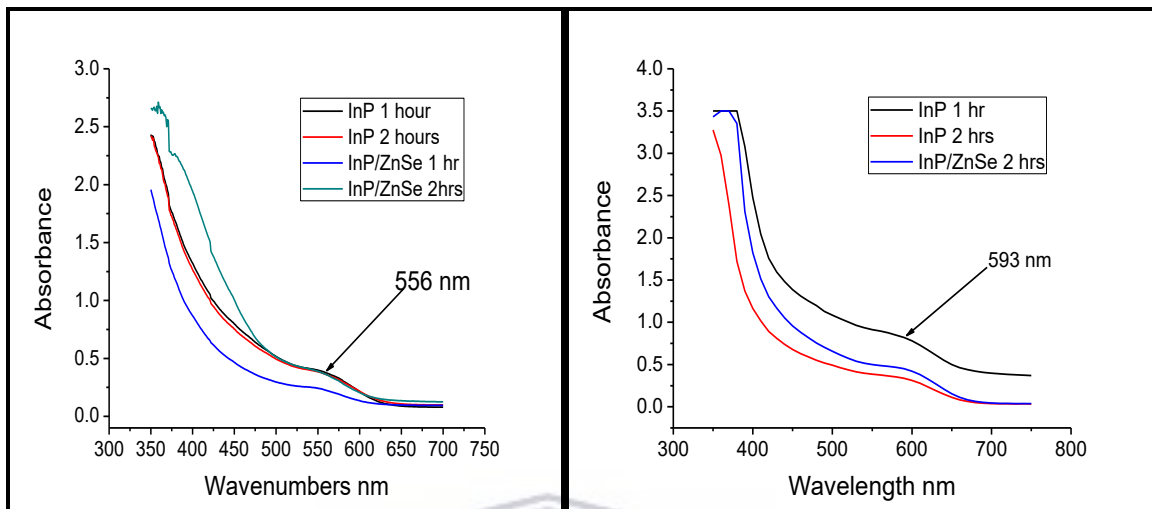


**Figure 4.11:** The UV/Vis spectra of the aliquots taken during synthesis of InP/ZnSe nanocrystals in small scale (A) UV/Vis spectra for the aliquots of InP/ZnSe nanocrystals in scaled up by a factor of two (B)

All aliquots for the small scale synthesis of the nanocrystals showed an absorption characteristic peak at around 556 nm. The aliquots for the scaled up synthesis of the nanocrystals showed absorption peak at around 593 nm. It was observed that in both levels of synthesis there was a slight red shift after the introduction of the ZnSe shell. The shift in the position of the absorption peak upon up scaling of the synthesis is expected due to the difficulty in controlling shell growth during nucleation process<sup>165</sup>. The absorption spectra in all cases were within the visible region of the radiation spectrum suggesting that the nanocrystals prepared are suitable for biological application such as *in vivo* imaging.

#### 4.7 Fluorescing intensities of InP/ZnSe nanocrystals

The intended biological imaging application is dependent on the fluorescence of the synthesized quantum dots. The trend in fluorescence was monitored for both small scale and scaled up synthesis of the InP/ZnSe nanocrystals. Again, the fluorescence of the aliquots for both levels of synthesis is shown in Figure 4.12 below.

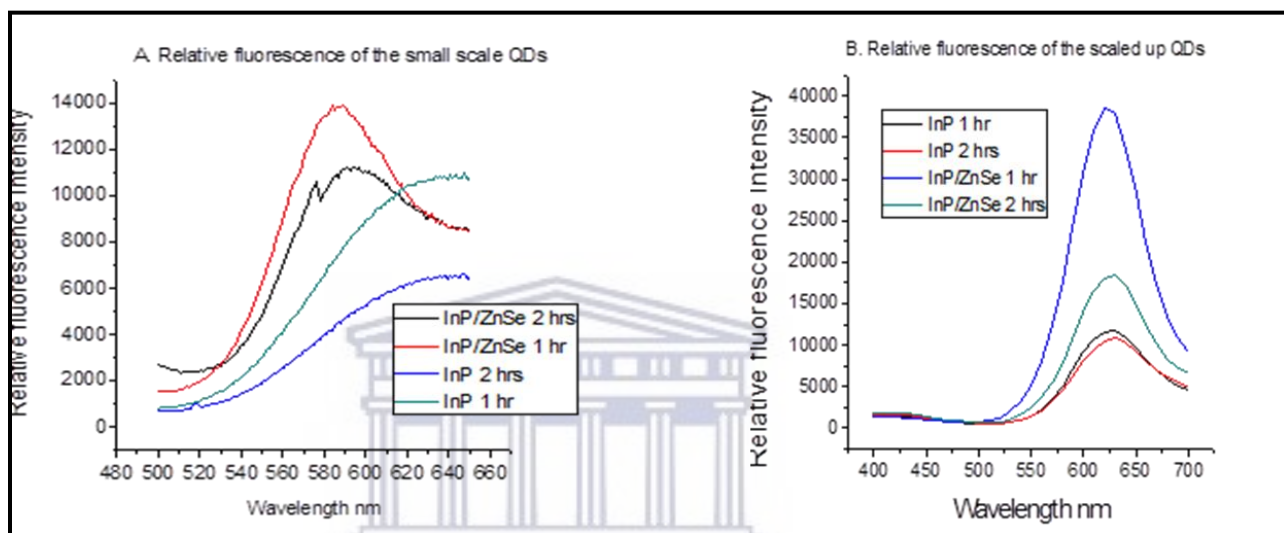


**Figure 4.12: The fluorescence intensities for aliquots of InP/ZnSe nanocrystals synthesized in small (A) and scaled up by a factor of 2 (B)**

It is the fluorescent properties of QDs that make these nanoparticles so useful for applications in biological imaging. In this study, we compared the fluorescence intensity of all the aliquots collected during the synthesis in order to establish the trend of fluorescence as well as the significance of coating with the inorganic shell. The first observation was that the trends of the fluorescence for the four samples collected during the small scale and the scaled up synthesis were similar. The product achieved within the first one hour of core (InP) development showed higher fluorescence emission compared to the product collected in the second hour. Interestingly upon injection of zinc and

selenium precursor, there was a significant increase in fluorescence emission. However, when the shell was allowed to develop for one hour, the fluorescence of the product was higher compared to the product collected after the second hour. Despite this observation, we are not sure of the stability of the product, which has the highest fluorescence. Future studies could investigate the stability of the product developed within one hour of the core development (InP) and the product obtained one hour into development of InP/ZnSe nanocrystals. If these products prove to be stable then a great milestone will have been achieved in synthesis of InP/ZnSe QDs since it will have reduced the duration of the synthesis significantly.

#### **4.8 Band gap calculations**

The determination of band gap for the synthesized semiconductor was essential to obtain the basic solid state physics. Band gap indicates the difference in energy of an electron occupying the highest allowed orbitals in the valence shell and the lowest orbitals in the conduction band usually measured in electron volt (eV). It is related to the electric conductivity of the materials. Generally, metals have no band gap, insulators have very wide band gap and the semiconductors have band gap value which is intermediate between band gap energy of metals and insulators. Tauc's plot which is obtained from diffuse reflectance spectra is often used to calculate the band gap. The data used in this study was generated by measuring the percentage reflectance at the range of wavelength from 330-700nm.

The Kubelka- Munk equation<sup>172</sup> was used to calculate the band gap of the as-prepared materials using a diffuse reflectance spectrum as follows;

$$F(R_{\infty}) = \frac{(1-R/100)^2}{2(R/100)} = \frac{K}{S} \dots \dots \dots \text{Equation 4.3}$$

Where  $R_{\infty} = \frac{R_{\text{sample}}}{R_{\text{reference}}}$ , K is absorption coefficient and S is scattering coefficient

On the other hand, the band gap  $E_g$ , and absorption coefficient  $\alpha$  of indirect band gap semiconductor are related through the well-known Tauc's relation

$$\alpha h\nu = C_1 (h\nu - E_g)^2 \dots \dots \dots \text{Equation 4.4}$$

Where  $h\nu$  is the photon energy and  $C_1$  is proportionality constant. When the material scatters in a perfect manner, the absorption coefficient K becomes equal to  $2\alpha$  ( $K=2\alpha$ ). Considering the scattering coefficient S as a constant with respect to wavelength, and using equations 4.3 and 4.4, the following expression can be written:

$$[F(R_{\infty}) * h\nu]^2 = C_2 (h\nu - E_g) \text{ or } (K * h\nu)^2 = C_2 (h\nu - E_g) \dots \dots \dots \text{Equation 4.5}$$

By plotting  $[K * h\nu]^2$  against  $h\nu$  and fit the linear region with a tangent and extend it to the energy axis (X-axis) as shown in Figure 4.13 below, then one can easily obtain  $E_g$  by extrapolating the linear regions to  $[K * h\nu]^2 = 0$ .

During synthesis, the core InP was allowed to grow for two hours and also the shell ZnSe to grow for another two hours. The trend in changes of the band was monitored during the development of the core as well as during the growth and during the shell growth at the surface of the core as shown in Figure 4.13.

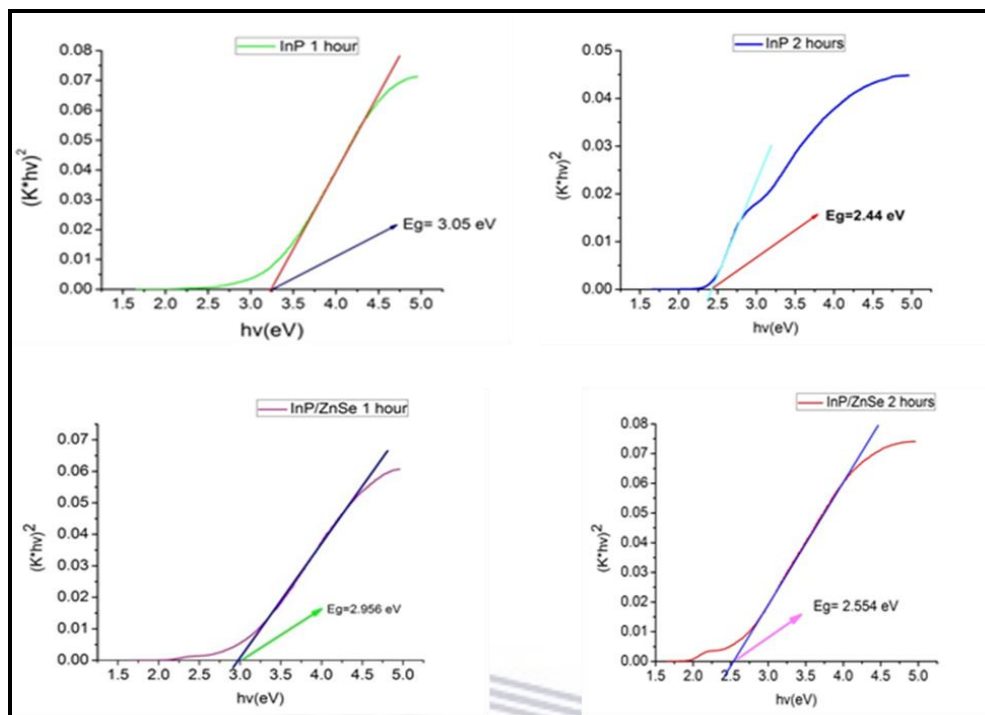


**Figure 4.13: The band gaps of the aliquots obtained during growth of core/shell of the InP/ZnSe nanocrystals**

The band of the material gave on varying throughout the synthetic process. The band gap of the InP for the core was 3.05 eV after the first hour and reduced as the nucleation process extended. There was an increase in the band gap when the shell was introduced, however, when the shell was given more time to grow, the band gap of the material reduced to 2.55 eV. The band gap was quite comparable to that of the InP/ZnSe nanocrystals obtained after purification steps. The crude product InP/ZnSe nanocrystals (product immediately after synthesis) were purified by centrifugation to remove unreacted products, precipitation using acetone followed by re-dispersion in hexane. The band gap of the purified nanocrystals was determined using Tauc's plot as shown in Figure 4.14 below.



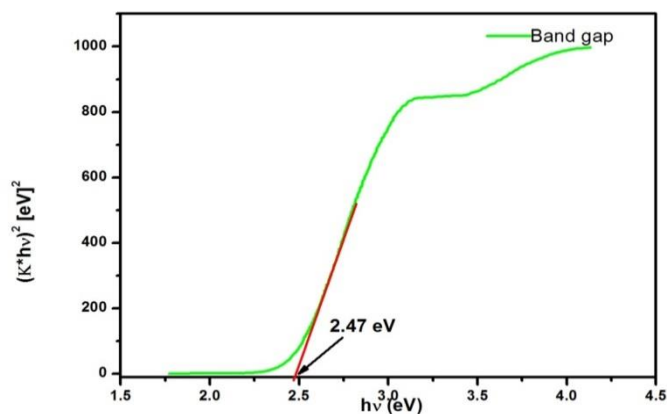


**Figure 4.14: The band gap of the purified InP/ZnSe nanocrystals**

The tangent was extrapolated to cut the x-axis and the band gap was determined to be 2.47 eV. The value falls within the theoretical range of semiconductors which is between 0 and 3.5 eV. It indicates also that there was successful coating process since the band gap increased from 1.35 eV reported for InP<sup>173</sup>. The band gap value of 2.47 is quite comparable to 2.06, 2.26 and 2.43 eV that was obtained by Byun *et. al.*<sup>174</sup> during solvothermal of InP/ZnS.

#### **4.9 Size sorting**

The synthesized InP/ZnSe nanocrystals were subjected to size sorting process to afford nanocrystals of almost similar size and also narrow emission spectra. Fractions of different sizes of nanocrystals were collected by precipitation using acetone. Subsequent fractions were recovered by separating the pellet by centrifugation and subjecting the supernatant to more precipitation. The process was repeated until the last supernatant was clear (contains no more nanocrystals). The photoluminescence nanolog was used to characterize fractions

that were collected. Emission peak and FWHM were the chosen parameters to compare the characteristics of the collected fractions and also to evaluate the relevance of size sorting process. Figure 4.15 presents the photoluminescence spectra of the three fractions that were obtained during size sorting process.

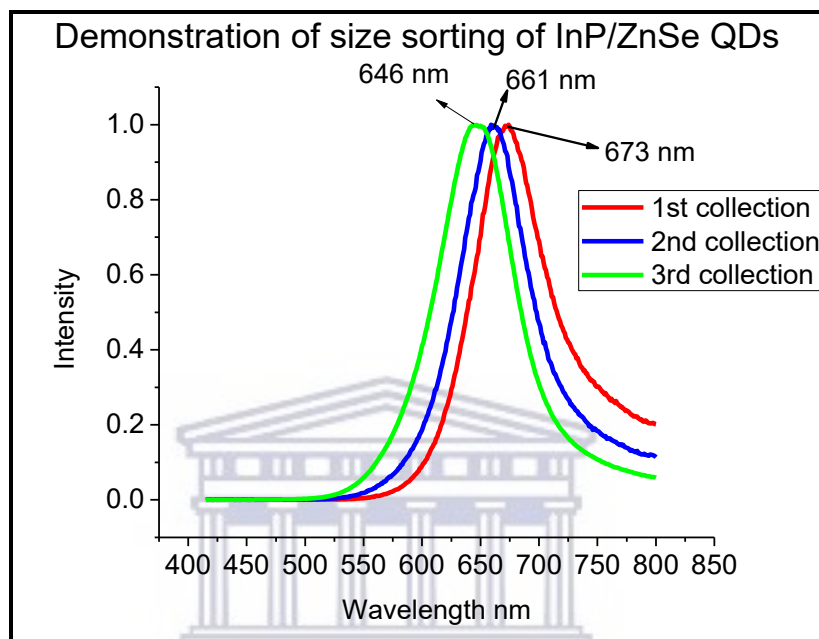


**Figure 4.15: The normalized photoluminescence spectra for different fractions of nanocrystals obtained during size sorting process**

Three fractions were obtained during the size sorting process. The first fraction which is expected to constitute large sized nanocrystals had a higher emission wavelength of 673 nm, the second fraction demonstrated some slight blue shift with an emission wavelength of 661 nm and the last fraction had an emission wavelength of 646 nm which underwent slight blue shift in comparison to the first and second fractions. During precipitation, it is expected that large nanocrystals are precipitated out first and small sizes are precipitated out last<sup>174</sup>. Byun *et. al.*<sup>174</sup> synthesized InP/ZnS nanocrystals and subjected them to size

sorting process using the incremental amount of methanol. They were able to collect 14 fractions and they made several deductions using a UV-Visible spectrophotometer, HRTEM, and PL analysis. The first deduction was that the first fraction had an excitonic absorption peak of 622 nm and the excitonic absorption peak of the subsequent peaks went down till 497 nm for the last fraction. Their HRTEM analyses revealed also that the sizes of the nanocrystals decreased from the first fraction to the last fraction, for instance, the fraction number 2, 6 and 10 had sizes of 3.3 nm, 2.8 nm, and 2.3 nm, respectively. The negative observation from their study is that the PL intensities of several fractions they collected was very low and could be due to defective QD surface. Similar size sorting process was subjected to InP nanocrystals in a separate study by Byun *et. al.*<sup>91</sup>. They synthesized bare InP nanocrystals through the solvothermal process and subjected the product to size sorting where they obtained 16 fractions. They observed a blue shift from 617 nm for the first fraction down to 473 nm for the last fraction. They noted also that the sizes of the particles decreased sequentially, for instance, fraction number 2 and 10 had sizes of 3.2 nm and 2.3 nm, respectively as estimated from HRTEM micrographs. Lastly, they noted that for fractions 1-6 the quantum yield increased from 5.3 all the way to 12.5 %.

#### **4.10 Ligand exchange process**

Luminescent quantum dots can only suit biomedicine when the nanocrystals are compatible with the aqueous media<sup>175</sup>. Quantum dots can be made water soluble by introducing bifunctional hydrophilic capping ligands through ligand exchange reactions. Solubilization of quantum dots allows further functionalization by conjugation to a

number of biological molecules. Generally, there are three modes of attaching the biomolecules to the surface of the QDs namely covalent attachment, direct and non-covalent electrostatic attachments<sup>176</sup>. The water-soluble quantum dots were prepared by carrying out ligand exchange process. The ligand exchange process involves phase transfer of the hydrophobic ligand at the surface of the nanocrystal and replacing it with the hydrophilic ligand. The palmitic acid layer which was used during the growth of the nanocrystals contributed to hydrophobicity nature of the QDs hence need for ligand exchange. Successful ligand exchange was carried out by adopting procedure developed by Brunetti *et. al.*<sup>95</sup> with some modifications. In this study, 3-mercaptopropionic acid was chosen. The MPA ligand provides a thiol group for anchoring the ligand to the nanocrystal surface<sup>177</sup> and terminal carboxyl group provides functionality for both hydrophilicity and allowance for bioconjugation to other biomolecules<sup>178,179</sup>. Figure 4.16 shows how the red-brown quantum dots suspended in organic solvent were successfully transferred to the aqueous layer after the ligand exchange process.

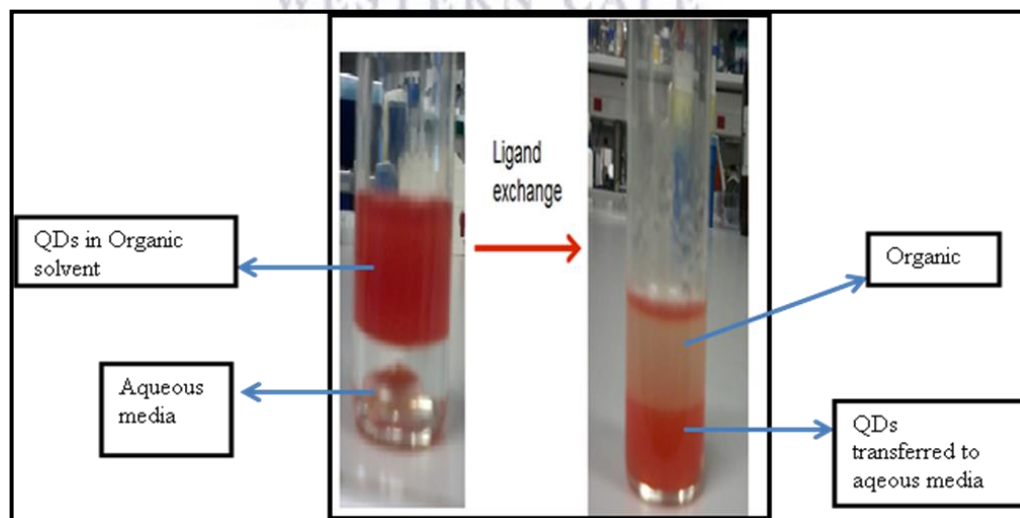


**Figure 4.16: Diagram showing effective transfer of quantum dots from the organic layer to aqueous layer**

The diagram clearly shows success in transfer of the quantum dots from the organic solvent (toluene) to the aqueous layer borate buffer. The idea of ligand exchange was to make the QDs water soluble to enhance its compatibility for biological applications and also to allow easy coupling with the iron oxide nanoparticles which had been prepared and dispersed in water. The as-prepared water soluble quantum dots were further characterized by investigating its optical properties. The first optical property investigated was photoluminescence characteristic of the water soluble QD to determine the retained fluorescence. The emission spectra of the water-soluble quantum dots were measured and two unique observations were made after the ligand exchange and coupling process as follows: 1) the resulting photoluminescence curve was rugged and 2) significant red shift was observed compared to the hydrophobic QDs. The two observations were sufficient evidence for successful ligand exchange process and also an indication of a success in the formation of the  $\alpha\text{-Fe}_2\text{O}_3\text{-InP/ZnSe}$  nanocomposite. Figure 4.17 below shows photoluminescence spectrum of water soluble InP/ZnSe QDs.

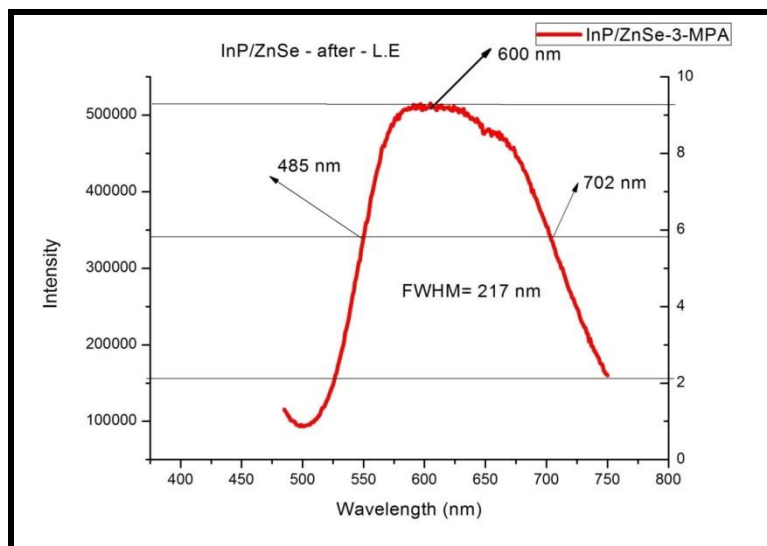


**Figure 4.17: PL spectra of the InP/ZnSe nanocrystals after the ligand exchange process**

The drop in fluorescence intensity could be attributed to the solvent change and changes in electronic density on the surface of the QD due to the immobilization of the 3-mercaptopropionic acid<sup>121</sup>. To ascertain whether we successfully introduced 3-mercaptopropionic acid to the surface of the quantum dots during the ligand exchange process the FTIR experiment was done. The 3-mercaptopropionic acid has two thiol functional groups and two carboxyl groups. During the ligand exchange process, one of the two functional groups is expected to be implanted to the surface of the quantum dots and the other is suspended in water making it water soluble. So the FTIR is expected to show presence or disappearance of carboxyl (C=O and O-H) usually around  $1700\text{ cm}^{-1}$  or the thiol (-SH) above  $2500\text{ cm}^{-1}$  depending on the functional group anchored to surface of the QD. Figure 4.18 shows the FTIR spectra for the water soluble InP/ZnSe QDs.

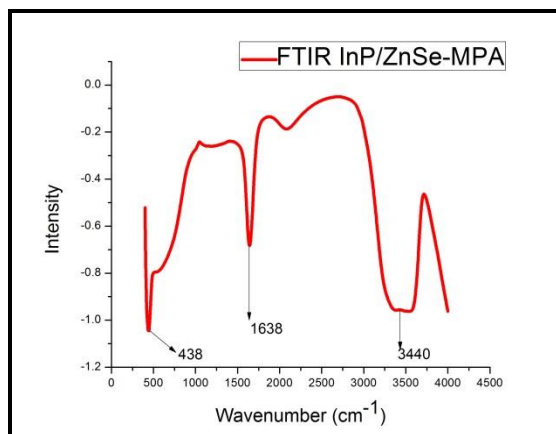


**Figure 4.18: The FTIR spectra of 3-Mercaptopropionic capped InP/ZnSe nanocrystals**

The 3-mercaptopropionic acid has two thiol functional groups and carboxyl, during ligand exchange process one of the two functional groups is implanted on the surface of the QDs and the other is suspended in water making it water soluble. The FTIR spectra (figure 4.18) show three distinct picks. The peak appearing at  $1638\text{ cm}^{-1}$  could be associated with  $\text{COO}^-$  vibrations, the peak at  $3440\text{ cm}^{-1}$  could be associated with the stretching of OH group and the peak at  $438\text{ cm}^{-1}$  could be associated with In-P, P-Zn or Zn-Se bond. Similar observations were made by Sukanya and Sagayaraj (2015) when they synthesized CdSe and CdSe/ZnS nanocrystals and capped them with 3-mercaptopropionic acid<sup>180</sup>.

#### 4.11 Streptavidin Conjugation

Streptavidin was chosen as an appropriate candidate for conjugation to the quantum dots since it is known to have high binding affinity for biotin. Success in the conjugation of the streptavidin to the quantum dots could allow easy conjugation of biomolecule through biotin. Streptavidin is known to have extraordinary high-affinity to biotin through noncovalent interaction with dissociation constant on the order of  $\approx 10^{-14}$ . To evaluate the

success of the introduction of streptavidin, we carried out UV/vis measurement (Figure 4.19)

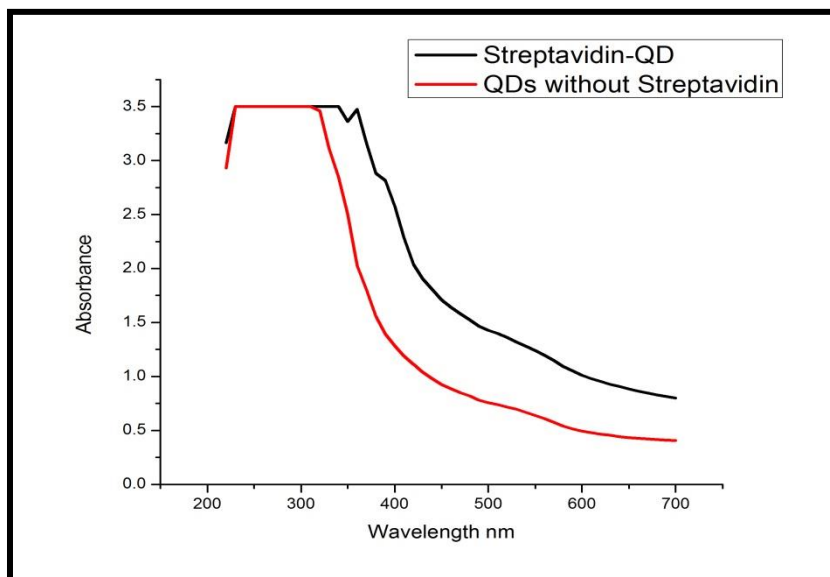


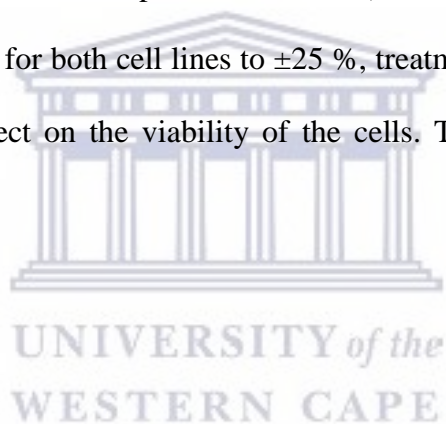
**Figure 4.19: UV-VIS spectra confirming success in introduction of streptavidin**

The absorption of the QDs with and without streptavidin is expected to be different. When streptavidin encapsulates the QDs, the absorption is expected to increase because the size of the resulting particles is bigger compared to the size of the bare QDs. The expectation is quite evident in the UV/Vis spectra shown in figure 4.19 above. This observation is supported by earlier evidence where the nanoparticles with streptavidin settle at the bottom of the Eppendorf tube, unlike the QDs without the streptavidin. However, due to compromised fluorescence properties of the water soluble InP/ZnSe QDs, its biological applications was limited hence we could not continue with it. We therefore called for future optimization to enhance its properties by continuing with the gains made during this study.



#### 4.12 Cytotoxicity of InP/ZnSe nanocrystals

Indium based quantum dots has been perceived to be less toxic compared to the dominant cadmium-based quantum dots. Many studies have been focused on the toxicity of InP/ZnS. In this study, we present for the first time the comprehensive study on the cytotoxicity of InP/ZnSe through *In vitro* test. To evaluate cytotoxic effects of the water-soluble InP/ZnSe nanocrystals, we exposed human cell cultures for 24 hours to increasing concentrations (0.1 to 5nM) of the nanocrystals and assessed the viability of the cells using the MTT assay. While the positive control (cells treated with 50uM ceramide) reduced the cell viability for both cell lines to  $\pm 25\%$ , treatments with the nanocrystals did have any significant effect on the viability of the cells. The results are summarized in Figure 4.20.



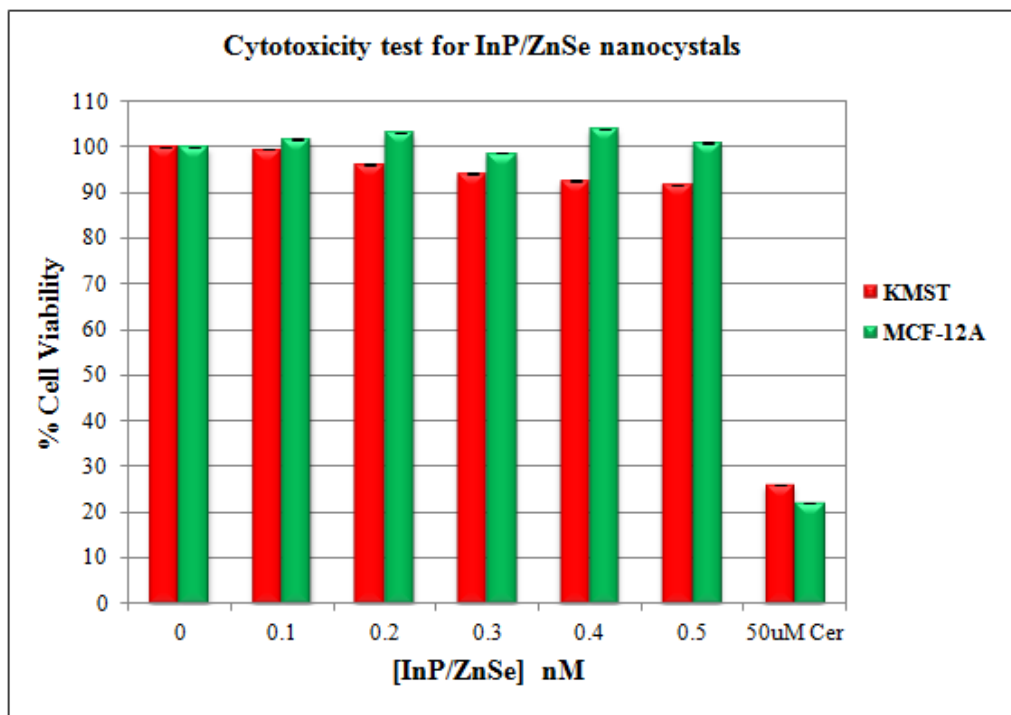


**Figure 4.20: Cytotoxicity studies of InP/ZnSe nanocrystals using MCF-12A and KMST 6 cell lines**

UNIVERSITY of the  
WESTERN CAPE

Figure 4.20 shows that the viability of MCF-12A cells was comparable to that of the untreated control and there was no significant difference (p-value = 0.07519). There was a moderate decrease in the viability of KMST-6 cells in response to the nanocrystals, which appeared to be concentration dependent, but this reduction in viability is not statistically significant (p-value = 0.1647 ). This suggested that the synthesized InP/ZnSe quantum dots are not toxic to KMST-6 and MCF-12A cells at the tested concentrations and exposure time. This could possibly also mean that these InP/ZnSe nanocrystals are safe for other biological applications and could be an alternative to Cd based quantum dots. Brunetti *et. al.*<sup>95</sup> carried out *in vitro* cytotoxicity studies to compare the toxicity of

InP/ZnS and CdSe/ZnS. In their study, they exposed neural cell line SH SY5Y and epithelial cell line A549 to various concentrations of the nanocrystals ranging from 1pM to 5nM. The viability of cells they treated with the CdSe/ZnS QDs was reduced by 27 % within 24 hours of exposure and to 46 % after 48 hours. They recorded less loss in cell viability of 33 % for the highest concentration of CdSe/ZnS when exposed to epithelial cell line A549. In contrast, the reduction of cell viability upon exposure of InP/ZnS to both cell lines was less than 10 % after 24 hours. The findings of this study show that the toxicity of InP/ZnS is comparable to that of InP/ZnSe. Since Brunetti *et. al.*<sup>95</sup> concluded that InP/ZnS are safer alternatives of CdSe/ZnS, we equally conclude that InP/ZnSe is much safe compared to Cd based quantum dots.

#### 4.13 Application of quantum dots in Molecular beacons design

Conventionally organic fluorophore is used in the design of molecular beacons. However, inorganic quantum dots have been seen to be more advantageous and could easily substitute organic fluorophores in the design of MBs. Inorganic nanocrystals are considered to be photostable compared to organic fluorophores which are easily photo-degraded. InP/ZnSe nanocrystals that we synthesized suffered the challenge of low quantum efficiency of 13 % before ligand exchange and reduced farther after ligand exchange. We therefore synthesized CdTe/ZnS and applied them in the synthesis of MB for the purpose of biomarker detection. Despite criticism of toxicity of Cd-based quantum dots, this was not a factor in our choice since the application of molecular beacons is done *in vitro*. We synthesized the 3-mercaptopropionic capped CdTe/ZnS QDs adopted from

Yuan *et. al.*<sup>143</sup>. Various techniques were adopted to establish the physical and optical properties of the synthesized quantum dots. The shape and particle size distribution of the nanocrystals were determined using HRTEM (model-TECNAI F30ST). The quantum dots obtained in this study were spherical, monodisperse and highly crystalline (Figure 4.21).

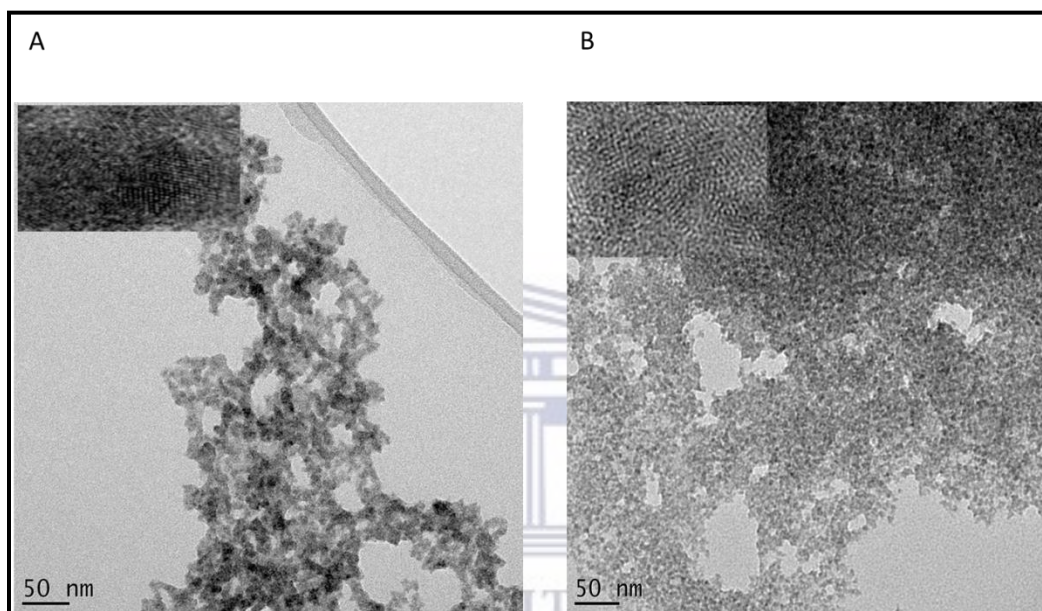


**Figure 4.21: HRTEM micrographs of CdTe/ZnS quantum dots (A) Streptavidin modified CdTe/ZnS quantum dots**

The HRTEM micrographs together with ImageJ software were used to estimate the average sizes of the synthesized QDs. The sizes of both bare and streptavidin modified QDs were determined to be approximately  $6.11 \pm 0.68$  nm. Melvin nanosizer was used to confirm the hydrodynamic sizes and the charge of the 3-MPA capped CdTe/ZnS and the streptavidin modified nanoparticles (Figure 4.22)

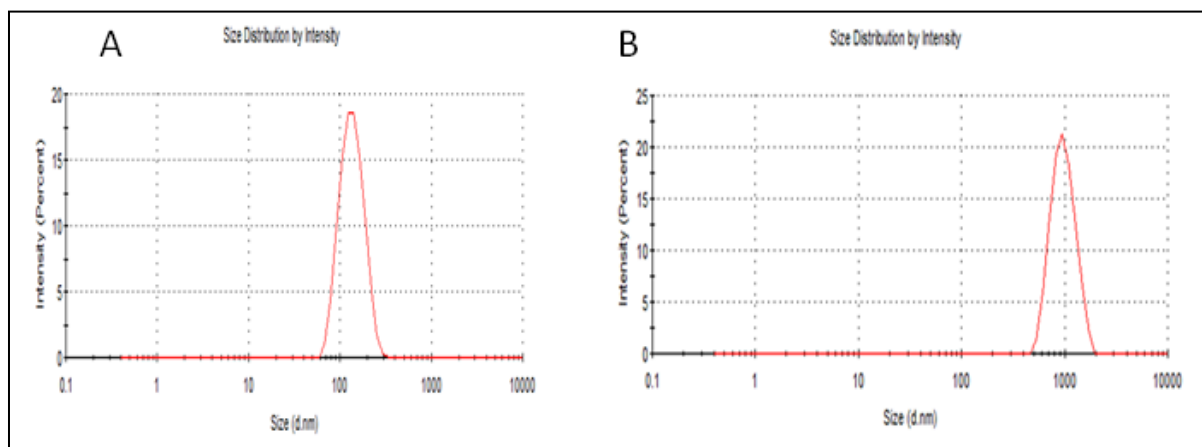


**Figure 4.22: The determined hydrodynamic sizes of the 3-MPA capped CdTe/ZnS (A) and streptavidin modified CdTe/ZnS (B)**

The hydrodynamic sizes of the 3-MPA-capped were determined to be 124.3 nm with a polydispersity index (PDI) of 0.197 (Figure 4.22 A) and that one of the S.A modified quantum dots was found to be 955.4 nm with PDI of 0.163 (Figure 4.22 B). The change in hydrodynamic size was expected to increase due to the presence of large streptavidin biomolecule. Adegoke *et. al.*<sup>48</sup> got also a surprisingly large size of 47.3 nm for CdZnSeTeS QDs when measured using DLS compared to 9 nm obtained from TEM analysis. The huge difference was attributed to the fact that the QDs was surrounded by scattering solvent molecules and the surface capped ligand causing the hydrodynamic size to be extremely high. In contrast, Cady *et. al.*<sup>39</sup> purchased quantum dots (Qdot ITK carboxyl) and modified its surface with streptavidin, they reported the sizes to have increased to  $15.7 \pm 3.7$  nm for streptavidin modified QDs from  $7 \pm 2.2$  nm of carboxylated

QDs. Their size measurement was conducted using Malvern instrument (Worch-estershire, UK) Zetasizer Nano ZS. The presence of streptavidin at the surface of the QDs brought also about changes in the zeta potential. The overall charge of the MPA-capped QDs was measured to be -22.0833 mV and that for the streptavidin modified QDs were determined to be -13.52 mV. We postulated that the increase in the charge was attributed to the fact that streptavidin is neutrally charged while the 3-MPA capped QDs were negatively charged hence increasing the overall charge of the carboxylated QDs. The charge of streptavidin has been reported by Almonte *et. al.*<sup>181</sup>. They established the charge of streptavidin to be neutral whereas the charge of the avidin to be positively charged. They used atomic force microscopy to study the charge of the two molecules.

The optical activity of the synthesized quantum dots was investigated using a UV-Visible spectrophotometer. The UV-vis spectrum was used to determine the approximate excitation wavelength of the synthesized material (Figure 4.23 A). The success in the incorporation of carboxylate functional groups through functionalization of CdTe/ZnS QDs was confirmed by carrying out FTIR analysis (Figure 4.23 B).

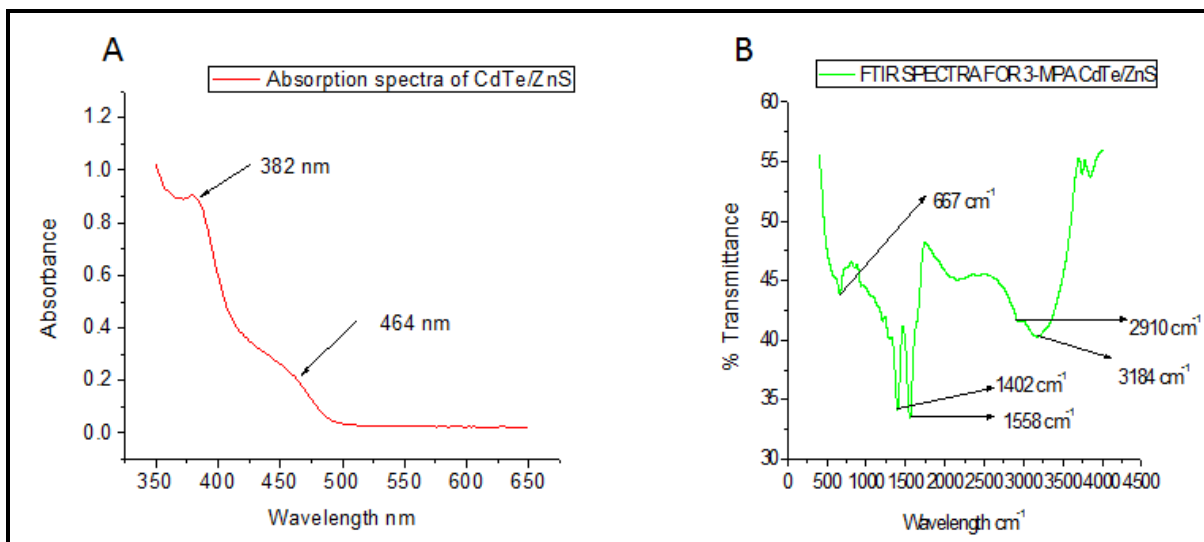
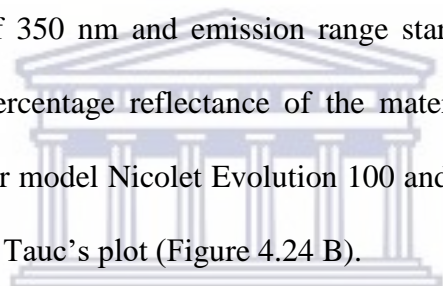


**Figure 4.23: Absorption (A) and FTIR (B) spectra for CdTe/ZnS quantum dots**

The absorption spectrum shows two characteristic peaks. The peak observed at 382 nm could possibly be attributed to residual ZnS while the peak at around 464 nm could be due to CdTe/ZnS nanocrystals. UV-vis findings prompted the establishment of the appropriate excitation wavelength between 350 to 500 nm for our material. The FTIR spectrum clearly depicts success in the introduction of 3-MPA to the surface of the QDs. The peaks are seen at 1558  $\text{cm}^{-1}$  and 1402  $\text{cm}^{-1}$  could be attributed to vibration of  $\text{COO}^-$  bond. The peaks at 2910  $\text{cm}^{-1}$  and 3184  $\text{cm}^{-1}$  could be due to vibration of  $\text{CH}_2$  and  $\text{OH}$  bonds, respectively. Silva *et. al.*<sup>182</sup> had a similar observation. In their study, they synthesized CdTe and modified its surface with four ligands namely 3-mercaptopropionic acid (3-MPA), Thioglycolic acid (TGA), 1-Thioglycerol (TGH) and Glutathione (GSH). Their FTIR analysis revealed that for TGA and 3-MPA modified QDs the peaks observed at 1562  $\text{cm}^{-1}$  and 1397  $\text{cm}^{-1}$  could be assigned to vibration of deprotonated  $\text{COO}^-$  bond. According to the researchers, at the pH of 10 deprotonations of  $-\text{COOH}$  occurs since the  $\text{pK}_{\text{COOH}}$  value

is equal to 3.67. Another major observation they made which is similar to our study is the fact that after anchoring TGA and MPA to the surface of the QDs, the peak assigned to thiol group at  $2574\text{ cm}^{-1}$  disappeared. This is in accordance with the postulate that thiol groups have a higher affinity of inorganic nanocrystals and gold nanoparticles. In our subsequent fluorescence and photoluminescence measurements, we used excitation wavelength within the range where characteristic absorption peak was observed. The ability of our material to absorb electromagnetic radiation in the form of photons and re-emit in the form of photons was established by carrying out photoluminescence measurements. The analysis was done using Nanolog HORIBA FL3-22-TRIAX with an excitation wavelength of 350 nm and emission range starting from 365 nm to 650 nm (Figure 4.24 A). The percentage reflectance of the material was measured using UV-visible spectrophotometer model Nicolet Evolution 100 and we used to calculate the band gap of the material using Tauc's plot (Figure 4.24 B).



UNIVERSITY of the  
WESTERN CAPE



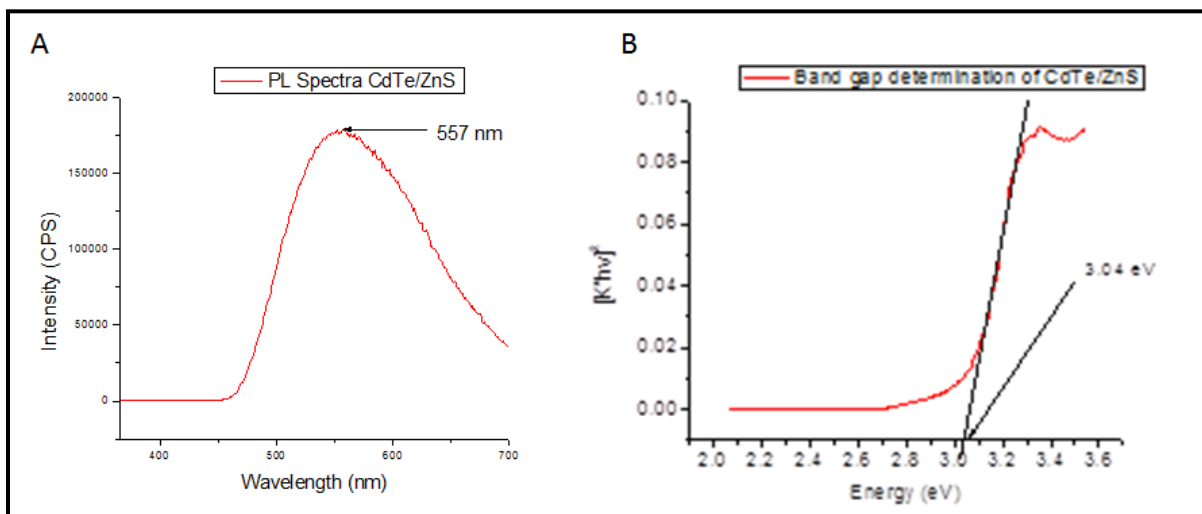


**Figure 4.24: The photoluminescence characteristics of CdTe/ZnS quantum dots (A) Tauc's plot for band gap determination of CdTe/ZnS nanocrystals**

The synthesized quantum dots showed characteristic emission peak at 557 nm. This is supported by the color of the prepared QDs which were greenish yellow in color. Shen *et al.*<sup>183</sup> synthesized 3- MPA capped CdTe nanocrystals and collected aliquots after 15, 30, 60, 90, 120, 150, 210 and 270 minutes. The observed an emission at 559 nm similar to ours after 1 hour, the slight deviation could be attributed to the presence of ZnS shell in our material. The band gap of the material was measured to be 3.04 eV (figure 4.24 B). Surface modification of quantum dots is known to affect the mechanism of photoluminescence. Therefore, we employed this spectroscopic technique to confirm subsequent modification. For instance, during the introduction of the streptavidin and formation of the molecular beacon, the technique was employed for confirmation.

#### 4.13.1 Surface modification of the quantum dots and design of the MB

The streptavidin was attached to the 3-MPA capped quantum dots using carbodiimide chemistry as discussed earlier in the methodology section. To confirm this attachment we conducted PL measurements (Figure 4.25 A). The same technique was used to confirm whether the biotinylated probe containing the quencher (Iowa Black) had been successfully bio-conjugated to the streptavidin modified QDs (Figure 4.25 B).

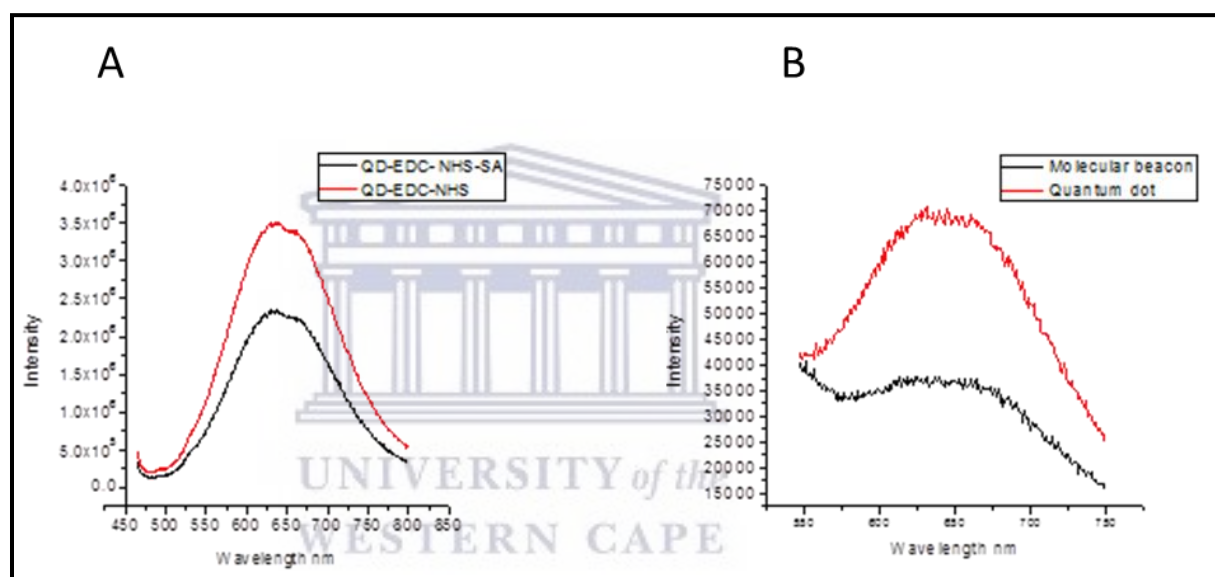


**Figure 4.25: PL spectra for equal amounts of QD with and without the streptavidin (A) comparison of fluorescence intensity of bare quantum dot and the formed molecular beacon (B)**

The comparison of success or failure using the PL technique was made possible by employing the same volume of QD and compensating the amount of the reagent using phosphate buffer solution. In Figure 4.25 A, clearly shows that the QD without the streptavidin had higher fluorescence. Similarly, Figure 4.25 B demonstrates success in the formation of the molecular beacon when compared to the same amount of uncoupled

quantum dot. Iowa black belongs to a new class of family of dark quenchers. They are developed by IDT and are offered as modifiers at either 5'- or 3'-end of an oligo. They have excellent properties for use in fluorescence quenched probes. They are stable in the wide range of conditions including pH and heat. The quencher is ideal for fluorescence materials that emit in the green to pink spectral range. The ratio of modified QD to the biotinylated probe is an important step towards designing of the molecular beacon. Again, we confirmed quenching by measuring the fluorescence intensity (endpoint) using two different types of fluorescence microplates. BioTek Synergy H1 Hybrid Multi-Mode Microplate Reader with Gen5 Software and POLARstar Omega microplate reader. The advantage of using BioTek Synergy spectroscopy was obviated by the fact it allows combinations of different excitation and emission wavelengths and also the emission spectra is achieved. The spectra (figure 4.26 A & B) clearly distinguishes the fluorescence emission profile between free QD and the molecular beacon formed upon successful conjugation of the streptavidin modified quantum dots to the DNA probe with the quencher.

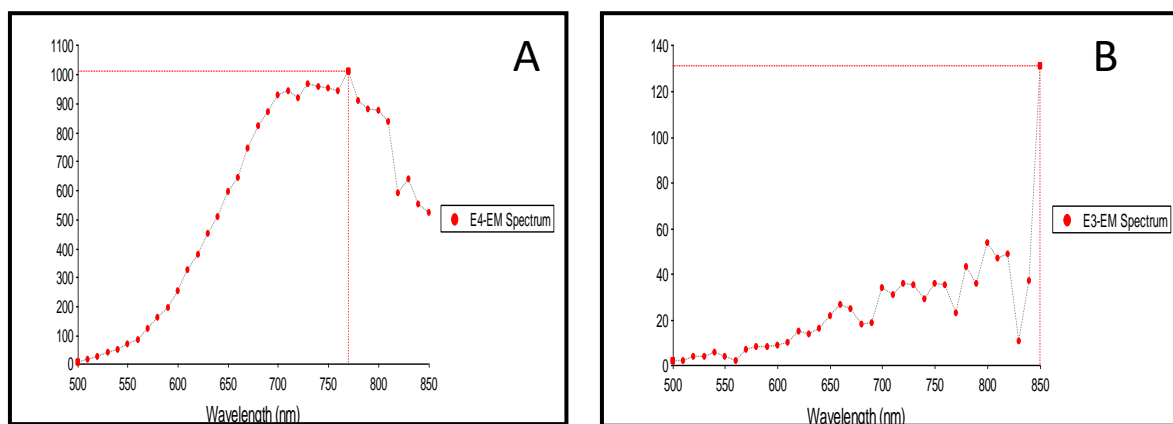


**Figure 4.26: Fluorescence spectra comparing emission spectrum of free QDs (A) and the constituted molecular beacon (B)**

The spectra demonstrate the ability of the Iowa black to absorb photons emitted when it is coupled together with CdTe/ZnS QDs. In our future publication, we are going to calculate the FRET efficiency for this combination. The determination of the fluorescence intensity by spectral scanning was considered inappropriate for comparison especially for monitoring of fluorescence dependence on the concentration of the target bound to the probe of the MB. We, therefore, decided to use end point approach in order to obtain discrete values of the intensities. The excitation and emission wavelength were chosen arbitrarily and their resulting intensities compared (Figure 4.27 A) by employing the same QD (control) and the MB. Figure 4.27 B shows the fluorescence intensity of free QD and designed MB measured using the POLARstar microplate reader with an excitation wavelength of 355 nm and an emission wavelength of 620 nm.

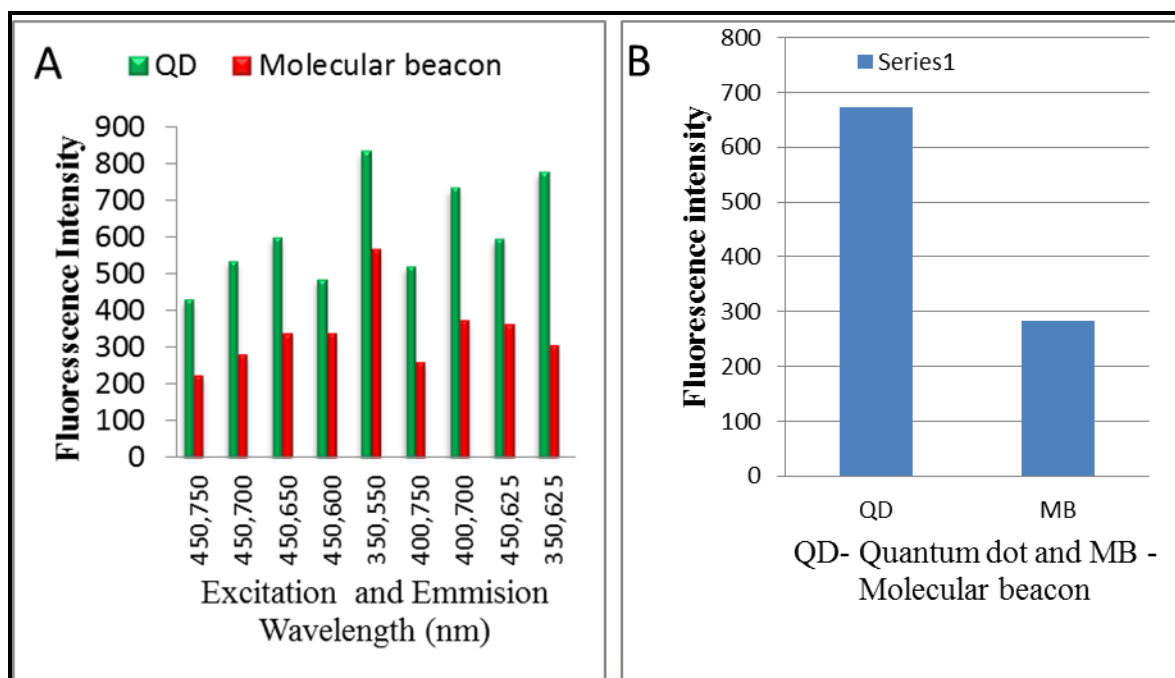


**Figure 4.27: Comparison of discrete fluorescence intensities obtained from same sample of QD and MB at different excitation and emission wavelengths using BioTek Synergy H1 Hybrid Multi-Mode Microplate Reader (A) Fluorescence of the free QD and MB ready for target introduction measured by using POLARstar Omega microplate reader (B)**

The first microplate reader clearly demonstrated that in spite of varying excitation and emission wavelength a certain amount of intensity is recorded and in all cases the fluorescence intensity of the designed molecular beacon was lower compared to that one of the free quantum dot. Based on availability of the instrument we used POLARstar Omega microplate reader and measured the samples at the said excitation and emission wavelength. The measurements also confirmed success in coupling between the quantum dot and the probe.

#### 4.14 Application of the QD based molecular beacon for biomarker detection

The oligo with a sequence of 5' **GCG AGA** AGG CAT ACG AAC AGG CAC **TCT CGC** '3 which targets a potential biomarker that we have identified was chosen for this study. The short stem was attached to the ends of the loop (bold and underlined see above). The short stem was chosen over long stem because the long stem has been associated with lower target affinity<sup>36</sup>. The 5' end of the probe was further modified with biotin-PEG and 3' end was bioconjugated to Iuwa black. The streptavidin modified QDs were attached to the 5' end containing biotin. The success in fluorescence resonance energy transfer is evident in Figure 4.26 and 4.27. The performance of the designed molecular beacon was evaluated in two steps. In the first step, the complementary target was used. In the second step, we used cDNA synthesized from cultured MCF 7 and MCF 12 cells. The evaluation process was done in the following order; the intensity of the designed molecular beacon was measured and compared to that one of the free QD as shown in figures 4.27 A and 4.27 B. Secondly, the complementary target is introduced, incubated for 15 minutes and the intensity determined. More and more target was added until there was no increase in the fluorescence. We started the evaluation with high concentration of the complementary target (Figure 4.28 A). Again, we designed another MB and used lower concentration of the complementary target (Figure 4.28 B)

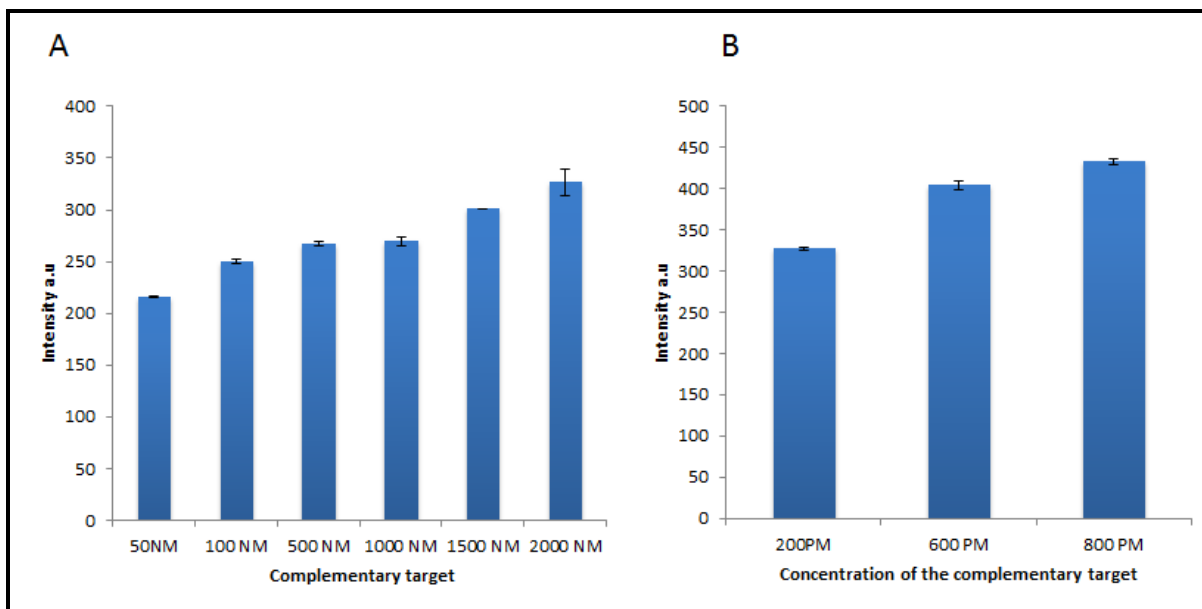


**Figure 4.28: Detection of varied concentrations of complementary target using QD-based molecular beacon**

In the absence of target, the fluorescence intensity is low due to the close proximity of the quencher and the QD. Similarly, when the target concentration is low the fluorescence increase relative to the fluorescence of the MB in the absence of the target. This is ascribed to the fact that the arms anneal to form stem-loop structure bringing the quencher close to the fluorophore<sup>36</sup>. When the target sequence was present, hybridization took place destabilizing the stem, thus increasing the distance between quencher and fluorophore and increasing the relative fluorescence intensity values<sup>184</sup>. The same setup was repeated but using cDNA synthesized from cultured MCF 7 and MCF 12 cells as shown in figure 4.29 A and 4.29 B, respectively.

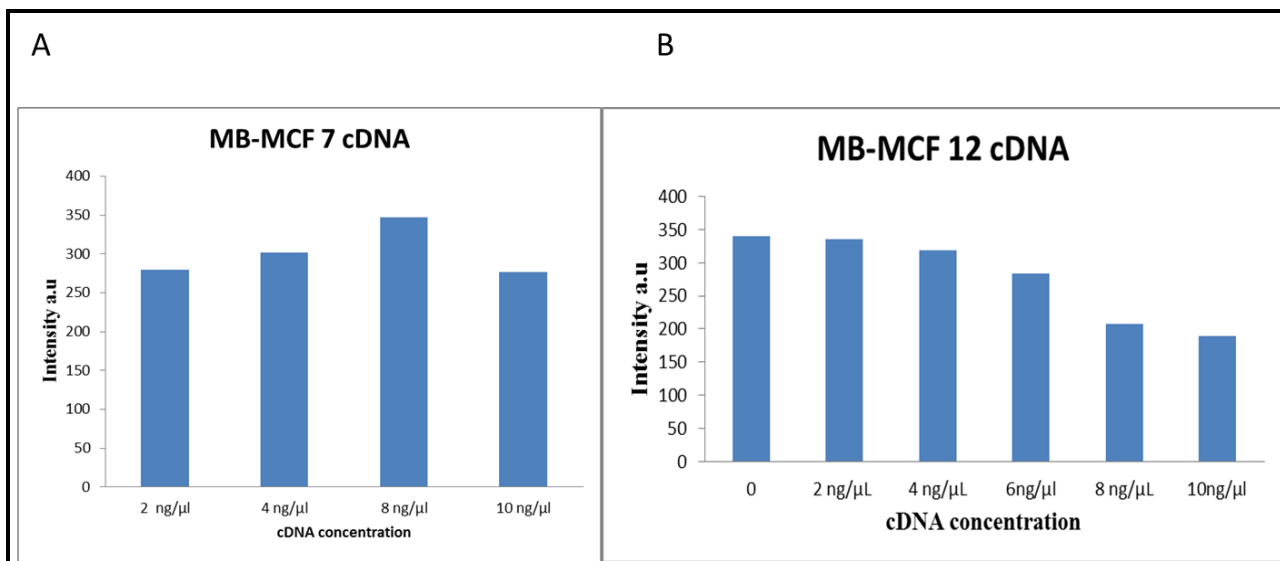


**Figure 4.29: Detection of target present in lower concentration of cDNA using QD-based molecular beacon**

The designed molecular beacon based on quantum dots responded well. However, saturation of the binding site was reached with the addition of high concentrations. The fluorescence increased with increase in target concentration and after saturation, the fluorescence decreased. We believe that any added target could not increase the fluorescence of the QD but instead leads to dilution of the QD hence observed a decrease in fluorescence. The fluorescence intensity for the constituted molecular beacons in the absence of the complementary target or cDNA target remains relatively high. This could be due to low FRET efficiency for the streptavidin modified QDs conjugated to Iowa black. Cady *et. al.*<sup>39</sup> reported that the maximum FRET efficiency of streptavidin modified QDs to black Iowa could be 14 %.



#### 4.15 Conclusion

Fluorescence InP/ZnSe inorganic nanocrystals were successfully synthesized and characterized. The quantum yield of the particles was calculated to be 13.2 % which was higher than the reported 6 %. The increase in quantum yield could be attributed to slightly lower temperature for the ripening of the core InP nanocrystals. New ligand exchange method was adopted from ligand exchange process for InP/ZnS. The method was efficient and the particles were able to retain some of its optical properties when dispersed in water. Success in ligand exchange process allowed easy introduction of streptavidin to the surface of water-soluble InP/ZnSe nanocrystals. This success paves way for future biological applications once fluorescing properties of the water soluble InP/ZnSe QDs are enhanced. The band gap of the aliquots of InP and InP/ZnSe was found to be 2.44 eV and 2.55 eV, respectively. The toxicity of the InP/ZnSe nanocrystals were further investigated using two cell lines namely KMST6 and MCF 12 cells. The cytotoxicity study revealed that InP/ZnSe are less toxic with less than 10 % loss in cell viability in both cell lines at the highest concentration tested. The molecular beacons that we designed based on CdTe/ZnS quantum dots proved to be sensitive. The beacon was able to detect as low as 200 pm of the complementary target and 2 mg/ $\mu$ L of the cDNA synthesized from MCF 7 cancerous cells.

## 5 CHAPTER FIVE: SYNTHESIS AND CHARACTERIZATION OF THE LUMINESCENCE NANOCOMPOSITE

### 5.1 Introduction

In this chapter we present the characteristics of the fabricated luminescent magnetic nanocomposites. Specifically, we presented physical properties, photoluminescence properties, magnetic properties, and electronic properties. Lastly, we presented cytotoxicity studies of the nanocomposite that was constituted for the first time.

### 5.2 Synthesis of $\alpha$ -Fe<sub>2</sub>O<sub>3</sub>-InP/ZnSe nanocomposite

The magnetic material (Fe<sub>2</sub>O<sub>3</sub>) discussed in chapter three was coupled with the fluorescing material InP/ZnSe nanocrystals discussed in chapter four to afford a nanocomposite featuring fluorescence and magnetic properties. The last two decades have witnessed strategies to synthesize Cd-free quantum dots. It is within the same age when a lot of effort was put forward to develop multifunctional materials with both magnetic and fluorescence properties. However, the nanocomposites made in the last one decade constitute Cd based quantum dots. For instance, in 2004 for the first time, Wang *et. al.*<sup>97</sup> reported the synthesis of superparamagnetic  $\gamma$ -Fe<sub>2</sub>O<sub>3</sub> beads coupled with CdSe/ZnS quantum dots. In this study, we report for the first time synthesis of Fe<sub>2</sub>O<sub>3</sub>-InP/ZnSe nanocomposite. The composite was synthesized following a procedure designed by Wang *et. al.*<sup>97</sup> with lots of modification. The magnetic nanoparticles were functionalized with meso-2,3- dimercaptosuccinic acid. On the other hand, the prepared quantum dots were hydrophobic and were made to be hydrophilic by carrying out ligand exchange with the use of the 3-mercaptopropionic acid. The DMSA modified magnetic nanoparticles were

dispersed in PBS (pH 7.4) and water soluble quantum dots were also dispersed in PBS (pH 7.4), the thiol chemistry was utilized to couple them together. A representative HRTEM image for  $\text{Fe}_2\text{O}_3$ -InP/ZnSe is shown in figure 5.1 below.

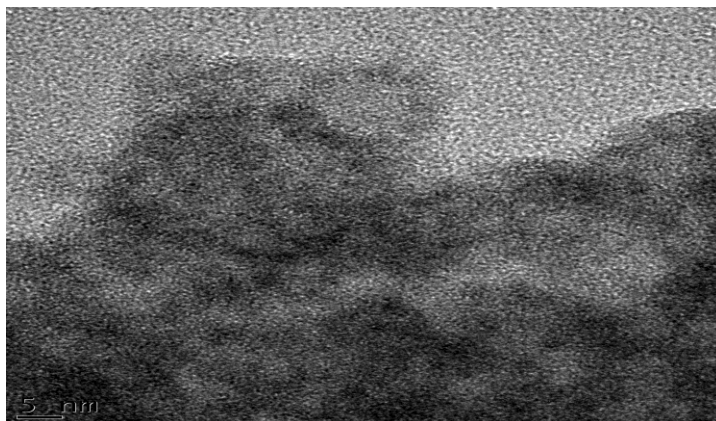


**Figure 5.1: The HRTEM micrograph of  $\text{Fe}_2\text{O}_3$  - InP/ZnSe nanocomposite**

The FTIR confirmed that carboxyl groups of the meso-2,3-dimercaptosuccinic acid were anchored to the surface of the iron oxide nanoparticles as presented and discussed in chapter 3. The thiol groups were available to allow the coupling of the InP/ZnSe nanocrystals. To minimize the quenching of fluorescing capabilities of the InP/ZnSe quantum dots, the use of the InP/ZnSe in large excess compared to a number of magnetic nanoparticles led to enormous crowding of the particles. This scenario led to crowding of the particles making it difficult to determine the average size of nanocomposite particles since the quantum dots filled the spaces between the  $\alpha$ - $\text{Fe}_2\text{O}_3$  as seen in the micrograph. The energy dispersive spectroscopy (EDS) analysis was carried out to determine the constituents of the nanocomposite. Figure 5.2 below shows EDS spectrum of the  $\alpha$ - $\text{Fe}_2\text{O}_3$ -InP/ZnSe nanocomposite.

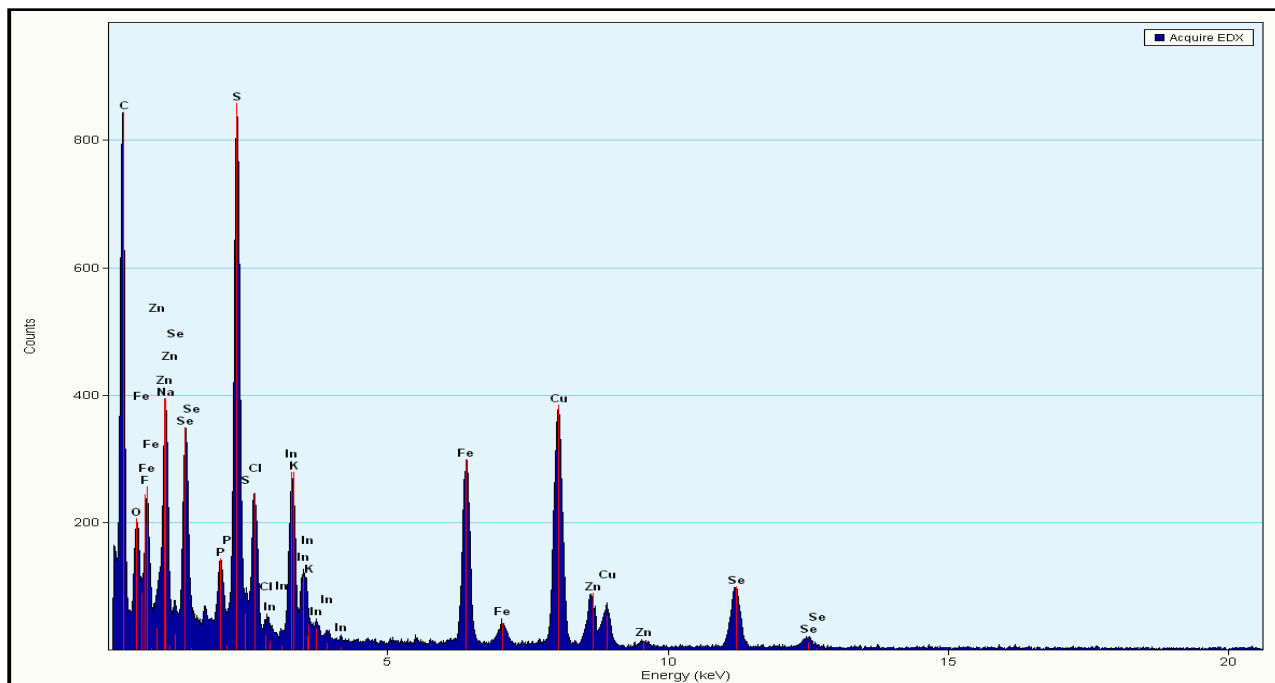


**Figure 5.2: Energy dispersive spectroscopy spectrum for  $\alpha$ -Fe<sub>2</sub>O<sub>3</sub>-InP/ZnSe nanocomposite**

The energy dispersive spectroscopy spectrum shown in Figure 5.2 clearly indicates that all the elements from both the magnetic and fluorescing material were present in the nanocomposite. The presence of the copper in the spectrum was due to the copper grid which was used to hold the sample during HRTEM analysis. The observed sulphur could possibly have originated from L-cysteine, 3-mercaptopropanionic acid or meso-2,3-dimercaptosuccinic acid which were used as functionalizing agent, ligand exchange and coupling agent, respectively. Subsequently, the photoluminescence experiment could have confirmed that the  $\alpha$ -Fe<sub>2</sub>O<sub>3</sub>-InP/ZnSe nanocomposite was successfully formed. In this study, it was discovered that in spite of the ratio of the QDs to MNPs being 100:1 the black magnetic nanoparticles quenched the fluorescing capability of the QDs. Figure 5.3 (A) and 5.3 (B) shows the PL characteristics of both InP/ZnSe and  $\alpha$ -Fe<sub>2</sub>O<sub>3</sub>-InP/ZnSe nanocomposites.

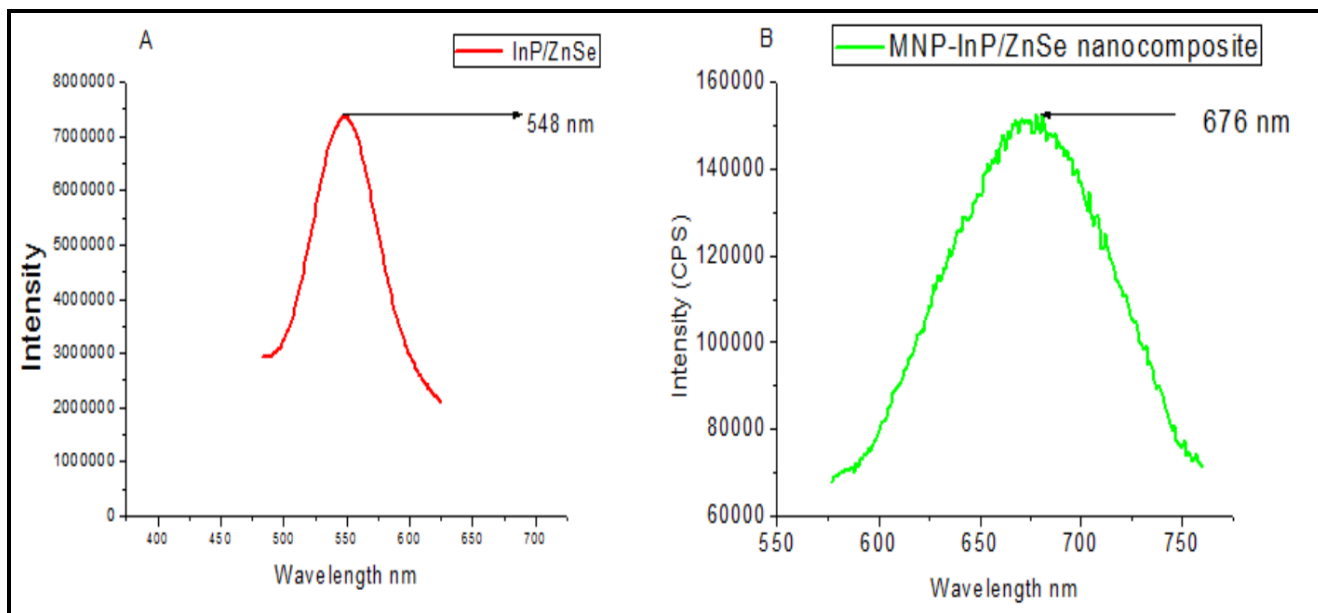


**Figure 5.3: PL spectra of InP/ZnSe nanocrystals dispersed in hexane (A) PL spectra of  $\alpha$ -Fe<sub>2</sub>O<sub>3</sub>-InP/ZnSe nanocomposite dispersed in PBS (B)**

In Figure 5.3 (A) it can be seen that the intensity is quite high, with a smooth peak absorbance at 548 nm. In contrast figure 5.3 (B), the curve is rugged with quite low PL intensity. It is also clear that the absorption peak red shifted to 676 nm. This observation was also sufficient evidence for the successful formation of the nanocomposite. The quenching could be possibly due to energy transfer process resulting from contact between the quantum dots and the surface of the iron oxide particles<sup>107</sup>. Similar observation was reported by Jeong *et. al.*<sup>121</sup> when they fabricated a nanocomposite of the type Fe<sub>3</sub>O<sub>4</sub>-CdSe/ZnS. The group pointed out that the reduced PL intensity occurs due to the replacement of the hydrophobic ligands at the surface of the quantum dots by the hydrophilic ligands which leads to insufficient passivation of the quantum dots. However, partial displacement of ligands occurs on the surface of the quantum dots since the majority of the ligand utilized for coupling are on the surface of the Fe<sub>2</sub>O<sub>3</sub>. It is this phenomenon that leads to partial loss of fluorescence intensity after the coupling process<sup>121</sup>. Du *et. al.*<sup>185</sup> recorded very

low quantum efficiency 2-3 % when they fabricated  $\text{Fe}_3\text{O}_4/\text{CdSe}$ . They attributed the low quantum yield to the crystal mismatch between magnetic nanoparticles and semiconductor QDs which affected the crystals of the QDs. The quantum yield, however, increased to 10-15 % when they passivated its surface with ZnS. The increase in quantum yield could be due to compensation of surface defects upon deposition of the ZnS layer. Figure 5.4 below compares the PL quantum dots before and after constituting the nanocomposite.

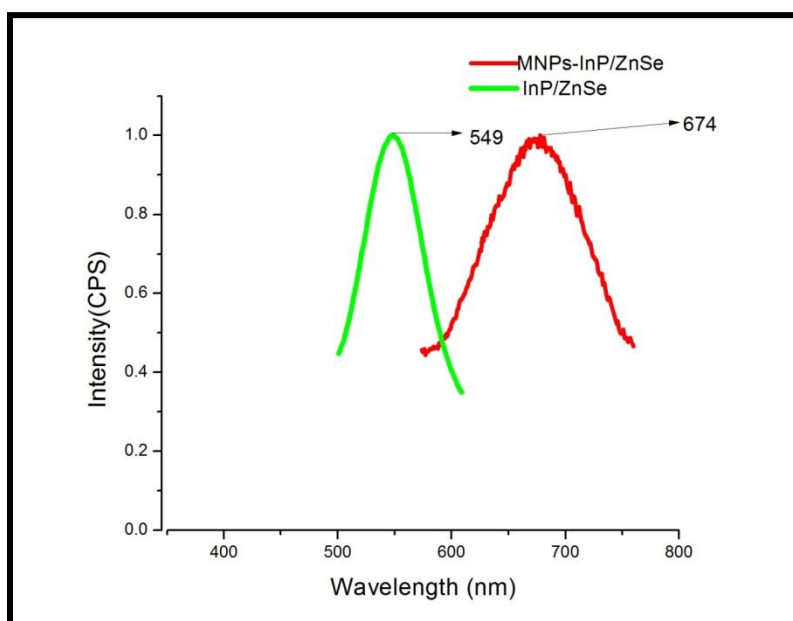


**Figure 5.4: Photoluminescence spectra of InP/ZnSe (green line) and InP/ZnSe- $\text{Fe}_2\text{O}_3$  nanocomposite (red line)**

The red shift emission observed in this study could be attributed to modification at the surface of the quantum dots brought by hydrophilic ligands and also immobilization of the iron oxide nanoparticles. Similar observation was observed by Du *et. al.*<sup>185</sup> when they passivated  $\text{Fe}_3\text{O}_4/\text{CdSe}$  with ZnS. They recorded red shift both in absorption spectra as well as the PL

spectra. Wang *et. al.*<sup>97</sup> had observed a blue shift when they coupled CdSe/ZnS with Fe<sub>2</sub>O<sub>3</sub>. They attributed the blue shift to the change in the surface state of the QDs due to the immobilization of the magnetic beads. In another study, Ahmed *et. al.*<sup>117</sup> observed red shift when they coupled Fe<sub>3</sub>O<sub>4</sub> with CdTe. The emission wavelength shifted from 522 nm for CdTe to 540 nm for the fluorescent magnetic nanocomposite. According to this group, free nanoparticles could have aggregated to form small clusters through electrostatic force. The clustering of the nanoparticles causes slight degradation of energy level leading to narrow energy band gap and broadening of the PL spectra.

### **5.3 Magnetic properties of the nanocomposite**

The magnetic properties of the fabricated luminescence nanocomposite were determined using SQUID magnetometer similar to the previous samples. It was important to determine the magnetic properties of the newly fabricated material to determine its suitability for a biological application like cell separation. It was also important to evaluate the effect of incorporation of the diamagnetic InP/ZnSe semiconductor to the iron oxide magnetic nanoparticles. Figure 5.5 presents the saturation magnetization of the constituted luminescent magnetic nanocomposite.

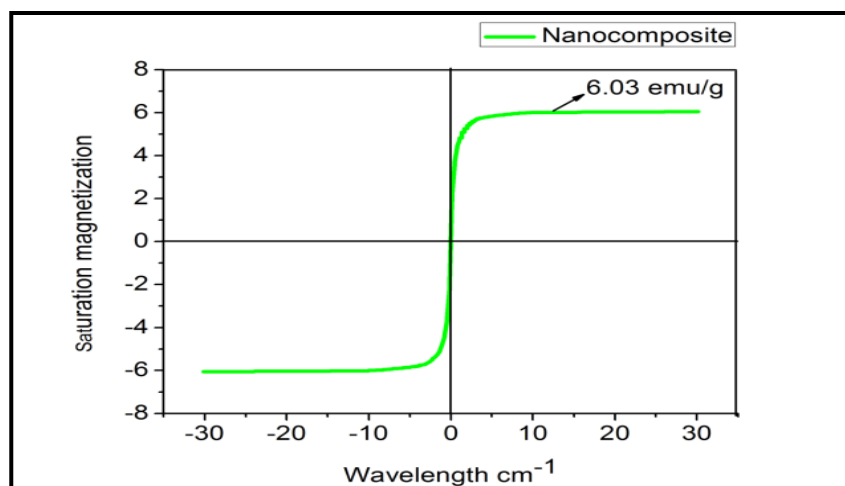


**Figure 5.5: Magnetic nanomaterial of bare iron oxide and luminescence magnetic nanocomposite**

The bare magnetic nanoparticles and  $\alpha\text{-Fe}_2\text{O}_3\text{-InP/ZnSe}$  nanocomposite had a saturation magnetization of 65.67 emu/g and 6.03 emu/g, respectively. The magnetic saturation reduced significantly this could be attributed to the diamagnetic material (InP/ZnSe) coating the superparamagnetic (iron oxide) nanomaterial. The question here is whether this amount of magnetic saturation was still sufficient for the biological application. To answer the question we compared the obtained value of our nanocomposite with similar studies in literature. Jeong *et al.*<sup>121</sup> noted the reduction in saturation magnetization from 55.5 emu/g to 31.9 emu/g when they coupled  $\text{Fe}_3\text{O}_4$  with CdSe/ZnS. In another study Tong *et al.*<sup>113</sup> synthesized and investigated properties of the  $\text{Fe}_3\text{O}_4/\text{Y}_2\text{O}_3:\text{Eu}^{3+}/\text{Y}_2\text{O}_3:\text{Eu}^{3+}$ . The composite exhibited both luminescence and magnetic properties. The magnetization saturation decreased significantly from 55.85 emu/g for  $\text{Fe}_3\text{O}_4/\text{C}$  which was the starting material to 1.99 emu/g for the product  $\text{Fe}_3\text{O}_4/\text{Y}_2\text{O}_3:\text{Eu}^{3+}/\text{Y}_2\text{O}_3:\text{Eu}^{3+}$ . It is worth noting that despite the drop in the Ms Strength of the product, it was still suitable for magnetic separation and targeting applications. A nanocomposite



material of the type Fe/C/YBO<sub>3</sub>:Eu<sup>3+</sup> was prepared by Li *et. al.*<sup>112</sup> and an investigation of the luminescent and magnetic properties carried out. The vibrating specimen magnetometer (VSM) was used to investigate the trend in the magnetic properties for the core Fe<sub>3</sub>O<sub>4</sub> and the subsequent products Fe<sub>3</sub>O<sub>4</sub>/C and Fe/C/YBO<sub>3</sub>:Eu<sup>3+</sup>. It was noted that the value of the saturation which was 2.17 emu/g was lower than the Ms value of the Fe<sub>3</sub>O<sub>4</sub> and the decrease attributed to the shell of the phosphor powder. In another strategy for synthesizing the bifunctional composites, Ma *et. al.*<sup>110</sup> coupled the NH<sub>2</sub>-SiO<sub>2</sub>/Y-Fe<sub>2</sub>O<sub>3</sub> with the MPA-capped CdTe QDs. The prepared composite exhibited both superparamagnetic characteristics and excellent luminescence properties. The recorded saturation magnetization of the bifunctional nanoparticles was 10.8 emu/g. This Ms value incidentally was much lower compared to 83.2 emu/g of the Y-Fe<sub>2</sub>O<sub>3</sub>. The decreased magnetism property was possibly due to the thick silica coat which was applied on the MNPs. Nonetheless, the magnetic property of the BNPs was still sufficient for the bio-separation process. We therefore conclude that despite reduced magnetic saturation of α-Fe<sub>2</sub>O<sub>3</sub>-InP/ZnSe nanocomposite, it is worth noting that 6.03 emu/g was still sufficient for biological separation.

#### 5.4 Band gap of the nanocomposite

We speculated that the nanocomposite that was constituted by coupling the iron oxide nanoparticles and the InP/ZnSe nanocrystals could still show some semiconductor properties. Therefore, we investigated the size of the band gap of the nanocomposite and compared it with the band gap of the uncoupled InP/ZnSe nanocrystals. The diffuse reflectance of the nanocomposite was determined using UV/Vis spectrophotometer and Tauc's plot described in chapter 4 used to determine the band gap. The Tauc's plot for the nanocomposite is shown in figure 5.6

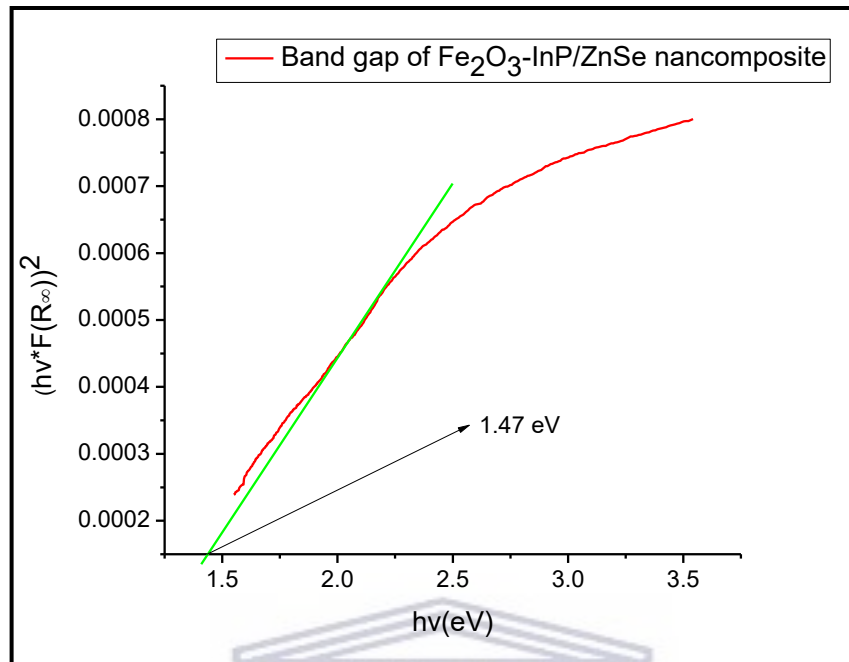


**Figure 5.6: The band gap of the synthesized  $\alpha$ -Fe<sub>2</sub>O<sub>3</sub>-InP/ZnSe nanocomposite**

The band gap of the nanocomposite was determined to be 1.47 eV. This band gap energy is much lower compared to 2.47 eV of the InP/ZnSe nanocrystals. In contrast, Roychowdhury<sup>107</sup> *et al.* observed that the band gap of ZnS increased from 4.15 eV to 4.27 eV. When they prepared nanocomposite that constituted Fe<sub>3</sub>O<sub>4</sub>/ZnS. In another study by Island *et al.*<sup>186</sup> the doped Fe<sub>3</sub>O<sub>4</sub> with Zn to have Zn<sub>x</sub>Fe<sub>3-x</sub>O<sub>4</sub>, the group observed an increase of indirect band gap of 0.1 eV of Fe<sub>3</sub>O<sub>4</sub> increased to 1.26 eV for Zn<sub>0.025</sub>Fe<sub>3-0.025</sub>O<sub>4</sub>. However, the band gap reduced to 0.43 eV when the amount of Zn doping was increased to x= 0.125. In our context, we believe that our case was similar to the later where the  $\alpha$ -Fe<sub>2</sub>O<sub>3</sub> formed the core of the NCs and not the QDs hence the band gap 1.47 eV calculated was an increment from the theoretical eV of the Fe<sub>2</sub>O<sub>3</sub>. Ahmed *et al.*<sup>117</sup> attribute the decrease in energy band gap to the formation of clusters resulting from electrostatic attraction of the free nanoparticles.

## 5.5 Cytotoxicity of the $\text{Fe}_2\text{O}_3\text{-InP/ZnSe}$ nanocomposite

The cytotoxicity of the individual materials namely InP/ZnSe nanocrystals and  $\alpha\text{-Fe}_2\text{O}_3$  nanoparticles were investigated and reported in chapter 3 and chapter 4, respectively. We were interested in investigating the cytotoxicity of the material that resulted by combining the two materials. The nanocomposites were exposed to both MCF-12A and KMST 6 cell lines. The cell lines were cultured as reported in chapter two and MTT assay was used to study the cytotoxicity of the particles. The cytotoxicity of the nanocomposite is presented in Figure 5.8 below.

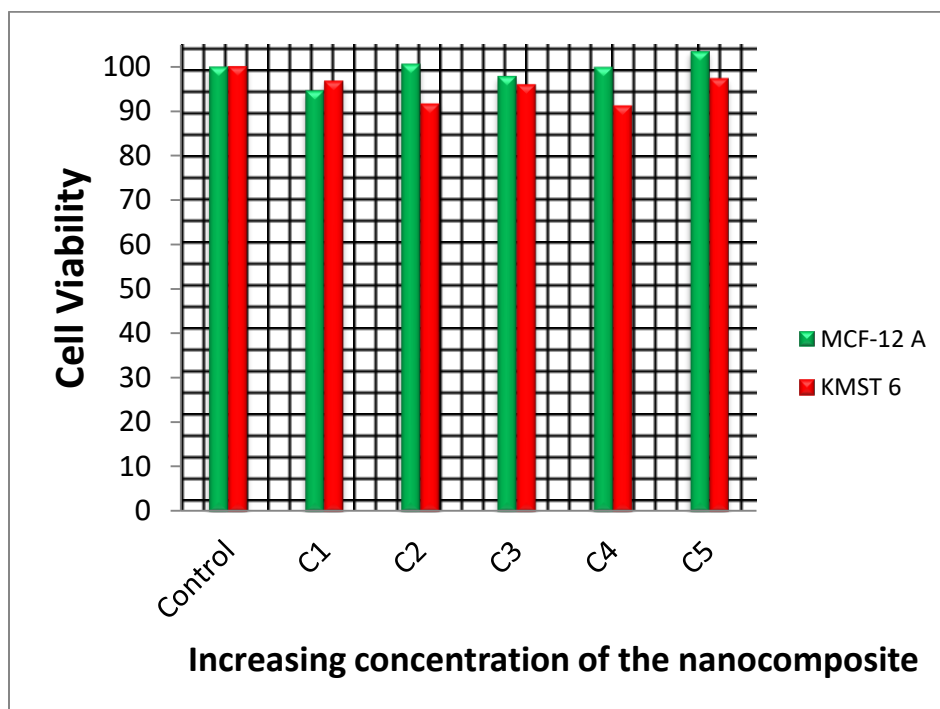


**Figure 5.7: Cytotoxicity of the  $\alpha\text{-Fe}_2\text{O}_3\text{-InP/ZnSe}$  nanocomposite carried out using MCF 12A and KMST 6 cell lines**

The cytotoxicity results for the nanocomposite were very similar to those of the individual materials. The cell viability was greater than 90 % for all concentrations of the nanocomposite. The findings suggest that the nanocomposites are less toxic. The truth of our findings holds also

when this toxicity study is compared with other Cd based nanocomposite cytotoxic studies. Shen *et. al.*<sup>103</sup> constituted a nanocomposite (carboxymethyl-based folate/Fe<sub>3</sub>O<sub>4</sub>/CdTe) and carried out *in vitro* cytotoxicity study. In their study, they exposed the nanocomposite to two cell lines human hepatocytes L02 (normal) and HepG2 (cancerous) cell lines. By varying the concentration of the nanocomposite from 200 to 1000 µg/mL the cell viability varied from 80-70 % within 12 hours which is quite low compared to our study.

## 5.6 Conclusion

The ultimate objective of the study was realized under this chapter. The idea to fabricate the luminescent nanocomposite was discussed herein. The magnetic nanoparticles discussed in chapter 3 were successfully coupled to InP/ZnSe nanocrystals discussed in the chapter. The nanocomposite exhibited both magnetic properties and luminescent properties despite being compromised. The magnetic saturation was measured to be 6.03 emu/g. There was significant dropped as compared to magnetic saturation of uncoupled iron oxide nanoparticles which had Ms value of 65.67 emu/g. Similarly, the fluorescence of the nanocomposite dropped significantly to around 40,000 arbitrary units compared to 7,000,000 intensity arbitrary units for the uncoupled InP/ZnSe quantum dots. The compromised properties of the nanocomposite prompted us to apply the iron oxide nanoparticles and quantum dots separately has discussed at the end of chapter 3 and end of chapter 4.

## 6 CHAPTER SIX: SUMMARY OF RESULTS, CONCLUSION AND RECOMMENDATION FOR FURTHER STUDY

### 6.1 Introduction

This chapter presents a summary of major achievements that were realized during the study. Success in synthesizing iron oxide and modifying its surface has been described as well as applying them for biomarker isolation. We have summarized the characteristics of the synthesized quantum dots and their applications. We have given summary of the cytotoxic studies and the safety of the tested materials. Lastly, we have given summary of potential future work in regard to the studied materials.

### 6.2 Conclusion

We successfully synthesized the iron oxide nanoparticles with an average size of 8.5 nm by co-precipitation method. The particles were of the cubic structure as confirmed by XRD analysis. The XRD analysis also confirmed that the nanoparticles were of maghemite type ( $\text{Fe}_2\text{O}_3$ ). Despite the oxidation of  $\text{Fe}_3\text{O}_4$  to  $\alpha\text{-Fe}_2\text{O}_3$  the particles exhibited good magnetic properties with the magnetic saturation of 65.67 emu/g. Such amount of magnetic saturation is sufficient for biological processes such as bioseparation. The particles were successfully functionalized with suitable ligands to enhance their biocompatibility. L-cysteine, DMSA, and 3-mercaptopropionic were successfully introduced to their surfaces. Despite, implanting the ligands onto the surface of the iron oxide nanoparticles there was no significant loss in the magnetic properties as well as the change in the particle sizes and the lattice structure of the magnetic nanoparticles. The functionalized magnetic nanoparticles allowed the introduction of streptavidin (SA) which aided further conjugation to biotinylated aptamers. The streptavidin modified magnetic nanoparticles were bioconjugated to MUC1-binding aptamer to enhance specificity to MUC 1 proteins and

subsequent utilization in isolation of MUC 1 proteins from MCF 7 lysates. Separately, fluorescing InP/ZnSe nanocrystals were synthesized and their properties investigated prior to coupling them with the magnetic nanoparticles to constitute the nanocomposite. The synthesized InP/ZnSe nanocrystals were highly crystalline and monodisperse. The fluorescing nanoparticles had an average size of 4.614 nm and Zinc blende structure as revealed by XRD analysis. The quantum yield of the fluorescing nanoparticles was 13 %. The band gap of the semiconductor was determined to be 2.47 eV. We were able to demonstrate the possibility of scaling up the synthesis of InP/ZnSe nanocrystals by a factor of 2, 4 and 6. The scaling up process was successful without compromising the fluorescing properties of the nanocrystals. However, we acknowledge the challenge of the cost of  $P(TMS)_3$  which might limit production of InP/ZnSe at industrial scale. Again, we demonstrated the ability to sort the nanocrystals into different sizes from the crude product. In the size sorting process we confirmed that just like InP/ZnS-based nanocrystals the emission wavelength of the nanocrystals can be tuned resulting to particles with narrow emission spectra. We further carried out ligand exchange process to obtain water soluble quantum dots for them to be compatible with the projected biological application. There was a significant decline in fluorescence intensity of the material after the ligand exchange process which we attributed to changes in ligands and solvents surrounding the nanocrystals. Owing to the reduced fluorescence of InP/ZnSe, we went ahead and synthesized CdTe/ZnS quantum dots. We incorporated this new set of quantum dots in the gene detection by designing molecular beacons. Our quantum dot based molecular beacon was sensitive and was able to detect as low as 200 pm of the complementary target and up to 2 mg/ $\mu$ L of cDNA synthesized from MCF7 cancerous cells. In chapter 5 we utilized the materials synthesized in chapter 3 and 4 to fabricate the luminescence magnetic nanocomposite which was the main objective of the study. We took

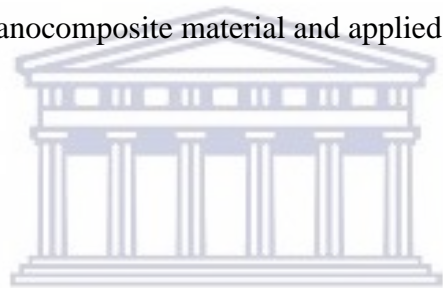
advantage of thiol and carboxyl groups present at the surface of the iron oxide nanoparticles to couple it together with the fluorescing InP/ZnSe nanocrystals to form the nanocomposite. The properties of the nanocomposite were investigated using various characterization techniques. The HRTEM analysis confirmed that the nanocomposites was cloudy and not separated particles hence it was difficult to estimate their sizes. The magnetic saturation of the nanocomposite was determined using SQUID to be 6.08 emu/g. This was a significant decline in magnetic saturation as compared to uncoupled iron oxide magnetic nanoparticles. We were only discouraged by a significant decline in fluorescence which can limit biological processes such as *in vivo* imaging. The coupling of the InP/ZnSe nanocrystals with the iron oxide resulted in red shift in emission wavelength. To conclude the study we carried out extensive *in vitro* cytotoxicity study to evaluate the toxicity of the iron oxide nanoparticles, functionalized iron oxide nanoparticles, InP/ZnSe nanocrystals, and Fe<sub>2</sub>O<sub>3</sub>-InP/ZnSe nanocomposite. KMST 6 and MCF-12A cell lines were used. The cell lines were exposed to increasing concentration of the nanoparticles. The cells were incubated with the nanoparticles for 24 hours and the cell viability was determined using MTT assay. The cell viability for all types of the nanomaterials was greater than 90 % using both MCF-12A and KMST6 cell lines. This suggested that the particles are safe hence not limiting their biological applications and also safe in regard to handling.

### **6.3 Recommendations and Future work**

- The functionalization of iron oxide nanoparticles and bioconjugation steps developed in this study can be optimized and applied in the design of an aptamer based lateral flow device
- Future work should look into employing recombinant proteins instead of lysates that we used in this study to test efficiency of MUC 1 binding aptamers conjugated to MNPs for

biomarker enrichment. Future work should also involve use of other cancerous non target proteins to evaluate specificity of MUC 1 binding aptamers other than MCF 12 A that was used in this study.

- There is urgent need to search for an alternative source of phosphorous which can ease manipulation in synthetic steps which could result in nanocrystals with better quantum efficiency. There is also urgent need to come up with a method of directly synthesizing water soluble InP/ZnSe QDs since ligand exchange process contributes to loss of fluorescence.
- Further studies can be carried out to enhance the magnetic and fluorescent properties of the  $\alpha$ -Fe<sub>2</sub>O<sub>3</sub>-InP/ZnSe nanocomposite material and applied in other suitable applications.



UNIVERSITY *of the*  
WESTERN CAPE



## 7 Reference

- 1 C. Karamboulas and L. Ailles, *Biochim. Biophys. Acta*, 2013, **1830**, 2481–95.
- 2 W. C. Hahn, I. F. Dunn, S. Y. Kim, A. C. Schinzel, R. Firestein, I. Guney and J. S. Boehm, *Biochim. Biophys. Acta - Gen. Subj.*, 2009, **1790**, 478–484.
- 3 P. Anand, A. B. Kunnumakara, C. Sundaram, K. B. Harikumar, S. T. Tharakan, O. S. Lai, B. Sung and B. B. Aggarwal, *Pharm. Res.*, 2008, **25**, 2097–2116.
- 4 R. C. L. R. Lawrence H. Kushi, Colleen Doyle, Marji McCullough and K. A. T. G. Wendy Demark-Wahnefried, Elisa V. Bandera, Susan Gapstur, Alpa V. Patel, *CA. Cancer J. Clin.*, 2012, **62**, 30–67.
- 5 L. C. Knight, J. E. Romano, B. Krynska, S. Faro, F. B. Mohamed and J. Gordon, *J. Mol. Biomark. Diagn.*, 2010, **1**, 1–15.
- 6 H. Akasaka, R. Sasaki, K. Yoshida, I. Takayama, T. Yamaguchi, H. Yoshida and Y. Mizushina, *Biochim. Biophys. Acta - Gen. Subj.*, 2013, **1830**, 2517–2525.
- 7 J. Sariego, *Am. Surg.*, 2010, **76**, 1397–400.
- 8 P. Boyle and B. Levin, *World Cancer Report 2008*, 2008.
- 9 G. Malherbe, H. C. Steel, S. Cassol, T. De Oliveira, C. J. Seebregts, R. Anderson, E. Cassol and T. M. Rossouw, *Mediators Inflamm.*, 2014, **2014**, 1–8.
- 10 R. D. Rosenberg, W. C. Hunt, M. R. Williamson, F. D. Gilliland, P. W. Wiest, C. A. Kelsey, C. R. Key and M. N. Linver, *Radiology*, 1998, **209**, 511–8.
- 11 M. Sant, C. Allemani, R. Capocaccia, T. Hakulinen, T. Aareleid, J. W. Coebergh, M. P. Coleman, P. Grosclaude, C. Martinez, J. Bell, J. Youngson, F. Berrino, A. Kupp, G. Hedelin, G. Chaplain, C. Exbrayat, B. Tretarre, J. Mace-Lesech, A. Danzon, M. Mercier, N. Raverdy, E. Artioli, M. Federico, A. Barchielli, E. Paci, G. Gatta, P. Crosignani, D. Speciale, M. R. Ruzza, E. Frassoldi, A. Verdecchia, L. Gafa, R. Tumino, M. La Rosa, A. Voogd and E. M. I. Williams, *Int. J. Cancer*, 2003, **106**, 416–422.
- 12 A. M. Ugnat, L. Xie, J. Morriss, R. Semenciw and Y. Mao, *Br. J. Cancer*, 2004, **90**, 1138–43.
- 13 P. C. Gøtzsche and M. Nielsen, *Cochrane database Syst. Rev.*, 2011, CD001877.
- 14 U.S. Preventive Services Task Force, *Ann. Intern. Med.*, 2009, **151**, 716–726.
- 15 B. Friedenson, *MedGenMed*, 2000, **2**, E9.
- 16 P. Marić, P. Ozretić, S. Levanat, S. Orešković, K. Antunac and L. Beketić-Orešković, *Coll. Antropol.*, 2011, **35**, 241–247.

- 17 S. E. Bates, *Ann. Intern. Med.*, 1991, **115**, 623.
- 18 A. Jemal, R. Siegel, J. Xu and E. Ward, *CA. Cancer J. Clin.*, **60**, 277–300.
- 19 F. Lumachi, S. M. M. Basso, A. A. Brandes, D. Pagano and M. Ermani, *Anticancer Res.*, **24**, 3221–4.
- 20 L. H. Li, T. Kang, L. Chen, W. Zhang, Y. Liao, J. Chen and Y. Shi, *Int. J. Mol. Med.*, 2014, **33**, 77–82.
- 21 B. L. Stehouwer, W. J. M. van der Kemp, P. R. Luijten, M. A. A. J. van den Bosch, W. B. Veldhuis, J. P. Wijnen and D. W. J. Klomp, *Breast Cancer Res. Treat.*, 2014, **144**, 583–9.
- 22 H. A. Brauer, M. D’Arcy, T. E. Libby, H. J. Thompson, Y. Y. Yasui, N. Hamajima, C. I. Li, M. A. Troester and P. D. Lampe, *Breast Cancer Res. Treat.*, 2014, **144**, 299–306.
- 23 J. Chen, J. Lin, X. Zhang, S. Cai, D. Wu, C. Li, S. Yang and J. Zhang, *Anal. Chim. Acta*, 2014, **817**, 42–7.
- 24 K. Heer, H. Kumar, J. R. Read, J. N. Fox, J. R. T. Monson and M. J. Kerin, *Clin. Cancer Res.*, 2001, **7**, 3491–3494.
- 25 H. V. Pascal Bamford, Srinivas Chukka, Jim F. Martin, Anindya Sarkar, Olcay Sertel, Ellen Suzue, 2014.
- 26 N. T. Brewer, T. Salz and S. E. Lillie, *Ann. Intern. Med.*, 2007, **146**, 502–10.
- 27 E. Baldrich, J. L. Acero, G. Reekmans, W. Laureyn and C. K. O. Sullivan, *Anal. Chem.*, 2005, **77**, 4774–4784.
- 28 K. Liu, B. Lin and X. Lan, *J. Cell. Biochem.*, 2013, **114**, 250–255.
- 29 T. Šmuc, I. Y. Ahn and H. Ulrich, *J. Pharm. Biomed. Anal.*, 2013, **81–82**, 210–217.
- 30 X. Wu, J. Chen, M. Wu and J. X. Zhao, *Theranostics*, 2015, **5**, 322–44.
- 31 P. Hong, W. Li and J. Li, *Sensors*, 2012, **12**, 1181–1193.
- 32 S. Tyagi and F. R. Kramer, *Nat. Biotechnol.*, 1996, **14**, 303–308.
- 33 S. Marras, S.A.E., Kramer, F.R.Tyagi, *Humana Press Inc., Totowa, NJ*, 2003, **212**, 111–128.
- 34 P. Herdewijn, *Oligonucleotide Synthesis*, Humana Press, New Jersey, 2004, vol. 288.
- 35 L. Yang, Z. Cao, Y. Lin, W. C. Wood and C. A. Staley, *Cancer Biol. Ther.*, 2005, **4**, 561–70.
- 36 A. Tsourkas and G. Bao, *Brief.Funct.Genomic.Proteomic.*, 2003, **1**, 372–384.
- 37 J. H. Kim, D. Morikis and M. Ozkan, *Sensors Actuators B Chem.*, 2004, **102**, 315–319.

- 38 S. Song, L. Wang, J. Li, J. Zhao and C. Fan, *Trends Anal. Chem.*, 2008, **27**, 108–117.
- 39 N. C. Cady, A. D. Strickland and C. a. Batt, *Mol. Cell. Probes*, 2007, **21**, 116–124.
- 40 Q. Guo, Z. Bai, Y. Liu and Q. Sun, *Biosens. Bioelectron.*, 2016, **77**, 107–110.
- 41 W. Tan, K. Wang and T. J. Drake, *Curr. Opin. Chem. Biol.*, 2004, **8**, 547–553.
- 42 C. Ma, Z. Tang, X. Huo, X. Yang, W. Li and W. Tan, *Talanta*, 2008, **76**, 458–461.
- 43 G. Orru, F. Coghe, G. Faa, S. Pillai, C. Manieli, C. Montaldo, F. Pilia, G. Pichiri, V. Piras and P. Coni, *Diagnostic Mol. Pathol.*, 2010, **19**, 1–8.
- 44 M. Culha, D. L. Stokes, G. D. Griffin and T. Vo-Dinh, *Biosens. Bioelectron.*, 2004, **19**, 1007–1012.
- 45 J. Zhao, D. He, H. He, L. Li, L. L. Zhang and X. Y. Wang, *Urology*, 2007, **70**, 60–64.
- 46 Y. Xue, R. An, D. Zhang, J. Zhao, X. Wang, L. Yang and D. He, *Eur. J. Obstet. Gynecol. Reprod. Biol.*, 2011, **159**, 204–208.
- 47 D. Deng, D. Zhang, Y. Li, S. Achilefu and Y. Gu, *Biosens. Bioelectron.*, 2013, **49**, 216–221.
- 48 O. Adegoke, T. Kato and E. Y. Park, *Biosens. Bioelectron.*, 2016, **80**, 483–490.
- 49 D. Weller and T. McDaniel, *Adv. Magn. Nanostructures*, 2006, 1–508.
- 50 A. Demortière and C. Petit, *Langmuir*, 2007, **23**, 8575–84.
- 51 A.-H. Lu, E. L. Salabas and F. Schüth, *Angew. Chem. Int. Ed. Engl.*, 2007, **46**, 1222–44.
- 52 J. Cheon and J.-H. Lee, *Acc. Chem. Res.*, 2008, **41**, 1630–40.
- 53 J. Mccarty and R. Weissleder, *Adv. Drug Deliv. Rev.*, 2008, **60**, 1241–1251.
- 54 D. Bahadur and V. P. Dravid, *Adv. Drug Deliv. Rev.*, 2011, **63**, 1227.
- 55 Y. W. Jun, J. W. Seo and J. Cheon, *Acc. Chem. Res.*, 2008, **41**, 179–189.
- 56 H. M. Joshi, Y. P. Lin, M. Aslam, P. V Prasad, E. A. Schultz-Sikma, R. Edelman, T. Meade and V. P. Dravid, *J. Phys. Chem. C. Nanomater. Interfaces*, 2009, **113**, 17761–17767.
- 57 Q. A. Pankhurst, N. T. K. Thanh, S. K. Jones and J. Dobson, *J. Phys. D. Appl. Phys.*, 2009, **42**, 224001.
- 58 R. K. Zheng, H. Gu, B. Xu, K. K. Fung, X. X. Zhang and S. P. Ringer, *Adv. Mater.*, 2006, **18**.
- 59 Z. Xu, C. Shen, Y. Tian, X. Shi and H.-J. Gao, *Nanoscale*, 2010, **2**, 1027–1032.

- 60 S. Laurent, D. Forge, M. Port, A. Roch, C. Robic, L. Vander Elst and R. N. Muller, *Chem. Rev.*, 2008, **108**, 2064–110.
- 61 G. Salazar-Alvarez, H. Lidbaum, A. L-peç-Ortega, M. Estrader, K. Leifer, J. Sort, S. Suriach, M. D. Bar and J. Nogus, *J. Am. Chem. Soc.*, 2011, **133**, 16738–16741.
- 62 C. Pereira, A. M. Pereira, C. Fernandes, M. Rocha, R. Mendes, A. Guedes, P. B. Tavares, J. Grene, P. Arau and C. Freire, *Am. Chem. Soc.*, 2012, **4**, 1496–1504.
- 63 R. Ahmadi, E. Ranjarnodeh and N. Gu, *Mater. Sci.*, 2012, **30**, 382–389.
- 64 Z. R. Marand, M. Helmi, R. Farimani and N. Shahtahmasebi, *Nanomedicine J.*, 2014, **1**, 238–247.
- 65 S. Wu, A. Sun, F. Zhai, J. Wang, W. Xu, Q. Zhang and A. a. Volinsky, *Mater. Lett.*, 2011, **65**, 1882–1884.
- 66 H. J.-M. Lin Chia-Chang, *Ceram. Int.* **40**, 2014, **101**, 2–5.
- 67 J. Hu, X. Hu, A. Chen and S. Zhao, *J. Alloys Compd.*, 2014, **603**, 1–6.
- 68 Y. Liu, S. Jia, Q. Wu, J. Ran, W. Zhang and S. Wu, *Catal. Commun.*, 2011, **12**, 717–720.
- 69 I. Sharifi and H. Shokrollahi, *J. Magn. Magn. Mater.*, 2013, **334**, 36–40.
- 70 J. B. Mamani, A. J. Costa-Filho, D. R. Cornejo, E. D. Vieira and L. F. Gamarra, *Mater. Charact.*, 2013, **81**, 28–36.
- 71 Y. Wei, B. Han, X. Hu, Y. Lin, X. Wang and X. Deng, *Procedia Eng.*, 2012, **27**, 632–637.
- 72 S. Gyergyek, D. Makovec, A. Kodre, I. Arçon, M. Jagodič and M. Drogenik, *J. Nanoparticle Res.*, 2010, **12**, 1263–1273.
- 73 Y. Köseoğlu, *J. Magn. Magn. Mater.*, 2006, **300**, e327–e330.
- 74 A. Mandal, S. Sekar, M. Kanagavel, N. Chandrasekaran, A. Mukherjee and T. P. Sastry, *Biochim. Biophys. Acta*, 2013, **1830**, 4628–33.
- 75 A. Kiplagat, M. O. Onani, M. Meyer, T. A. Akenga and F. B. Dejene, *Phys. B Condens. Matter*, 2015, **480**, 1–9.
- 76 Z. Paulsen, M. O. Onani, G. R. J. Allard, A. Kiplagat, J. O. Okil, F. B. Dejene and G. M. Mahanga, *Phys. B Phys. Condens. Matter*, 2015, **480**, 1–7.
- 77 T. L. Kalber, C. J. Smith, F. A. Howe, J. R. Griffiths, A. J. Ryan, J. C. Waterton and S. P. Robinson, *Invest. Radiol.*, 2005, **40**, 784–91.
- 78 B. Zhang, B. Chen, Y. Wang, F. Guo, Z. Li and D. Shi, *J. Colloid Interface Sci.*, 2011, **353**, 426–32.
- 79 C. C. Lin and J. M. Ho, *Ceram. Int.*, 2014, **40**, 10275–10282.

- 80 A. Quarta, R. Di Corato, L. Manna, A. Ragusa and T. Pellegrino, *IEEE Trans. Nanobioscience*, 2007, **6**, 298–308.
- 81 A. L. Efros and M. Rosen, *Phys. Rev. Lett.*, 1997, **78**, 1110–1113.
- 82 F. Pinaud, X. Michalet, L. A. Bentolila, J. M. Tsay, S. Doose, J. J. Li, G. Iyer and S. Weiss, *Biomaterials*, 2006, **27**, 1679–87.
- 83 L. Li, M. Protière and P. Reiss, *Chem. Mater.*, 2008, **20**, 2621–2623.
- 84 L. Li and P. Reiss, *J. Am. Chem. Soc.*, 2008, **150**, 11588–11589.
- 85 D. C. Gary, B. a. Glassy and B. M. Cossairt, *Chem. Mater.*, 2014, **26**, 1734–1744.
- 86 E. Ryu, S. Kim, E. Jang, S. Jun, H. Jang, B. Kim and S. Kim, 2009, **21**, 2425–2427.
- 87 P. Reiss, M. Protière and L. Li, *Small*, 2009, **5**, 154–168.
- 88 M. Hines and P. GuyotSionnest, *J. Phys. Chem.*, 1996, **100**, 468–471.
- 89 G. Rousserie, A. Sukhanova, K. Even-Desrumeaux, F. Fleury, P. Chames, D. Baty, V. Oleinikov, M. Pluot, J. H. M. Cohen and I. Nabiev, *Crit. Rev. Oncol. Hematol.*, 2010, **74**, 1–15.
- 90 U. Resch-Genger, M. Grabolle, S. Cavaliere-Jaricot, R. Nitschke and T. Nann, *Nat. Methods*, 2008, **5**, 763–75.
- 91 H. J. Byun, J. C. Lee and H. Yang, *J. Colloid Interface Sci.*, 2011, **355**, 35–41.
- 92 M. R. Kim, J. H. Chung, M. Lee, S. Lee and D. J. Jang, *J. Colloid Interface Sci.*, 2010, **350**, 5–9.
- 93 P. Mushonga, M. O. Onani, A. M. Madiehe and M. Meyer, *Mater. Lett.*, 2013, **95**, 37–39.
- 94 Y. Kim, C. Ippen, T. Greco, J. Lee, M. S. Oh, C. J. Han, A. Wedel and J. Kim, *Opt. Mater. Express*, 2014, **4**, 1436.
- 95 V. Brunetti, H. Chibli, R. Fiammengo, A. Galeone, M. A. Malvindi, G. Vecchio, R. Cingolani, J. Nadeau and P. P. Pompa, *Nanoscale*, 2012, 307–317.
- 96 A. B. Iliuk, L. Hu and W. A. Tao, *Anal. Chem.*, 2011, **83**, 4440–4452.
- 97 D. Wang, J. He, N. Rosenzweig and Z. Rosenzweig, *Nano Lett.*, 2004, **4**, 3–7.
- 98 S. Amala Jayanthi, T. Manovah David, J. Jayashainy, D. Muthu Gnana Theresa Nathan and P. Sagayaraj, *J. Alloys Compd.*, 2014, **606**, 254–261.
- 99 Y. Xiong, C. Deng and X. Zhang, *Talanta*, 2014, **129**, 282–289.
- 100 M. Mascini, I. Palchetti and S. Tombelli, *Angew. Chem. Int. Ed. Engl.*, 2012, **51**, 1316–32.

- 101 Z. A. Peng and X. Peng, *J. Am. Chem. Soc.*, 2001, **123**, 183–184.
- 102 C. Shi, J. Meng and C. Deng, *Chem. Commun. (Camb)*., 2012, **48**, 2418–20.
- 103 J.-M. Shen, W.-J. Tang, X.-L. Zhang, T. Chen and H.-X. Zhang, *Carbohydr. Polym.*, 2012, **88**, 239–249.
- 104 X. Xu, C. Deng, M. Gao, W. Yu, P. Yang and X. Zhang, *Adv. Mater.*, 2006, **18**, 3289–3293.
- 105 Y. Xu, A. Karmakar, D. Wang, M. W. Mahmood, F. Watanabe, Y. Zhang, A. Fejleh, P. Fejleh, Z. Li, G. Kannarpady, S. Ali, A. R. Biris and A. S. Biris, *J. Phys. Chem. C*, 2010, **114**, 5020–5026.
- 106 Y. Xu, M. Mahmood, Z. Li, E. Dervishi, S. Trigwell, V. P. Zharov, N. Ali, V. Saini, A. R. Biris, D. Lupu, D. Boldor and A. S. Biris, *Nanotechnology*, 2008, **19**, 435102.
- 107 A. Roychowdhury, S. P. Pati, S. Kumar and D. Das, *Powder Technol.*, 2014, **254**, 583–590.
- 108 D. Das A. Roychowdhury, S.P. Pati, A.K. Mishra, S. Kumar, *J. Phys. Chem. Solids*, 2013, **74**, 811–818.
- 109 J. J. Li, Y. A. Wang, W. Guo, J. C. Keay, T. D. Mishima, M. B. Johnson and X. Peng, *J. Am. Chem. Soc.*, 2003, **125**, 12567–75.
- 110 J. Ma, Q. Fan, L. Wang, N. Jia, Z. Gu and H. Shen, *Talanta*, 2010, **81**, 1162–1169.
- 111 S. AKYUZ and T. AKYUZ, *Vib. Spectrosc.*, **42**, 387–391.
- 112 Q. Li, L. Tong, X. Chen, J. Shi, X. Ren and H. Yang, *J. Alloys Compd.*, 2013, **580**, 533–537.
- 113 L. Tong, X. Ding, X. Ren, X. Yang and H. Yang, *Dye. Pigment.*, 2014, **113**, 117–120.
- 114 G. Wang, C. Wang, W. Dou, Q. Ma, P. Yuan and X. Su, *J. Fluoresc.*, 2009, **19**, 939–946.
- 115 N. Gaponik, D. V Talapin, A. L. Rogach, K. Hoppe, V. Shevchenko, A. Kornowski, A. Eychmller, H. Weller, E. V Shevchenko and A. Eychmu, *J. Phys. Chem. B*, 2002, **106**, 7177–7185.
- 116 S. R. Ahmed, S. C. Hong and J. Lee, *Front. Mater. Sci.*, 2010, **5**, 40–49.
- 117 S. Ahmed, J. Dong, M. Yui, T. Kato, J. Lee and E. Y. Park, *J. Nanobiotechnology*, 2013, **11**, 28.
- 118 F. Ye, Å. Barrefelt, H. Asem, M. Abedi-Valugerdi, I. El-Serafi, M. Saghafian, K. Abu-Salah, S. Alrokayan, M. Muhammed and M. Hassan, *Biomaterials*, 2014, **35**, 3885–3894.
- 119 W. Zhang, Y. Li, H. Zhang, X. Zhou and X. Zhong, *Inorg. Chem.*, 2011, **50**, 10432–8.

- 120 E. Murugan and J. Nimita Jebaranjitham, *Chem. Eng. J.*, 2014, **259**, 266–276.
- 121 J. Jeong, E. K. Kwon, T. C. Cheong, H. Park, N. H. Cho and W. Kim, *ACS Appl. Mater. Interfaces*, 2014, **6**, 5297–5307.
- 122 W. Ki Bae, J. Kwak, J. W. Park, K. Char, C. Lee and S. Lee, *Adv. Mater.*, 2009, **21**, 1690–1694.
- 123 R. Abdullah Mirzaie, F. Kamrani, A. Anaraki Firooz and A. A. Khodadadi, *Mater. Chem. Phys.*, 2012, **133**, 311–316.
- 124 B. Prélôt, W. Janusz, F. Thomas, F. Villiéras, R. Charmas, W. Piasecki and W. Rudzinski, *Appl. Surf. Sci.*, 2002, **196**, 322–330.
- 125 V. Biju, Y. Makita, A. Sonoda, H. Yokoyama, Y. Baba and M. Ishikawa, *J. Phys. Chem. B*, 2005, **109**, 13899–905.
- 126 H. C. Gardner, D. E. Gallardo, C. Bertoni and S. Dunn, in *Photonics Europe*, eds. D. L. Andrews, J.-M. Nunzi and A. Ostendorf, International Society for Optics and Photonics, 2006, p. 61950N–61950N–8.
- 127 B. Liu, W. Xie, D. Wang, W. Huang, M. Yu and A. Yao, *Mater. Lett.*, 2008, **62**, 3014–3017.
- 128 B. Zhang, B. Chen, Y. Wang, F. Guo, Z. Li and D. Shi, *J. Colloid Interface Sci.*, 2011, **353**, 426–432.
- 129 J. Kim, J. E. Lee, S. H. Lee, J. H. Yu, J. H. Lee, T. G. Park and T. Hyeon, *Adv. Mater.*, 2008, **20**, 478–483.
- 130 J. E. Lee, N. Lee, T. Kim, J. Kim and T. Hyeon, *Acc. Chem. Res.*, 2011, **44**, 893–902.
- 131 N.-H. Cho, T.-C. Cheong, J. H. Min, J. H. Wu, S. J. Lee, D. Kim, J.-S. Yang, S. Kim, Y. K. Kim and S.-Y. Seong, *Nat. Nanotechnol.*, 2011, **6**, 675–82.
- 132 J. J. Moon, B. Huang and D. J. Irvine, *Adv. Mater.*, 2012, **24**, 3724–46.
- 133 A. Bershteyn, M. C. Hanson, M. P. Crespo, J. J. Moon, A. V Li, H. Suh and D. J. Irvine, *J. Control. Release*, 2012, **157**, 354–65.
- 134 Q. A. Pankhurst, J. Connolly, S. K. Jones and J. Dobson, *J. Phys. D. Appl. Phys.*, 2003, **36**, R167–R181.
- 135 V. S. Kalambur, B. Han, B. E. Hammer, T. W. Shield and J. C. Bischof, *Nanotechnology*, 2005, **16**, 1221–1233.
- 136 Y. Xu, M. Mahmood, Z. Li, E. Dervishi, S. Trigwell, V. P. Zharov, N. Ali, V. Saini, A. R. Biris, D. Lupu, D. Boldor and A. S. Biris, *Nanotechnology*, 2008, **19**, 435102.
- 137 D. Wang, J. He, N. Rosenzweig and Z. Rosenzweig, *Nano Lett.*, 2004, **4**, 409–413.

- 138 H. Akasaka, R. Sasaki, K. Yoshida, I. Takayama, T. Yamaguchi, H. Yoshida and Y. Mizushima, *Biochim. Biophys. Acta*, 2013, **1830**, 2517–25.
- 139 O. Chen, H. Wei, A. Maurice, M. Bawendi and P. Reiss, *Mater. Res. Soc.*, 2013, **38**, 696–702.
- 140 H. Tumturk, F. Sahin and E. Turan, *Analyst*, 2014, **139**, 1093–100.
- 141 L. I. U. Li, *Nat. Sci. Tech.*, 2008, **19**, 370–375.
- 142 M. Stanisavljevic, L. Janu, K. Smerkova, S. Krizkova, N. Pizurova, M. Ryvolova, V. Adam, J. Hubalek and R. Kizek, *Chromatographia*, 2013, **76**, 335–343.
- 143 Z. Yuan, A. Zhang, Y. Cao, J. Yang, Y. Zhu and P. Yang, *J. Fluoresc.*, 2012, **22**, 121–127.
- 144 J. S. Riffle, L. Harris-shekhawat, A. Carmichael-baranauskas, F. Mark, J. P. Dailey and D. Bardenstein, *Mol. Pharm.*, 2009, **6**, 1417–1428.
- 145 S. Naqvi, M. Samim, M. Z. Abdin, F. J. Ahmed, A. N. Maitra, C. K. Prashant and A. K. Dinda, *Int. J. Nanomedicine*, 2010, **5**, 983–989.
- 146 W. Zhao, R. Yang, T. Qian, X. Hua and W. Zhang, *Int. J. Mol. Sci.*, 2013, **14**, 12073–12089.
- 147 C. Sun, J. Lee and M. Zhang, *Adv. Drug Deliv. Rev.*, 2008, **60**, 1252–1265.
- 148 M. Houshiar, F. Zebhi, Z. Jafari, A. Alidoust and Z. Askari, *J. Magn. Magn. Mater.*, 2014, **371**, 43–48.
- 149 X. Li, Z. Li, D. Pan, Z. Xiang, S. Yoshimura and H. Saito, *Mater. Lett.*, 2014, **125**, 36–39.
- 150 J. B. Mamani, a. J. Costa-Filho, D. R. Cornejo, E. D. Vieira and L. F. Gamarra, *Mater. Charact.*, 2013, **81**, 28–36.
- 151 H. Meng, Z. Zhang, F. Zhao, T. Qiu and J. Yang, *Appl. Surf. Sci.*, 2013, **280**, 679–685.
- 152 B. Bajaj, B. D. Malhotra and S. Choi, *Thin Solid Films*, 2010, **519**, 1219–1223.
- 153 R. a Sperling and W. J. Parak, *Philos. Trans. A. Math. Phys. Eng. Sci.*, 2010, **368**, 1333–1383.
- 154 S. Singh, K. C. Barick and D. Bahadur, *J. Hazard. Mater.*, 2011, **192**, 1539–1547.
- 155 P. S. Haddad, T. M. Martins, L. D’Souza-Li, L. M. Li, K. Metze, R. L. Adam, M. Knobel and D. Zanchet, *Mater. Sci. Eng. C*, 2008, **28**, 489–494.
- 156 T. Burks, M. Avila, F. Akhtar, M. Göthelid, P. C. Lansåker, M. S. Toprak, M. Muhammed and A. Uheida, *J. Colloid Interface Sci.*, 2014, **425**, 36–43.
- 157 Y. Na, S. Yang and S. Lee, *Desalination*, 2014, **347**, 34–42.



- 158 B. R. White, B. T. Stackhouse and J. A. Holcombe, *J. Hazard. Mater.*, 2009, **161**, 848–853.
- 159 N. S. Holden and C. E. Tacon, *J. Pharmacol. Toxicol. Methods*, 2011, **63**, 7–14.
- 160 C. H. Liu, S. L. Sahoo and M. H. Tsao, *Colloids Surfaces B Biointerfaces*, 2014, **115**, 150–156.
- 161 Z. A. Peng and X. Peng, *J. Am. Chem. Soc.*, 2001, **123**, 183–184.
- 162 Y. W. Cao and U. Banin, *J. Am. Chem. Soc.*, 2000, **122**, 9692–9702.
- 163 M. T. Harrison, S. V. Kershaw, M. G. Burt, A. Eychmüller, H. Weller and A. L. Rogach, *Mater. Sci. Eng. B Solid-State Mater. Adv. Technol.*, 2000, **69**, 355–360.
- 164 P. M. Allen, B. J. Walker and M. G. Bawendi, *Angew. Chem. Int. Ed. Engl.*, 2010, **49**, 760–2.
- 165 D. C. Gary and B. M. Cossairt, *Chem. Mater.*, 2013, **25**, 2463–2469.
- 166 D. C. Gary, M. W. Terban, S. J. L. Billinge and B. M. Cossairt, *Chem. Mater.*, 2015, **27**, 1432–1441.
- 167 J. Park, S. Kim, S. Kim, S. T. Yu, B. Lee and S. W. Kim, *J. Lumin.*, 2010, **130**, 1825–1828.
- 168 A. T. R. Williams, S. A. Winfield and J. N. Miller, *Analyst*, 1983, **108**, 1067.
- 169 F. J. Lifei Xi, Kardynal, Beata, *Nanowires solid state Light.* "
- 170 K. Senthilkumar, T. Kalaivani, S. Kanagesan, V. Balasubramanian and J. Balakrishnan, *J. Mater. Sci. Mater. Electron.*, 2013, **24**, 692–696.
- 171 M. D. Abràmoff, P. J. Magalhães and S. J. Ram, *Biophotonics Int.*, 2005, **11**, 36–43.
- 172 T. Ma, W. M. Johnston and a Koran, *J. Dent. Res.*, 1987, **66**, 1438–1444.
- 173 L. Langof, L. Fradkin, E. Ehrenfreund, E. Lifshitz, O. I. Micic and a. J. Nozik, *Chem. Phys.*, 2004, **297**, 93–98.
- 174 H.-J. Byun, W.-S. Song and H. Yang, *Nanotechnology*, 2011, **22**, 1–6.
- 175 W. C. Chan and S. Nie, *Science*, 1998, **281**, 2016–8.
- 176 K. E. Sapsford, T. Pons, I. L. Medintz and H. Mattoussi, *Sensors*, 2006, **6**, 925–953.
- 177 D. Chen, R. Viswanatha, G. L. Ong, R. Xie, M. Balasubramanian and X. Peng, *J. Am. Chem. Soc.*, 2009, **131**, 9333–9.
- 178 R. Xie and X. Peng, *J. Am. Chem. Soc.*, 2009, **131**, 10645–51.

- 179 D. Mocatta, G. Cohen, J. Schattner, O. Millo, E. Rabani and U. Banin, *Science*, 2011, **332**, 77–81.
- 180 D. Sukanya and P. Sagayaraj, *Int.J. ChemTech Res.*, 2015, **7**, 1421–1425.
- 181 L. Almonte, E. Lopez-Elvira and A. M. Baro, *ChemPhysChem*, 2014, **15**, 2768–2773.
- 182 F. O. Silva, M. S. Carvalho, R. Mendonca, W. a a Macedo, K. Balzuweit, P. Reiss and M. a Schiavon, *Nanoscale Res. Lett.*, 2012, **7**, 536.
- 183 M. Shen, W. Jia, Y. You, Y. Hu, F. Li, S. Tian, J. Li, Y. Jin and D. Han, *Nanoscale Res. Lett.*, 2013, **8**, 2–6.
- 184 H. Xu and M. Hepel, *Anal. Chem.*, 2011, **83**, 813–819.
- 185 G. H. Du, Z. L. Liu, Q. H. Lu, X. Xia, L. H. Jia, K. L. Yao, Q. Chu and S. M. Zhang, *Nanotechnology*, 2006, **17**, 2850–2854.
- 186 K. Island, Z. R. Marand, N. Shahtahmasbi, M. R. Roknabadi, M. Hosseindokht, M. B. Mohagheghi, M. H. R. Farimani and R. Etefagh, *Nanomedicine J.*, 2014, **1**, 238–247.



UNIVERSITY of the  
WESTERN CAPE